CRANFIELD UNIVERSITY

BORIS SNAPIR

SAR REMOTE SENSING OF SOIL MOISTURE

SCHOOL OF ENGINEERING

Astronautics and Space Engineering

PhD

Academic Year: 2013-2014

Supervisor: Dr Stephen Hobbs

December 2014

CRANFIELD UNIVERSITY

SCHOOL OF ENGINEERING

Astronautics and Space Engineering

PhD

Academic Year: 2013 - 2014

BORIS SNAPIR

SAR Remote Sensing of Soil Moisture

Supervisor: Dr Stephen Hobbs

December 2014

This thesis is submitted in partial fulfilment of the requirements for the degree of PhD

Abstract

Synthetic Aperture Radar (SAR) has been identified as a good candidate to provide high-resolution soil moisture information over extended areas. SAR data could be used as observations within a global Data Assimilation (DA) approach to benefit applications such as hydrology and agriculture. Prior to developing an operational DA system, one must tackle the following challenges of soil moisture estimation with SAR: (1) the dependency of the measured radar signal on both soil moisture and soil surface roughness which leads to an ill-conditioned inverse problem, and (2) the difficulty in characterizing spatially/temporally surface roughness of natural soils and its scattering contribution.

The objectives of this project are (1) to develop a roughness measurement method to improve the spatial/temporal characterization of soil surface roughness, and (2) to investigate to what extent the inverse problem can be solved by combining multi-polarization, multi-incidence, and/or multi-frequency radar measurements.

The first objective is achieved with a measurement method based on Structure from Motion (SfM). It is tailored to monitor natural surface roughness changes which have often been assumed negligible although without evidence.

The measurement method is flexible, affordable, straightforward and generates Digital Elevation Models (DEMs) for a SAR-pixel-size plot with mm accuracy. A new processing method based on band-filtering of the DEM and its 2D Power Spectral Density (PSD) is proposed to compute the classical roughness parameters. Time series of DEMs show that non-negligible changes in surface roughness can happen within two months at scales relevant for microwave scattering.

The second objective is achieved using maximum likelihood fitting of the Oh backscattering model to (1) full-polarimetric Radarsat-2 data and (2) simulated multi-polarization / multi-incidence / multi-frequency radar data.

Model fitting with the Radarsat-2 images leads to poor soil moisture retrieval which is related to inaccuracy of the Oh model. Model fitting with the simulated data quantifies the amount of multilooking for different combinations of measurements needed to mitigate the critical effect of speckle on soil moisture uncertainty. Results also suggest that dual-polarization measurements at L- and C-bands are a promising combination to achieve the observation requirements of soil moisture.

In conclusion, the SfM method along with the recommended processing techniques are good candidates to improve the characterization of surface roughness. A combination of multi-polarization and multi-frequency radar measurements appears to be a robust basis for a future Data Assimilation system for global soil moisture monitoring.

Keywords: soil moisture, surface roughness, Synthetic Aperture Radar, Structure from Motion, chi-square

Acknowledgements

First my deep gratitude goes to my supervisor Dr Steve Hobbs for his valuable help throughout the three years of this research work. His insightful advice have always guided me from the writing of the PhD proposal to the writing of this thesis.

I also thank Dr Toby Waine particularly for his help on the interpretation of the roughness measurements.

I must also thank Ceri Dawson who provided me with the equipments to measure soil moisture.

I would like to thank Paul Colburn, the owner of the Holcotmoors farm, for his help throughout the experiments.

I also thank the Canadian Space Agency and MacDonald, Dettwiler and Associates Ltd. for providing RADARSAT-2 data via the SOAR Education International initiative, and also Fabiola Virich from MDA Geospatial Services who was very helpful when ordering the Radarsat-2 images.

I thank Dr Michael James from Lancaster University for his help with SfM georef and Dr Matthew Westoby who introduced me to Structure from Motion.

I must also thank all the persons who have not been directly involved in this research work, but who have made this 3 year experience invaluable.

First, I must thank Dr Laszlo Konozsy and Dr Uyi Igie who encouraged me to pursue a PhD at Cranfield University.

Then, I would like to thank all my friends met throughout my studies at Cranfield University, with special thanks to my PhD friends and my flatmates/housemates from India, Singapore, Malaysia, Germany, Netherlands, and Hong Kong. Beyond the technical knowledge gained during the PhD research, these persons gave me everlasting memories and tremendously enriched my personal experience.

I must also thank my parents for their constant support, and my girlfriend Sabrina who has always encouraged me and has brightened the few bad days.

Contents

List of Figures

List of Tables

Nomenclature

Abbreviations

ANN Artificial Neural Network

CSA Canadian Space Agency

DEM Digital Elevation Model

DFT Discrete Fourier Transform

ECMWF European Centre for Medium-Range Weather Forecasts

EO Earth Observation

FFT Fast Fourier Transform

FIR Finite Impulse Response

GeoSAR Geosynchronous SAR

GEWEX Global Energy and Water Cycle Experiment

IIR Infinite Impulse Response

LEO Low Earth Orbit

LUT Look Up Table

NBMI Normalized radar Backscatter soil Moisture Index

NWP Numerical Weather Prediction

OSCAR Observing Systems Capability Analysis and Review

PCA Principal Component Analysis

PDF Probability Distribution Function

PSD Power Spectral Density

SAR Synthetic Aperture Radar

SfM Structure from Motion

SIA Seasonal and Inter-Annual

SIFT Scale Invariant Feature Transform

SLC Single Look Complex

SMOS Soil Moisture and Ocean Salinity

TOPC Terrestrial Observing Panel for Climate

VSRF Very Short Range Forecasting

Symbols

ϵ Real part of the dielectric constant

ϵ Soil dielectric constant

f_s Sampling frequency ..... Hz

Γ_0 Fresnel reflectivity of the surface at nadir

k Wave number ..... rad/m

λ Wavelenght ..... m

m_v Volumetric soil moisture ..... m^3/m^3

ω_c Angular cutoff frequency ..... rad/s

p Co-polarized ratio

q Cross-polarized ratio

σ^0 Backscattering coefficient

θ Incidence angle ..... rad

Chapter 1

Introduction

This chapter provides (1) a description of the problem, (2) the objective of the research work, (3) an outline of the thesis, and (4) a list of publications and reviewed documents.

1.1 Problem statement

Soil moisture has been identified as a key parameter for many applications including numerical weather prediction (rainfall forecasting can be improved with soil moisture prediction[1]), flood forecasting and flood risk mapping (soil moisture dictates the partition between runoff and ground infiltration[2]), greenhouse gas accounting, and agriculture [3]. For agriculture, soil moisture can be used as a proxy to monitor crop temporal and spatial variation, to schedule irrigation, to select optimal crops for given soil conditions and to optimally reallocate water supplies during dry periods.

In situ measurements already provide reliable soil moisture measurements [4]. They are well suited for point measurements but cannot provide global information on the state of soil moisture over extended areas.

Spaceborne instruments are better candidates to sense moisture over larger areas. Soil moisture can be remotely sensed because soil emission from 1 to 5 GHz is strongly dependent on the soil dielectric constant ϵ which varies according to the level of soil moisture - $\epsilon \approx 6$ for dry soils and $\epsilon \approx 80$ for wet soils.

Passive spaceborne instruments (microwave radiometers) already provide usable products [5]. Their main limitation remains their coarse resolution. The Soil Moisture and Ocean Salinity mission (SMOS) provides soil moisture maps with a 50 km resolution which are useful for climatology[6], but are hardly usable for hydrology and agriculture. Such applications require field-scale resolution (0.1-1 km) [7]. This is achievable with Synthetic Aperture Radar (SAR).

Several SARs are now regularly providing images mainly at C- and X-band. Ultimately, these SAR observations could be used as the main inputs of a Data Assimilation system to routinely provide global soil moisture information. In practice, the assimilation of the SAR observations will be effective only once the core challenges of soil moisture estimation using SAR are solved. Theses challenges are

primarily related to soil surface roughness and vegetation. The vegetation challenge is due to the complex scattering mechanisms between vegetation cover and the underlying soil surface. Understanding these mechanisms supposes that scattering from bare soil surface alone is understood. This is not the case because of surface roughness. That is why the surface roughness challenge over bare soils is the focus of this research project.

More precisely, the surface roughness problem is twofold. First, while radar measurements show that the rougher the soil surface, the stronger the scattered radar signal, modeling explicitly the interaction between the incident radar wave and surface roughness of natural soils remains challenging. This is a critical obstacle because at high resolution, soil surface roughness is known to affect the radar signal as much as does soil moisture [8].

Second, regardless of the poor modeling of soil surface roughness, removing the ambiguity soil moisture / surface roughness by combining images with different radar configurations (multi-polarized, multi-frequency, or multi-incidence acquisitions [9, 10, 11]) is also arduous because the inverse problem is often ill-conditioned.

Several authors have related the first hurdle to a poor characterization of surface roughness over natural soils due to the limited capabilities of current in situ roughness measurement methods and processing tools [12, 13, 14, 15, 16]. Therefore the first aim of this project is to design a flexible measurement method which could allow investigating the surface roughness characterization problem.

A better roughness characterization is also desirable to investigate the validity of change detection methods relying on multitemporal acquisitions. These methods assume that soil surface roughness remains roughly constant throughout a series of observations [17, 18, 19, 20]. Following this assumption, changes in radar measurements are seldom due to variations in soil moisture and the constant scattering contribution of surface roughness can be discarded. This is a very attractive technique as the scattering contribution of surface roughness does not need to be explicitly modeled. However, at the moment there are no reliable data to confirm the stability of surface roughness over time. While the temporal and spatial variability of soil moisture has been widely investigated in hydrology [21, 22, 23, 24], knowledge about temporal roughness dynamics remains poor. That is why the design of the new roughness measurement method will be tailored to provide a better temporal characterization of surface roughness in order to verify the validity of change detection methods.

As for the second point - solving the ill-conditioned inverse problem for both soil moisture and surface roughness - combining images with different polarizations / frequencies / incidence does not guarantee that soil moisture and surface roughness will be properly estimated. Because of ill-conditioning, noise on the radar measurements (primarily speckle) or rounding errors during the computation can lead to very inaccurate model inversion [25]. That is why the second aim of the project is to investigate to what extent soil moisture and surface roughness can be retrieved, in particular with multi-polarized and multi-frequency radar measurements.

1.2 Objectives

The aim of this study is to investigate the feasibility of estimating soil moisture at field scale from radar measurements.

Two groups of objectives can be identified. The first group is related to obtaining a better temporal characterization of surface roughness from a new roughness measurement method, and the second group addresses the feasibility of retrieving soil moisture and surface roughness from different combinations of radar measurements.

O.0 Assess the feasibility of retrieving soil moisture at field scale from radar measurements

O.1 Design a measurement process suitable for investigating surface roughness spatial/temporal characterization for microwave scattering

The measurement process must include an acquisition method and a processing method suitable to estimate the roughness parameters required in backscattering model.

O.1.1 Assess roughness measurement error with regard to soil moisture estimation

Roughness measurements must be done at a level of accuracy which is acceptable for using in for soil moisture estimation

O.1.2. Assess the validity of the constant-roughness assumption made by change detection techniques

This requires assessing the error on soil moisture when eventual changes in surface roughness are neglected.

O.1.2.1. Characterize surface roughness temporal changes

This requires setting up an experiment which will generate time series of roughness measurements

O.1.2.1.1. Setup an experiment to compare the dynamics of surface roughness with the dynamics of soil moisture

O.2 Assess the robustness of model inversion based on the combination of multi-polarized / multi-frequency / multi-incidence radar measurements

This requires analyzing whether or not a given combination of measurements leads to a poorly-conditioned configuration with regard to noisy measurements.

O.2.1. Identify the parameters which drive uncertainty on the retrieved parameters

This includes identifying the different sources of uncertainty and how they propagate to uncertainty on the retrieved parameters.

O.2.2. Assess uncertainty on the retrieved soil moisture / surface roughness for different combinations of polarizations

Combining multi-polarized measurements is an attractive method because several operational satellites can provide at least dual-polarization images.

O.2.2.1. Test model inversion with real multi-polarization radar measurements
The method implemented to combine multi-polarization radar measurements will be tested with a set of full-polarimetric Radarsat-2 images acquired over Cranfield.

O.2.3. Assess uncertainty on the retrieved soil moisture / surface roughness for different combinations of incidences / frequencies
The performance obtained by combining multi-polarization measurements will be compared to combining different incidences / frequencies. The comparison will be based on simulations only.

O.2.4. Identify obstacles in meeting all the observation requirements defined for operational soil moisture monitoring
One must check that model inversion based on different SAR configurations is able to satisfy not only the uncertainty requirements, but also requirements on spatial resolution, time sampling, coverage, timeliness, and penetration depth.

1.3 Outline

The thesis is divided into eight chapters.

Chapter 1 describes the problem statement and the objectives of the research work.

Chapter 2 is a literature review which provides (2.1) a description of the surface roughness characterization problem with emphasis on the measurement methods available and the measurement requirements, (2.2) a survey of the backscattering models available for bare soil, and (2.3) an overview of the different soil moisture estimation methods.

Chapter 3 presents the methodology of the project. It includes (3.1) a list of the requirements to meet the objectives of the research, (3.2) a description of the setup for the first experiment, (3.3) a description of the setup for the second experiment, (3.4) the preprocessing steps of the Radarsat-2 images, and (3.5) a list of the observation requirements for soil moisture and surface roughness.

Chapter 4 describes all the measurements acquired during (4.1) the first experiment and (4.2) the second experiment.

Chapter 5 presents the results related to the roughness measurements with SfM. It comprises (5.1) an assessment of the performance of the SfM method, (5.2) results with regard to the spatial characterization of roughness, (5.3) results on the temporal variability of roughness, and (5.4) a summary of the chapter.

Chapter 6 presents the results related to model inversion with multiple radar measurements. It includes (6.1) soil moisture estimation with the multi-polarized Radarsat-2 measurements and simulated multi-polarized data, (6.2) soil moisture estimation with simulated multi-frequency data, and (6.3) a trade-off on the combination of radar measurements.

Chapter 7 is a global discussion of the thesis and on the soil moisture estimation problem.

Chapter 8 gives (8.1) a summary of the main findings of the research work, (8.2) a conclusion of the thesis with regard to the initial objectives, and (8.3) recommendations for future work.

1.4 Publications and others

Within the framework of the PhD research project, a research proposal and a journal article [26] have been written and accepted.

The research proposal was written in response to an announcement of opportunity [27] from the Canadian Space Agency (CSA) to investigate the benefits of the full-polarimetric imaging mode of Radarsat-2. The proposal has been reviewed and accepted by the CSA as part of the Science and Operational Applications Research Education International (SOAR-EI) Initiative.

Journal article:
Snapir, B., S. Hobbs, and T. W. Waine. "Roughness measurements over an agricultural soil surface with Structure from Motion." ISPRS Journal of Photogrammetry and Remote Sensing 96 (2014): 210-223.

Early results were also disseminated at conferences (without proceedings) such as the European Geosciences Union General Assembly 2012 [28], the Remote Sensing and Photogrammetric Society annual conference 2012.

Other journal articles / conference proceedings have been published as co-author. These are not directly related to the work presented in this thesis.

Hobbs, S.; Mitchell, C.; Forte, B.; Holley, R.; Snapir, B.; Whittaker, P., “System Design for Geosynchronous Synthetic Aperture Radar Missions”, Geoscience and Remote Sensing, IEEE Transactions on , vol.52, no.12, pp.7750,7763, Dec. 2014

Hobbs, S.E.; Snapir, B.; Corstanje, R.; Mitchell, C.; Forte, B.; Holley, R.; Whittaker, P.; Graham, K.; Burren, R., “Simulation of geosynchronous radar and atmospheric phase compensation constraints”, Radar Conference 2013, IET International , vol., no., pp.1,6, 14-16 April 2013

Kingston, J.; Hobbs, S.; Roberts, P.; Juanes-Vallejo, C.; Robinson, F.; Sewell, R.; Snapir, B.; Virgili Llop, J. and Patel, M., “Use of CYPRES™ cutters with a Kevlar clamp band for hold-down and release of the Icarus De-Orbit Sail payload on TechDemoSat-1”, Acta Astronautica, 100 pp. 82–93, (2014).

Chapter 2

Literature review

This chapter covers (1) the challenges posed by surface roughness characterization and overview of Surface from Motion, (2) a description of the backscattering models available for bare soils, and (3) an overview of the different soil moisture estimation methods.

2.1 Surface roughness characterization

2.1.1 Available measurement methods

The most common instruments used to measure surface roughness are: rope, meshboard, pin profiler, laser profiler, laser scanner, photogrammetry [14]. Each of them has advantages and disadvantages.

Ropes, pin profilers, laser profilers and meshboards take measurements along a profile. Among these measurement techniques, the laser profiler gives the most accurate results with vertical accuracy of a couple of millimeter[14]. Ropes are seldom used because of their poor accuracy. The main disadvantage of pin profilers and meshboards is that they are contact instruments which may modify the surface profile being measured. Because all these methods provide only 2D measurements they are poorly suitable for roughness characterization over agricultural soils which often present some degrees of anisotropy due to tillage operations[14].

Because microwave scattering is the result of the interaction of the incident electromagnetic wave with the soil surface, 3D measurements are preferable. Methods based on laser scanner and on photogrammetry have then been implemented to measure roughness parameters over Digital Elevation Models (DEMs), and have improved spatial analysis of roughness. Today both methods can produce quality DEMs with accuracy of a few millimeters even in outdoor conditions [29]. A higher robustness can be expected from 3D measurements because of the larger number of measurement points available[12]. The main downside of laser scanners with millimeter accuracy over extended area and resilience to outdoor conditions, is their cost. Photogrammetry might be more affordable but has other limitations. In particular, it can be accurate only if special care is taken for the setup (camera calibration, sturdy stand for targets/cameras, accurate knowledge of external orientation)[30]. This required setup accuracy might also be difficult to achieve

with muddy soils or windy conditions. Moreover, even though photogrammetry is becoming more accessible, post-processing still requires knowledge of photogrammetry. Therefore there is need for a more robust, systematic and accessible method to measure surface roughness. The novel method implemented in this study relies on a 3D imaging technique called Structure from Motion (SfM). The next section describes the principles of this technique.

2.1.2 Structure from Motion

Similarly to photogrammetry, SfM takes as input a set of pictures acquired with a commercial grade camera. The main difference is that these acquisitions are unconstrained which is a major practical advantage for SfM. The camera can be hand-held and a large variety of view points can be combined. Several commercial software (PhotoScan, Acute3D, Photomodeler) and open-source software (Photosynth, Photosynth Toolkit, SfM Toolkit, VisualSfM) are now available. Figure 2.1 shows the main steps of the 3D reconstruction pipeline[31].

The output of SFM Toolkit is a point cloud with arbitrary scale. If reference points are included in the imaged surface then the point cloud can be scaled with an additional open-source software, SfM-georef[32].

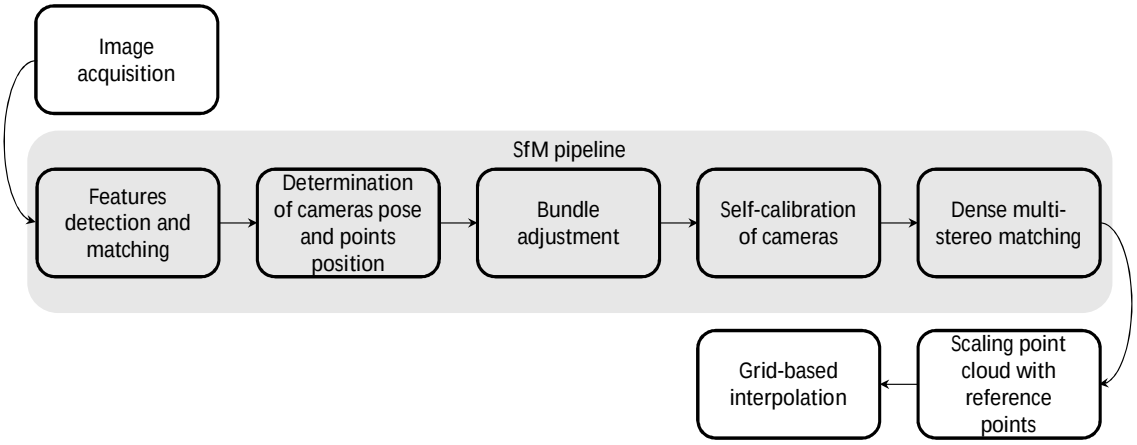

Figure 2.1: Typical SfM pipeline

Below is a brief description of the different processing steps involved in SfM. A more exhaustive description can be found in [31].

Features detection and matching/tracking The first processing step consists in identifying candidate features in each image. Each new feature is added to a common database of features. Then these features are tracked across the entire set of images. This step relies on the same techniques than those used for object/feature recognition. Scale Invariant Feature Transform (SIFT) is the feature detection method commonly implemented with SfM. Beyond its computational efficiency, this method is also robust against affine distortion, addition of noise, and change in illumination [33]. The latest point is very attractive for outdoor measurements for which light conditions can change throughout the acquisition step.

Robustness against distortion is also a serious advantage to deal with optical distortions of wide angle lens which are often used to limit the number of images while maintaining enough overlap.

Determination of cameras pose and points position The relative position of features identified for an initial stereo pair are used to retrieve the position of a first camera. This first camera is taken as the origin. The position of the other cameras is then added successively from the set of common features identified with the SIFT algorithm. At this point, the overall structure (3D position of cameras and features identified by SIFT) is determined up to an arbitrary scale.

Bundle adjustment Bundle adjustment consists in refining the structure. A least-squares minimization method such as the Levenberg-Marquardt algorithm is often implemented. The cost function to be minimized involves the *reprojection error.* For a given image, it is the distance between the projection of a 3D point and its true position on the image. Bundle adjustment can be computationally intensive for large project when it has to handle a few hundreds of view points with a few thousands of 3D points.

Self-calibration of cameras This step consists in estimating the interior orientation of each camera. It is important to correct for optical distortion when wide angle lens are used. Radial and tangential distortions are first estimated with a polynomial model, then corrected for each image.

Dense multi-stereo matching The sparse point cloud, cameras pose and corrected images are then used to reconstruct much more 3D points. The output of this step is an unscaled dense point cloud.

Geo-referencing In order to geo-reference or simply scale the point cloud, at least three points with known 3D position must appear on some overlapping images. More than three points, preferably around the edges of the imaged zone, should be used for a more accurate scaling.

SfM has been used for diverse applications including architectural conservation [34, 35], in geosciences to study hardly accessible landscapes such as volcano or coastal cliffs [36, 37, 32]. Use of SfM to assist on-orbit servicing for space missions has also been investigated [38]. At the time of writing there are no examples in the literature of soil roughness measurements with SfM. Nonetheless, useful information on measurement uncertainty can be extracted from some of the aforementioned publications.

With SfM, Irschara *et al.* generated a 3D model of a building (several tens of meters) from 615 still images taken with a commercial-grade camera on-board a UAV, with a estimated RMS error of 3.2 cm [35].

In [36], Westoby *et al.* produced several DEMs of landscape scenes of tens of meters from a set of ~800 images, with a mean error of 0.124 m, 0.058 m and 0.031 m respectively for the x-, y-, z-coordinates.

In [32], James and Robson applied SfM to three scenes of various sizes. For the first scene - a volcanic bomb sample with a size of ~10 cm - the DEM uncertainty was about 0.5 mm. The second scene - a coastal cliff of ~50 m - led to an uncertainty of 15 mm. Finally the third scene - the Summit Craters of Piton de la Fournaise with a typical scale of 1.6 km - was reconstructed with an uncertainty of 10 cm. From these three examples, the authors concluded that the ratio *measurement error : mean acquisition height* was about 1:1000, *i.e.* with a set of pictures taken at a height of 1 m SfM can reach a 1 mm measurement error. This ratio roughly matches the results obtained in [35] and [36] (cm error for a scene of several tens of meters).

2.1.3 Surface roughness parameters

Most backscattering models account for surface roughness with three parameters: RMS height s, Autocorrelation function r, and correlation length l [12, 14]. This set of parameters assumes that surface roughness can be described as a single scale stationary process. Fractals have been used to represent multiscale surfaces, but the complexity of these descriptions (larger number of roughness parameters) is poorly suitable when the inverse problem must be solved[14]. Therefore only the classical single scale description is considered in this study.

The RMS height, equivalent to the standard deviation of height, is given by

$$s^2 = \frac{1}{n-1}\sum_{i=1}^{n}(z(i)-\bar{z})^2 \tag{2.1}$$

with n the number of height measurements, $z(i)$ the i^{th} height measurement, and $\overline{z}$ the mean height. The $z(i)$ can be measurements along a transect or over a surface.

The autocorrelation function is commonly estimated from the empirical semi-variogram γ following that $r = s^2 - \gamma$ [39]. And γ is given by

$$\gamma(x) = \frac{1}{2}\mathrm{Var}\left[z(i+x) - z(i)\right] \tag{2.2}$$

with $\mathrm{Var}[\cdot]$ the variance.

The semi-variogram can be computed along a transect or all over the DEM. In the latter case, it is called omnidirectional semi-variogram as it ignores the direction of the measurements [12].

Finally, the correlation length is usually taken as the distance by which the normalized autocorrelation function decreases by $1/e$. In practice, an exponential or Gaussian model is fitted to the empirical autocorrelation function

$$r_{exp}(x) = e^{-x/l} \tag{2.3}$$

$$r_{gauss}(x) = e^{-(x/l)^2} \tag{2.4}$$

where l is adjusted through least square regression. Compared to the Gaussian ACF, the exponential ACF is characterized by a faster decrease at small lags. This makes

the exponential ACF better suited to describe small-scale roughness features [14]. The majority of previous roughness measurements over agricultural soil surfaces suggests that the exponential model is usually more suitable than the Gaussian model [40].

While the previous expressions were defined in the spatial domain, it is also possible to compute the roughness parameters in the frequency domain from the Fourier transform. The main advantage of the Fourier based method is its computational efficiency. This advantage becomes particularly noticeable for large data sets. For example in [39, 15, 12], whether the semi-variogram is computed along transects or all over the DEM, the method is too slow to handle high resolution 3D measurements. The semi-variogram has to be computed either for reduced-sized DEMs, or for sub-sampled DEMs. There are only a couple of studies making use of the Fourier transform to compute the roughness parameters [41, 42], certainly because the gain in computational time is not significant for roughness measurements made along profiles which do not have many sampling points.

Both the RMS height and the autocorrelation function can be computed from the power spectral density (PSD) of the height measurements. The 2D PSD can be estimated from the periodogram which is determined with the Discrete Fourier Transform (DFT) of a given DEM [43]. One can write the DFT Z of a DEM z as follows,

$$Z_{p,q} = \sum_{m=0}^{M-1} \sum_{n=0}^{N-1} z_{m,n} \exp\left(-2\pi i \left(\frac{mp}{M} + \frac{nq}{N}\right)\right) \tag{2.5}$$

Then the coefficients of the 2D periodogram, by analogy with the 1D periodogram [43], can be written as follows after accounting for redundant coefficients,

$$\begin{aligned}
S_z(0,0) &= 1/(MN)^2 \left|Z_{0,0}\right|^2 \\
S_z(p,q) &= 1/(MN)^2 \left(\left|Z_{p,q}\right|^2 + \left|Z_{p,N-q}\right|^2 + \left|Z_{M-p,q}\right|^2 + \left|Z_{M-p,N-q}\right|^2\right) \\
S_z(p,v) &= 1/(MN)^2 \left(\left|Z_{p,v}\right|^2 + \left|Z_{M-p,v}\right|^2\right) \\
S_z(u,q) &= 1/(MN)^2 \left(\left|Z_{u,q}\right|^2 + \left|Z_{u,N-q}\right|^2\right) \\
S_z(0,N/2) &= 1/(MN)^2 \left|Z_{0,N/2}\right|^2 \\
S_z(M/2,0) &= 1/(MN)^2 \left|Z_{M/2,0}\right|^2 \\
S_z(M/2,N/2) &= 1/(MN)^2 \left|Z_{M/2,N/2}\right|^2
\end{aligned} \tag{2.6}$$

with $p = 1, 2, \ldots, (M/2-1)$, $q = 1, 2, \ldots, (N/2-1)$, $u = 0\,\text{or}\,M/2$, and $v = 0\,\text{or}\,N/2$.

From Parseval identity, the variance of z is the integral of its PSD, hence the RMS height is given by,

$$s^2 = 1/(MN-1)\left(\sum_{m=0}^{M/2}\sum_{n=0}^{N/2} S_z(m,n) - S_z(0,0)\right) \tag{2.7}$$

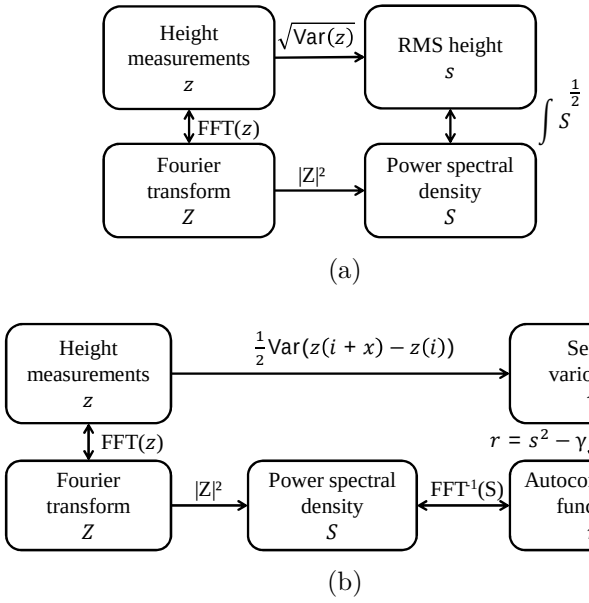

Figure 2.2: Computation of (a) RMS height and (b) autocorrelation function in the spatial domain and in the frequency domain

As for the autocorrelation function, it is given by the inverse Fourier transform of the full PSD. For a given transect, the normalized autocorrelation can be expressed as,

$$r(k) = 1/(MS_z(0)) \sum_{m=0}^{M-1} S_z(j) \exp(i2\pi km/M) \tag{2.8}$$

Figure 2.2 summarizes the different steps of the spatial-domain method and the frequency-domain method. In the end both methods lead to the same results. In practice, with the Fast Fourier Transform (FFT), computing r with this method is more suitable when dealing with large number of points, compared to the time-expensive semi-variogram method.

While equation 2.8 expresses the 1D autocorrelation function, a similar expression can be derived for the 2D autocorrelation. It is the inverse Fourier transform of the 2D PSD. However, to the author knowledge, it is not straightforward to compute the equivalent of the omnidirectional autocorrelation function from the Fourier transform.

In practice, it is not clear whether a directional autocorrelation function (from a 1D or 2D autocorrelation function) or an omnidirectional autocorrelation is the most suitable for microwave scattering. Previous studies have been using mainly directional estimations along transects because 3D measurements were not available. The few studies which introduced 3D measurements with laser or photogrammetry, highlighted the benefits of omnidirectional estimations in terms of their statistical robustness and not because they may be more adapted than directional estimations [12, 39]. As the radar response is the result of interactions of the incident electromagnetic wave with the soil surface and not with soil profiles, directional estimations parallel to the direction of the wave vector from the 2D autocorrelation function of the soil surface could give a more sensible roughness characterization.

Roughness class	**Scale** [mm]	**Characteristic features**
micro roughness	≤ 2	soil texture
random roughness	$2 - 200$	soil aggregates, clods
oriented roughness	$200 - 400$	tillage patterns
topography	≥ 400	field slope

Table 2.1: Typical roughness classes for agricultural fields [44]

This processing method is investigated in the Results section (section 5.2.5).

2.1.4 Surface roughness spatial and temporal variability

Spatial variability The spatial variability of roughness over agricultural soil has been mainly investigated with measurements along transects[14], with only a few studies making use of 3D measurements[39, 44, 12]. These studies report an increase in RMS height with the length of the transect (or the size of the DEM). The convergence of the RMS height toward an asymptotic value is not always clear. This is due to either a too short profile length, or the presence of multiple scales of surface roughness.

With simulated roughness profiles which match the assumptions of single scale roughness with exponential correlation function, Oh *et al.* showed that in order to reach a precision of $\pm 10\%$ on the RMS height and the correlation length, the profile length must be at least $40\bar{l}$ long and $200\bar{l}$ long respectively, with $\bar{l}$ the true correlation length which is unknown in practice [45]. Similar results were found with simulations by Dierking [46].

Even when the profile is long enough, the roughness parameters might not converge when surface roughness cannot be described as a single scale random process. This is often the case of tilled soils. Marzahn *et al.* identified four roughness classes which are listed in table 2.1 [44]. As a result, when the profile length increases, the inclusion of larger roughness scales increases height variance which lead to an increase in RMS height. And because large scale features tend to remain correlated over long distances, the correlation length also increases with profile length.

Temporal variability In order to simplify the retrieval of soil moisture from radar measurements, surface roughness is sometimes assumed to be constant over a given period[47, 48, 17, 18, 19, 20, 49]. This assumption allows applying a change detection method to a series of radar measurement for which soil moisture is said to be the only changing parameter. At the moment there are no reliable observations to confirm this assumption. Knowledge about temporal roughness dynamics remains poor.

Surface roughness changes primarily because of tillage operations and weather conditions (rainfall, freeze/thaw) [50, 51]. While tillage operations produce noticeable and relatively deterministic changes according to the tool used [50], natural changes especially from rainfalls are less easily traceable. Previous studies related to changes due to rainfall can be found mainly in soil erosion research which investigates rill network formation and soil transport [52, 53, 54, 55]. C. Huang *et*

al. thoroughly described the series of transformation through which the soil surface goes under rainfalls - it goes "from a loosely aggregated condition to a consolidated crust and then toward the development of erosional features such as rills"[56]. Exponential models were used to describe the decrease in roughness with the amount of rain. Zobeck *et al.* suggested the following empirical equation to predict change in roughness due to rainfall [50]:

$$s_{t2} = 0.89 s_{t1} e^{-0.0026\,\mathrm{Rain}} \tag{2.9}$$

with s_{t1} and s_{t2} the RMS height before and after rainfall, and Rain the rainfall amount in mm.

However, as these erosion studies rely on experiments with simulated storms (40 mm/h) or in tropical region [57], with highly inclined soil surface (10°), applicability of these results to roughness changes due to light rainfall (a few mm of rain per hour) is questionable.

In research related to radar remote sensing, very few analysis of natural changes in roughness are available. Callens *et al.* analyzed the effect of natural rainfall on their roughness measurements along transects which spanned almost over three months [58]. They could detect a slight decrease in RMS height over a cultivated plot, while the rest of the measurements did not reflect any meaningful variations. Marzahn *et al.* also noticed a smoothing effect due to natural rainfall characterized by a decrease in RMS height and an increase in correlation length for some DEMs acquired 5 months apart [12]. Alvarez-Mozos *et al.* analyzed changes in roughness parameters for 5 acquisition dates across 4 months, with measurements along transects [51]. However, for each date, the measurements were not made at the exact same locations. The observed variations were rather erratic, without correlation between RMS height and correlation length. In summary, there is no trace in the literature of analysis of a time series of roughness measurements systematically acquired over the same plot.

2.1.5 Resolution, extent, and accuracy of roughness measurements for microwave scattering

This section is of particular importance as it reports information about the requirements which must be met by the roughness measurements. It will be referred to when defining the requirements of the SfM based measurement setup.

Resolution As a rule of thumb, the incident electromagnetic wave is not sensitive to roughness features smaller than $\lambda/10$, with λ the radar wavelength. Table 2.2 gives the wavelengths of interest for remote sensing of soil moisture. Usually, the L- and C-bands are preferred for their higher sensitivity to soil moisture. Even with the shortest wavelength (X-band), the incident wave would be insensitive to details smaller than 2.5 mm. Therefore roughness measurements should not account for micro roughness.

Extent It is still not clear which of the larger spatial scales need to be captured to account for their effect in backscattering models [13]. Manninen points that rough-

Frequency band	$\boldsymbol{\lambda}$[cm]
P / UHF	$30 - 100$
L	$15 - 30$
S	$7.5 - 15$
C	$3.75 - 7.5$
X	$2.5 - 3.75$

Table 2.2: Useful frequency bands to sense soil moisture

ness statistics should ideally be characterized over a pixel-size surface [59]. Current spaceborne SAR instruments, such as RADATSAT-2 [60], can achieve standard resolution of about 10 m, hence the measurements should cover a surface of about $10 \times 10\,\mathrm{m}$. It is worth noting that this is not necessarily true since it implies that multiple scattering occurs on the scale of the full pixel which is unlikely. In comparison, Ulaby *et al.* [61] argues that only the small roughness scales relative to the radar wavelength should be included in the roughness parameters, while larger scales of a pixel should be accounted for directly in the backscattering model. There is also evidence from the *flashing field* phenomenon that oriented roughness from tillage affects microwave scattering [16, 62, 63, 64]. Perpendicular to the tillage direction, strong backscattering responses have been observed and related to the tillage structure.

In summary, the following statements seem reasonable:

- micro roughness is irrelevant,
- random roughness has to be captured,
- oriented roughness might be relevant especially when the wave incidence plane is quasi-orthogonal to the row tillage direction,
- topography should be accounted for in the backscattering model (local incidence angle), but not in the roughness parameters.

Accuracy Lievens *et al.* investigated the effect of uncertainty on height measurements with ten 4 m long simulated surface profiles with a 1 mm resolution [13]. They report that a 5 mm uncertainty produces up to a $0.08\,\mathrm{m}^3/\mathrm{m}^3$ uncertainty on soil moisture, when soil moisture is estimated with the Integral Equation Model (IEM), using a single radar polarization over a wet and smooth soil. They recommend a 2 mm uncertainty on height measurement as it produces at worst a $0.02\,\mathrm{m}^3/\mathrm{m}^3$ uncertainty on soil moisture. This is fortunate since current outdoor roughness measurements are hardly more accurate than a couple of millimeters. From the previous applications of SfM (section 2.1.2), mm accuracy seems achievable with images taken at a height of ~1 m.

Measurement requirements will be discussed further in section 3.2.2.1 (Methodology). The next section describes the different types of backscattering models available to relate radar measurements with soil moisture and surface roughness.

2.2 Backscattering models for bare soils

2.2.1 Overview of available models

There are three types of backscattering models: (1) empirical models, (2) theoretical models, (3) semi-empirical models.

2.2.1.1 Empirical models

Empirical models are attractive because of their simplicity and their good accuracy under restricted conditions [65, 66, 67]. These models usually assumes an affine relationship between backscattering coefficient σ^0 and soil moisture m_v[68],

$$\sigma^0 = am_v + b \tag{2.10}$$

with a and b two constants which are determined by data fitting. The data can be real radar measurements [68], or simulated measurements from a more complicated/global theoretical model [18]. The constant a depends on the radar configuration (polarization, incidence angle, frequency). The constant b accounts for the effect of surface roughness and also depends on the radar configuration. Therefore this model is determined for a given radar configuration, and a given surface roughness. Soil moisture is the only variable. It follows that the validity of the model is limited in space because neighboring fields may have a different surface roughness, and limited in time because surface roughness can change with time. Radar images must also undergo some normalizations to account for eventual changes in radar configurations.

These models are the basis of the simplest change detection methods. Typically, a radar measurement σ^0_{dry} acquired under dry soil condition is taken as reference. With a second acquisition σ^0 with wet soil condition and the same surface roughness, one can write,

$$\sigma^0 - \sigma^0_{dry} = a(m_v - m_{v,dry}) \tag{2.11}$$

Assuming that $m_{v,dry}$ is small compared to m_v, the model simplifies into $\sigma^0 - \sigma^0_{dry} \approx am_v$ [69]. The validity of the model is not limited in space anymore since the constant b disappeared. It still limited in time, as it assumes that surface roughness remains the same relative to the measurement reference σ^0_{dry}.

Under the same assumptions, Shoshany *et al.* defined the Normalized radar Backscatter soil Moisture Index (NBMI) [48],

$$\text{NBMI} = \frac{\sigma^0_{t1} + \sigma^0_{t2}}{\sigma^0_{t1} - \sigma^0_{t2}} \tag{2.12}$$

Thoma *et al.* also defined a $\Delta - \text{index}$[70]

$$\Delta - \text{index} = \left| \frac{\sigma^0_{wet} - \sigma^0_{dry}}{\sigma^0_{dry}} \right| \tag{2.13}$$

Both indices reflect a change solely attributed to soil moisture from a reference acquisition to a second acquisition. The main advantage of these change detection

techniques is that the dependency to surface roughness, however complicated it might be, does not need to be explicitly known. On the downside, the method is valid only over a limited period of time, and required same radar configuration for all images or some form of radar normalization.

In summary, empirical models are attractive for their simplicity and effectiveness but they are not suitable for long term operational applications because of their specificity to a given radar configuration and surface roughness.

2.2.1.2 Theoretical models

All the theoretical are based on numerical or analytical solutions of Maxwell's equations for the interaction of the incident electric and magnetic fields in a conducting medium.

Numerical solutions have been used to test the validity of analytical solutions[69]. In practice, because they are computationally intensive, their applicability is limited to two dimensions or to surface area of 8-10 times the wavelength.

The most widely used analytical solutions are the Kirchhoff approximation, the Small Perturbation approximation and the Integral Equation Model[69]. The first two approximations have a narrow range of validity.

The Kirchhoff approximation is valid for surface roughness with large dimensions relative to the wavelength. Two modifications can then be applied to obtain an analytical solution[71]. The first one leads to the Geometric Optics Model which is valid for very rough surface ($ks > 2$). The second one leads to the Physic Optics Model which is valid for rough surface ($ks > 0.25$).

In comparison, the Small Perturbation Model can be applied to surface roughness with small dimensions relative to the wavelength.

The IEM is by far the most widely used theoretical model because of its wider range of validity. It also provides a good approximation of the Geometric Optics Model and the Small Perturbation Model. From its introduction in 1992 by Fung *et al.* [72], the IEM has been modified numerous times to improve its applicability. In particular, Chen *et al.* suggested a more complete expression of the single-scattering terms [73]. It is called the Advanced IEM (AIEM) and agrees with numerical simulation over a wider range of roughness than the original IEM. Nonetheless, not denying the mathematical validity of the model, its applicability to natural soil surfaces led to poor results [69, 74]. This has been attributed to a bad adequacy between the IEM surface roughness assumptions (single scale stationary random process) and natural surface roughness. Baghdadi *et al.* improved the agreement between simulated σ^0 and measured σ^0 by treating the correlation length as a calibration parameter [75]. However, similarly to the limitations of empirical models, this calibration step makes the IEM site specific.

Another downside of the IEM is its relative complexity, especially for the cross-polarization σ^0_{vh}, compared to empirical models. As a result, inversion of the IEM usually relies on Look Up Tables (LUT) [76, 77], or on a simplified fit of the IEM[18, 78].

2.2.1.3 Semi-empirical models

Semi-empirical models are a good tradeoff between the complexity of theoretical models and the specificity of empirical models. They are based on a fit of sensible functional forms to a large data set. The data set covers a wide range of radar configurations (frequency band, incidence angle) and soil configurations (soil moisture, surface roughness) to avoid site specificity. The two most used semi-empirical models are the model from Oh *et al. [79]* and the model from Dubois[80].

The Dubois model The Dubois model gives an expression for the co-polarized backscattering coefficients σ^0_{hh} and σ^0_{vv}, but ignores the cross-polarization σ^0_{vh} which is too sensitive to system noise [80]. The model was obtained by fitting the function forms for σ^0_{hh} and σ^0_{vv} to a dataset comprising truck-mounted radar measurements (RASAM data set) and airborne radar measurements (POLARSCAT data set). No explicit information on the quality of the fit is given. The authors only report the RMS error on soil moisture (4.5%) and surface roughness (0.34 cm) when the model is inverted with the data sets use for fitting.

$$\sigma^0_{hh} = 10^{-2.75}\frac{\cos^{1.5}\theta}{\sin\theta^5}10^{0.028\epsilon\tan\theta}\left(ks\sin^{1.4}\theta\right)\lambda^{0.7} \tag{2.14}$$

$$\sigma^0_{vv} = 10^{-2.35}\frac{\cos^{3}\theta}{\sin\theta}10^{0.046\epsilon\tan\theta}\left(ks\sin^{3}\theta\right)^{1.1}\lambda^{0.7} \tag{2.15}$$

with θ the incidence angle, k the wave number, and ϵ the real part of the dielectric constant.

The model is valid for frequencies between 1.5 and 11 GHz, RMS height between 3 and 30 mm, and incidence angle between 30 and 65°. Dubois *et al.* note that the model does not agree with predictions from the Small Perturbation Model. Therefore they further restrict the model to $ks \leq 2.5$ and $\theta \geq 30°$.

The dielectric constant ϵ can be related to soil moisture through empirical polynomial expressions from Hallikainen *et al.* [81]. This step further decreases the validity of the model to soil moisture below $0.35\,\mathrm{m}^3/\mathrm{m}^3$.

The Oh model The Oh model went through a series of modifications since its initial formulation in 1992 [79]. The initial formulation gives an expression for the co-polarized ratio $p \equiv \sigma^0_{hh}/\sigma^0_{vv}$ and the cross-polarized ratio $q \equiv \sigma^0_{vh}/\sigma^0_{vv}$,

$$p = \left[1 - \left(\frac{\theta}{90°}\right)^{(3\Gamma_0)^{-1}} e^{-ks}\right]^2 \tag{2.16}$$

$$q = 0.23\sqrt{\Gamma_0}\left(1 - e^{-ks}\right) \tag{2.17}$$

where

$$\Gamma_0 = \left|\frac{1-\sqrt{\epsilon}}{1+\sqrt{\epsilon}}\right|^2 \tag{2.18}$$

is the Fresnel reflectivity of the surface at nadir.

	σ^0_{vh}	p	q
RMSE [dB]	2.35	0.82	2.06

Table 2.3: RMS error for the data-fitting of the Oh model

Model	**Parameter**	**Scattering range**
σ^0_{vh}	ks	20.9 dB
	θ	10.3 dB
	m_v	6.0 dB
p	ks	7.1 dB
	θ	6.2 dB
	m_v	4.1 dB
q	ks	7.9 dB
	θ	7.0 dB
	s/l	4.2 dB

Table 2.4: Sensitivity of the Oh model to each parameter in its 95% range [83]

The expression for q was modified in [82] to account for the incidence angle,

$$q = 0.25\sqrt{\Gamma_0}\left(0.1 + \sin^{0.9}\theta\right)\left(1 - e^{-(1.4-1.6\Gamma_0)ks}\right) \tag{2.19}$$

The expression for p and q were further modified in [83] and an expression for σ_{vh} was added,

$$\sigma^0_{vh} = 0.11 m_v^{0.7}(\cos\theta)^{2.2}\left[1 - \exp(-0.32(ks)^{1.8})\right] \tag{2.20}$$

$$p = \frac{\sigma^0_{hh}}{\sigma^0_{vv}} = 1 - \left(\frac{\theta}{90^\circ}\right)^{0.35 m_v^{-0.65}} \exp\left(-0.4(ks)^{1.4}\right) \tag{2.21}$$

$$q = \frac{\sigma^0_{vh}}{\sigma^0_{vv}} = 0.1\left(\frac{s}{l} + \sin 1.3\theta\right)^{1.2}\left[1 - \exp\left(-0.9\,(ks)^{0.8}\right)\right] \tag{2.22}$$

Note that the model which links the dielectric constant to soil moisture is now included in the expressions of σ^0_{vh}, p, and q. The RMS errors obtained after the data-fitting process are given in table 2.3. The RMS error for σ^0_{vh} is the largest which must be due to the weak backscattering response at cross-polarization. Since q depends on σ^0_{vh}, it also has a large RMS error compared to p. Table 2.4 shows the sensitivity of the Oh model to each parameters of the model. At best, the range of soil moisture leads to a scattering range of $4 - 6$ dB. Therefore the RMS errors of a couple of dBs obtained for the fitting of the Oh model are not negligible. This suggests that reliable soil moisture estimation will require combining multiple measurements, even when soil moisture is the only unknown.

Finally, after noticing that q was only weakly dependent on the correlation length l, Oh suggested a simplified expression for q which depends only on the RMS height [10],

$$q = 0.095\,(0.13 + \sin 1.5\theta)^{1.4}\left[1 - \exp\left(-1.3\,(ks)^{0.9}\right)\right] \tag{2.23}$$

This model is valid for $0.04 < m_v < 0.291\,\mathrm{m}^3/\mathrm{m}^3$, $0.13 < ks < 6.98$, and $10° < \theta < 70°$. Oh indicates that the simplified version of q is best suited for $ks < 3.5$, and $m_v > [-6.286/\ln(\theta/90)]^{-1.538}$ ($m_v \geq 0.09\,\mathrm{m}^3/\mathrm{m}^3$ for $\theta \geq 24°$).

The simulation on Fig. 2.3c confirms that the simplified q is a good approximation for small RMS height. For rough soil surface, the difference between simplified and non-simplified q is less than 1 dB which is acceptable considering that Radarsat-2 radiometric error is close to ±1 dB [60].

The function forms of the Oh model have been fitted to a large set of truck-mounted scatterometer measurements and airborne SAR measurements, and extensive in situ measurements of soil moisture and surface roughness. In particular, most of the roughness measurements were made with a laser profilometer along multiple 1-m profiles [83, 84]. A few measurements were also made with a 3.5-m chart paper and spray paint.

In [83], Oh *et al.* reports that the model agrees with the IEM and the Geometrical Optics model. Baghdadi *et al.* tested the agreement of the Oh model, the Dubois model, and the IEM with C-band data [85] and X-band data [86]. None of the models perfectly agreed with measurements from ERS-2, Radarsat-1 and ASAR [85]. And with TerraSAR-X data, better agreements were obtained with the Oh model. All in all there is no consensus on the use of correction factors as both under- and over-estimations are reported in different studies [69]. This could be attributed to the fact that the in situ measurements used to test the models are assumed to provide the true soil parameters. While this assumption is reasonable for soil moisture measurements, it is disputable for roughness measurements since roughness characterization over natural soils is known to be challenging.

The main advantage of the Oh model is that it provides a straightforward expression for every polarizations - σ^0_{vh}, σ^0_{hh}, and σ^0_{vv} [87].

$$\sigma^0_{vh} = 0.11 m_v^{0.7} (\cos\theta)^{2.2} \left[1 - \exp\left(-0.32\,(ks)^{1.8}\right)\right] \tag{2.24}$$

$$\sigma^0_{vv} = \frac{\sigma^0_{vh}}{0.095\left(0.13 + \sin(1.5\theta)^{1.4}\right)\left[1 - \exp\left(-1.3\,(ks)^{0.9}\right)\right]} \tag{2.25}$$

$$\sigma^0_{hh} = \sigma^0_{vv}\left[1 - \left(\frac{\theta}{90°}\right)^{0.35 m_v^{-0.65}} \exp\left(-0.4\,(ks)^{1.4}\right)\right] \tag{2.26}$$

The simplified Oh model was selected for this research work for two main reasons. First, unlike the Dubois model, it provides an expression for all polarizations which makes the use of full-polarimetric measurements possible. Second, the model is relatively simple compared to the IEM.

2.2.2 Radar measurement uncertainty - Speckle modeling

The backscattering models presented in the previous section links the soil parameters to the characteristic backscattering response σ^0 of the soil [87]. In practice, σ^0 is not directly available. Distributed targets such as agricultural soils are affected by speckle which can be modeled as an intrinsic multiplicative noise [88]. For a single

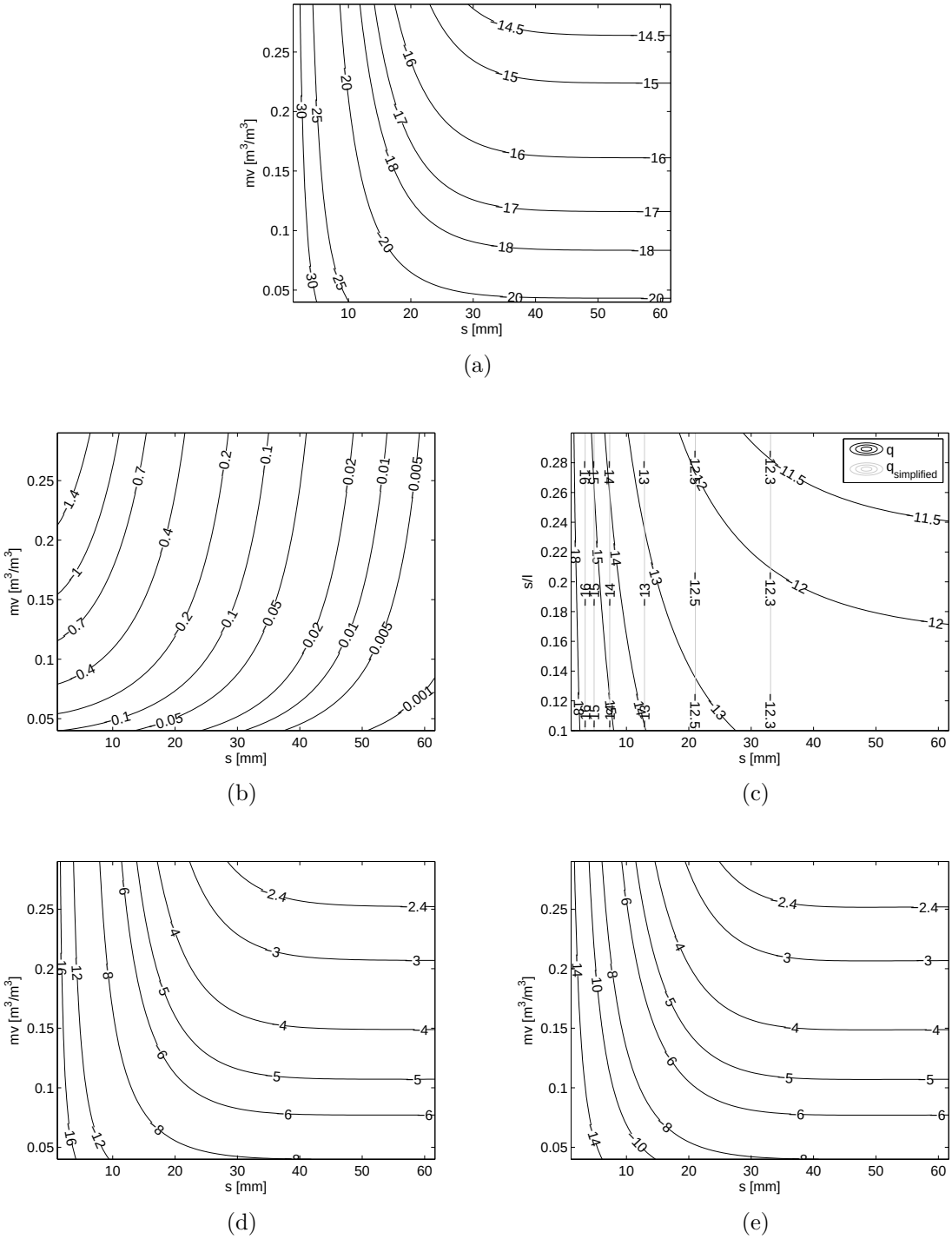

Figure 2.3: Simulation of (a) σ^0_{vh}, (b) p, (c) q, (d) σ^0_{hh}, and (c) σ^0_{vv} with the Oh backscattering model

look complex image, the observed intensity at each pixel of a distributed target can be described as a random variable I as follows,

$$I = \sigma N \tag{2.27}$$

with σ the mean intensity of the distributed target and $N \sim \mathcal{E}(1)$ the multiplicative speckle. Therefore $I \sim \mathcal{E}(1/\sigma)$ which has both mean and standard deviation equal to σ.

From this model it can be derived that the logarithm of the intensity $D = \ln I$ follows a Fischer-Tippett distribution

$$P_D(d) = \frac{e^d}{\sigma} \exp\left(-\frac{e^d}{\sigma}\right) \tag{2.28}$$

whose mean value and variance are respectively $\ln\sigma - \gamma_E$ and $\pi^2/6$. The symbol γ_E is Euler's constant whose approximate value is 0.57722.

This Probability Distribution Function (PDF) is easily transformed into that for the intensity in dB. Since $D_{dB} = 10\log_{10} I = (10\log_{10} e)D$, one can write $P_{D_{dB}}(d_{dB}) = \frac{1}{K} P_D(d_{dB}/K)$ where $K = 10\log_{10} e$. And the mean and variance are respectively $K(\ln\sigma - \gamma_E)$ and $K^2\pi^2/6$.

Averaging or *multilooking* is commonly used to minimize the effect of speckle before using the data for remote sensing. This averaging is called *incoherent averaging* because it is applied on the intensity for which there is no phase information. After averaging L independent looks or pixels belonging to the same distributed target, the mean intensity is still σ, but the variance is now σ^2/L. Averaging the intensity is optimal in terms of reducing the variance of the measurements [88]. Averaging in log-intensity provides inferior estimates of σ.

After averaging L independent pixels, the L-look average intensity becomes Gamma distributed with order parameter L

$$P_I(i) = \frac{1}{\Gamma(L)} \left(\frac{L}{\sigma}\right)^L i^{L-1} e^{-Li/\sigma} \tag{2.29}$$

with mean σ and variance σ^2/L.

The previous distributions are valid for all polarizations. Lee *et al.* also derived the PDF of the ratio of two multilook average intensity $Z = I_1/I_2$, *i.e.* the ratio of two Gamma-distributed random variables with order parameter L [89],

$$P_Z(z) = \frac{2\tau^L \Gamma(2L)\,(1-\rho_i)^L\,(\tau + z^2)\,z^{2L-1}}{\Gamma(L)G(L)\left[(\tau+z^2)^2 - 4\tau\rho_i z^2\right]^{(2L+1)/2}} \tag{2.30}$$

with $\Gamma(\cdot)$ the Gamma function, ρ_i the correlation coefficient between I_1 and I_2, and $\tau = \sigma_1/\sigma_2$ ($\sigma_1 = E(I_1)$, $\sigma_2 = E(I_2)$).

This PDF can be used for the co- and cross-polarized ratio p and q. In theory, the co-polarized components hh and vv are correlated, while the co- and cross-polarized components are uncorrelated. In practice, the co- and cross-polarized components might be slightly correlated because of channel crosstalk and thermal noise.

All the previous PDF were described in term of the observed mean power σ and not in term of the calibrated quantity σ^0. To transform the observed mean power into σ^0, one must take into account [88],

1. a scaling factor due to propagation, antenna pattern, and SAR processing effects,
2. a bias due to thermal noise,
3. Spatial correlation induced by oversampling in the SAR processing.

In the end, the observed voltage at azimuth position x can be written,

$$\mathcal{U}(x) = C\,(R)\,S\,(x) * k(x) * l(x) + n(x) * l(x) \tag{2.31}$$

$k(x)$ is a pre-filtering term which accounts for the beam weighting of the antenna in the azimuth direction, and the Doppler shift due to the relative motion between the radar and the scatterer.

$l(x)$ is the SAR processing filter whose main function is the removal of the Doppler shift.

$S(x)$ is the complex scattering amplitude of the target.

$n(x)$ accounts for system noise.

$C\,(R)$ is a range dependent term whose magnitude is given by

$$|C\,(R)|^2 = \frac{P_T G_R^2 \lambda^2 G_P}{(4\pi)^3 R^4 L} \tag{2.32}$$

with P_T the peak transmitted power, G_R the one-way power gain of the antenna pattern, G_p the processing gain due to the range compression, R the range, and L a term accounting for system losses.

After deriving the spatial autocorrelation function of the voltage $R_{\mathcal{U}}(x)$, Oliver *et al.* give the following expression which relate the observed mean power $\sigma = R_{\mathcal{U}}(0)$ with σ^0,

$$\sigma = R_{\mathcal{U}}(0) = \sigma^0 \,|C(R_0)|^2 \,\frac{\lambda R_0}{2} R_l(0) + N R_l(0) \tag{2.33}$$

for a pixel at range R_0.

Because the calibration depends on the range, one would expect the PDF of σ^0 to be different from the exponential distribution of the observed intensity. In practice section 3.4 (Methodology) shows that the range dependency is minor for small distributed targets such as agricultural fields, therefore all the previous developments made for σ can be directly applied to the calibrated images of σ^0.

2.3 Soil moisture estimation methods

This section gives an overview of the main methods available to retrieve soil moisture. Methods requiring in situ measurements of surface roughness are not included as they are not suitable for soil moisture retrieval over extended areas. Change detection methods have already been introduced when presenting the empirical backscattering models (section 2.2.1.1). Analytical inversions are usually not straightforward for semi-empirical models and theoretical models.

2.3.1 Overview of inversion methods

Many variations of a given method can be found, and it may be nearly impossible to review all of them. They can nonetheless be grouped in three main categories:

1. Look-up table,
2. Possibility theory and Fuzzy method,
3. Artificial Neural Network (ANN),
4. Bayesian approach.

Look-up table It is a very common method particularly to invert the IEM [76, 77]. A data base of backscattering coefficients is generated by running the model in forward mode for a range of parameters. Then for a given radar measurement, the algorithm output the set of parameters which correspond to the closest pre-computed backscattering coefficient. Interpolation can be used when the measured value falls between two pre-computed values. It is a computationally efficient for repeated inversions because the data base is only computed once.

Possibility theory and Fuzzy methods Only a few authors have used methods which fall in this category. These methods are based on approximate reasoning which can be used to bypass limitations of the rigorous Probability theory. For example, using Possibility theory, Kweon *et al.* estimate $n + 1$ unknowns from only n measurements [90]. More precisely, from a series of n multitemporal single polarization radar measurements, they estimate n soil moisture levels for each acquisition and 1 RMS height value which they assumed constant across the n radar measurements.

Possibility theory is an extension of Fuzzy logic. The later has been applied by Verhoest *et al.* as a faster method than possibility distributions to estimate soil moisture from radar measurements and uncertain in situ roughness measurements [91].

Artificial neural networks ANNs are an increasingly-popular method which has found applications in pattern recognition, clustering/categorization, function approximation, prediction/forecast, optimization, content-addressable memory, and control [92].

When applied to soil moisture estimation, backscattering models are implemented within a computational structure similar to human's central nervous system.

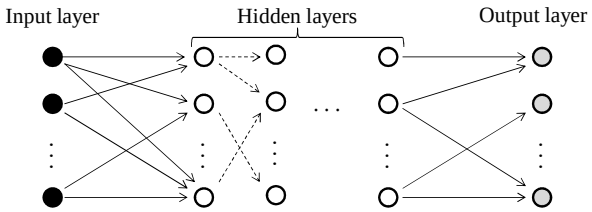

Figure 2.4: A feed-forward artificial neural network. Drawing adapted from [92].

This structure is made of inter-connected neurons grouped in different hidden layers which connect neurons of an input layer to neurons of an output layer (Fig. 2.4). The feed-forward network for which connections are only going in the forward direction has been found to be the most suitable structure for inversion and classification [93]. In practice, the neurons of the input layer can be a set of radar measurements and the neurons of the output layer will be the soil parameters of interest. The main difficulties with ANNs are (1) choosing the number of hidden neurons and hidden layers which will best relate radar measurements to soil parameters, and (2) training the network [94]. There are no rules regarding the first point. As for the second point, training the ANN consists in defining the links between the different neurons using either a large data set of radar measurements and soil parameters measurements, or set of simulated data using a backscattering model in forward mode. A given neuron is expressed as a linear combination of other neurons plus an offset. The coefficients of the linear combination can be determined by least-square regression. Training has to be carefully controlled to avoid over-training. When the network is over-trained, it becomes really good at finding the output for the training data set, but it cannot determine accurately the output for an independent data set.

ANNs have been implemented for soil moisture estimation in [95, 96, 97]. Notarnicola *et al.* compared a Bayesian approach and an ANN for soil moisture retrieval with scatterometer and radiometer data [94]. The main difference they noted is that with the Bayesian approach the error in soil moisture increased when the number of inputs increased, while it decreased for the ANN. However this is more due to the way the Bayesian method is implemented rather than a characteristic disadvantage of the Bayesian approach.

In summary, the main downside of both the Possibility/fuzzy method and the ANNs may be that their implementation requires subjective choices which may affect the final performance for a given study. The next paragraph introduces the more rigorous framework of the Bayesian approach.

Bayesian approach The Bayesian approach outputs more than a simple estimation of the parameters of interest, it provides the PDF of the parameters for a given set measurements. From this PDF, an estimation of the parameters can be obtained from the mean or the mode of this PDF. Noting $\mathbf{x}$ the vector of parameters and $\mathbf{y}$ the vector of measurements. The Bayes' theorem gives the following relationship [98]:

$$p(\mathbf{x}|\mathbf{y}) = \frac{p(\mathbf{y}|\mathbf{x})p(\mathbf{x})}{p(\mathbf{y})} \tag{2.34}$$

$p(\mathbf{y}|\mathbf{x})$ is the *data distribution* or *measurement distribution.* Concretely, if $\mathbf{y}$ are noisy measurements of the parameters $\mathbf{x}$, then $p(\mathbf{y}|\mathbf{x})$ represents the measurement errors.

$p(\mathbf{x})$ is the *prior distribution* of the parameters. It accounts for any prior information on the parameters.

$p(\mathbf{y})$ is often considered as a normalizing constant in the Bayes theorem which can be expressed as $p(\mathbf{y}) = \int p(\mathbf{y}|\mathbf{x})p(\mathbf{x})d\mathbf{x}$.

Finally, $p(\mathbf{x}|\mathbf{y})$ is the *posterior distribution.* It is the output of the Bayesian approach - the distribution of the parameters given the measurements.

This is the most general form of the Bayesian approach. It has been implemented for soil moisture estimation in [94, 87, 99, 100]. The implementation is slightly different for each study mainly due to different strategies in modeling the measurement errors.

To use this method, the first step consists in defining the PDFs $p(\mathbf{y}|\mathbf{x})$ and $p(\mathbf{x})$. Usually a given PDF is postulated, not necessarily Gaussian, and the parameters of this PDF are determined from a data set or are set to reasonable values. Most of the time the prior distribution $p(\mathbf{x})$ is chosen to restrict the range of physically possible values for the parameters. For example, over natural soils, soil moisture remains between $m_{v,min} = 0.05\,\mathrm{m}^3/\mathrm{m}^3$ and $m_{v,max} = 0.40\,\mathrm{m}^3/\mathrm{m}^3$. Therefore $p(m_v)$ can be defined as,

$$p(m_v) = \begin{cases} 1/(m_{v,max} - m_{v,min}) & \text{if } m_{v,min} \leq m_v \leq m_{v,max} \\ 0 & \text{otherwise} \end{cases} \tag{2.35}$$

The main limitation of the Bayesian approach is its poor computational efficiency when applied to high-dimensional problems. It provides the PDF of each parameter while in the end only the mean/mode and the variance of these PDFs will be used. More efficient methods can be derived from the Bayesian approach at the cost of additional mathematical assumptions. One of them is the χ^2 method, it is thoroughly presented in the next section as it will be used intensively in this thesis to investigate soil moisture estimation with different combinations of radar measurements.

2.3.2 The χ^2 method

χ^2 is an attractive method as it provides quantitative goodness-of-fit which reflects the chance of the model to be wrong, only from knowledge of radar measurement uncertainty. This is an interesting alternative to verify that a backscattering model is consistent, without relying on additional and potentially erroneous in situ measurements of soil moisture and surface roughness. If the model appears to be valid, the fitted parameters and their variance can then be analyzed.

2.3.2.1 Derivation of the χ^2

The inverse problem can be formulated as follows,

$$\mathbf{y} = \boldsymbol{\mathcal{F}}(\mathbf{x}) \tag{2.36}$$

where $\boldsymbol{\mathcal{F}}$ is a model which maps the parameter space to the measurement space. For SAR remote sensing of soil moisture, $\boldsymbol{\mathcal{F}}$ is a backscattering model which relates soil moisture and roughness parameters to radar measurements.

Solving the inverse problem consists in finding the most probable soil parameters $\mathbf{x}$ for a given set of radar measurements $\mathbf{y}$. Note that $\mathbf{x}$ is a vector of size n, and $\mathbf{y}$ is a vector of size M, with $M \geq n$. Using the notation of the Bayesian approach, one is looking for,

$$\max_{\mathbf{x}} P(\mathbf{x}|\mathbf{y}) \tag{2.37}$$

Using a *non-informative prior* ($P(\mathbf{x}) = \text{cte}$), maximizing $P(\mathbf{x}|\mathbf{y})$ is equivalent to maximizing $P(\mathbf{y}|\mathbf{x})$, *i.e.*

$$\arg\left(\max_{\mathbf{x}} P(\mathbf{x}|\mathbf{y})\right) = \arg\left(\max_{\mathbf{x}} P(\mathbf{y}|\mathbf{x})\right) \tag{2.38}$$

So one is now looking for $\mathbf{x}$ which maximizes the probability of observing the measurements $\mathbf{y}$. The Bayesian approach can handle any sorts of PDFs. In comparison, the χ^2 approach requires the measurement error affecting $\mathbf{y}$ to be independent, additive, and distributed as a Gaussian distribution around the true model $\boldsymbol{\mathcal{F}}(\mathbf{x})$. In this case, $P(\mathbf{y}|\mathbf{x})$ can be written as [101],

$$P(\mathbf{y}|\mathbf{x}) \propto \prod_{i=0}^{M-1} \left[\exp\left(-\frac{1}{2}\left(\frac{y_i - \mathcal{F}_i(\mathbf{x})}{\sigma_i}\right)^2\right)\Delta y\right] \tag{2.39}$$

where σ_i is the standard deviation affecting measurement y_i. M is the total number of measurements. Δy is a small constant of variation around each measurement to avoid $P(\mathbf{y}|m_v, s)$ to be zero for continuous data. It does not have any consequences in what follows.

Taking the negative of the logarithm of equation 2.39 leads to

$$\left[\sum_{i=0}^{M-1} \frac{(y_i - \mathcal{F}_i(\mathbf{x}))^2}{2\sigma_i^2}\right] - M\ln(\Delta y) \tag{2.40}$$

Since M and and Δy are constant, maximizing equation 2.39 is equivalent to minimizing the squared sum

$$\chi^2 \equiv \sum_{i=0}^{M-1} \frac{(y_i - \mathcal{F}_i(\mathbf{x}))^2}{\sigma_i^2} \tag{2.41}$$

A common routine to minimize the χ^2 with nonlinear models is the *Levenberg-Marquardt* algorithm. Details about this method can be found in [101].

2.3.2.2 Goodness-of-fit

When the model $\boldsymbol{\mathcal{F}}$ is linear, the probability distribution of the values at the minimum of equation 2.41, follows a χ^2 distribution with $M-n$ degrees of freedom, with n the number of parameters, hence the name of the method. According to [101], it is not too wrong to assume that this result holds even for models which are not linear

in the n parameters, which is the case with the semi-empirical model presented in section 2.2.1.3.

It follows that the goodness-of-fit is given by the probability Q that the χ^2 should exceed its value found after minimizing equation 2.41. If Q is small, either the model is wrong, or the errors σ_i are actually larger than the ones stated. If Q is too close to 1, it means that the specified σ_i are too conservative. Typical values for the χ^2 should be close to the number of degrees of freedom, which lead to $Q \approx 0.5$. In summary, for the goodness-of-fit to be meaningful, the measurement error must be independent, additive, Gaussian with zero mean, and reasonable values must be given to the standard deviations σ_i.

2.3.2.3 Uncertainty in the fitted parameters

Covariance matrix of the fitted parameters Different methods are available to investigate the uncertainty on the fitted parameters. The most straightforward method is to use the Jacobian matrix $\mathbf{J}$ of the model $\boldsymbol{\mathcal{F}}$ which is available from the *Levenberg-Marquardt* algorithm.

After the algorithm meets one of its convergence criteria, the covariance matrix $\mathbf{C}$ of the fitted parameters can be computed as follows

$$\mathbf{C} = \left((\boldsymbol{\sigma}\mathbf{J})^t (\boldsymbol{\sigma}\mathbf{J}) \right)^{-1} \tag{2.42}$$

with $\boldsymbol{\sigma}$ a $M \times M$ diagonal matrix containing the standard deviation σ_i, and $\cdot^t$ the operator for transposition.

Confidence region from the covariance matrix of the fitter parameters This covariance matrix can be used to derive confidence regions on the fitted parameters. The confidence region of dimension n is given by

$$(\mathbf{x} - \mathbf{x}_0)^t \, \mathbf{C}^{-1} \, (\mathbf{x} - \mathbf{x}_0) = \Delta^2 \tag{2.43}$$

where $\mathbf{x}_0$ is the fitted value of $\mathbf{x}$, and a is a constant which sets the extent of the confidence region.

If (1) the measurement errors are Gaussian, and if (2) either the model is linear or the uncertainty in the parameters remains in a region where the nonlinear model could reasonably be linearized, then it is possible to quantify the confidence level p of the confidence region because [101]

$$\Delta^2 \sim \chi^2_n \tag{2.44}$$

with χ^2_n is the χ^2 distribution with n degrees of freedom.

It follows that one can set the value of Δ such that the probability of a χ^2 variable with n degrees of freedom being less than Δ is p. Table 2.5 shows values of Δ^2 for common values of confidence level and different dimensions /degrees of freedom n. In particular in one dimension, it is well known that the 68.27% confidence interval is $\pm\sigma_0$ with σ_0 the standard deviation of x_0, and the 95.45% confidence interval is $\pm 2\sigma_0$. In dimension 2, the confidence ellipse for the bi-variate Gaussian distribution of $\mathbf{x}$ is an ellipse, and it is an ellipsoid in dimension 3.

	n			
p	1	2	3	4
68.27%	1.00	2.30	3.53	4.72
90%	2.71	4.61	6.25	7.78
95.45%	4.00	6.18	8.02	9.72
99%	6.63	9.21	11.3	13.3
99.73%	9.00	11.8	14.2	16.3
99.99%	15.1	18.4	21.1	23.5

Table 2.5: Δ^2-value for different confidence levels p and degrees of freedom n

$$\boldsymbol{C} = \begin{bmatrix} C_{11} & C_{12} & C_{13} & C_{14} \\ C_{12} & C_{22} & C_{23} & C_{24} \\ C_{13} & C_{23} & C_{33} & C_{34} \\ C_{14} & C_{24} & C_{34} & C_{44} \end{bmatrix} \longrightarrow \boldsymbol{C}_{proj} = \begin{bmatrix} C_{22} & C_{14} \\ C_{24} & C_{44} \end{bmatrix}$$

Figure 2.5: Derivation of the covariance matrix for only the second and the fourth parameters

So far the confidence region was given for the vector $\mathbf{x}$ of size n. It is also possible to extract a confidence region for ν degrees of freedom with $\nu < n$. To do so, one simply needs to extract the intersections between the ν rows and columns which correspond to the parameters of interest [101]. These $\nu \times \nu$ intersections form a new covariance matrix $\mathbf{C}_{proj}$ (Fig. 2.5). The confidence region for the ν parameters is given by

$$(\mathbf{x}_{proj} - \mathbf{x}_{0,proj})^t \, \mathbf{C}_{proj}^{-1} \, (\mathbf{x}_{proj} - \mathbf{x}_{0,proj}) = \Delta_{proj}^2 \sim \chi_\nu^2 \tag{2.45}$$

with $\mathbf{x}_{proj}$ and $\mathbf{x}_{0,proj}$ vectors containing only the ν parameters.

This confidence region can be seen as the projection of the confidence region given by 2.43 on the parameters space of dimension ν.

Confidence region from Monte Carlo simulation With the previous method, for a given level of confidence, the extent of the confidence region depends only on the specified measurement errors σ_i and the linear approximation of the model with its Jacobian $\mathbf{J}$. When the measurement errors are not exactly Gaussian, or the linear approximation of the backscattering model is poor, the confidence region from equation 2.43 might not be meaningful. In this case, a more flexible method based on Monte Carlo simulation can be used to analyze uncertainty any measurement errors and nonlinear models.

The Monte Carlo simulation relies on synthetic data sets $(\mathbf{y}_k)$, with $k = 1 \ldots N_{mc}$ and N_{mc} the number of Monte Carlo simulation. These synthetic data sets can be generated from the assumed multivariate Gaussian distribution $\mathcal{N}(\mathbf{y}, \boldsymbol{\sigma})$, or by sampling with replacement from the original set of measurements, *i.e. bootstrapping*. The latter is convenient when the PDF of the measurement errors is not exactly known. The synthetic data sets are then input in the χ^2 to determine the corresponding parameters $(\mathbf{x}_k)$.

When the dimension of $\mathbf{x}$ is less than or equal to 3, the set of $(\mathbf{x}_k)$ with $k = 1 \dots N_{mc}$ can be plotted as a point cloud which allows visualizing the shape and the extent of the uncertainty on the parameters. When the point cloud is approximately distributed as a multivariate Gaussian distribution, then confidence regions can be determined from a *Principal Component Analysis* (PCA).

The Principal Components are an orthonormal basis of eigenvectors of the covariance matrix of the point cloud. These eigenvectors are sorted in ascending order with the first vector defining the direction of greatest variance in the data. The eigenvalue associated to a given eigenvector is the variance of the data in the direction of this vector.

First one needs to remove the mean of the point cloud $(\mathbf{x}_k)$. Second the covariance matrix $\mathbf{\Sigma}$ of this point cloud is computed and decomposed as

$$\mathbf{\Sigma} = \mathbf{v}\mathbf{\Lambda}\mathbf{v}^t \tag{2.46}$$

with $\mathbf{\Lambda}$ a diagonal matrix containing the eigenvalues in ascending order, and $\mathbf{v}$ an $n \times n$ matrix whose columns are the corresponding orthonormalized eigenvectors.

Then equation 2.43 can be rewritten as

$$\begin{aligned} (\mathbf{x}-\mathbf{x}_0)^t \left(\mathbf{v}\mathbf{\Lambda}\mathbf{v}^t\right)^{-1} (\mathbf{x}-\mathbf{x}_0) &= \Delta_{mc}^2 && (2.47)\\ (\mathbf{x}-\mathbf{x}_0)^t \mathbf{v} \left(\mathbf{v}\mathbf{\Lambda}\right)^{-1} (\mathbf{x}-\mathbf{x}_0) &= \Delta_{mc}^2 && (2.48)\\ (\mathbf{x}-\mathbf{x}_0)^t \mathbf{v}\mathbf{\Lambda}^{-1}\mathbf{v}^t (\mathbf{x}-\mathbf{x}_0) &= \Delta_{mc}^2 && (2.49) \end{aligned}$$

Noting $\mathbf{z} = \mathbf{v}^t\mathbf{x}$ and $\mathbf{z}_0 = \mathbf{v}^t\mathbf{x}_0$, the equation of the confidence region becomes,

$$(\mathbf{z}-\mathbf{z}_0)^t \mathbf{\Lambda}^{-1} (\mathbf{z}-\mathbf{z}_0) = \Delta_{mc}^2 \tag{2.50}$$

The operation $\mathbf{z} = \mathbf{v}^t\mathbf{x}$ can be seen as the projection of the components of $\mathbf{x}$ on the principal axis. Equation 2.50 is the equation of an ellipsoid in the basis formed by the principal components. Fig. 2.6 shows the 68.27% confidence ellipse obtained for a bi-variate Gaussian distribution with the PCA.

Because the covariance matrix $\mathbf{\Sigma}$ is estimated from the point cloud whose number of points is the number of synthetic data sets N_{mc}. The estimation of $\mathbf{\Sigma}$ can be poor if N_{mc} is small because of computational limitations. To account for this uncertainty on $\mathbf{\Sigma}$, the constant Δ_{mc}^2 follows a Fisher–Snedecor distribution [102] as follows

$$\frac{(N_{mc}-n)}{n\,(N_{mc}-1)} \Delta_{mc}^2 \sim F_{n,N_{mc}-n} \tag{2.51}$$

Table 2.6 gives some examples of values of Δ_{mc}^2 for $n = 2$ and different values of N_{mc}. For large N_{mc}, the value of Δ_{mc} converges toward the value Δ for the same n and the same confidence level.

It is also possible to extract a confidence region only for a subset of parameters by extracting the corresponding elements of $\mathbf{\Sigma}$ into $\mathbf{\Sigma}_{proj}$ and applying the PCA to $\mathbf{\Sigma}_{proj}$.

Again the derivation of elliptical confidence regions with the PCA is meaningful only for point clouds with a multivariate Gaussian distribution. For example,

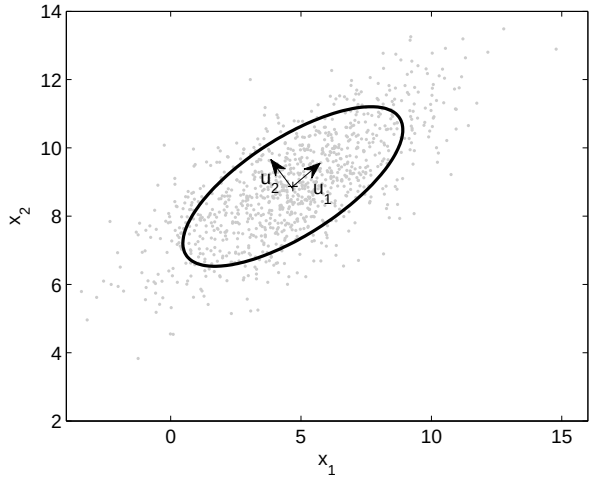

Figure 2.6: 68.27% confidence region from PCA with $n = 2$. Vectors $\mathbf{u_1}$ and $\mathbf{u_2}$ are the first and second principal directions.

	N_{mc}			
p	10	10^2	10^3	10^4
68.27%	2.99	2.35	2.30	2.30
90%	7.00	4.76	4.62	4.61
95.45%	10.49	6.44	6.21	6.18
99%	19.46	9.76	9.26	9.22
99.73%	30.48	12.70	11.91	11.84
99.99%	81.00	20.47	18.61	18.44

Table 2.6: Δ^2_{mc}-values for $n = 2$, different confidence levels and different values of N_{mc}

nonlinear models can lead to a banana-shaped point cloud [103] for which an elliptical confidence region is not adapted since one usually wishes the extent of the confidence region to be as small as possible. As mentioned in section 2.2.2, radar measurements are affected by speckle which makes the backscattering coefficient σ^0 over a distributed target follow an exponential distribution. In order to make the PCA method applicable, section 3.4.3 presents a method to transform multiplicative exponential speckle noise into additive Gaussian noise.

2.3.3 Data Assimilation methods derived from the Bayesian approach

With the χ^2 method, no a priori information on the unknown parameters is combined with the measurements. Data Assimilation methods combine measurement of the current parameters (and possibly past and future) with a priori information on the parameters to produce the best estimate of the current parameters. The most common Data assimilation methods are Variational methods, Kalman filters/smoothers, and Particle filters/smoothers. All of them can be derived from the Bayesian ap-

proach. A detailed presentation is not necessary here, as none of these methods will be used in the thesis. However it is worth mentioning their main advantages and limitations, as this will be needed for the discussion.

Disregarding their respective mathematical assumptions, Kalman filters and Particle filters are more adapted for applications which requires frequent updates of the parameters as soon as new measurements are available. While Variational methods are more suitable for estimating parameters after gathering a large collection of measurements. For example, Kalman filters are very popular for guidance, navigation and control of aircraft and spacecraft, as such applications require a sequential assimilation of measurements with an update of the estimated parameters at every time step [104]. On the other hand, Variational method are commonly used in weather forecasting. For example for a forecast 2 weeks ahead, the European Centre for Medium-Range Weather Forecasts (ECMWF) assimilates every 12 hours more than 10 million observations to update 80 million variables which model the atmosphere.

Table 2.7 summarizes the attributes of the different Data Assimilation methods.

	Description	**Mathematical requirements**	**Limitations**
3D-var	Minimization of cost function. The mode gives the optimal estimation.	Gaussian statistics, ~nonlinear models	No time evolution. No estimation uncertainty. Can return local minimum
4D-var	Minimization of cost function. The mode gives the optimal estimation.	Gaussian statistics, ~nonlinear models	No estimation uncertainty. Can return local minimum. Hard to make parallel
KF	Recursive Bayesian filter for multivariate normal distributions.	Gaussian statistics, ~nonlinear models	Not suitable for large problems
EnKF	Run the KF equations with ensemble of N samples which represent measurement and prior Gaussian distributions. The mean gives the optimal estimation.	Gaussian statistics, ~nonlinear models	Needs tuning for large problem with small ensemble, weak theoretical background
Particle filter	Assign probabilistic weights to ensemble of samples which represent any shapes of distribution. The mean gives the optimal estimation.	Non Gaussian stats, all nonlinear models	Implementation requires tuning (proposal density). Not so efficient for very large problems

Table 2.7: Outlines of the main Data Assimilation methods

Chapter 3

Methodology

This chapter presents the different methods involved in the project. Section 3.1 gives a list of requirements derived from the objectives of the project. These requirements will drive the setup of the different experiments. Then sections 3.2 and 3.3 describe in details the different measurement methods involved in the two experimental campaigns. Section 3.4 presents the preprocessing steps for the Radarsat-2 images. Finally section 3.5 gives the observation requirements for soil moisture and surface roughness which will be taken as references when assessing the performance of model inversion with different combinations of radar measurements.

3.1 Aim and requirements of the experimental campaigns

The experimental campaign has been designed in order to address two objectives of the project.

O.1.2.1.1. Setup an experiment to compare the dynamics of surface roughness with the dynamics of soil moisture

O.2.2.1. Test model inversion with real multi-polarization radar measurements

Therefore the experimental campaign can be divided in two parts referred as *experiment 1* and *experiment 2* have been elaborated around these two objectives.

The aim of experiment 1 is to generate time series of measurements which allow investigating the temporal variability of surface roughness compared to that of soil moisture. Therefore it focuses on routinely generating roughness measurements.

The aim of experiment 2 is to generate a data set which allows investigating soil moisture estimation from multi-polarized SAR data. It focuses more on the acquisition of in situ measurements in parallel of Radarsat-2 acquisitions.

A list of requirements can be derived from the aim of experiment 1 and 2.

Requirements for experiment 1

R.1. The experiment must provide data which allows investigating the temporal variability of surface roughness parameters compared to that of soil moisture.

R.1.1. The data must include both surface roughness and soil moisture measurements which can be compared.

R.1.1.1. Multitemporal roughness measurements must be done over the same patch of soil.

R.1.1.1.2. The setup must include landmarks which remain at the same position throughout the experiment.

R.1.1.2 Soil moisture measurements must be at least as frequent as surface roughness measurements.
This is because soil moisture is expected to change more frequently than surface roughness.

R.1.2. Measurements must capture changes in roughness relevant for microwave scattering

R.1.2.1 Measurements must be frequent enough
Irrelevant changes are changes too small to be measurable, or too small to affect the radar signal.

R.1.2.1.1 The location of the experiment must be close to Cranfield University for frequent access.

R.1.2.1.2 The measurement methods must be straightforward, without the intervention of more than one person.
If too many persons are required, the frequency of measurements will heavily depend on the availability of the persons involved.

R.1.2.1.3 Roughness measurements must be planned to avoid useless acquisitions / waste of time.

R.1.2.1.3.1 The time sampling of measurements must be variable, allowing for time periods with very frequent measurements, and scarcer measurements when no changes are expected.

R.1.2.2. Roughness measurements must be accurate enough.

R.1.2.2.1. Measurement methods must be robust against outdoor conditions.
Outdoor conditions include rain, wind, high/low temperature, sun light...

R.1.2.3. Roughness measurements must allow computing the typical roughness parameters involved in backscattering models (RMS height, correlation length).

R.1.2.4. Measurements must be carried out over a surface area which capture the roughness scales that the electromagnetic wave is sensitive to.

R.1.2.5. The spatial resolution must be fine enough to capture features that the electromagnetic wave is sensitive to.

R.1.3. The experiment must be done over soils as representative as possible of standard agricultural fields.

R.1.4 Only natural changes of roughness must be monitored.

R.1.4.1 The imaged surfaces must be protected from perturbation originating from man-made sources, excluding tillage operations.
For example, the measured surface must be free of footprints.

R.1.4.2 Measurements must be carried out over a period covering the whole breeding cycle.
The experiment focuses on agricultural application of soil moisture estimation. The various weather conditions throughout the breeding cycle are likely to affect surface roughness in different ways.

R.1.4.3 Measurements must not modify the surface roughness.
Measurement methods involving contact with the surface should be avoided.

R.1.4.4 When possible, parameters correlated to changes in soil moisture or/and changes in surface roughness must be measured.
Such parameters include soil temperature, solar radiation, rainfall.

Requirements for experiment 2

R.2 The experiment must provide a data set of in situ measurements of soil moisture and surface roughness, acquired simultaneously with Radarsat-2 image acquisitions.

R.2.1. Soil moisture and surface roughness must be measured repeatedly at different locations.

R.2.1.1 The measurement process must be quick and portable.

R.2.2. Measurements must capture roughness features relevant to microwave scattering.

R.1.2.1. Roughness measurements must be accurate enough.

R.1.2.1.1. Measurement methods must be robust against environmental conditions.
Environmental conditions include rain, wind, temperature, sun light...

R.1.2.2. Measurements must be carried out over a surface area which capture the roughness scales that the electromagnetic wave is sensitive to.

R.1.2.3. The spatial resolution must be fine enough to capture features that the electromagnetic wave is sensitive to.

R.1.2.4. Roughness measurements must allow computing the typical roughness parameters involved in backscattering models (RMS height, correlation length).

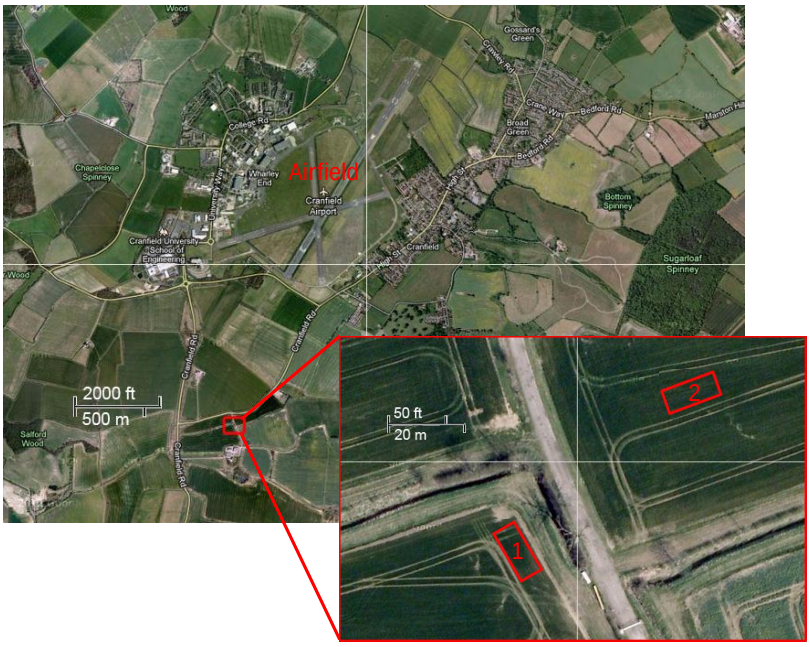

Figure 3.1: Location of the Holcotmoors Farm and the two patches

R.2.3. The sampled fields must be as bare as possible.

Some requirements are common to experiment 1 and 2, in particular regarding the fact that in both cases the roughness measurements must capture roughness features relevant to microwave scattering. More details about this requirement are given in section 3.2.2.1.

The main difference is that experiment 1 requires multitemporal acquisitions over the same patch of soil in order to track changes in roughness. While experiment 2 requires the setup to be portable to make roughness measurements at multiple locations in order to test the inversion with Radarsat-2 measurements over different fields. These two points are contradictory as the first one would require the setup to be anchored, while the second asks for more portability. This is why it was decided to elaborate two distinct setups.

3.2 Setup for experiment 1

3.2.1 Location and duration

The experimental campaign is carried out over the Holcotmoors farm which is conveniently located only 3 km away from Cranfield University. After discussion with the owner of the farm, Mr Paul Colburn, it was decided that the experiment could be made over two patches of soil from two different fields as shown on Fig. 3.1. The experiment lasted from May 06 2013 to July 12 2014.

The fact that it is a real farm guarantees that the monitored soil surfaces are representative of agricultural soils. The only disadvantage being that the deployed setup must not interfere with the farm activities.

3.2.2 Roughness measurements with SfM

3.2.2.1 Extent, resolution, and accuracy of measurements

Measurement extent As explained in section 2.1.5, the interaction between the incidence radar wave and the soil surface is bandwidth limited, with the lower limit fixing the measurement resolution and the higher limit fixing the measurement extent. At the moment, the latter is not clear. The worst-case scenario corresponds to the interpretation of Manninen which argues that pixel-size roughness statistics is needed [59]. Therefore measurements should be done over a $\sim 10 \times 10\,\mathrm{m}$ plot. Producing a $10 \times 10\,\mathrm{m}$ DEM with SfM would require using a camera mounted on a pole to image the centre of the patch without disrupting the surface with footsteps. Such a setup would be cumbersome and not very practical for frequent acquisitions. Therefore it was decided to make the measurements only over a $10 \times 2\,\mathrm{m}$ patch.

The short side (2 m) allowed for convenient access on foot all around the patch. This reduced width meant that a simple hand held camera could take images of any part of the site to a resolution of a few mm or better using a wide angle lens. And the longer side (10 m) still guaranteed that the pixel-scale features were captured.

Note that even if interactions between the incidence radar wave and the soil surface is unlikely to happen at large-scale roughness features (>1 m), it is still interesting to monitor them to study eventual changes over time. In particular one could verify that large-scale features change over time-scales longer than the small scale features.

Measurement resolution A resolution which matches the $\lambda/10$ threshold is targeted. C-band and L-band are the most suitable frequency bands to sense soil moisture. The most stringent requirement occurs at C-band. With $\lambda_C = 5\,\mathrm{cm}$, measurements must be sensitive to millimeter-scale features. Therefore 1 mm resolution is desirable.

Measurement accuracy It was said in section 2.1.5 that Lievens *et al.[13]* recommend a 2 mm accuracy on the height measurements. Their conclusion was based on ten synthetic 4 m long profiles with a 1 mm resolution (4×10^4 height measurement points), to which they added noise uniformly distributed between -2 mm and 2 mm. A $10 \times 2\,\mathrm{m}$ DEM with the same resolution will lead to 2×10^7 measurement points which will make the estimation of the roughness parameters more robust. However, even with an infinite number of points there will still be a positive bias at least on the RMS height estimation. Indeed, the uniformly distributed height error between -2 and 2 mm has a variance of $1.3\,\mathrm{mm}^2$ which will be added to the true height variance s^2 (square of the RMS height). This is why the 2 mm accuracy will be kept as a requirement for this study. It is also consistent with the 1 mm measurement resolution.

3.2.2.2 Overall description of the measurement process

The measurement process can be decomposed in four main parts: (1) setup of reference targets, (2) image acquisition, (3) image processing with SfM, (4) computation

of roughness parameters (Fig. 3.2).

1. The first step is required (1) to scale the final DEM, and (2) to make multitemporal acquisitions of the same soil surface possible. For the first point, reference targets with known 3D positions must be included on the imaged scene. As for the second point, the same patch must be imaged each time in order to capture roughness changes with time. To this end, the reference targets are inserted into the soil where they remain for the whole duration of the measurement campaign. The same targets are used both for scaling and to delimit the imaged patch. Setting up these targets and measuring their relative 3D position is only needed once.

2. Image acquisition is done with a commercial-grade camera (table 3.1). For most acquisition dates, two sets of images are taken. For the first set (*set A*), the camera is hand-held at a height of about 1 m (waist level) and a total of approximately 600 images are taken to cover the entire plot which is about $2 \times 11\,\mathrm{m}$. The second set (*set B*) which also contains ~600 images, focuses on a fraction of the same plot ($2 \times 3.4\,\mathrm{m}$) and combines the images taken at a height of 1 m with close range images (20 cm from soil surface) to capture small roughness features. Figure 3.3 illustrates the acquisition strategy. Such a separation is justified by the fact that large-scale roughness features can be captured over the $2 \times 11\,\mathrm{m}$ patch without detailed images of the soil, while small-scale roughness features can be properly sampled over a reduced surface area only with close range images. DEMs generated from the first set will be referred as *DEMs A,* while DEMs generated from the second set will be referred as *DEMs B.* Because roughness changes are mainly expected to happen at small/medium scales, DEMs B are generated for every acquisition dates, while DEMs A are generated less frequently. Table 3.2 summarizes the characteristics of both DEMs. The acquisition height is approximate since the camera is hand-held, and the number of images is an average value computed for all the acquisitions of experiment 1.

3. The third step is image processing with SfM. First image resolution is decreased from 2592×1728 pixels (3.1 Mo) to 1728×1152 pixels (1.4 Mo), then images are compressed from 1.4 Mo per image (raw size at 1728×1152) down to a size of ~510 Ko per image (compression factor of 2.7) to keep reasonable both computational time with SfM (~5 h), and the total storage space required to archive all the images of every acquisition. Then SfM takes as input a set of images and generates the corresponding point cloud which is finally scaled using the reference points. Table 3.2 shows that with the close range images the point cloud density of DEMs B is five times the density of DEMs A.

4. The last step consists in computing soil surface statistics which, for radar backscattering, typically include RMS height and correlation length. To do so, the point cloud output by SfM is interpolated over a 1 mm grid. Such a resolution guarantees that no information from the dense point clouds is lost in under-sampling, while keeping file size reasonable.

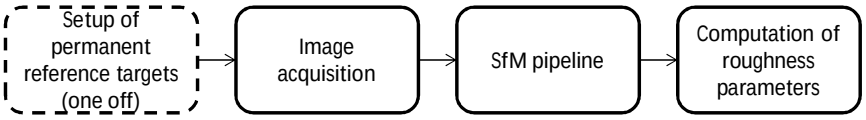

Figure 3.2: Measurement steps

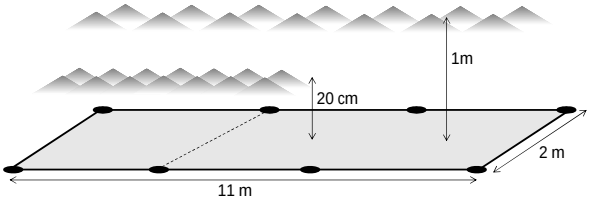

Figure 3.3: Image acquisition strategy. The gray triangles symbolize the field of view of each camera pose. The black dots are the reference targets. DEM A is generated from images taken at a height of 1 m, covering the entire plot. DEM B is obtained from images taken at 1 m and 20 cm, covering only 1/3 of the total plot.

The next section details the method used to accurately determine the 3D position of the reference targets delimiting the 2×11 m patch.

Parameter	Values
Camera	Canon EOS 550D (1.6 crop factor)
Lens	Sigma 10-20 mm f/3.5, set at 10 mm
Resolution [pixels]	1728×1152
Image size [Mo]	6 (raw), 0.6 (compressed)
Sensor size [mm]	22.3×14.9
Focal length [mm]	16

Table 3.1: Characteristics of the camera

Parameter	DEMs A	DEMs B
Image acquisition height	1 m	1 m and 20 cm
Number of images	573	210 (1 m) + 325 (20 cm)
Image overlap	90%	90% (1 m) and 50% (20 cm)
DEM size	2×11 m	2×3.4 m
Average point cloud density	11 points/cm^2	57 points/cm^2
DEM grid resolution	1 mm	1 mm

Table 3.2: Characteristics of DEMs A and DEMs B

3.2.2.3 Reference points

A total of eight reference targets are evenly spaced around each of the two imaged patch. Figure 3.4a shows the setup of a target. Each target is a 20-cm-high cylinder made of nylon which is screwed on a nylon post itself buried 50 cm deep into the

soil. This guarantees that the target remains in the same position throughout the measurement campaign. Nylon material was chosen to limit undesirable backscattering contributions from the targets during eventual Radarsat-2 acquisitions. The actual reference points are identified by a marker printed on paper and glued on top of each cylinder. The nylon cylinders are detached from the posts after each acquisition to protect the targets from outdoor conditions. The number of targets was chosen as a trade-off between (1) having targets close enough to each other to allow accurate measurement of their relative position, and (2) not having too many targets to attach into the soil and to measure (lengthy process).

The relative 3D position of targets is measured with a laser range finder (Leica DISTO X310) and an optical level (Leica Jogger 20). Table 3.3 summarizes the characteristics of each measurement.

The optical level is set up horizontally on the soil surface using its built-in spirit level. It gives the relative height of the targets from readings of the scale glued to each nylon cylinder (Fig. 3.4a). From repeated measurements of all the targets, the uncertainty on the measured height was found to be about 1 mm.

The laser range finder has a standard tripod screw thread which allows its attachment on top of every post (after removing the target screwed on it). It gives the distance of all neighboring targets (Fig. 3.4d). Repeated measurements showed a 2 mm uncertainty on the range measurements which is acceptable considering the stated accuracy of 1 mm of the instrument. This uncertainty was further decreased by averaging the measured range from target i to target $i+1$ and from target $i+1$ to target i. The x, y coordinates were then retrieved by trilateration.

Fig. 3.5 shows the overall arrangement of the targets around the two imaged patches. Fig. 3.5b illustrates a standard configuration for which the coordinates (x_1, y_1) of target 1 can be retrieved according to equations 3.1 from the range measurements between target 1,7 and 8 (R_{17}, R_{18}, and R_{78}).

$$\begin{cases} x_1 &= \frac{R_{18}^2+R_{78}^2-R_{17}^2}{2R_{78}} \\ y_1 &= \sqrt{R_{18}^2 - x_1^2} \end{cases} \tag{3.1}$$

Similarly, the coordinates of target 3 are first determined in a reference frame centered on target 2 (Fig. 3.5c) with the x-axis toward target 7. The obtained coordinates are then expressed in the main reference frame centered on target 8. One by one the coordinates of all the points are determined in a local reference frame then expressed in the main reference frame centered on target 8. Figure 3.6 shows the measured position of the 8 targets of field 2. The delimited surface area is approximately 11x2.4 m^2. Because the targets along each edge are not perfectly aligned, the final interpolation is done over a rectangular area (dashed line on Fig.3.6) whose edges are 20 cm within the rectangle delimited by targets (8, 5, 1).

The final uncertainty on x and y due to range uncertainty is not straightforward to assess as it depends on the relative positions of the targets used in the trilateration. Because the y coordinate corresponds to the short side of the plot, it is more accurate than the x coordinate (long side of the plot). The worst case for the x coordinate occurs when the targets of one side are aligned. In that case, the errors on the range measurement directly add up. Summing the variance over 3 intervals leads to a maximum uncertainty of 3.5 mm on x (figure 3.4d).

Parameter	Optical level	Laser range finder
Instrument	Leica Jogger 20	Leica DISTO X310
Measured quantity	z	Range target$_{i \to i+1}$
Uncertainty [mm]	$\sigma_z = 1$	$\sigma_r = 2$
Post processing	-	Trilateration of x and$y$
Final uncertainty [mm]	$\sigma_z = 1$	$\sigma_x \leq 3.5$, $\sigma_y < \sigma_x$

Table 3.3: Characteristics of 3D position measurements. The optical level provides directly the z coordinate. The laser range finder gives x and y after trilateration.

Because both the targets, the optical level and the laser range finder are set to be in the local horizontal plane, x, y defines the local horizon and z is the corresponding height. This is an interesting point when the slope of the DEM is of interest. It might not be the case for microwave scattering (roughness measurements are usually linearly detrended), but it is certainly an interesting parameter for applications related to soil erosion [105].

3.2.3 Soil moisture, temperature and rainfall measurements

Soil moisture can change significantly within a few hours, therefore moisture measurements have to be automatic. To do so, a set of soil moisture probes is connected to a data logger which saves measurements every 30 min. The same data logger is used to save soil moisture, temperature and rainfall measurements. The data logger has been built around an open-source electronics prototyping platform called *Arduino*. The system has been alternatively installed next to field 1 and field 2. The following gives more details about the hardware selected for the data logger.

Soil moisture Soil moisture is measured with three theta probes made available by the National Soil Resources Institute at Cranfield University. These theta probes are analog sensors with an output voltage proportional to the soil dielectric constant. They sense the impedance of the soil by applying a 100 MHz sinusoidal signal to an array of four rods [106]. This frequency is selected to maximize sensitivity to the dielectric constant. The probe can be used without specific calibration with an accuracy of ± 0.05 m^{3}m^{-3}. For mineral soils, the following model transforms the output voltage into the corresponding volumetric soil moisture.

$$m_v = 0.5286V - 0.0595 \tag{3.2}$$

The theta probes were separated from each other by a few meters. The spread of the probes was limited by the cables which connect them to the data logger.

Temperature Soil temperature at a depth of ~3 cm and air temperature are measured with two digital sensors with an accuracy of ± 0.5°C.

Rainfall Rainfall is monitored with a tipping bucket rain gauge. The rain collected with a funnel tips and actuates a swing which closes an electronic circuit. Table 3.4

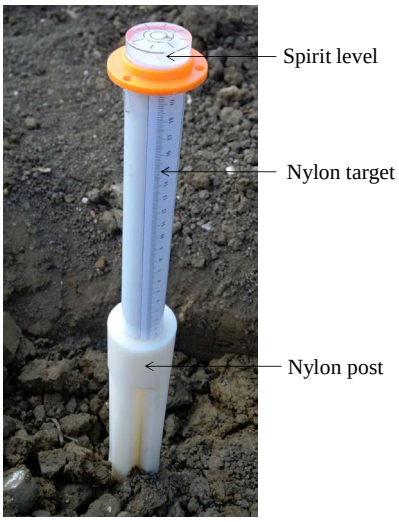

(a) The cylindrical reference target is screwed on top of a buried nylon post. A spirit level is used to check verticality

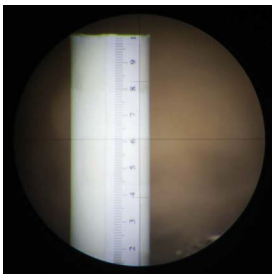

(b) View finder of the optical level

(c) Images are acquired with a hand-held camera (Image date 24/04/2014)

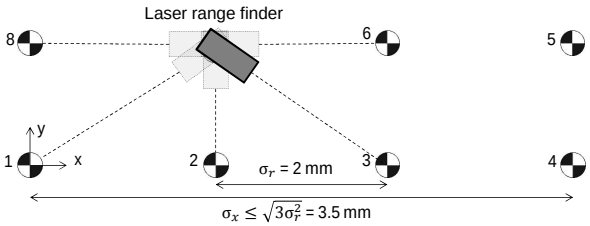

(d) Distance measurement with laser range finder

Figure 3.4: Setup of reference targets

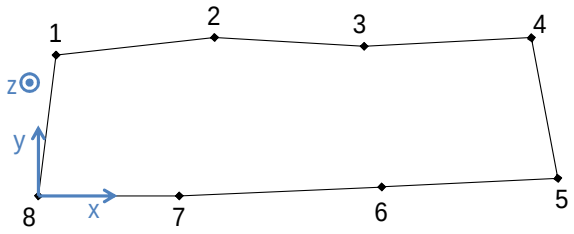

(a) Overall configuration of the 8 targets for field 2

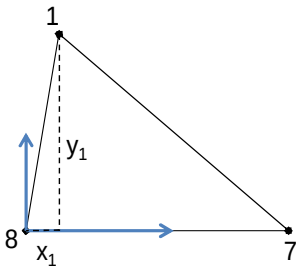

(b) Frame of reference used to determine the position of target 1

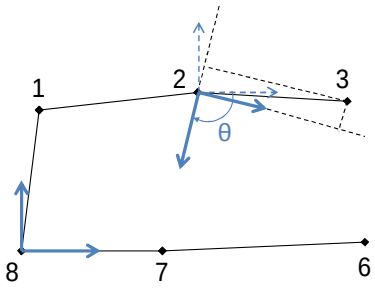

(c) Frame of reference used to determine the position of target 3

Figure 3.5: Trilateration of the (x, y) coordinates of each target from range measurements

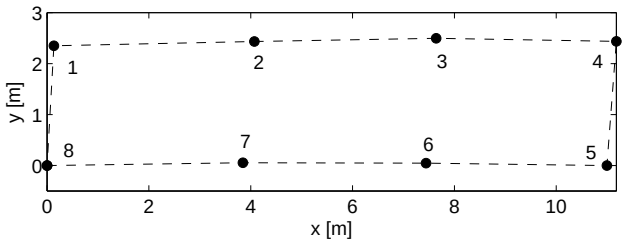

Figure 3.6: Measured position of the targets of field 2 after trilateration

Calibration	Nber of swings	ml/swing	mm/swing
1	140	7.1	0.220
2	137	7.3	0.224
3	138	7.2	0.223
4	137	7.3	0.224
5	139	7.2	0.221
Mean	138.2	7.2	0.222

Table 3.4: Calibration of the rain gauge

shows the calibration of the rain gauge obtained by pouring 1 l of water and counting the number of swings, the process was repeated 5 times. While moisture sensors and temperature sensors can be switched off during the 30 min interval which separates two acquisitions, the number of actuations of the rain gauge has to be monitored permanently.

All the measurements are saved on an SD card, with a time tag provided by a real time clock module. Figure 3.7 shows the different components of the weather station.

Power management In order to keep power consumption low, the main processing board (Arduino board) enters a sleep mode, and a dedicated circuit monitors the rain gauge. This circuit includes (1) a signal conditioning circuit with a RC low-pass filter and a Schmidt trigger, (2) a counter which counts the number of actuations of the swing, and (3) a 16-channel multiplexer which makes the connection with the Arduino board. The counter is a 12-bit binary counter, hence it can counts a maximum of 2048 actuations before reaching saturation. Since there is hardly more than one actuation of the rain gauge per second, this counter is suitable to monitor rain over a 30-min window. After 30 min, the Arduino board (1) wakes up, (2) reads the value of the soil moisture probes and of the temperature probes, (3) reads the value of the counter through the multiplexer, and (4) resets the counter before going back to sleep for the next 30 min.

The system is powered by a 12V 7Ah lead-acid battery. While sleeping the system consumes only 5 mA, and the consumption increases up to 65 mA for about 10 s when moisture and temperature are measured. So the battery should provide about 56 days of autonomy.

As shown on figure 3.8 all the components are housed in an airtight container which makes the data logger weatherproof.

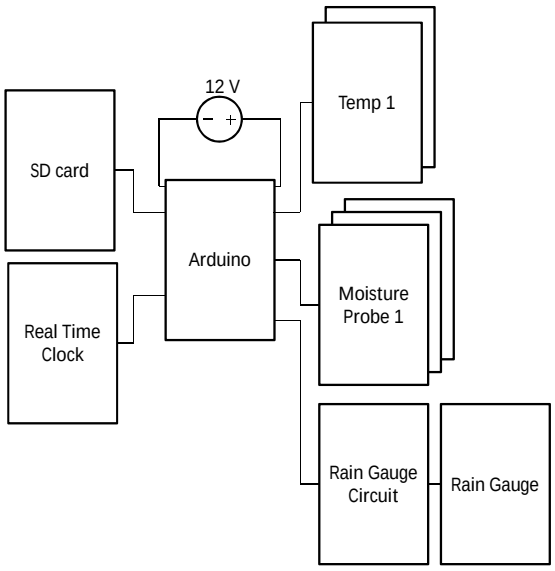

Figure 3.7: Main components of the weather station

Figure 3.8: Data logger

3.3 Setup for experiment 2

3.3.1 Location and duration

Experiment 2 took place over the same farm location but included more sampled fields than experiment 1 in order to test the soil moisture retrieval algorithms with several candidate fields. Fig. 3.9 shows the location of the 14 sampled fields. Not all the fields were systematically sampled for each Radarsat-2 acquisition, section 3.9 gives more details about the available data. These fields were selected because they were bare or with light vegetation cover. The experiment spanned from 18 October 2013 to 19 December 2013.

Figure 3.9: Location of the 14 fields sampled during experiment 2

3.3.2 Roughness measurements with SfM

3.3.2.1 Extent, resolution and accuracy of measurements

The resolution and accuracy of the roughness measurements are the same than those of experiment 1. Since the setup has to be portable to carry measurements over the 14 fields, the use of anchored reference targets was not suitable. Instead, a more conventional setup using a rectangular frame, like in [12, 44, 39], was thought more appropriate. The frame was retrieved from an unused table. It is made of four square-section iron rods welded at there extremities. The size of the frame is 1.530×0.716 m (measured with the laser range finder).

3.3.2.2 Overall description of the measurement process

The measurement process is similar to that of experiment 1: (1) setup of the frame, (2) image acquisition, (3) image processing with SfM, (4) computation of roughness parameters.

1. The setup of the frame is simple. The frame is just laid on the soil surface. No precaution is taken to have the plane of the frame in the horizontal plane. Any trend on the final DEM will be removed by plane fitting. This simple setup makes multiple acquisitions over different fields straightforward.

2. Image acquisition is fast since the surface area to be imaged is small. About 80 images are taken for each acquisition with 25 images taken at a height of 1 m and 55 images taken at a height of 20 cm.

Step 3 and step 4 are as described before.

(a)

(b)

Figure 3.10: Frame used for the roughness measurements of experiment 2. Reference targets are glued at different height on the four corners of the frame.

Figure 3.11: Theta probe and readout unit

3.3.2.3 Reference points

The four legs of the table have been cut down to four different heights (7 cm, 10 cm, 15 cm, 20 cm). Targets made of paper have been glued on top of each foot and are used as reference points to scale the DEMs (Fig. 3.10).

3.3.3 Soil moisture measurements

Soil moisture needs to be measured along with surface roughness for each fields. Using the data logger with its three theta probes would not be practical. Instead, a portable theta probe with a soil moisture meter readout unit (Fig. 3.11) is used to carry multiple and rapid sampling.

Note that measurements from the data logger are also valuable for experiment 2 as they provide continuous measurements of soil moisture / temperature / rainfall. In particular these data can be used to infer drying or wetting trends between two radar acquisitions, and to cross-check soil moisture measurements between the different devices.

3.4 Preprocessing of Radarsat-2 images

3.4.1 Description of the Single Look Complex product

Different formats are available with Radarsat-2 products. They can be grouped into slant range product and ground range products. The only slant range product available is the Single Look Complex (SLC) format. Many ground range products are

available and differ mainly according to the resampling method used to transform the data from the geocoded radar coordinate system to a geocorrected Earth coordinate system. The SLC format was chosen because the other formats undergo image processing steps which may not be fully tractable. This also means that the SLC images will need to be geocorrected before being used for soil moisture estimation.

Each acquisition contains the following files

- Four geotiff files for the $vh-$, $hv-$, $hh-$, and $vv-$images. Each files contains meta-data about the acquisition and two layers corresponding to the in-phase and quadrature components of the radar measurements.
- Three lookup tables to convert the measured intensity into calibrated quantities σ^0, β^0, and γ^0.

3.4.2 Geocorrection

The SLC images are processed with the open source Next ESA SAR Toolbox (NEST). Each image is georeferenced (the geographic coordinates of the corners of the image is known), but they are not geocorrected. In particular, geocorrection is required to account for topography with a DEM of the imaged area. For example the freely available DEM from the Shuttle Radar Topography Mission (SRTM) is already projected on the WGS 84 ellipsoid. Hence the SLC image must first be projected on the same Earth coordinate system.

Geocorrection can be done by NEST with the *range-doppler terrain correction* (RDTC) tool. The RDTC applies a sequence of operations including (1) transformation from slant-range to ground-range, (2) projection onto an Earth coordinate system, (3) radiometric correction, and (4) orthorectification to compensate for overlays.

1. The slant-range to ground-range transformation accounts for the distortion highlighted by Fig. 3.12. It is corrected from the knowledge of the incidence angle from the near range to the far range.
2. The radar image is projected on the WGS 84 ellipsoid.
3. Radiometric correction makes use of the lookup table for σ^0 given with the SLC image and the SRTM DEM available for the imaged area. More precisely, the lookup table allows transforming the measured intensity into $\sigma^0_{ellipsoid}$. Then the local incidence relative to the DEM is used to account for topography with the following equation,

$$\sigma^0_{DEM} = \sigma^0_{ellipsoid} \frac{\sin\theta_{DEM}}{\sin\theta_{ellipsoid}} \tag{3.3}$$

   with $\theta_{ellipsoid}$ the local incidence relative to the ellipsoid, and θ_{DEM} the local incidence relative to the DEM.
4. Orthorectification applies the range Doppler method presented in [107].

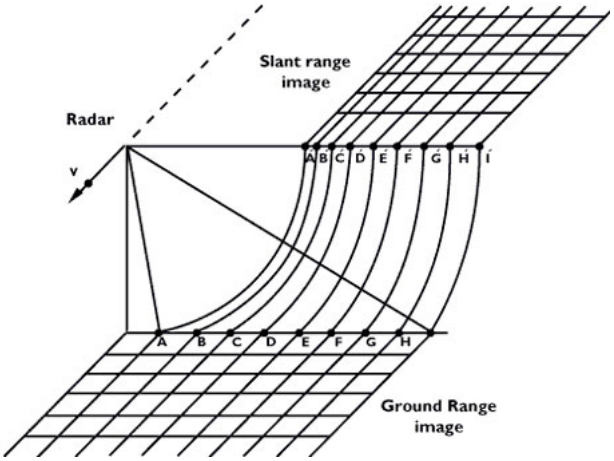

Figure 3.12: Slant-range to ground-range transformation. Image adapted from [108].

The projection on the WGS 84 ellipsoid requires selecting a resampling method. With the default method, *bilinear interpolation*, each resampled pixel is a weighted combination of four neighboring pixels. As a result, the intensity is not exponentially distributed as described in section 2.2.2. If resampling was done by arithmetic averaging of four pixels, the operation would be equivalent to multilooking with four looks, hence according to equation 2.29 the resulting intensity would be $\Gamma(4)$-distributed. Fig. 3.13a shows the histogram for a group of pixels which belong to the same field (field 12) after geocorrection with bilinear interpolation. The data clearly do not follow a $\Gamma(4)$ distribution. Bilinear interpolation is similar to a weighted average which is different from the arithmetic average.

The simple *nearest neighbor interpolation* was selected for this project as a more tractable alternative because it preserves the exponential distribution (Fig. 3.13b). Note that when the selected pixels contain strong scatterers the scene cannot be considered as a distributed target and the distribution of intensity is not exponential (Fig. 3.14). This is an interesting test to do on a collection of pixels before trying to retrieve soil moisture. When the selected pixels do not follow an exponential distribution, it is a sign that some of the pixels might belong to a different field, or that the studied field is not homogeneous in soil moisture / surface roughness.

3.4.3 From exponential multiplicative noise to Gaussian additive noise

As showed in the previous section, after nearest neighbor resampling, the intensity over a given field remains exponentially distributed. In other words, the model with exponential multiplicative speckle still applies. In order to apply the χ^2 to a group of Radarsat-2 pixels, the exponential multiplicative speckle must be transformed into Gaussian additive noise with zero mean. This can be done by first applying a *power transform* to a group of pixels which belong to the same distributed target. The power transform is a family of transformations recommended to make exponentially distributed data approximately Gaussian [109]. It is simply defined by

$$z_i = y_i^{\lambda} \tag{3.4}$$

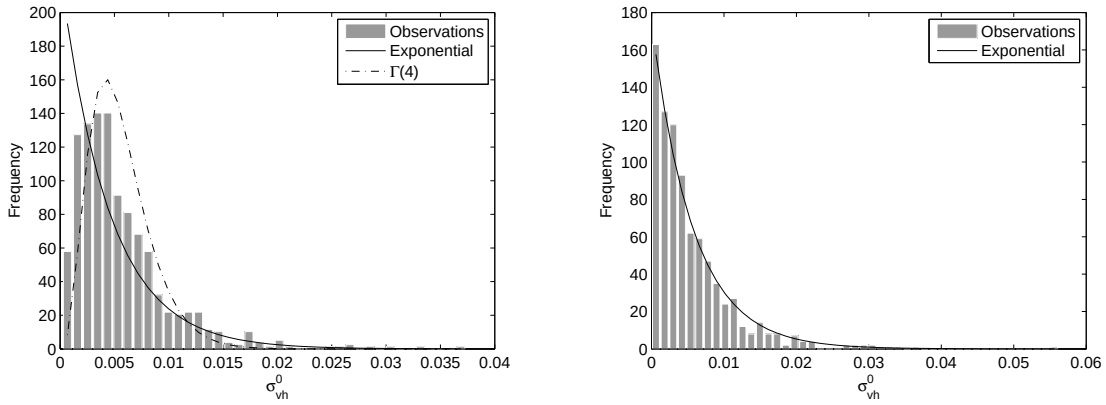

(a) (b)

Figure 3.13: Distribution of σ^0_{vh} for a Radarsat-2 image of field 12 after geo-correction with (a) a bilinear interpolation, and (b) a nearest neighbor interpolation. The nearest neighbor interpolation preserves the exponential distribution of speckle.

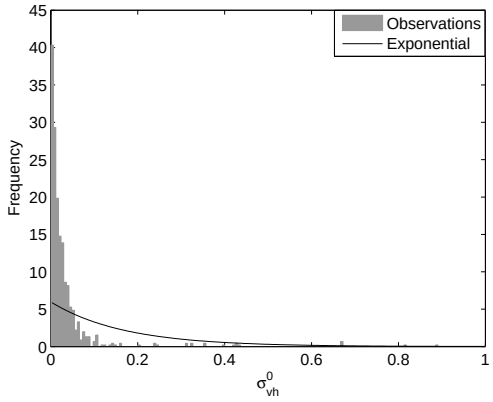

Figure 3.14: Distribution of σ^0_{vh} after nearest neighbor interpolation for a scene with multiple strong scatterers

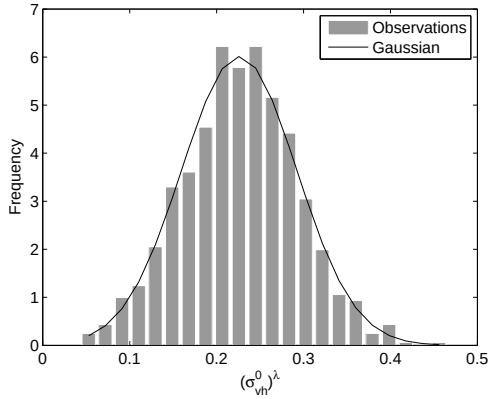

Figure 3.15: Distribution of σ^0_{vh} over field 12 after nearest neighbor interpolation and power transform with $\lambda = 0.27$

with $\lambda > 0$.

As suggested by Box *et al.*, the optimal λ is classically determined by minimization of a log-likelihood function [110]. After transformation with the optimal exponent λ, Gaussianity can be tested by applying a *Kuiper test* [111]. In practice, for an exponential distribution, good results are obtained with $\lambda \approx 0.2654$.

From equation 2.27, the transformed intensity I^λ can be written as follows

$$I^\lambda = \left(\sigma^0\right)^\lambda N^\lambda \tag{3.5}$$

Since for a given distributed target σ^0 is constant, both the transformed speckle and the transformed intensity follow a Gaussian distribution,

$$N^\lambda \sim \mathcal{N}(\alpha, \beta) \tag{3.6}$$

$$I^\lambda \sim \left(\sigma^0\right)^\lambda \mathcal{N}(\alpha, \beta) \tag{3.7}$$

The transformed intensity can equivalently be expressed as a constant affected by additive zero-mean Gaussian noise

$$I^\lambda \sim \alpha \left(\sigma^0\right)^\lambda + \mathcal{N}\left(0, \left|\sigma^0\right|^\lambda \beta\right) \tag{3.8}$$

with constant standard deviation $\left|\sigma^0\right|^\lambda \beta$.

For the retrieval to be consistent, the backscattering model must be modified to map the soil parameters to the transformed intensity $\alpha \left(\sigma^0\right)^\lambda$, *i.e.*

$$z_i = \alpha \left(\mathcal{F}_i \left(m_v,\, s\right)\right)^\lambda \tag{3.9}$$

The optimal exponent λ is known ($\lambda \approx 0.2654$), and α can be computed from the theoretical mean of the transformed speckle

$$\alpha = E\left[N^\lambda\right] = \lambda\Gamma\left(\lambda\right) \tag{3.10}$$

with Γ the *Gamma function.* Thus the transformed backscattering model is

$$\mathcal{F}'_i = \lambda\Gamma\left(\lambda\right)\left(\mathcal{F}_i\right)^\lambda \tag{3.11}$$

Alternatively, α can also be determined empirically as follows

$$\alpha = \frac{E\left[I^{\lambda}\right]}{E\left[I\right]^{\lambda}} \tag{3.12}$$

In this project, the $\mathcal{F}_i$ are given by the simplified Oh model. After transformation, the equations become

$$\sigma^0_{vh} = \lambda\Gamma\left(\lambda\right)\left[0.11 m_v^{0.7}\left(\cos\theta\right)^{2.2}\left[1-\exp\left(-0.32\left(ks\right)^{1.8}\right)\right]\right]^{\lambda} \tag{3.13}$$

$$\sigma^0_{vv} = \lambda\Gamma\left(\lambda\right)\left[\frac{\sigma^0_{vh}}{0.095\left(0.13+\sin\left(1.5\theta\right)^{1.4}\right)\left[1-\exp\left(-1.3\left(ks\right)^{0.9}\right)\right]}\right]^{\lambda} \tag{3.14}$$

$$\sigma^0_{hh} = \lambda\Gamma\left(\lambda\right)\left[\sigma^0_{vv}\left[1-\left(\frac{\theta}{90^\circ}\right)^{0.35 m_v^{-0.65}}\exp\left(-0.4\left(ks\right)^{1.4}\right)\right]\right]^{\lambda} \tag{3.15}$$

3.5 Uncertainty requirements for remote sensing of soil moisture and surface roughness

This section defines observation requirements for soil moisture and surface roughness. These requirements will be referred to when analyzing the performance of model inversion.

Remote sensing of soil moisture As mentioned in the introduction, soil moisture is a valuable parameter for many applications. For each application, the requirements in terms of spatial resolution, temporal resolution, and uncertainty are different. The Observing Systems Capability Analysis and Review (OSCAR) Tool makes available a list of observation requirements for different variables and their applications. Table 6.28 lists the requirements identified for soil moisture. For each application, the first value corresponds to the ideal value, the second value indicates the requirements associated with a breakthrough, and the third value is the threshold value from which measurements become useful.

This study focuses on field-scale estimation of soil moisture, *i.e.* high resolution estimation. Such resolution is required for agricultural meteorology and hydrology. For both applications, the largest acceptable uncertainty is $0.05\,\mathrm{m}^3/\mathrm{m}^3$, and agricultural meteorology has the strictest minimum resolution threshold of 1 km.

For both applications, measurements start being useful if the uncertainty is less than $\pm 0.05\,\mathrm{m}^3/\mathrm{m}^3$. Here uncertainty is to be understood as standard deviation σ_{m_v}. Assuming that the error affecting soil moisture is Gaussian, the interval $m_v \pm \sigma_{m_v}$ corresponds to 68.3% confidence interval. Therefore in this study, uncertainty is always given with a confidence level of 68.3%.

The threshold resolution requirement for agricultural meteorology is the most stringent (1 km). Such a threshold is a key parameter as it sets the maximum number of pixels that can be averaged over a field in order to mitigate measurement

noise. Considering that SARs, including Radarsat-2, can achieve resolution of about 10 m, multilooking could be done with a maximum of 10 000 pixels to reach the required $\pm 0.05\,\mathrm{m}^3/\mathrm{m}^3$ uncertainty.

Remote sensing of surface roughness Surface roughness estimation could benefits applications such as soil erosion [12] as there is a preferred runoff direction defined by the furrow direction (oriented roughness), and the intensity of this runoff is influenced by the random roughness [112]. It could also be used for agricultural land classification since tillage operations lead to a rather deterministic range of RMS height (see table 3.6) [113, 112, 50]. For example Trudel *et al.* investigated surface roughness classification from multi-polarized ENVISAT-ASAR acquisitions (C-band) [114]. From a time series of the cross-polarized ratio $\sigma^0_{vh}/(\sigma^0_{hh} + \sigma^0_{vv})$, they could discriminate ploughed fields (rough) and pastures (smooth).

However there is no trace of measurement requirements. This could be attributed to the fact that, unlike for soil moisture, even in situ measurements are often said to give unreliable/inadequate roughness characterization which can lead to inaccurate soil moisture estimation [69]. Since over agricultural soils, RMS height typically ranges from 5 mm to 50 mm [113], a 20% uncertainty will be taken as requirement for this study. This leads to the extrema $s = 5 \pm 1\,\mathrm{mm}$ and $s = 50 \pm 10\,\mathrm{mm}$. This 20% uncertainty is acceptable to discriminate the main tillage classes listed in table 3.6.

As for the other requirements listed in table 6.28 (spatial resolution, temporal resolution, timeliness), they will be a priori less demanding than those for soil moisture. For example, it is unlikely that daily roughness classification would be of any use. In the end, the estimation methods investigated in this project aim at estimating soil moisture and surface roughness simultaneously. Therefore, meeting the soil moisture requirements will be more than satisfactory with regard to the less demanding requirements for surface roughness.

Application (confidence)	**Uncertainty** [m^3/m^3]	**Resolution** [km]	**Time sampling**	**Timeliness**
	0.01	*0.01*	*1 d*	*1 d*
Hydrology	*0.017*	*0.3*	*34 h*	*5 d*
(reasonable)	*0.05*	*250*	*3 d*	*144 d*
Agricultural	*0.01*	*0.1*	*1 d*	*1 d*
meteorology	*0.017*	*0.215*	*46 h*	*41 h*
(reasonable)	*0.05*	*1*	*7 d*	*5 d*
	0.01	15	1 d	10 d
GEWEX[1]	0.02	50	3 d	15 d
(tentative)	0.05	250	10 d	30 d
	0.02	5	3 h	3 h
Global NWP[2]	0.04	15	1 d	1 d
(reasonable)	0.08	100	5 d	5 d
High Res	0.02	1	1 h	30 min
NWP	0.04	5	3 h	1 h
(reasonable)	0.08	40	6 h	6 h
Nowcasting	0.01	5	1 h	1 h
/ VSRF[3]	0.02	10	6 h	6 h
(reasonable)	0.05	50	1 d	1 d
	0.01	50	1 d	1 d
SIA forecasts[4]	0.02	100	2 d	2 d
(reasonable)	0.05	500	5 d	5 d
	0.005	50	7 d	1 y
TOPC[5]	0.007	60	11 d	1 y
(speculative)	0.01	100	30 d	2 y

[1]Global Energy and Water Cycle Experiment, [2]Numerical Weather Prediction,
[3]Very Short Range Forecasting,[4]Seasonal and Inter-Annual Forecasts,
[5]Terrestrial Observation Panel for Climate

Table 3.5: Observation requirements for soil moisture as defined by the OSCAR tool [7]. For each application, the first value corresponds to the ideal requirement, the second value indicates the requirements associated with a breakthrough, and the third value is the threshold value from which measurements become useful. The confidence indicates how likely such a soil moisture product would benefit a given application.

Tillage operation	**s [cm]**
Large offset disk	5.0
Moldboard plow	3.2
Lister	2.5
Chisel plow	2.3
Disk	1.8
Field cultivator	1.5
Row cultivator	1.5
Rotary tillage	1.5
Harrow	1.5
Anhydrous applicator	1.3
Rod weeder	1.0
Planter	1.0
No till	0.7
Smooth	0.6

Table 3.6: Average RMS height for different tillage operations [50]

Chapter 4

Material

4.1 Data set of experiment 1

Roughness measurements with SfM Tables 4.1, 4.2, 4.3 and 4.4 list all the roughness measurements made with SfM. Tables 4.1 and 4.2 correspond to two periods of measurements over field 1. Over the first period, the field has not been tilled because of inappropriate weather conditions. At the end of the first period, tillage operations took place for the new crop cycle and required to remove the anchored targets. The second period started after re-inserting the targets into the soil. Similarly, there are two periods of measurements over field 2 (table 4.3 and 4.4) with no tillage operations during the first period. The main consequence of not having the usual tillage operations during the first period is that no oriented roughness was visible. The aspect of the soil surface resulted primarily from random roughness and large features attributable to topography.

For each table, *Day* is the number of days from the first SfM acquisition of a given period. *Pictures used* is sometimes different from *Pictures taken* when SfMtoolkit discards images for which no common features were found. The column *# of points* gives the total number of points of the reconstructed point cloud. The column *Comments* reports whether the acquisition corresponds to a DEM A or B, and the focal length selected to take the pictures. Where there is no mention of the focal length, the acquisition has been done with $f = 10$ mm.

At the beginning of period 1, different focal lengths were tested. From tables 4.1 and 4.3, it appears that acquisitions with a 20 mm focal length lead to larger point clouds than acquisitions with a 10 mm focal length. Still the 20 mm case was deemed unsuitable because the resulting point clouds had many gaps probably coming from insufficient overlapping between the pictures. Increasing overlapping would require a much larger number of images which is not practical for repeated measurements. Therefore the 10 mm configuration was selected as a good compromise between a reasonable amount of images and a good-enough point cloud density.

In total, there are 113 SfM measurements. Not all of them have been georeferenced as the manual identification of the reference targets on the pictures is a very repetitive process. Nonetheless, all these acquisitions will be useful to investigate how the number of points of the point cloud tends to increase with the number of

pictures.

Table 4.1: List of SfM measurements for field 1, period 1

#	Date	Day	Pic taken	Pic used (1m/20cm)	# of points	Comments
1	31/03/2013	1	562	560	6392970	A, f^* 18 mm
2	08/04/2013	9	453	431	7002939	A, f 28 mm
3	12/04/2013	13	236	231	3059745	B, f 20 mm
4	17/04/2013	18	367	367	4537451	B, f 20 mm
5	24/04/2013	25	517	516	7184949	B, f 20 mm
6	24/04/2013	25	536	294	4036995	B, f 15 mm
7	24/04/2013	25	241	241	2029676	B, f 10 mm
8	06/05/2013	37	733	730	4452698	A
9	06/05/2013	37	692	692 (317/375)	5460422	B
10	14/05/2013	45	808	808	3607810	A
11	14/05/2013	45	699	699 (319/380)	4996874	B
12	20/05/2013	51	818	818	3811887	A
13	20/05/2013	51	685	685 (324/361)	5343147	B
14	27/05/2013	58	848	749	4332492	A
15	27/05/2013	58	736	734 (301/433)	6205519	B
16	03/06/2013	65	587	584 (243/341)	4906906	B
17	03/06/2013	65	663	663	4163206	A
18	17/06/2013	79	758	757 (287/470)	4329732	B
19	17/06/2013	79	735	735	3661451	A
20	25/06/2013	87	675	670 (291/379)	5836721	B
21	25/06/2013	87	671	671	3791479	A

*focal length

Table 4.2: List of SfM measurements for field 1, period 2

#	Date	Day	Pic taken	Pic used (1m/20cm)	# of points	Comments
1	23/08/2013	1	620	620	3469238	A
2	03/09/2013	12	620	620 (247/373)	6123207	B
3	03/09/2013	12	632	632	3614752	A
4	08/09/2013	17	476	469 (224/245)	4116259	B

5	08/09/2013	17	567	564	3376092	A
6	10/09/2013	19	404	383 (181/202)	3868271	B
7	17/09/2013	26	400	370 (181/189)	4044667	B
8	23/09/2013	32	460	460	2972679	A
9	28/09/2013	37	475	475	3027471	A
10	30/09/2013	39	436	435 (153/282)	4757537	B
11	30/09/2013	39	444	416 (152/264)	4982449	B
12	08/10/2013	47	363	333 (139/194)	3295141	B
13	08/10/2013	47	457	457	2949988	A
14	14/10/2013	53	471	451 (159/292)	4766654	B
15	14/10/2013	53	518	518	2787424	A
16	18/10/2013	57	500	498 (152/346)	5921910	B
17	18/10/2013	57	461	461	2760945	A
18	25/10/2013	64	515	515 (169/346)	5339471	B
19	25/10/2013	64	544	544	2881423	A
20	01/11/2013	71	481	481 (169/312)	5906133	B
21	01/11/2013	71	461	461	2805128	A
22	11/11/2013	81	439	439 (158/281)	4419957	B
23	11/11/2013	81	477	477	2497155	A
24	20/11/2013	90	367	365 (136/229)	3572364	B
25	25/11/2013	95	351	351 (122/229)	3748963	B
26	25/11/2013	95	378	373	1131886	A
27	05/12/2013	105	377	377 (141/236)	3576036	B
28	05/12/2013	105	393	393	2211438	A
29	12/12/2013	112	393	393 (132/261)	4244022	B
30	12/12/2013	112	413	413	2422590	A
31	18/12/2013	118	365	365 (121/244)	4434234	B
32	18/12/2013	118	387	387	2177521	A
33	17/01/2014	148	422	422 (144/278)	4352526	B
34	17/01/2014	148	456	456	2266047	A

35	24/03/2014	214	548	548 (192/356)	4602338	B
36	24/03/2014	214	626	626	2897781	A
37	02/05/2014	253	619	619 (238/381)	5551613	B
38	02/05/2014	253	785	785	3290938	A
39	12/06/2014	294	586	586 (214/372)	6079582	B
40	12/06/2014	294	670	670	3037674	A

Table 4.3: List of SfM measurements for field 2, period 1

#	Date	Day	Pic taken	Pic used (1m/20cm)	# of points	Comments
1	31/03/2013	1	348	348	3754311	A, f 18 mm
2	08/04/2013	9	408	221	4023178	A, f 28 mm
3	12/04/2013	13	461	461	4461480	B, f 20 mm
4	17/04/2013	18	509	299	3424665	B, f 20 mm
5	21/04/2013	22	1013	634	7464905	A, f 20 mm
6	24/04/2013	25	1219	520	6290204	A, f 20 mm
7	24/04/2013	25	544	269	3633324	B, f 20 mm
8	06/05/2013	37	737	737	3363789	A
9	06/05/2013	37	608	608 (258/350)	4364772	B
10	14/05/2013	45	700	700	3015467	A
11	14/05/2013	45	659	659 (257/402)	5296086	B
12	20/05/2013	51	768	768	3157724	A
13	20/05/2013	51	644	644 (303/341)	4947349	B
14	27/05/2013	58	639	639	3263529	A
15	27/05/2013	58	663	663 (238/425)	5531622	B
16	03/06/2013	65	512	512	3295793	A
17	17/06/2013	79	674	668 (276/392)	6197339	B
18	17/06/2013	79	669	669	3548231	A
19	25/06/2013	87	822	814 (342/472)	7447918	B
20	25/06/2013	87	811	811	2732320	A
21	01/07/2013	93	720	708 (269/439)	6397026	B
22	01/07/2013	93	728	728	3667572	A
23	10/07/2013	102	913	892 (348/544)	7804785	B

24	10/07/2013	102	754	753 (328/425)	6618484	B
25	21/07/2013	113	754	705 (251/454)	6975068	B
26	21/07/2013	113	245	245	1405210	B (1 m pic)
27	21/07/2013	113	661	658	3594270	A
28	24/07/2013	116	236	236	1369315	B (1 m pic)
29	27/07/2013	119	696	681 (237/444)	6818803	B
30	30/07/2013	122	626	602 (236/366)	6305476	B
31	30/07/2013	122	646	646	3768430	A

Table 4.4: List of SfM measurements for field 2, period 2

#	Date	Day	Pic taken	Pic used (1m/20cm)	# of points	Comments
1	18/10/2013	1	543	543	2812168	A
2	25/10/2013	8	406	404	1913639	A
3	01/11/2013	15	453	453	2338856	A
4	11/11/2013	25	380	380 (193/187)	3054957	B
5	11/11/2013	25	494	494	2562997	A
6	20/11/2013	34	382	380 (145/235)	3174669	B
7	20/11/2013	34	461	457	2376543	A
8	25/11/2013	39	347	346 (145/201)	3449811	B
9	25/11/2013	39	386	385	2306387	A
10	05/12/2013	49	351	350 (134/216)	3317381	B
11	05/12/2013	49	419	419	2316592	A
12	12/12/2013	56	364	364 (129/235)	3891256	B
13	12/12/2013	56	399	399	2302393	A
14	18/12/2013	62	366	366 (132/234)	3835792	B
15	18/12/2013	62	359	359	2023317	A
16	17/01/2014	92	400	400 (174/226)	3878450	B
17	24/03/2014	158	406	406 (131/275)	4059060	B
18	02/05/2014	197	535	535 (172/363)	5643067	B
19	02/05/2014	197	565	564	2977065	A

20	12/06/2014	238	569	566 (215/351)	6070505	B
21	12/06/2014	238	623	621	3210762	A

Data from data logger Table 4.5 summarizes the data available from the data logger. There are two main periods. Over the first period, the data logger was set up in field 2 for about 3 months. The second period covers nearly one year for which the data logger remained in field 1. All in all, there are no significant gaps in the data. The main gap corresponds to a loss of one of the three soil moisture probe because its cable was cut during tillage operations.

Period	Location	Gap in data	Reason
17 Jun 2013 - 21 Aug 2013 (66 days)	field 2	Loss of a soil moisture probe on 21 Jul 2013	Cable cut during tillage
24 Aug 2013 - 12 Jun 2014 (293 days)	field 1	Logger off from 2 May 2014 to 5 May 2014	Repairs on rain gauge

Table 4.5: Comments on data recorded by the data logger

4.2 Data set of experiment 2

In situ measurements Table 4.6 provides a list of all in situ measurements. All in all, more and more fields have been sampled throughout the experiment to increase the number of comparison between in situ measurements of soil parameters and soil parameters estimated from the radar measurements.

For fields 1 and 2, in situ measurements of soil moisture and surface roughness have been systematically taken for all acquisition dates. Soil moisture was evenly sampled about 10 times over each fields. Surface roughness was sampled from 3 to 10 times depending on the overall roughness homogeneity.

For fields 3 to 5, roughness measurements are not available because vegetation cover made SfM measurements impossible. For these 3 fields, there are no soil moisture measurements on 19 Dec because of lack of time. Fields 6 to 8 have been systematically sampled for moisture and roughness from the second acquisition. Moisture and roughness measurements for field 9 are only available from the 25$^{\text{th}}$ of November. Finally fields 10 to 14 were sampled only for the last three acquisitions.

Table 4.7 provides a qualitative description of each field in terms of surface roughness and vegetation cover which will be helpful to interpret the results.

Radatsat-2 data A proposal to study soil moisture estimation from full-polarimetric Radarsat-2 images was reviewed and accepted by the Canadian Space Agency (CSA) as part of the Science and Operational Applications Research Education International (SOAR-EI) Initiative [27].

Radarsat-2 acquisitions were planned with the Radarsat-2 acquisition planning tool. In theory, every three days, Radarsat-2 can image Cranfield twice a day (ascending and descending paths). A time series of acquisitions every 3 days could

Field	18 Oct	25 Oct	1 Nov	11 Nov	25 Nov	5 Dec	12 Dec	19 Dec
1	m_v s	m_v s	m_v s	m_v s	m_v s	m_v s	m_v s	m_v s
2	m_v s	m_v s	m_v s	m_v s	m_v s	m_v s	m_v s	m_v s
3		m_v	m_v	m_v	m_v	m_v	m_v	
4		m_v	m_v	m_v	m_v	m_v	m_v	
5		m_v	m_v	m_v	m_v	m_v	m_v	
6		m_v s	m_v s	m_v s	m_v s	m_v s	m_v s	m_v s
7		m_v	m_v s	m_v s	m_v s	m_v s	m_v s	m_v s
8		m_v	m_v s	m_v s	m_v s	m_v s	m_v s	m_v s
9					m_v s	m_v s	m_v s	m_v s
10						m_v s	m_v s	m_v s
11						m_v s	m_v s	m_v s
12						m_v s	m_v s	m_v s
13						m_v s	m_v s	m_v s
14						m_v s	m_v s	m_v s

Table 4.6: Available in situ measurements for each acquisition date (m_v for soil moisture, s for SfM acquisition)

Field	Surface roughness	Vegetation cover
1	Rough (ploughed)	Winter Canola, light cover for first acquisitions to thick cover for last acquisitions
2	cf field 2	cf field 2
3	NA	Pasture
4	Smooth (rolled)	Wheat, light cover for first acquisitions to medium cover for last acquisitions
5	cf field 5	cf field 5
6	cf field 5	cf field 5
7	cf field 5	cf field 5
8	cf field 5	cf field 5
9	Rough (ploughed)	Bare
10	Rough (ploughed)	Bare
11	Very rough (ploughed)	Bare
12	Smooth until 5 Dec, Very rough from 12 Dec	Bare
13	Rough (ploughed)	Bare
14	Rough (ploughed)	Bare

Table 4.7: Qualitative description of the sampled fields

be interesting to investigate soil moisture retrieval from change detection. However in practice, the users registered as part of SOAR-EI initiative do not have priority on commercial users. Therefore, planning the acquisitions mainly consisted in using any opportunity available while trying to maximize the number of acquisitions with the same viewing configuration (ascending/descending path, incidence angle). Same viewing configuration is desirable to limit the number of parameters changing between two acquisitions.

Acquisition orders could be sent to MDA Geospatial Services Inc. as late as two days before the actual acquisition, and the images could be downloaded one or two days after acquisition. This timely delivery allowed adjusting the measurement strategy for the in situ measurements before the next radar acquisition in order to make better use of each image.

Table 4.8 shows that the data set contains 3 acquisitions at 40.2°, 3 acquisitions at 32.4°, 2 acquisitions at 25.8°, and only 1 acquisition at 32.4°. The time gap between acquisitions varies between 7 days and 14 days.

As an example, Fig. 4.1 shows an RGB composite image from the first Radarsat-2 acquisition. The color association - Red=hh, Green=vh, Blue=vv - is chosen to give a realistic effect. Water reflections are higher at vv-polarization than at hh-polarization, and vegetation has a larger vh-response than average. All in all grassy fields appear green. Bare fields lead to magenta pixels, with black-magenta regions corresponding to smooth soil surfaces and white-magenta regions corresponding to rough soil surfaces. Finally white pixels and black pixels correspond respectively to buildings and roads.

#	**Date**	**Asc/Des**	**Acq[1] time**	**NR[2] incidence [°]**	**Time gap [day]**
1	18 Oct	Asc	17:56	40.2	-
2	25 Oct	Des	06:27	25.8	7
3	1 Nov	Asc	17:47	32.4	7
4	11 Nov	Asc	17:55	40.2	10
5	25 Nov	Asc	17:47	32.4	14
6	5 Dec	Asc	17:55	40.2	10
7	12 Dec	Des	06:27	25.8	7
8	19 Dec	Asc	17:47	32.4	7

[1]Acquisition, [2]Near Range

Table 4.8: List of Radarsat-2 acquisitions

Weather history On top of the measurements from the data logger, additional weather data is available from a local weather station at Cranfield airport. Archives of these data can be accessed from the Weather Underground website [115].

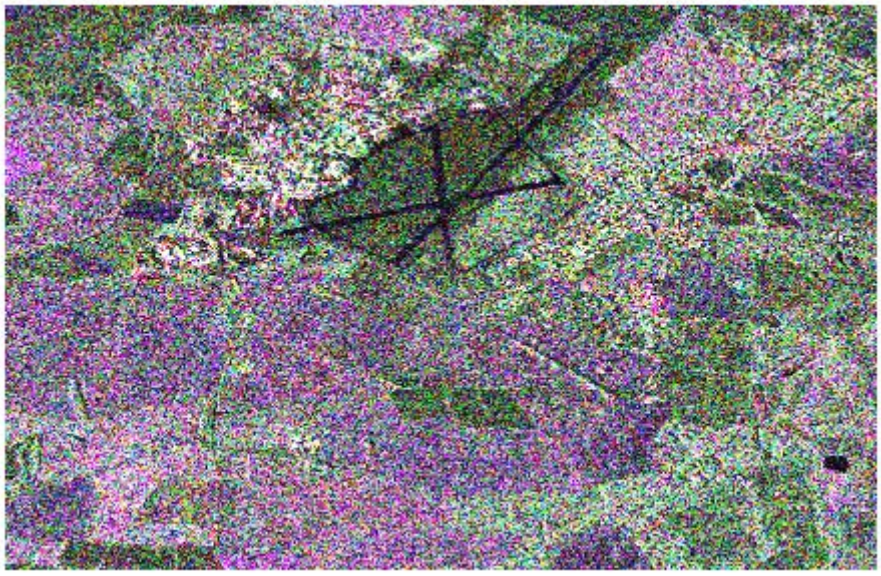

Figure 4.1: RGB composite image from Radarsat-2 acquisition 1, after histogram equalization. Red=HH, Green=VH, Blue=VV.

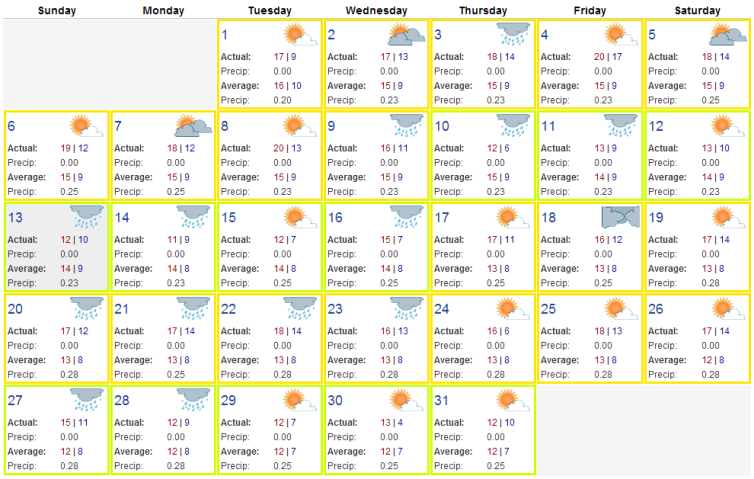

Sunday	Monday	Tuesday	Wednesday	Thursday	Friday	Saturday
		1 Actual: 17 | 9 Precip: 0.00 Average: 16 | 10 Precip: 0.20	2 Actual: 17 | 13 Precip: 0.00 Average: 15 | 9 Precip: 0.23	3 Actual: 18 | 14 Precip: 0.00 Average: 15 | 9 Precip: 0.23	4 Actual: 20 | 17 Precip: 0.00 Average: 15 | 9 Precip: 0.23	5 Actual: 18 | 14 Precip: 0.00 Average: 15 | 9 Precip: 0.25
6 Actual: 19 | 12 Precip: 0.00 Average: 15 | 9 Precip: 0.25	7 Actual: 18 | 12 Precip: 0.00 Average: 15 | 9 Precip: 0.25	8 Actual: 20 | 13 Precip: 0.00 Average: 15 | 9 Precip: 0.23	9 Actual: 16 | 11 Precip: 0.00 Average: 15 | 9 Precip: 0.23	10 Actual: 12 | 6 Precip: 0.00 Average: 15 | 9 Precip: 0.23	11 Actual: 13 | 9 Precip: 0.00 Average: 14 | 9 Precip: 0.23	12 Actual: 13 | 10 Precip: 0.00 Average: 14 | 9 Precip: 0.23
13 Actual: 12 | 10 Precip: 0.00 Average: 14 | 9 Precip: 0.23	14 Actual: 11 | 9 Precip: 0.00 Average: 14 | 8 Precip: 0.23	15 Actual: 12 | 7 Precip: 0.00 Average: 14 | 8 Precip: 0.25	16 Actual: 15 | 7 Precip: 0.00 Average: 14 | 8 Precip: 0.25	17 Actual: 17 | 11 Precip: 0.00 Average: 13 | 8 Precip: 0.25	18 Actual: 16 | 12 Precip: 0.00 Average: 13 | 8 Precip: 0.25	19 Actual: 17 | 14 Precip: 0.00 Average: 13 | 8 Precip: 0.28
20 Actual: 17 | 12 Precip: 0.00 Average: 13 | 8 Precip: 0.28	21 Actual: 17 | 14 Precip: 0.00 Average: 13 | 8 Precip: 0.25	22 Actual: 18 | 14 Precip: 0.00 Average: 13 | 8 Precip: 0.28	23 Actual: 16 | 13 Precip: 0.00 Average: 13 | 8 Precip: 0.28	24 Actual: 16 | 6 Precip: 0.00 Average: 13 | 8 Precip: 0.28	25 Actual: 18 | 13 Precip: 0.00 Average: 13 | 8 Precip: 0.28	26 Actual: 17 | 14 Precip: 0.00 Average: 12 | 8 Precip: 0.28
27 Actual: 15 | 11 Precip: 0.00 Average: 12 | 8 Precip: 0.28	28 Actual: 12 | 9 Precip: 0.00 Average: 12 | 8 Precip: 0.28	29 Actual: 12 | 7 Precip: 0.00 Average: 12 | 7 Precip: 0.25	30 Actual: 13 | 4 Precip: 0.00 Average: 12 | 7 Precip: 0.25	31 Actual: 12 | 10 Precip: 0.00 Average: 12 | 7 Precip: 0.25		

(a) October 2013

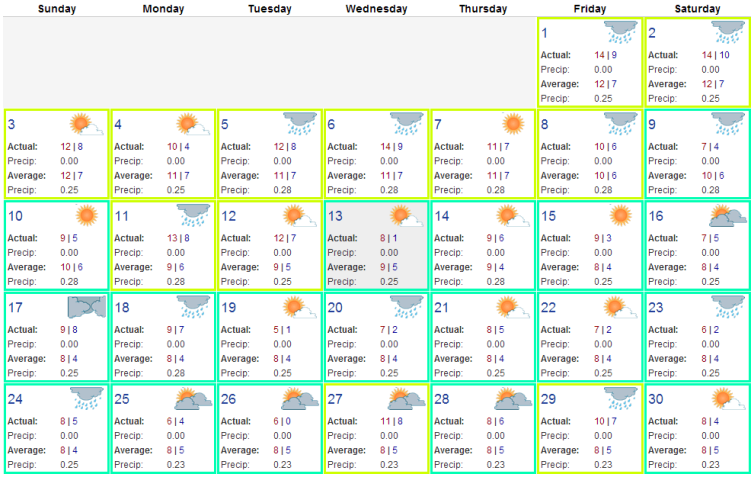

Sunday	Monday	Tuesday	Wednesday	Thursday	Friday	Saturday
					1 Actual: 14 | 9 Precip: 0.00 Average: 12 | 7 Precip: 0.25	2 Actual: 14 | 10 Precip: 0.00 Average: 12 | 7 Precip: 0.25
3 Actual: 12 | 8 Precip: 0.00 Average: 12 | 7 Precip: 0.25	4 Actual: 10 | 4 Precip: 0.00 Average: 11 | 7 Precip: 0.25	5 Actual: 12 | 8 Precip: 0.00 Average: 11 | 7 Precip: 0.28	6 Actual: 14 | 9 Precip: 0.00 Average: 11 | 7 Precip: 0.28	7 Actual: 11 | 7 Precip: 0.00 Average: 11 | 7 Precip: 0.28	8 Actual: 10 | 6 Precip: 0.00 Average: 10 | 6 Precip: 0.28	9 Actual: 7 | 4 Precip: 0.00 Average: 10 | 6 Precip: 0.28
10 Actual: 9 | 5 Precip: 0.00 Average: 10 | 6 Precip: 0.28	11 Actual: 13 | 8 Precip: 0.00 Average: 9 | 6 Precip: 0.28	12 Actual: 12 | 7 Precip: 0.00 Average: 9 | 5 Precip: 0.25	13 Actual: 8 | 1 Precip: 0.00 Average: 9 | 5 Precip: 0.25	14 Actual: 9 | 6 Precip: 0.00 Average: 9 | 4 Precip: 0.28	15 Actual: 9 | 3 Precip: 0.00 Average: 8 | 4 Precip: 0.25	16 Actual: 7 | 5 Precip: 0.00 Average: 8 | 4 Precip: 0.25
17 Actual: 9 | 8 Precip: 0.00 Average: 8 | 4 Precip: 0.25	18 Actual: 9 | 7 Precip: 0.00 Average: 8 | 4 Precip: 0.28	19 Actual: 5 | 1 Precip: 0.00 Average: 8 | 4 Precip: 0.25	20 Actual: 7 | 2 Precip: 0.00 Average: 8 | 4 Precip: 0.25	21 Actual: 8 | 5 Precip: 0.00 Average: 8 | 4 Precip: 0.25	22 Actual: 7 | 2 Precip: 0.00 Average: 8 | 4 Precip: 0.25	23 Actual: 6 | 2 Precip: 0.00 Average: 8 | 4 Precip: 0.25
24 Actual: 8 | 5 Precip: 0.00 Average: 8 | 4 Precip: 0.25	25 Actual: 6 | 4 Precip: 0.00 Average: 8 | 5 Precip: 0.23	26 Actual: 6 | 0 Precip: 0.00 Average: 8 | 5 Precip: 0.23	27 Actual: 11 | 8 Precip: 0.00 Average: 8 | 5 Precip: 0.23	28 Actual: 8 | 6 Precip: 0.00 Average: 8 | 5 Precip: 0.23	29 Actual: 10 | 7 Precip: 0.00 Average: 8 | 5 Precip: 0.23	30 Actual: 8 | 4 Precip: 0.00 Average: 8 | 5 Precip: 0.23

(b) November 2013

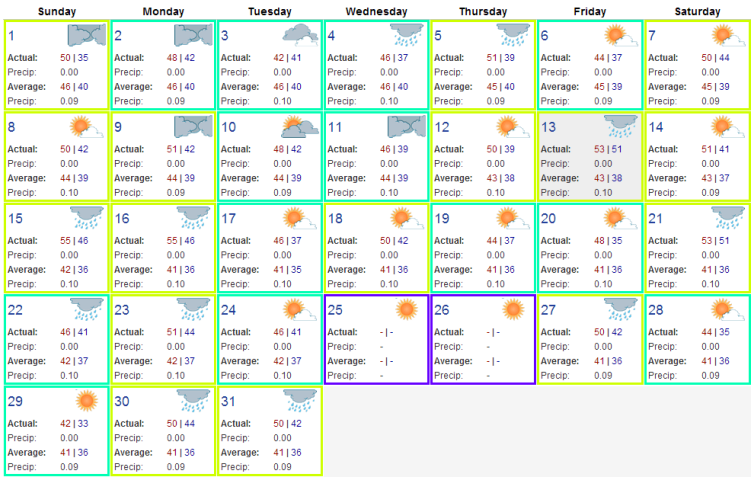

Sunday	Monday	Tuesday	Wednesday	Thursday	Friday	Saturday
1 Actual: 50 | 35 Precip: 0.00 Average: 46 | 40 Precip: 0.09	2 Actual: 48 | 42 Precip: 0.00 Average: 46 | 40 Precip: 0.09	3 Actual: 42 | 41 Precip: 0.00 Average: 46 | 40 Precip: 0.10	4 Actual: 46 | 37 Precip: 0.00 Average: 46 | 40 Precip: 0.10	5 Actual: 51 | 39 Precip: 0.00 Average: 45 | 40 Precip: 0.09	6 Actual: 44 | 37 Precip: 0.00 Average: 45 | 39 Precip: 0.09	7 Actual: 50 | 44 Precip: 0.00 Average: 45 | 39 Precip: 0.09
8 Actual: 50 | 42 Precip: 0.00 Average: 44 | 39 Precip: 0.10	9 Actual: 51 | 42 Precip: 0.00 Average: 44 | 39 Precip: 0.09	10 Actual: 48 | 42 Precip: 0.00 Average: 44 | 39 Precip: 0.09	11 Actual: 46 | 39 Precip: 0.00 Average: 44 | 39 Precip: 0.10	12 Actual: 50 | 39 Precip: 0.00 Average: 43 | 38 Precip: 0.10	13 Actual: 53 | 51 Precip: 0.00 Average: 43 | 38 Precip: 0.10	14 Actual: 51 | 41 Precip: 0.00 Average: 43 | 37 Precip: 0.09
15 Actual: 55 | 46 Precip: 0.00 Average: 42 | 36 Precip: 0.10	16 Actual: 55 | 46 Precip: 0.00 Average: 41 | 36 Precip: 0.10	17 Actual: 46 | 37 Precip: 0.00 Average: 41 | 35 Precip: 0.10	18 Actual: 50 | 42 Precip: 0.00 Average: 41 | 36 Precip: 0.10	19 Actual: 44 | 37 Precip: 0.00 Average: 41 | 36 Precip: 0.10	20 Actual: 48 | 35 Precip: 0.00 Average: 41 | 36 Precip: 0.10	21 Actual: 53 | 51 Precip: 0.00 Average: 41 | 36 Precip: 0.10
22 Actual: 46 | 41 Precip: 0.00 Average: 42 | 37 Precip: 0.10	23 Actual: 51 | 44 Precip: 0.00 Average: 42 | 37 Precip: 0.10	24 Actual: 46 | 41 Precip: 0.00 Average: 42 | 37 Precip: 0.10	25 Actual: - | - Precip: - Average: - | - Precip: -	26 Actual: - | - Precip: - Average: - | - Precip: -	27 Actual: 50 | 42 Precip: 0.00 Average: 41 | 36 Precip: 0.09	28 Actual: 44 | 35 Precip: 0.00 Average: 41 | 36 Precip: 0.09
29 Actual: 42 | 33 Precip: 0.00 Average: 41 | 36 Precip: 0.09	30 Actual: 50 | 44 Precip: 0.00 Average: 41 | 36 Precip: 0.09	31 Actual: 50 | 42 Precip: 0.00 Average: 41 | 36 Precip: 0.09				

(c) December 2013

Figure 4.2: Weather history from the local weather station at Cranfield airport [115]

Chapter 5

Results: Temporal/Spatial variability of surface roughness

This first Result chapter presents all the results related to the temporal and spatial variability of surface roughness which was investigated with the SfM measurements of experiment 1.

In section 5.1, the performance of the SfM measurements is quantified, and some practical limitations of the measurement method are given.

Section 5.2 investigates different methods to compute the roughness parameters and their effects on the spatial variability of these parameters.

Section 5.3 focuses on the temporal variability of surface roughness and on how it may affect soil moisture estimation relying on change detection methods.

Finally section 5.4 gives a summary and a discussion of the results of this chapter.

5.1 Measurement performance with SfM

Before analyzing the results related to the performance of the SfM measurements, it is worth giving a short definition of the different parameters which can be used when discussing the quality of measurements. Table 5.2 lists the most common parameters. A more exhaustive list with detailed definitions can be found in [116].

In summary, this table stresses that *accuracy* is not quantifiable because the true quantity value is never available. Accuracy can only be explored through *measurement error* which is the residual between measured quantity and a reference quantity. This measurement error has two components - the systematic error and the random error. Then, unlike measurement error, *precision* does not rely on a reference value but only on repeated measurements. When expressing precision, one must mention whether or not the measurement conditions were the same for every measurement. When the measurement conditions can be considered identical, measurement precision corresponds to measurement repeatability, otherwise it corresponds to measurement reproducibility. Finally, while the objective of the measurement error approach is to determine an estimate of the true value, the *uncertainty* approach only provides an interval of reasonable value for the measurand.

In the following, the performance of SfM will be assessed through measurement error, repeatability, and uncertainty.

Parameter	**Description**	**Comments**
Accuracy	Closeness between measured quantity value and true quantity value	Not a quantity. Measurement is accurate when it has small measurement error.
Trueness	Closeness between average of infinite number of replicates of a measured quantity and a reference quantity value	Not a quantity. Inversely related to systematic measurement error.
Precision	Closeness of agreement between repeated measured quantity, under specified conditions	Usually expressed as a standard deviation. Used to define repeatability or reproducibility.
Error	Measured quantity value minus reference quantity value	-
Systematic error	Component of error that in replicate measurements remains constant or varies in a predictable manner	Systematic error equals error minus random error. Can be compensated with correction.
Bias	Estimate of a systematic measurement error	-
Random error	Component of measurement error that in replicate measurements varies in an unpredictable manner	-
Repeatability	Measurement precision for repeated measurements under the same conditions.	-
Reproducibility	Measurement precision for repeated measurements under different conditions.	-
Uncertainty	Non-negative parameter characterizing the dispersion of measured quantity values. Commonly given as a standard deviation.	Includes components arising from systematic effects, such as components associated with corrections. Type A evaluation of uncertainty relies solely on a statistical distribution from repeated measurements. Type B evaluation of uncertainty is derived from PDFs based on experience or other information.

Table 5.2: Parameters related to measurement quality [116]

5.1.1 Error/repeatability assessment with a 50×50 cm scene

The performance of SfM is first assessed indoor for a reduced-size target using soil samples from field 2 and a set of LEGO® bricks attached to a LEGO plate. Figure 5.1a shows the overall scene. The soil sample makes the scene representative of the surface imaged over the farm fields. The LEGO bricks are used as reference points (red points) to scale the DEM and as control points (blue points) to assess the DEM uncertainty. These bricks provide accurate reference targets since the machine tolerance to manufacture them is $10\,\mu$m [117].

Five sets of 36 images are taken. All sets have similar view points, 9 panoramas (~0.5 m high) and 27 close range images (~0.25 m high). Each set has been acquired back to back so that light conditions are the same. The camera was hand held and with the focal length (10 mm) used for all acquisitions over the farm. And the pictures were down-sampled and compressed as explained in section 3.2.2.2.

Table 5.3 shows the number of points obtained for the 5 point clouds. Besides the fact that images with similar viewing angles have been used, set 5 leads to more points than set 3 (+35%). This difference can be explained from variability in acquisition height. Compared to the images of set 3, the close range images of set 5 are actually taken closer to the soil surface. This leads to point cloud 5 more detailed than point cloud 3. All in all, this explanation also explains for the differences observed between the other sets.

	Set 1	**Set 2**	**Set 3**	**Set 4**	**Set 5**
Number of points	246821	190784	189671	229064	249945

Table 5.3: Number of points obtained for the 5 point clouds generated from the 5 sets of images.

The scaling step with SfM-georef is done with 4 reference points located at the 4 corners of the LEGO plate (red dots on Fig. 5.1a). More reference points could be used, but this set of 4 points is representative of the limited number of reference points available with the farm fields. Each DEM is then interpolated over a grid with a 0.1 mm resolution.

Measurement error The measurement error of each DEM is estimated by checking the position of 8 control points (blue dots on Fig. 5.1a) against their known position taken as reference.

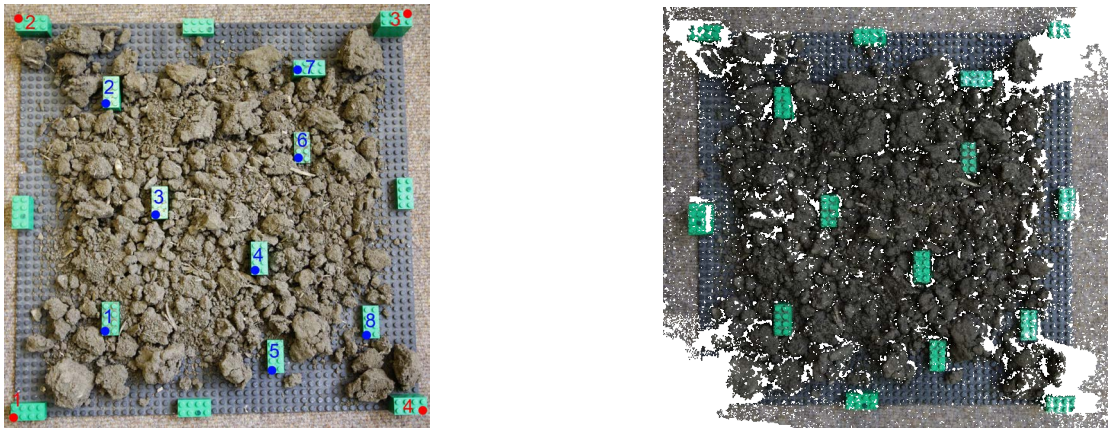

(a) (b)

Figure 5.1: (a)Scene used to assess measurement error and repeatability of SfM. Red points are used for scaling the DEM, while blue points are used as control points to estimate errors. (b) Point cloud resulting from set 1.

Table 5.4 shows the average error computed for the x, y and z coordinates of the 8 control points. Results for the z coordinate show that SfM is always underestimating the height of every control point with an average error of -0.709 mm which is more than acceptable. When comparing laser scanner with stereo-photogrammetry Aguilar *et al.* also noticed that stereo-photogrammetry gives a smoothed version of the soil surface [29]. The difference in horizontal errors between x and y certainly comes from the acquisition process. The 27 close range images contain some oblique views around the y-direction but no oblique views around the x-direction so soil features along the x-dimension are determined more accurately than those along the y-dimension. All in all the error in all directions is sub-millimetric which is similar to the performance achieved by laser profilers.

	x [mm]	**y [mm]**	**z [mm]**
Set 1	0.137	0.081	-0.709
Set 2	-0.051	0.193	-0.594
Set 3	-0.026	0.243	-0.907
Set 4	0.074	0.343	-0.521
Set 5	0.249	0.356	-0.815
Mean error	0.077	0.243	-0.709
Mean RMSE	0.489	0.439	0.888

Table 5.4: Average error for the 3D position of 8 control points

Repeatability Repeatability is assessed by computing the standard deviation for the set of 5 DEMs, *i.e.*

$$\boldsymbol{\sigma} = \sqrt{\frac{1}{4}\sum_{i=1}^{5}\left(\mathbf{z}_i - \bar{\mathbf{z}}\right)^2} \tag{5.1}$$

where $\mathbf{z}_i$ is a matrix containing the heights of all the points of point cloud i, and $\bar{\mathbf{z}}$ is a matrix with the average height of each point across the 5 DEMs ($\bar{\mathbf{z}} = \frac{1}{5}\sum_{i=1}^{5}\mathbf{z}_i$).

Finally taking the average of $\boldsymbol{\sigma}$ gives an estimation of the standard deviation of the measurements taken under the same conditions. After computation, the average standard deviation is $\bar{\boldsymbol{\sigma}} = 0.688\,\text{mm}$.

Both error and repeatability are sub-millimetric. From these results SfM is able to produce quality DEMs even though images are taken with a hand-held camera. This quality assessment was done for a scene which is much smaller ($\sim 50 \times 50\,\text{cm}$) than the sampled plots of fields 1 and 2. Measurement performance is likely to degrade for large scene in particular because the 3D position of the reference points is not known as accurately as that of the corners of the LEGO plate. In the next section, measurement quality is assessed for a DEM B ($2 \times 3.4\,\text{m}$).

5.1.2 Measurement performance for DEM B

Measurement error Measurement error is estimated by including LEGO bricks on the soil surface. Sets of bricks are positioned along the four edges of the plot. This is similar to the configuration of classic stereo-photogrammetry which makes use of a frame with control points on its edges.

Note that using artificial reference objects is not expected to underestimate the measurement error made over a natural soil surface. Indeed, the LEGO bricks have 90° angles which produce systematic shadowed sides at any viewing angles. Also, their surface is uniform in color which does not favor feature matching, and it is extremely smooth which makes it prone to different specular reflections of sun light. For these reasons, using LEGO bricks is unlikely to underestimate reconstruction errors.

In practice, the size of these bricks on the final DEM after interpolation on the 1 mm grid, is compared to their known size. The different dimensions are estimated by directly picking up points on the DEM. The length of the bricks gives information on horizontal errors, while the height is used to asses vertical errors. The RMS value of the residual for all bricks along the x-, y- and z-direction gives the RMS measurement errors (table 5.5). The RMS error along the x- and y-direction was found to be close to 1.5 mm. While the vertical RMS error (z-direction) was close to 3 mm.

It should be noted that the RMSE is usually estimated by controlling the 3D positions (x, y, z) of ground control points. While here, the RMSE is estimated from controlling the size of reference objects *i.e.* a difference (Δx, Δy, Δz) between two 3D positions. Assuming that the errors across the DEM are uncorrelated, the RMSE of z and Δz verify $(\text{RMSE}_{\Delta z})^2 = 2\,(\text{RMSE}_z)^2$, which for this study leads to $\text{RMSE}_z = 2.2$ mm. Whatever the quantity considered, as mentioned in section 2.1.5, such error magnitudes are expected to have a negligible effects when the measurements are used for soil moisture estimation with radar. As expected, measurement error is larger for DEM B than for the small LEGO plate.

Later in the project, measurement error was cross-checked using the 1.530×0.716 m frame presented in section 3.3.2. Horizontal error is estimated by comparing the distance between two corners of the frame on the DEM with the known distance between these corners. Vertical error is estimated by comparing the height of the

Measurement error [mm]	
RMSE Δx, Δy	1.5
RMSE Δz	3.1
RMSE x, y	1.1
RMSE z	2.2

(a)

Repeatability [mm]	
RMSE $z_{\mathrm{DEM}_1} - z_{\mathrm{DEM}_2}$	1.4
$\lvert s_{\mathrm{DEM}_1} - s_{\mathrm{DEM}_2} \rvert$	0.1
$\lvert l_{\mathrm{DEM}_1} - l_{\mathrm{DEM}_2} \rvert$	2.9

(b)

Table 5.5: Measurement error (RMSE) and repeatability of SfM

four corners relative to the base of the frame, with their known height. The main difference with the LEGO method is that the size of the frame is larger than the size of LEGO bricks. This allows verifying that the error made on the distance between two points does not increase with the actual distance. In the end, the horizontal error (Δx, Δy) was 2.0 mm, and the vertical error (Δz) was 2.44 mm which is close to the results obtained with LEGO bricks. These results suggest that there is no increase of the measurement error with the measured distance.

As could be expected, the measurement error for the $2 \times 3.4\,\mathrm{m}$ DEM B is larger than that obtained with the 50×50 cm LEGO plate. This degradation for DEM B certainly originates from the overall larger acquisition height and the larger uncertainty on the 3D position of the reference points.

James and Robson found that the ratio measurement error over observation distance was better than 1:1000 for SfM reconstructions with three scenes of size ranging from 0.1 m to 1600 m (see table 5.6). The ratio for the LEGO plate and DEM B is respectively about 1:600 and 1:250. This poorer performance can be explained by the fact that for all their examples James and Robinson used higher resolution images without additional JPEG compression, a longer focal length ($20 \leq f \leq 50\,\mathrm{mm}$), and more accurate reference points relative to the scene size. The first two points impact the reconstruction accuracy, while the third point affects the scaling accuracy. In summary, generating accurate DEMs requires both accurate SfM reconstruction and accurate scaling.

Millimeter accuracy is typical for stereo-photogrammetric systems [12, 29]. A direct comparison between the SfM setup and stereo-photogrammetric setups such as the one used by Marzahn *et al.* [12] is not straightforward. First, there is a difference in DEM area. In [12], the RMS error was computed from 22 DEMs ranging from 2.5 to $4\,\mathrm{m}^2$ without specifying the exact numbers of each size. In the best case scenario, one can consider that the 1.77 mm accuracy was computed for $4\,\mathrm{m}^2$ DEMs only. In this study, accuracy was estimated for a DEM 1.7 times larger ($6.8\,\mathrm{m}^2$). Scaling such a large DEM while maintaining accuracy has proved to be a difficult exercise. Second, additional compression was applied to all the images used with SfM. This improves computational time, but deteriorates image quality which certainly impacts reconstruction accuracy. Nonetheless, a comparison between the two setups is reported in table 5.7. Ignoring the differences in DEM area and image compression, the stereo-photogrammetric accuracy is 3.1 pixels against 5.5 pixels for SfM.

No definitive conclusion can be drawn from this comparison. The RMSE com-

Parameter	**Ex 1** [32]	**Ex 2** [32]	**Ex 3** [32]	**LEGO plate**	**DEM B**
f [mm]	50	28	20	10	10
Scene size [m]	0.1	50	1600	0.5	3
Mean height [m]	0.7	20	1000	0.3	0.5
Image res [pixels]	4272×2848	4272×2848	3072×2048	1728×1152	1728×1152
Sensor size [mm]	22.2×14.8	22.2×14.8	22.7×15.1	22.3×14.9	22.3×14.9
Compression factor	No	No	No	2.7	2.7
Uncertainty of ref points	0.5 mm	15 mm	100 mm	<1 mm	<5 mm
Measurement error : Mean height	1:2333	1:950	1:1000	1:600	1:250

Table 5.6: Comparison between measurement errors for the three examples in [32] and measurement error for the LEGO plate and DEM B

puted in this study can be used as a quality check, but a dedicated setup with identical camera/lens, image compression, soil surface, and RMSE estimation would be needed to compare the two methods rigorously. All in all, the information lost from using unconstrained acquisitions with SfM is made up by combining many images.

Parameter	Stereo-photogrammetric setup	SfM setup
Sensor size [mm]	35.8×23.9	22.3×14.9
Resolution [pixels]	4368×2912	1728×1152
Focal length [mm]	36	16
Mean height [mm]	2500	514
Pixel size [mm]	0.57	0.40
RMSE [pixels]	3.1	5.5
RMSE [mm]	1.77	2.2
Imaged area [m^2]	$2.5 - 4$	6.4

Table 5.7: Broad comparison between stereo-photogrammetric setup used in [12] and SfM setup

Repeatability Repeatability is assessed by taking two sets of images (acquisitions 23 and 24 in table 4.3) back to back so that the soil surface and light conditions remain the same. The corresponding DEMs are then compared point by point. The RMS difference between the two DEMs gives an estimation of the repeatability. It was found to be close to 1.4 mm. Therefore the method is rather repeatable. Variability can be explained from the fact that the two sets are similar but in no way are they identical since the camera is hand-held. Even the number of images is

quite different - 892 images for acquisition 23 and 753 images for acquisition 24.

Performance might also differ according to outdoor light conditions. It is reasonable to think that optimal conditions correspond to cloudy weather which produces uniform lighting without shadows. Sunny conditions may be more difficult to deal with as strong shadows of the camera can appear on some close-range images which might affect features matching. In practice, throughout the experiment, a few acquisitions with sunny conditions or sunny intervals have produced very sparse point clouds which were discarded. However, such behavior was not systematic, hence a more thorough analysis would be required to draw definitive conclusions.

Ultimately repeatability of measurements of RMS height and correlation length is what matters for radar backscattering. Computation of the RMS height for both data sets over the whole detrended DEMs ($\sim$ 7~million points) gives similar results, respectively $s_1 = 9.4\,\text{mm}$ and $s_2 = 9.3\,\text{mm}$. Similarly the correlation length along the x direction (long side) is computed for both DEMs. The autocorrelation function is computed along all rows (~2000 rows). After fitting the theoretical exponential model to the average autocorrelation function, the correlation lengths are $l_1 = 104.2\,\text{mm}$ and $l_2 = 107.1\,\text{mm}$.

Following the study from Lievens *et al.*, such differences, especially regarding the correlation length, would have a negligible impact on soil moisture estimation [13].

From this quality check, the SfM setup can be considered accurate and robust regarding its use for microwave scattering.

5.1.3 Point cloud density and acquisition strategy

This section looks at how the different acquisition strategies for DEM A and DEM B impact the final point cloud density.

5.1.3.1 Predicting the point cloud density from the number of images

Using all the acquisitions listed in tables 4.1, 4.2, 4.3, and 4.4, Fig. 5.2a shows that the number of points of the point cloud after SfM reconstruction against the number of used images. As expected, the number of points increases with the number of images. It is apparent that acquisitions for DEM A which contain 1 m pictures, lead to a different trend than acquisitions for DEM B which contain both 1 m and 20 cm pictures.

Because DEM A and DEM B also have different sizes, it is sensible to normalize the variables by the surface area of the DEMs, *i.e.* points per cm^2 and images per cm^2. And multiplying the number of images by the image resolution leads to a density of pixels which makes the variables more comparable. Note that these computed densities may be slightly optimistic because on the point cloud some points represent pieces of soil which are outside the delimited soil surface of interest, but this is of little importance for what follows. Fig. 5.2b highlights the fact that acquisitions A and acquisitions B may have the same amount of images (see Fig. 5.2a), but they do not have the same density of images/pixels. In the linear regression $y = ax+b$, the factor a can be thought as *factor of overlap*. For both acquisition A and acquisition B, a has a 10^{-3} order of magnitude, therefore it takes about 1000 pixels of the

	Acquisition A	**Acquisition B**
# of 1 m pictures	573	210
# of 0.2 m pictures	0	325
Mean acq height	1 m	0.51 m
Pixel size on soil	0.79 mm	0.40 mm

Table 5.8: Average pixel size on the soil surface for acquisitions A and B

collected images to generate one point of the point cloud. What seems to be a poorly efficient reconstruction may come from the fact that all the images undergo a lossy compression (JPEG) which certainly reduce the discrimination between pixels.

The difference between the regression for acquisitions A and the regression for acquisitions B may come from the fact that for the latter, the size of a pixel is different for the 20 cm pictures and for the 1 m pictures. From the characteristics of the camera listed in table 3.1, table 5.8 gives the average pixel size on the soil surface for acquisitions A and B. Dividing the density of pixels by the pixel size (in cm) leads to a quantity in point per cm^3 which is independent from the setup. This is why on Fig. 5.2c, the linear regressions for acquisitions A and B are now very similar so that a single linear regression (dashed line) can be applied to both data sets.

The dashed regression line is interesting as it indicates that for example, to obtain a point density of 30 points/cm^2, the setup must be designed so that density of pixels divided by pixel size is about 150 000 points/cm^3. Using the camera settings of this study, with an acquisition height of 30 cm, the pixel size on the soil is 0.023 cm. Therefore the density of pixels must be 3434.6 pixels/cm^2 which for an image resolution of 1728 × 1152 leads to ~17.3 images per m^2. Thus to generate a DEM for a 10 m^2 soil surface, one would need to take about 173 images. In comparison, for an acquisition height of 1.5 m, a total of 900 images would be required. The exact number of required images might be different from the one predicted by the regression line, but this method is useful to avoid setup which would lead to unrealistic numbers of images. To go further, independent data sets acquired over different surface area and with different cameras would be required to test the range of validity of the dashed regression line.

5.1.3.2 Comparison between DEM A and DEM B

As reported in table 3.2 the main difference between DEM A and DEM B, besides their size, is the resolution of their point cloud. Thanks to the images taken at a height of 20 cm, the point cloud obtained for DEM B is much denser than that of DEM A, respectively 57 points/cm^2 and 11 points/cm^2. Fig. 5.3 shows DEM B and the part of DEM A which is common to DEM B for the acquisition on December 5 2013 over field 2. Both DEMs are detrended by plane fitting. By eye, the two DEMs are similar. A point by point comparison shows that the average absolute height difference between the two DEM is 3.9 mm with a standard deviation of 3.6 mm and a maximum deviation of 70.4 mm. Fig. 5.4 shows the point by point difference between DEM B and DEM A. The result is not random, clear soil features

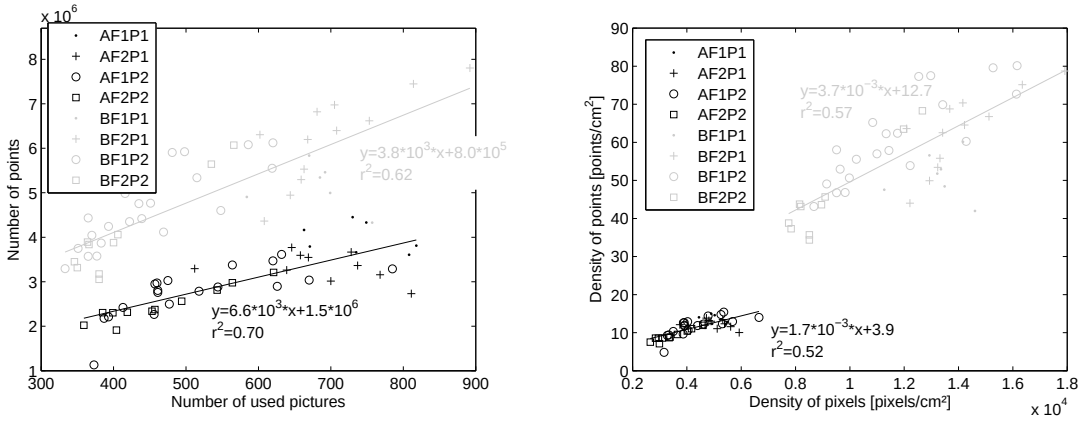

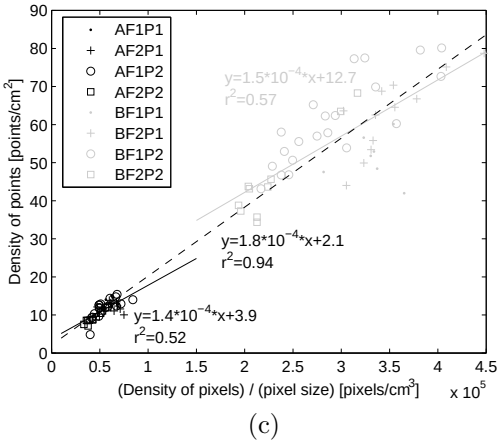

Figure 5.2: Linear regressions between (a) number of points and number of used pictures, (b) point density and pixel density, (c) point density and pixel density divided by pixel size. For plots (a) and (b), two distinct linear trends can be isolated for DEMs A and DEMs B. After transformations, plot (c) shows a linear regression common to DEMs A and DEMs B.

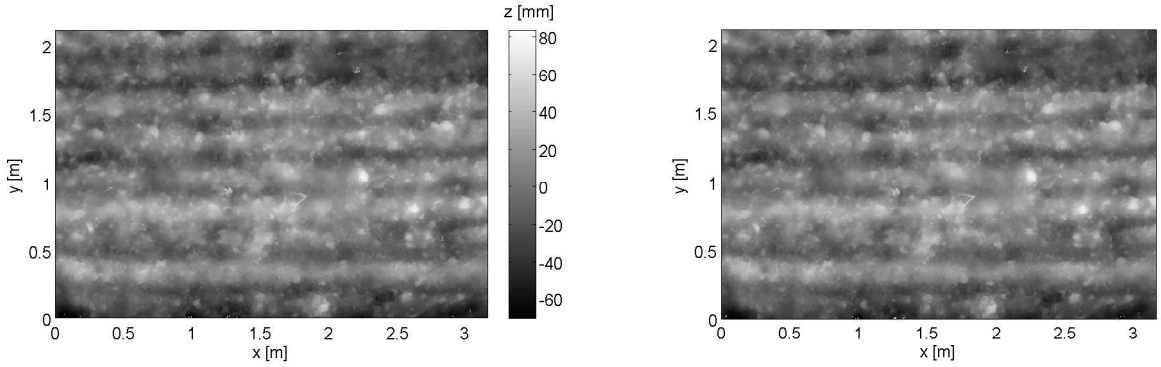

(a) (b)

Figure 5.3: (a) DEM A and (b) DEM B for field 2 on December 5 2013

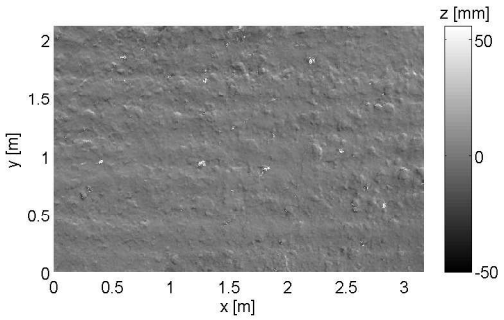

Figure 5.4: Point by point comparison, DEM B minus DEM A

are visible. This coincides with the idea that DEM B is a finer version of DEM A, able to capture smaller roughness features, over a reduced surface area.

5.1.4 Measurement limitation and adaptability

Vegetation The main limitation identified when measuring roughness over several months is inevitable vegetation growth. While sparse vegetation does not affect the DEM generation, denser vegetation is a problem for three main reasons.

1. With very dense vegetation, roughness measurements are impossible simply because the soil surface cannot be imaged by the camera.

2. When the soil is visible, vegetation can still compromise measurements in the presence of wind. Since image acquisition is sequential, the movement of vegetation with wind can make successive pictures of the same surface very different, so that common features cannot be identified by SfM.

3. Vegetation can also be an issue because of occlusion. Long stems hide different parts of the soil surface depending on the camera position. As a result a feature visible on an image may be hidden on its overlapping pair. While nothing can

be done for moving vegetation, occlusion can be dealt with to some extent by increasing the number of images and/or by taking images at higher height. Post-processing can also be done to remove vegetation after generating the point cloud. As SfM also maps the corresponding color of each point, sparse vegetation can be removed to some degree by removing all the green points in contrast to the brown points of the soil surface. In practice such post-processing was not always successful, when possible it is easier to prevent vegetation growth by regularly spraying weed killer.

Light conditions Another difficulty related to outdoor conditions, might be moving shadows and changes in light. As it takes about 5-10 min to take a set of images, significant changes in light conditions because of sunny intervals lead to noticeable differences in image exposure. Sunny conditions are also not ideal, as the shadow of the camera moves across successive images. Even though some DEMs have been successfully generated in sunny conditions, the SfM reconstruction did fail for some sets of images which had either shadows and/or sunny intervals. For these reasons, stable cloudy condition might be the most favorable scenario as diffuse light remains constant and does not produce shadows.

Measurement of smaller/larger scales All in all, DEM resolution is controlled by the number of images , projected pixel size (CCD pixel size, focal length, acquisition height), image resolution, and image compression. Following the regression analysis of section 5.1.3.1, one can easily adjust these parameters to meet the point density required for a given application. DEM accuracy is also related to the previous parameters, but it also depends on the accuracy of the scaling step. Here are some additional remarks which should be considered when adapting the current setup to image smaller or larger roughness features.

To capture smaller roughness features, one might think of increasing the number of images. In practice, processing time and storage space will be the main constraints. Moreover, as mentioned before, light conditions should ideally remain the same throughout the acquisition process. This is harder to achieve for very large image sets.

Similarly, larger features can be reconstructed with images covering a larger surface area. A remotely-triggered camera with a monopod could be used to include wider panoramas. Maintaining the same level of details will increase the number of images, which leads to the same limitations mentioned above. The scaling step can also become an issue. Keeping the same number of reference points means that their relative distance increases, and accurately measuring their position can become challenging. Adding more reference points will reduce their relative distance, but comes with the disadvantage of lengthening the initial setup (digging holes to anchor the targets, and measuring the 3D position of the targets).

All in all, a more in depth study would be required to fully understand the ca-

pabilities and limitations of the SfM method. Nonetheless from the quality checks performed above, this measurement method appears to be robust, flexible, and accurate enough for applications related with microwave scattering. And its affordability makes it an attractive alternative to the other laser-based and photogrammetric methods.

5.2 Roughness spatial variability

The spatial variability of surface roughness is analyzed for only one acquisition date (December 5 2013) for field 2 as it would be too long and worthless to repeat it for every DEM. At this time of the year, field 2 was tilled with clear oriented patterns. This corresponds to a more representative configuration than the acquisitions of the first period when no tillage operations had taken place.

Section 5.2.1 focuses on how the roughness parameters change according to the DEM size when the DEM is detrended by removal of a fitted plane.

Following the results obtained with a fitted plane, section 5.2.2 looks at the sensitivity of the roughness parameter to the DEM size when the DEM is first filtered with a high-pass filter.

Section 5.2.3 analyzes how the observed variability in the roughness parameters may impact backscattering simulation.

While the previous sections ignored the effects of surface anisotropy, section 5.2.4 looks at anisotropy in the roughness parameters with a 1° resolution.

Finally section 5.2.5 investigates the use of the 2D power spectral density of a DEM as a more sensible method to compute the roughness parameters.

5.2.1 Roughness parameters and DEM length, linear detrending

For soil surfaces characterized by a limited range of roughness scales, roughness parameters were found to increase with increasing transect length toward an asymptotic value [58, 14, 76]. Similar studies have been done with photogrammetric DEMs in [40] and [12]. In these two studies, after detrending a full-size DEM by removing a fitted plane, sets of reduced-size DEMs were randomly sampled over the detrended full-size DEM. However it appears that in both studies, the reduced-size DEMs were not detrended individually. In other words, they were reduced-size DEMs detrended with the full-size DEM trend which in practice would not be accessible if only the reduced-size DEMs were available. In the following, RMS height is computed for size-increasing DEM length, with and without individual detrending. Properly detrending each DEMs does lead to different parameter values which may affect the interpretation of the results.

RMS height Figure 5.5 shows the results with the detrended DEM A for field 12 on the 5 December 2013, without individual detrending of the reduced-size DEMs (gray line), and with individual detrending (black lines). For each DEM size, 50 DEMs were randomly sampled over the full-size DEM ($2 \times 11\,\mathrm{m}$). All DEMs have

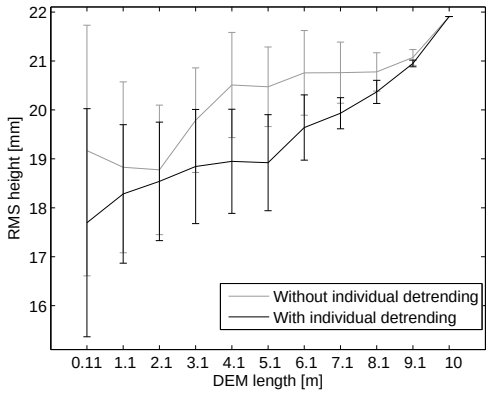

Figure 5.5: RMS height against DEM length, with and without individual detrending. The error bars show the standard deviation. There are no signs of convergence. Properly detrending each DEM shows a larger underestimation of the roughness parameters.

the same width (2 m) but a length ranging from 0.6 to 11 m. The RMS height was computed all over each DEM.

Without individual detrending, the roughness parameters estimated over reduced-size DEMs are closer to their value found for the full-size DEM. This is because the sub-DEMs capture trends due to large-scale roughness features which are not removed by linear detrending of the full-size DEM.

The results in [40] and [12] are reported in Fig. 5.6. There seem to be convergence of the RMS height, but not detrending each sub-DEM certainly leads to an underestimation of the minimum DEM length required to compute the asymptotic value of RMS height to a given accuracy .

In this study, one cannot talk about asymptotic values as there are no signs of convergence for both parameters. As the DEM length increases, large roughness features are included in the DEM. These features are not removed by the simple linear detrending and they increase height variability. This explains the steady increase in RMS height.

Correlation length The analysis for the correlation length is more delicate. Fig. shows the ACF computed for four DEM lengths. The ACF is computed along all rows of each detrended DEM (~2000 rows), then the average ACF is used to determine the correlation length. Fig. 5.7a shows that neither the exponential model nor the Gaussian model are a suitable model for the ACF. With a ploughed field such as field 2 over the second period, the correlation length is expected to be short. For example, Callens *et al.* found correlation length of 10-20 cm using 4 to 25 m long transects [58]. In comparison, the ACFs on Fig. 5.7a decreases very slowly as the lag increases. This is certainly due to the presence of large-scale features on the DEMs which cannot be removed by simple linear detrending and dictate the slow decorrelation of the transects. Only for short lags Fig. 5.7b shows that the initial decrease dictated by small-scale roughness is Gaussian.

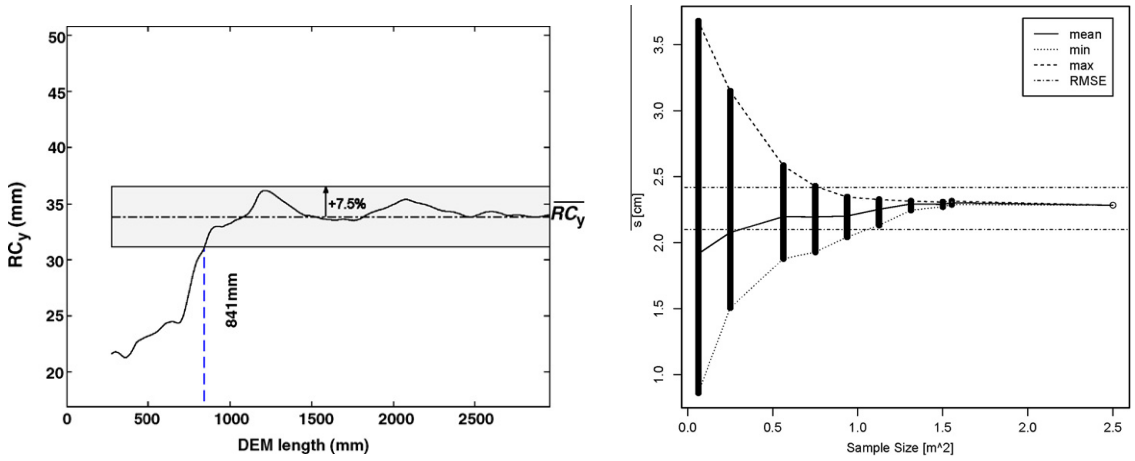

(a) (b)

Figure 5.6: Plots extracted from (a) [40] and (b) [12]. Both plots have been obtained without individual detrending of each sub-DEM which does not correspond to a realistic scenario.

In comparison, Fig. 5.8 shows a similar plot for field 2 on a different acquisition date, field 2 May 5 2013. This acquisition belongs to the first period for which the surface was much smoother. The RMS height computed for the full-size DEM is $s = 10.53$ mm. This time, the exponential model is appropriate for small DEM lengths and becomes invalid for longer DEMs again because of large-scale roughness.

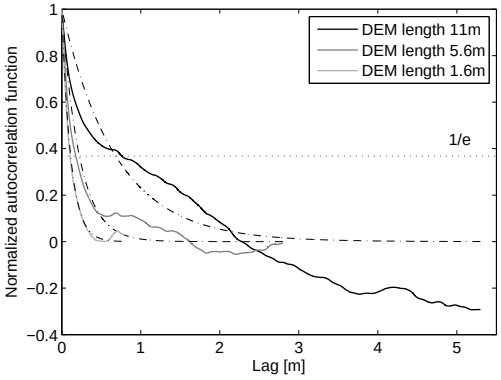

Figure 5.8: Normalized ACF for different DEM lengths (field 2, May 5 2013, $s = 10.53$ mm). The exponential model becomes invalid for very long DEMs because of large-scale roughness features.

As showed in [45], obtaining robust estimation of roughness parameters requires long DEM/transect. The issue is that large DEMs include medium-/large-scale roughness which make the stationary random roughness model not applicable.

In section 2.1.5, it was said that only the small-scale random roughness and the medium-scale oriented roughness are likely to be relevant for microwave scattering. Therefore larger roughness scales should be removed from the DEM before comput-

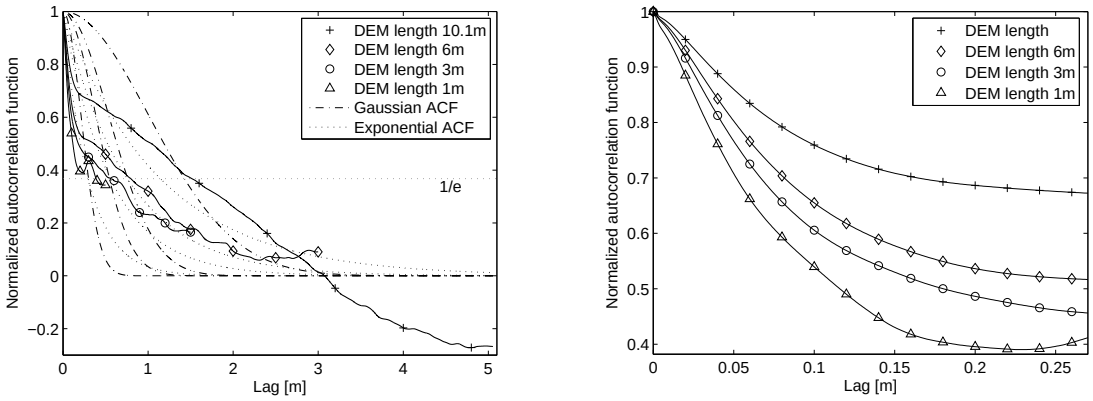

Figure 5.7: Normalized ACF computed for different DEM lengths (field 2, December 5 2013, $s = 20.17$ mm). (a) Both Gaussian and exponential models are not suitable. (b) For small lags, all ACFs have a Gaussian shape.

ing the roughness parameters. Here, the simple linear detrending appears to fail at removing these large scales. Other detrending methods have been investigated in the literature. In [58], a third-order polynomial was used to remove topography and in [44] Marshan *et al.* used a 9^{th}-order polynomial to detrend a 22 m^2 DEM. The major limitation of this method is that the choice of the order of the polynomial is arbitrary. Bryant *et al.* introduced a piecewise linear detrending for which a long profile is divided into sub-profiles which are individually detrended [76]. The main disadvantage of this technique is that the resulting profile can have large discontinuities.

Since the radar makes bandwidth-limited measurements, filtering the DEM with a 2D bandpass filter may be the most relevant technique. In the next section, the analysis is repeated with a high-pass filter.

5.2.2 Roughness parameters and DEM length, detrending with high-pass filter

The smallest scale captured by the 1 mm grid used for interpolation is 2 mm according to Nyquist criterion. This scale is still relevant for microwave scattering, that is why a simple high-pass filter is used instead of a band-pass filter.

A simple first-order high-pass filter is implemented as a case example. The continuous-time transfer function of the filter is given by,

$$H(\omega) = \frac{j\omega/\omega_c}{1 + j\omega/\omega_c} \tag{5.2}$$

with ω_c the angular cutoff frequency.

Within Matlab, all the signals are discrete, therefore the corresponding discrete-time filters must be determined. One can convert the continuous-time form into the discrete-time form by using the first-order approximation of the bilinear transform defined as follows,

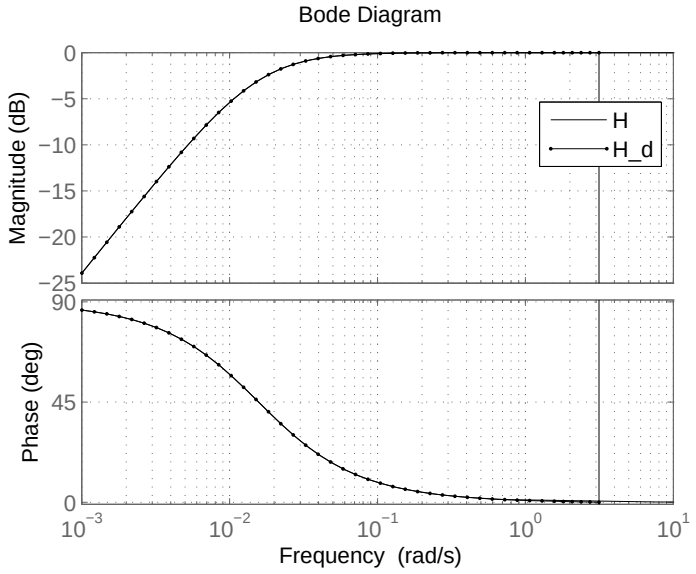

Figure 5.9: Bode diagram for the continuous and discrete transfer functions with $\omega_c \approx 1.57 \times 10^{-2}$ rad/s

$$j\omega = 2f_s \frac{1 - Z^{-1}}{1 + Z^{-1}} \tag{5.3}$$

with Z the equivalent of $j\omega$ for the discrete form and f_s the sampling frequency[118].

Applying equation 5.3 to H gives:

$$H_d(Z) = \frac{1 - Z^{-1}}{(1 + \frac{\omega_c}{2f_s}) + (\frac{\omega_c}{2f_s} - 1)Z^{-1}} \tag{5.4}$$

This filter is an Infinite Impulse Response (IIR) filter. Compared to a Finite Impulse Response (FIR) filter, it is not systematically stable. Here, stability is preserved by the bilinear transform. The disadvantage of this transform is that the mapping between continuous frequency and discrete frequency may not be accurate for high frequencies, *i.e.* frequencies close to f_s. On the other hand, an FIR filter must have high order terms to match the attenuation of an IIR filter which makes it computationally slower.

Fig. 5.9 shows a Bode diagram for the continuous and discrete transfer functions. The angular cutoff frequency is $\omega_c = 2\pi/400 \approx 1.57 \times 10^{-2}$ rad/s. There are no noticeable differences between the continuous filter and the discrete filter. As expected, this filter has an attenuation of -20 dB/decade.

Applying this filter to both the x- and y-direction leads to the filtered DEM on Fig. 5.10. Note that the angular cutoff frequency $\omega_c = 2\pi/400$ means that roughness features larger than 400 mm will be attenuated. Such a limit is reasonable considering that both random roughness and oriented roughness (table 2.1) are thought to be relevant for microwave scattering. After filtering, random roughness is the main remaining roughness components.

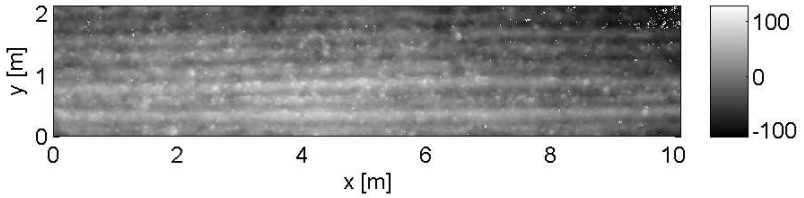

(a)

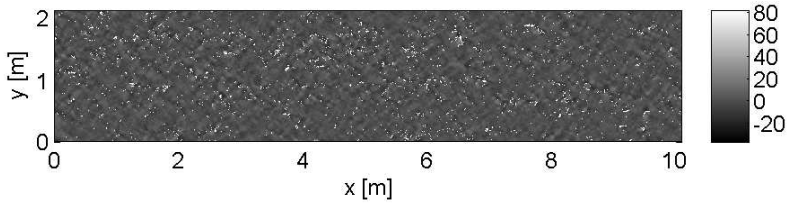

(b)

Figure 5.10: (a) non-filtered DEM A (Dec 5 2013), (b) corresponding filtered DEM

Fig. 5.11 shows the change in RMS height for different DEM length with and without individual high-pass filtering. First the RMS height values are much lower than those obtained with plane-fit detrending. Without individual filtering, on average the same value of RMS height is obtained for all DEM lengths. Only the error bar is larger for short DEMs, because fewer points are available to compute the RMS height and also because of the limited number of sampled sub-DEMs for long length. After filtering only scales below 40 cm are unattenuated. According to Nyquist sampling theorem, a plot longer than 80 cm is sufficient to capture the unattenuated roughness features. Therefore, it is not surprising that even with a length of 1.1 m, the average RMS height is close to the RMS height obtained with the full-size DEM. As for the black curve with individual filtering, the light increase in RMS height for short DEM lengths might be due to edge effects.

Finally, Fig. 5.12 shows that the normalized ACFs are very similar for all DEM lengths. Since the large-scale roughness has been removed, there is a fast decorrelation of the random roughness. The zoomed view on Fig. 5.12b shows that the ACFs lie between the Gaussian and the exponential models. In the end, the fitted correlation length is roughly the same for both models ($l_{Gauss} = 29$ mm and $l_{expo} = 25$ mm). Li *et al.* introduced a generalized power law model [119],

$$r(x) = e^{-(x/l)^n} \tag{5.5}$$

with l and n the two parameters to be determined by model fitting. For the longest DEM length (~10 m), a least square minimization leads to $l = 29$ mm and $n = 1.6$.

Using the generalized power law model, Fig. 5.13 shows the estimated correlation length for different DEM lengths. There is only a light increase in correlation length with the DEM length.

Using a high-pass filter for the acquisition on December 5 2013 leads to small roughness parameter values which would usually be attributed to a smooth soil

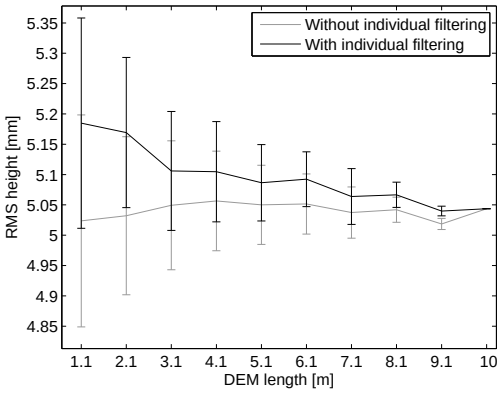

Figure 5.11: RMS height against DEM length, with and without individual high-pass filtering. The two curves are similar. The light increase in RMS height for short DEM lengths in the case of individual detrending might be due to edge effects.

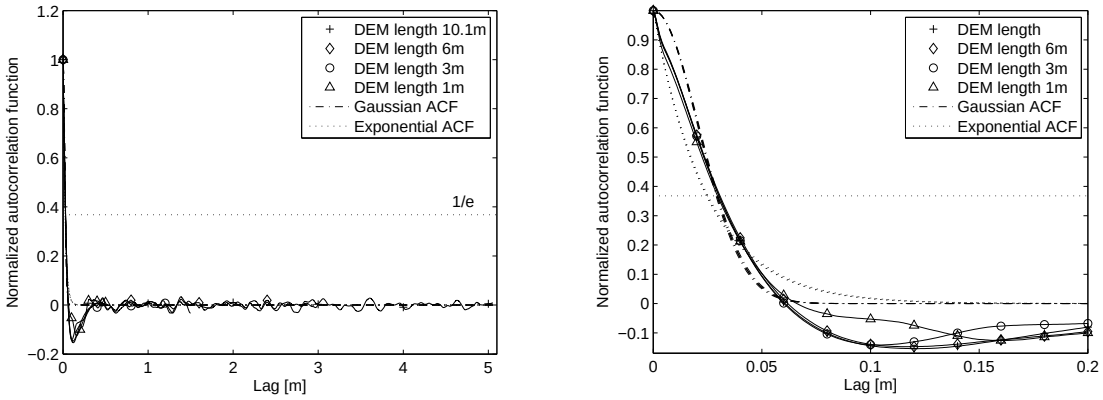

(a) (b)

Figure 5.12: Normalized ACF computed over filtered DEMs (field 2, December 5 2013). (a) Correlation decreases rapidly for all DEM lengths. (b) A zoom over small lags shows that the ACFs lie between the Gaussian and the Exponential models.

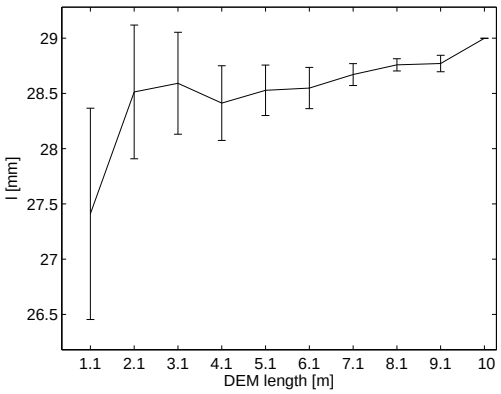

Figure 5.13: Correlation length against DEM length. For every DEM length, the exponent of the power law model remains close to 1.57.

surface. Nonetheless, even after high-pass filtering, rough and smooth surfaces are still distinguishable. For example for the smooth surface of field 2 on May 5 2013, the RMS height is 3 mm and the correlation length is 23 mm with the exponential ACF model. As expected, the RMS height is smaller. For a smooth surface, one would expect the correlation length to be larger than that of a rough surface. It is not the case here, but this is perfectly possible since the two acquisitions correspond to two very different soil surface conditions.

At the time of writing there is no trace of experiments which have tested whether filtered roughness measurements were improving the correlation between radar measurements and in situ measurements. Most of the experimental campaigns make use of roughness measurement along transects of 1-2 m which are simply linearly detrended [83, 84]. For example, with a data set of radar measurements and in situ measurements of soil moisture / surface roughness, filtering the roughness measurements with different cutoff frequencies could allow investigating which range of roughness scales is the most correlated with radar scattering.

The next section questions the impact of roughness parameter variability on soil moisture estimation.

5.2.3 Impact of roughness uncertainty on soil moisture estimation

Based on simulations with the IEM, Lievens *et al.* showed that when in situ roughness measurements are used to solve the inverse problem, *i.e.* to estimate soil moisture, a small error on RMS height impacts soil moisture much more than a ten times larger error on correlation length [13]. Because of this poor sensitivity to correlation length, Oh suggested a backscattering model which does not depend on the correlation length. However this may not be valid for small correlation length values such as the ones obtained with high-pass filtering. This point is apparent from the sensitivity analysis of Lievens *et al.* at vv-polarization and 23° incidence angle, with $s \approx 5$ mm, $l \approx 20$ mm and $m_v = 0.35\,\mathrm{m^3/m^3}$, an error of +1 mm on the correlation length would produce and error of $-0.04\,\mathrm{m^3/m^3}$ on soil moisture. Table 5.9 reports the worst case scenarios for an error on RMS height and an error on correlation length. Regarding the RMS height, in the worst case scenario, an error of +1 mm on s can lead to an underestimation of soil moisture by $0.30\,\mathrm{m^3/m^3}$. And an error of +1 mm on l can lead to an underestimation of soil moisture by $0.06\,\mathrm{m^3/m^3}$.

These results are not very encouraging as a 1 mm error on the roughness parameters can easily occur depending on the size of the DEM and the detrending technique. In practice, this means that for some soil conditions it will be difficult to derive a reliable backscattering model by fitting a function form to in situ measurements. Similarly it will be difficult to validate a given model by comparing measured values of σ^0 with simulated values from in situ measurements. The latter is a common practice. The validity of a model is tested against many in situ measurements without verifying whether or not small errors on these measurements would have a significant effect on the simulated σ^0 [85, 86].

s	l	m_v	$\frac{\partial m_v}{\partial s}$
3 mm	>250 mm	$0.35\,\mathrm{m}^3/\mathrm{m}^3$	$-0.30\,\mathrm{mm}^{-1}$

(a)

s	l	m_v	$\frac{\partial m_v}{\partial l}$
25 mm	20 mm	$0.35\,\mathrm{m}^3/\mathrm{m}^3$	$-0.06\,\mathrm{mm}^{-1}$

(b)

Table 5.9: Sensitivity of soil moisture to (a) RMS height and (b) correlation length

The values reported in table 5.9 may not be realistic depending on the detrending technique. For example in table 5.9b, a 20 mm correlation length is very unlikely when linear detrending is used. Therefore, a study looking at the correlation between radar measurements and in situ roughness measurements processed with different detrending methods should be carried out. Such a study would set the foundations regarding how in situ roughness measurements must be acquired to be used for microwave scattering.

So far, the RMS height has been computed all over the DEM (omnidirectional RMS height), and the correlation has been computed along transects parallel to the longest direction of the DEM. Since usually directional measurements along transects are used to estimate the roughness parameters, the section focuses on the variability in the roughness parameters due to anisotropy.

5.2.4 Roughness anisotropy

The computational efficiency of the Fourier-based method to estimate the roughness parameters makes it feasible to analyze anisotropy at fine angular resolution. In the following, 50 rainbows of 181 transects are randomly extracted over a DEM A (field 2, December 5 2013). The transects are 2 m long, separated by 1°, with origin taken at the bottom edge. On Fig. 5.14, each transect is linearly detrended before computing the RMS height and the correlation length from their 1D power spectrum. On Fig. 5.15, each transect is detrended with the high-pass filter used in section 5.2.2. In both cases, the total computational time was less than 4 min. In comparison, in [15, 12] transects were extracted only every 20° and the correlation length was interpolated for intermediate angles, here the time-efficient method can cope with a much finer discretization.

With linear detrending, the RMS height is clearly anisotropic. Perpendicular to the tillage direction, *i.e.* around the y-direction, s reaches values as high as 18.7 mm. Parallel to the tillage direction, s is as small as 11.5 mm. The interpretation is less obvious for the correlation length. Correlation length values are above the average for both the x- and y- directions. This was expected for the x-direction (parallel to tillage direction) as the soil surface is smoother (small RMS height). In the perpendicular direction, the large RMS height suggests that the soil surface is rougher, hence the correlation length should be small. This is not the case, certainly because the large RMS height is due to medium-scale oriented roughness and not

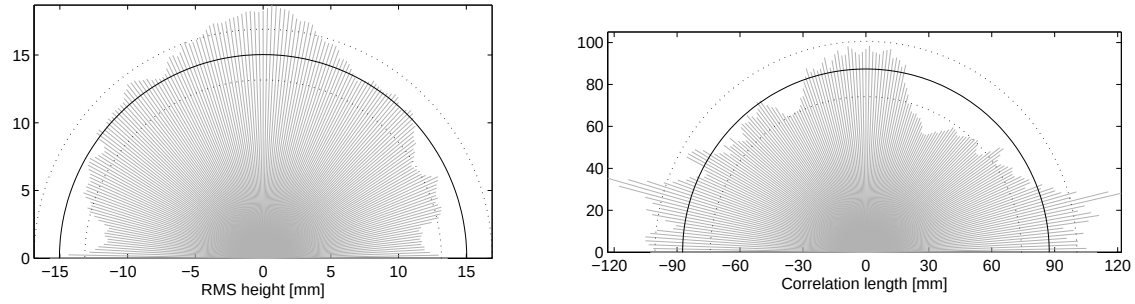

(a) Mean RMS height $s_{mean} = 15.0$ mm, standard deviation $s_{std} = \pm 1.9$ mm

(b) Mean correlation length $l_{mean} = 87.4$ mm, standard deviation $l_{std} = \pm 13.2$ mm

Figure 5.14: Anisotropy of (a) RMS height, and (b) correlation length with linear detrending of each transect

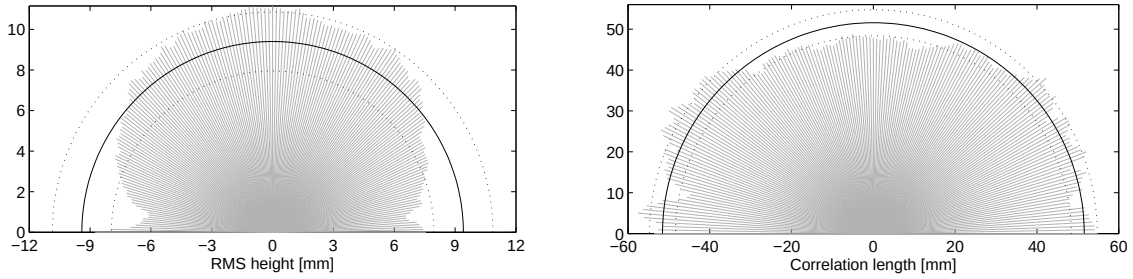

(a) Mean RMS height $s_{mean} = 9.4$ mm, standard deviation $s_{std} = \pm 1.5$ mm

(b) Mean correlation length $l_{mean} = 51.6$ mm, standard deviation $l_{std} = \pm 3.2$ mm

Figure 5.15: Anisotropy of (a) RMS height, and (b) correlation length with high-pass filtering of each transect

to a larger random roughness. This medium-scale oriented roughness contributes to making a given profile correlated over longer lags.

On average the index of the generalized power law model is $n = 1.8$, thus the measured ACF is close to the Gaussian model.

With high-pass filtering, the RMS height is less variable, but anisotropy is still noticeable. Around the y-direction s reaches its maximum 11.2 mm. And close to the x-direction s reaches its minimum 6.2 mm. As for the correlation length, this time the anisotropy of l appears inversely correlated to the anisotropy of s. The oriented roughness in the y-direction has been filtered out and does not lead to long correlation lengths as observed with linear detrending.

Again, the average index of the power law model is $n = 1.9$ which is close to a Gaussian model.

With both detrending methods, the observed anisotropy would have impacts on soil moisture retrieval. Therefore when transects are used to estimate the roughness parameters, one must choose between two different measurement strategies,

1. both parallel and perpendicular measurements can be averaged to obtain an estimate of omnidirectional roughness parameters [85, 86, 120],

2. the direction of the transects can be chosen parallel to the azimuth direction of the radar [84, 121].

At the moment, it is not clear which of these strategies gives the best results. However there are evidence from the *flashing field* phenomenon that over fields with strong oriented roughness patterns, the scattering of the soil depends on the radar azimuth direction. More precisely, radar backscattering has been observed to change by several dBs for a narrow look direction perpendicular to the tillage direction. This suggests that the roughness parametrization should account for this directionality. Therefore omnidirectional estimations may be suitable only in the absence of oriented roughness. The next section present a novel roughness characterization method which accounts for directionality and makes full use of the DEM generated by SfM.

5.2.5 Directional roughness characterization from 2D PSD

The flashing field phenomenon has been observed with airborne SAR measurements [122, 64] and spaceborne SAR measurements [63, 62] over agricultural fields with strong row structure. This sharp increase in σ^0 for a narrow direction perpendicular to the row direction is thought to originate from a Bragg resonance between adjacent rows [122]. Shin and Kong investigated the scattering from a randomly perturbed quasi-periodic surface. They identified three scattering terms, one accounting for the coherent field and the other two coming from the incoherent scattered field. They suggested a solution only for the first incoherent term. The resulting model could not predict the observed high directionality of σ^0. Later, Mattia developed another expression for the three scattering terms which predicts sharp peaks at different incidence angles in the plane perpendicular to the row direction [16]. The simulations show that these peaks originate primarily from the coherent scattering term, but that the first incoherent scattering term also depends on the viewing direction, *i.e.* it is also affected by the row structure. The expressions of the backscattering model are rather complex as six parameters are used to describe the soil surface. Even though the flashing phenomenon is not yet fully understood, Wegmüller *et al.* found that predictions with this model were in close agreement with measurements made by ERS-2 and ASAR [62].

In the following, the classic roughness parameters are estimated from the 2D PSD computed for a synthetic soil surface. The soil surface has a deterministic sinusoidal pattern, plus an isotropic Gaussian random roughness with Gaussian ACF. As could be expected, the 2D PSD reaches large values in the direction perpendicular to the sinusoidal pattern. This suggests that the 2D PSD might be a suitable tool to study the flashing phenomenon.

More generally, using the 2D PSD might be a more suitable method to compute the roughness parameters even when there is no row structure. This idea is supported by the fact that σ^0 is proportional to the Fourier transform of the ACF, *i.e.* the PSD, (or its n^{th} power) in theoretical models, such as the Small Perturbation Method, the Physic Optics Model, and the Integral Equation Method [123].

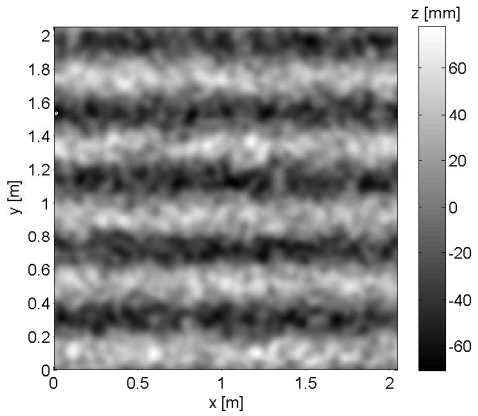

Figure 5.16: Simulated soil surface

5.2.5.1 Simulation of the soil surface

The simulated soil surface is the sum of a deterministic sinusoidal component and an isotropic Gaussian random component.

$$z\left(x,y\right) = A\sin\left(k_x x + k_y y + \phi\right) + z_r\left(x,y\right) \tag{5.6}$$

where A, k_x, k_y, and ϕ are constant.

In order to generate the correlated random height z_r, one can filter independent samples from a Gaussian distribution $\mathcal{N}\left(0,\epsilon\right)$ with an appropriate low-pass filter [64]. If the desired autocorrelation function is r, then z_r can be obtained after filtering in the frequency domain as follows,

$$z_r = \mathrm{FFT}^{-1}\left[\sqrt{|\mathrm{FFT}\left(\mathrm{r}\right)|}\mathrm{FFT}(\mathrm{z})\right] \tag{5.7}$$

The Fourier transform of a Gaussian function is still a Gaussian function. Therefore, for a correlation length l, the 2D low-pass filter can be written

$$F(f_x, f_y) = \exp\left(-\frac{\pi^2 l^2 (f_x^2 + f_y^2)}{2}\right) \tag{5.8}$$

Fig. shows the simulated soil surface for $A = 40$ mm, $k_x = 0$, $k_y = 8\pi$, $\phi = 0$, $\epsilon = 10^3$ mm and $l = 50$ mm. Such a surface is not fully representative of a real agricultural soil. First the rows are perfectly parallel which is not the case with a real surface because of topographic undulations. Second the low-pass filter used to correlated random samples gives a smoothed aspect to the random roughness which is not very realistic. Nonetheless, such a simulation is good enough for the purpose of highlighting the potential the benefits of the 2D PSD.

5.2.5.2 1D vs 2D RMS height

Fig. 5.18 shows the 1D PSD computed for a rainbow of transects as done in section 5.2.4. For every transect, there is a peak at the frequency of the sinusoidal

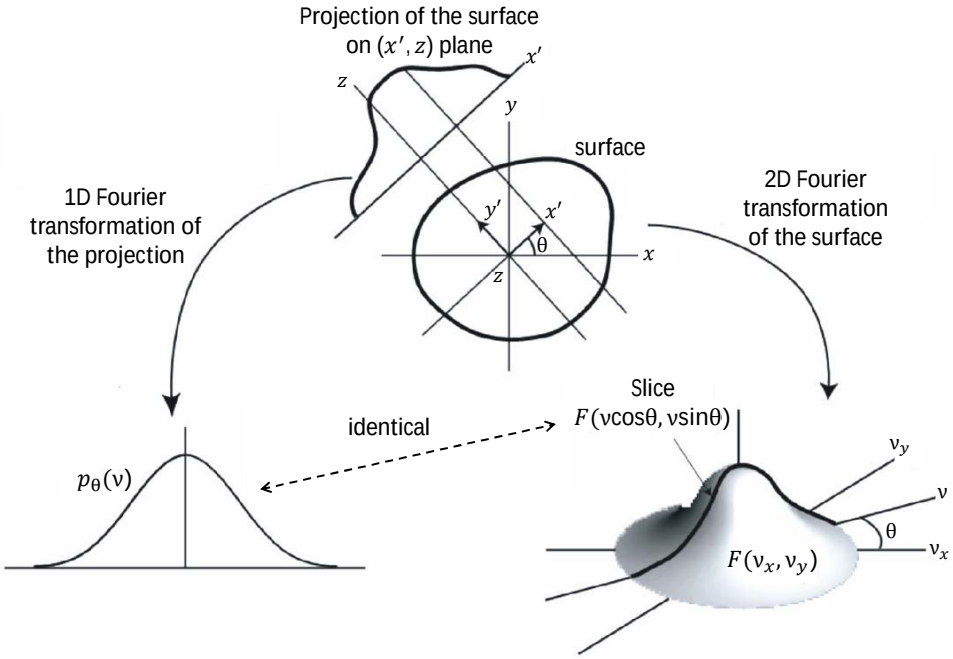

Figure 5.17: Illustration of the projection-slice theorem, adapted from [125]

component of the selected direction. Therefore, these 1D measurements capture a sinusoidal pattern in every direction except for the x-direction.

In comparison, the 2D PSD on Fig. 5.19 shows two symmetrical peaks in the y-direction at the frequency of the sinusoidal pattern. Away from this direction, the power density is significantly lower as it is the result of only the random component. This is in agreement with the *projection-slice theorem [124].* This theorem is valid for cases with more than 2 dimensions. In 2D, it stipulates that a slice of the 2D Fourier transform of a given surface, is equivalent to the 1D Fourier transform of the projection of the surface in a direction perpendicular to that slice. This is illustrated on Fig. 5.17. When applied to the surface of Fig. 5.16, the projected sinusoidal pattern cancels out for all the directions except for the slice in the y-direction for which the projected points are in phase. That is why the 2D PSD has two peaks only in the y-direction.

Fig. 5.20 shows the RMS height computed from the 1D PSD (dashed line) and from the 2D PSD (continuous line). As expected, with the 1D PSD, the RMS height is approximately the same in every direction except in the x-direction. After verification, the observed fluctuations are due to statistical uncertainty because the RMS height is computed with a limited number of points. With the 2D PSD, around the y-direction the RMS height is as large as that obtained with the 1D PSD, and it drops to a low value for the other directions. Again the small fluctuations comes from statistical uncertainty related to the random component. In theory, with an infinite soil surface in the x- and y-directions, the peaks obtained with the 2D PSD would

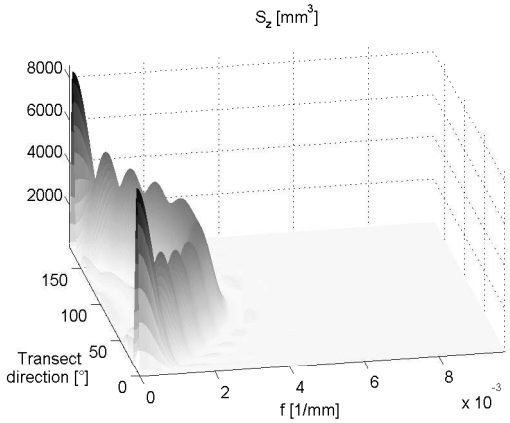

Figure 5.18: 1D PSD for transects oriented from 0 to 180°. Only the low frequencies of the positive side are displayed.

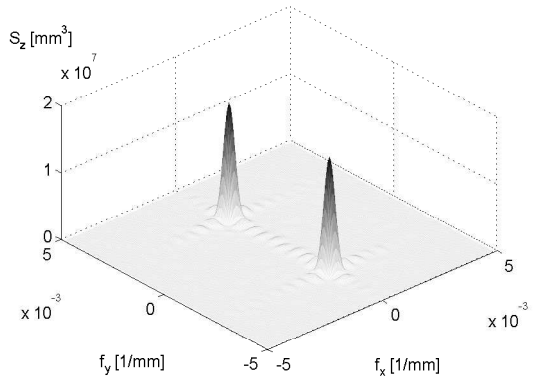

Figure 5.19: 2D PSD for the low frequencies

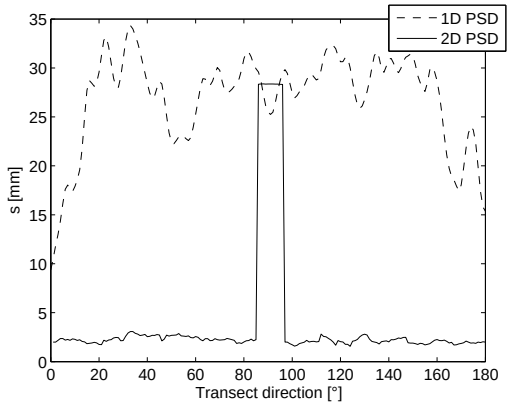

Figure 5.20: RMS height computed in different directions from 1D PSDs (dashed line) and from the 2D PSD (continuous line)

be two diracs, and the RMS height would be large exclusively in the y-direction. In practice, the surface is finite which leads to peaks with non-zero width.

Simulations at C-band with the Oh backscattering model for the hh polarization (equation 2.26) with $m_v = 0.20\,\mathrm{m}^3/\mathrm{m}^3$ and $\theta = 24°$ show that this "flash" of +22 mm in the y-direction with the 2D PSD, translates into a flash of +11.3 dB (see Fig. 5.21a). This value matches observations made in [62] and [122]. Also Dubois *et al.* reports a drop in σ^0 for directions 5° off the flashing direction [122]. This is exactly the case for the present simulations.

The main mismatch comes from the fact that according to Wegmüller *et al.,* flashing does not seem to occur at vh-polarization [62]. Flashing is thought to come from Bragg resonance which is a different scattering mechanism from the non-coherent scattering modeled by the classical backscattering models. Therefore, one cannot expect to fully explain the flashing field with simulations with these models. Nonetheless, the 2D PSD alone reflects the fact that the Bragg resonance happens only around the perpendicular direction. This suggests that the 2D PSD senses the soil surface in a similar way than does the radar. Hence it might be more suitable to compute the roughness parameters from the 2D PSD than from the classical transect measurements, even in absence of row structure.

Even though the previous results are encouraging, this directional roughness characterization from the 2D PSD will not be further developed as this method should first be validated against SAR measurements which goes beyond the scope of the report. In the following sections, the roughness parameters are computed in a more conventional way. The RMS height is calculated all over the DEMs and the correlation length is computed from the average ACF along all transects in the x-direction (long side of the DEM).

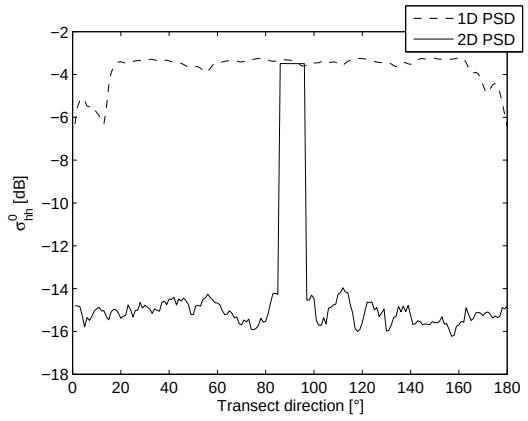

(a)

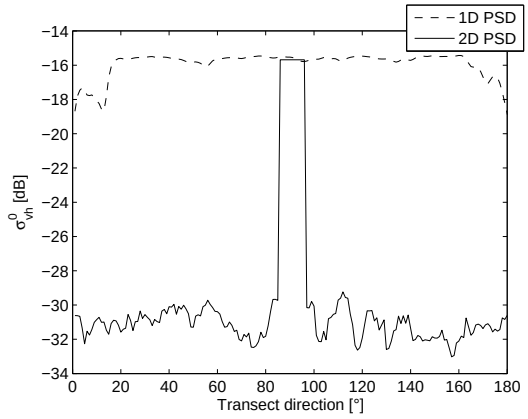

(b)

Figure 5.21: (a) σ^0_{hh} and (b) σ^0_{vh} simulated along different azimuth directions with RMS height from the 1D and the 2D PSDs

5.3 Temporal variability of surface roughness

This section looks at the temporal variability of surface roughness. Four time series of SfM measurements are investigated. They correspond to period 1 and period 2 for field 1 and field 2.

Section 5.3.1 comments on the visual changes observed for the four time series.

Section 5.3.2 studies the actual changes in roughness parameters.

Section 5.3.3 investigates which roughness scales are changing by looking at changes in PSD.

Finally in section 5.3.4, the effects of these roughness changes on backscattering are analyzed in order to test the validity of change detection methods which ignore variations in surface roughness.

5.3.1 Visual changes on time series of DEMs

The soil composition for fields 1 and 2 is 80% clay, 20% sand.

Period 1 Fig. 5.22 shows a series of 7 DEMs B for field 1 from May to June 2013. It is difficult to extract information about soil surface changes because the surface was covered with remains of dry weeds. During this period, no crops were planted and the field was left untouched with a lot of weed/grass. After applying weed-killer, vegetation disappeared within a couple of weeks, but dry stems remained for a longer period of time.

Fig. 5.23 shows the series of DEMs for field 2. There are no visible oriented roughness, but there are clear changes of the soil surface. On the 17 June 2013, the soil surface starts cracking. The cracks deepen until the 21 July. Then from the 27 July, the cracks slightly regress.

Such cracking can be expected from the high clay content of the soil. To go further, the cracks can be isolated by filtering out all the points above a given threshold. Fig. 5.24 shows the cracks after filtering on the 21 July, with a threshold of $-5\,\mathrm{mm}$. The soil surface contraction can then be estimated by counting the number of points corresponding to cracks relative to the total number of points forming the DEM. Here the soil surface area has contracted by 24%.

Period 2 For field 1 from September 2013 to June 2014, vegetation growth was well under control. The field was prepared for planting rapeseeds. Unfortunately, because the surveyed plot is in the corner of the field (see Fig 3.1), some of the tools used during tillage operations could not reach this corner. In the end the surveyed surface had a light pattern from the rolling operation, but it did not undergo deep ploughing like the rest of field 1. Fig. 5.25 shows a few DEMs of the time series. The full time series is in appendix A. Light rows originating the rolling procedure are visible across each DEM. Visually, there are no significant changes of the soil surface over the 9 months of observations.

Finally, Fig. 5.26 shows the DEMs for field 2 during period 2. Strong rows originating from deep ploughing are visible. Initially the soil surface seems stable.

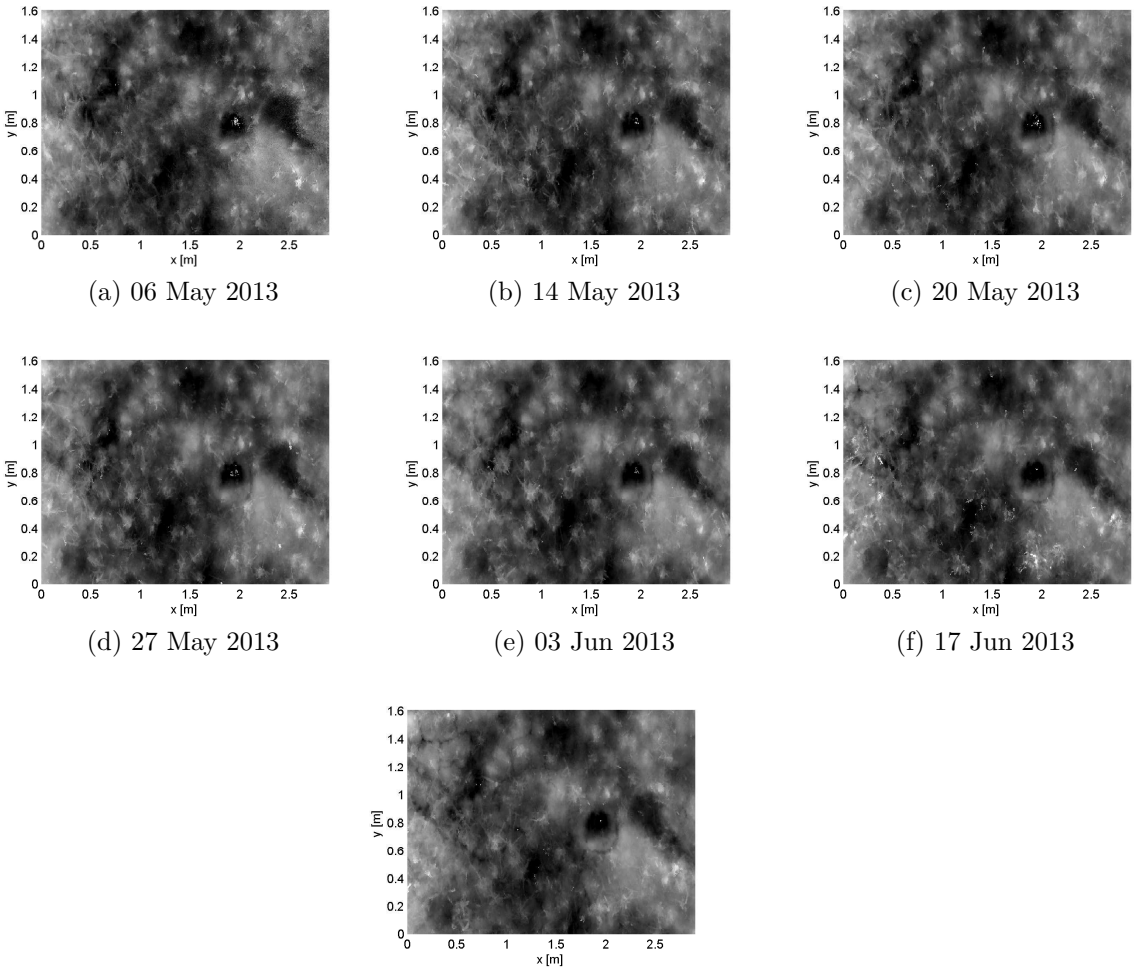

(a) 06 May 2013 (b) 14 May 2013 (c) 20 May 2013

(d) 27 May 2013 (e) 03 Jun 2013 (f) 17 Jun 2013

(g) 25 Jun 2013

Figure 5.22: Field 1 period 1

The rows starts smoothing from the 24 March 2014.

5.3.2 Changes in roughness parameters

Since backscattering models account for surface roughness with the RMS height and the correlation length, this section focuses on changes in these two parameters. For period 1, the analysis is done only for field 2 as field 1 was covered with dry weeds. For period 2, both fields 1 and 2 are considered. The roughness parameters are computed for time series of DEMs B because (1) roughness changes are expected to happen at small/medium scales, (2) scaling a DEM A with SfM-georef is two times more time consuming than scaling a DEM B.

For all the plots of RMS height and correlation length (Fig. 5.27, 5.28, 5.29), the error bars correspond to the standard deviation found when studying SfM repeatability for the RMS height (± 0.1 mm) and the correlation length (± 3 mm).

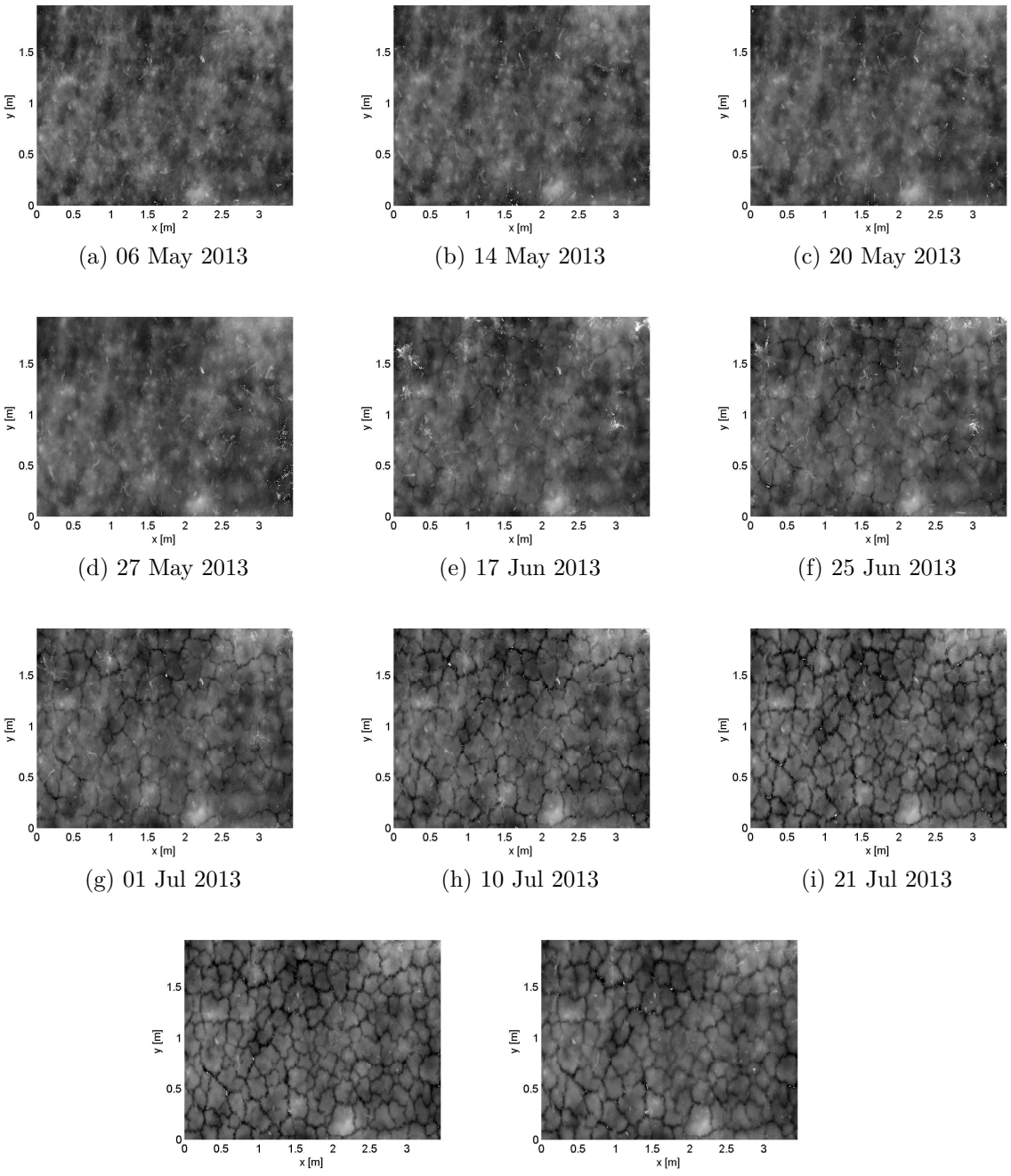

(a) 06 May 2013 (b) 14 May 2013 (c) 20 May 2013

(d) 27 May 2013 (e) 17 Jun 2013 (f) 25 Jun 2013

(g) 01 Jul 2013 (h) 10 Jul 2013 (i) 21 Jul 2013

(j) 27 Jul 2013 (k) 30 Jul 2013

Figure 5.23: Field 2 period 1

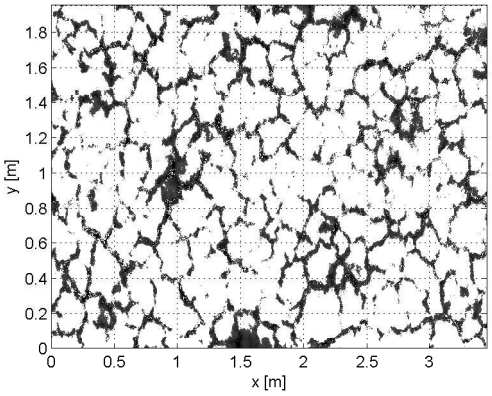

Figure 5.24: DEM after keeping only the points below −5 mm. This filtering isolates the cracks.

Period 1 Fig. 5.27 shows the RMS height for each DEM B after plane-fit removal, along with rainfall, soil moisture, soil temperature, and correlation length.

Considering the available weather data, three time periods (A, B, and C) with distinct weather conditions can be isolated (Table 5.10). First period A from 17 June to 1 July is characterized by light rain ($< 6\,\mathrm{mm/h}$), mild soil temperature (15-20°C), high soil moisture ($0.20 - 0.35\,\mathrm{m^3/m^3}$) and a slow decrease in RMS height because of the rain. Second, period B from 1 July to 21 July is much dryer, with warm soil temperature, dry soil ($\sim 0.15\,\mathrm{m^3/m^3}$). This period corresponds to the soil cracking observed on Fig. 5.23 which translates into a steep increase in RMS height. Finally period C from 21 July to 30 July is still warm ($20 < T_{soil} < 25$°C), but with several heavy rainfalls which lead to a fall in RMS height. The soil surface smoothes as cracks are refilled with small soil aggregates carried by runoff.

While the dynamics of soil moisture appears to be primarily dictated by rainfalls (wetting process) and soil temperature (drying process), RMS height changes are more complex. During period A, the RMS height slowly decreases with light rainfalls but it does not increase between rain events, probably because the soil temperature is not high enough to dry the soil in a short time. During period B, soil moisture falls below $0.20\,\mathrm{m^3/m^3}$. Below this threshold the soil surface starts cracking. During period C, the RMS height drops because of heavy rainfall, but the high soil temperature quickly dries the soil between rainfalls. This can be inferred from the sawtooth aspect of soil moisture. Even though the overall trend is a decrease in RMS height, a finer time sampling of roughness measurements over this period would have certainly shown temporary increases in RMS height between rainfalls.

All in all, RMS height dynamics seems to be the result of complex soil processes involving a combination of weather parameters. For the studied period, changes in RMS height seem to be well explained by soil temperature and soil moisture measurements. Only rainfall might not be an essential parameter to measure because it is already captured by soil moisture rises.

As noticed in [12], changes in correlation length are inversely correlated to changes in RMS height (Fig. 5.27d). Smoothing of the soil surface tends to in-

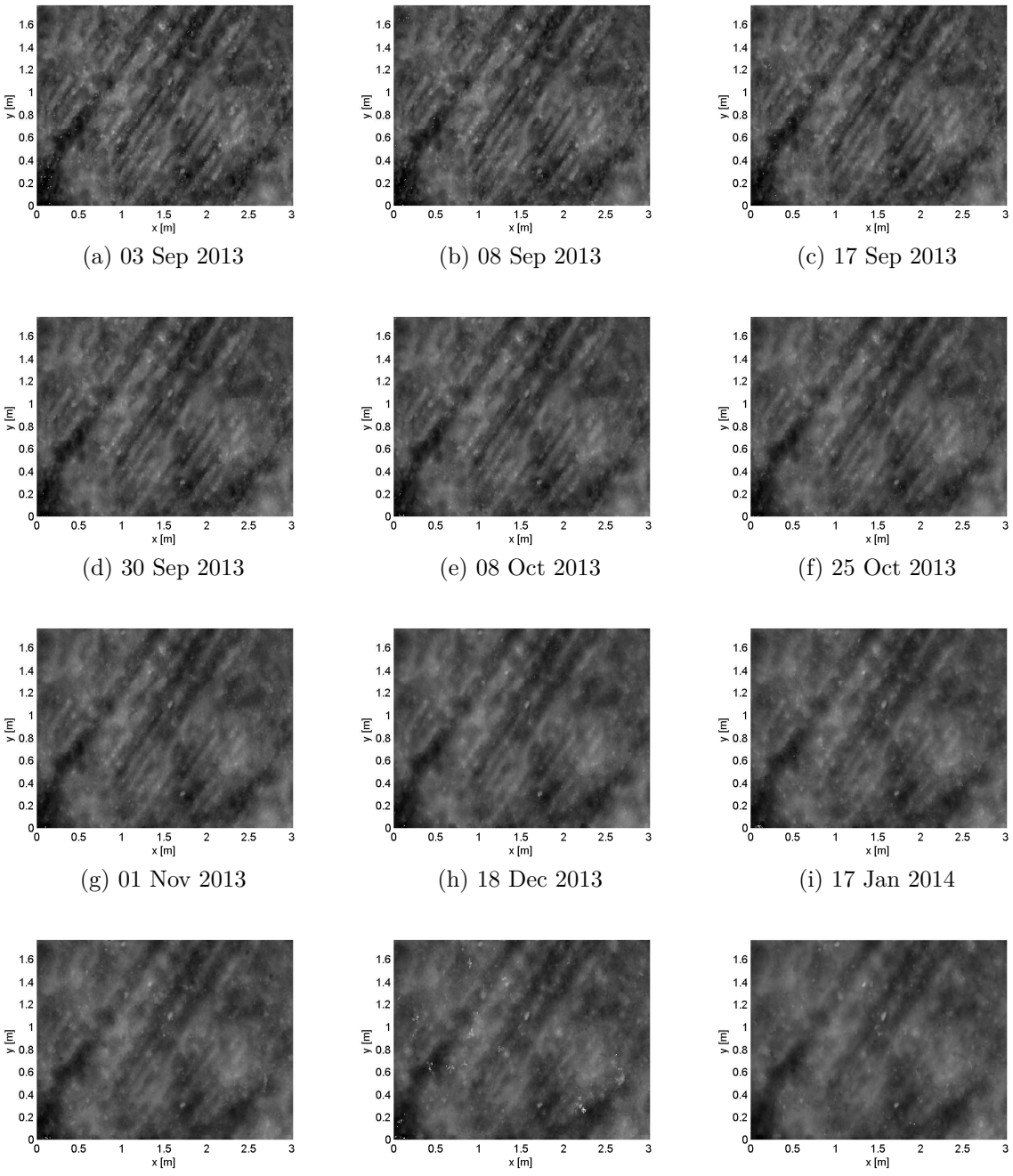

(a) 03 Sep 2013 (b) 08 Sep 2013 (c) 17 Sep 2013

(d) 30 Sep 2013 (e) 08 Oct 2013 (f) 25 Oct 2013

(g) 01 Nov 2013 (h) 18 Dec 2013 (i) 17 Jan 2014

(j) 24 Mar 2014 (k) 02 May 2014 (l) 12 Jun 2014

Figure 5.25: Field 1 period 1

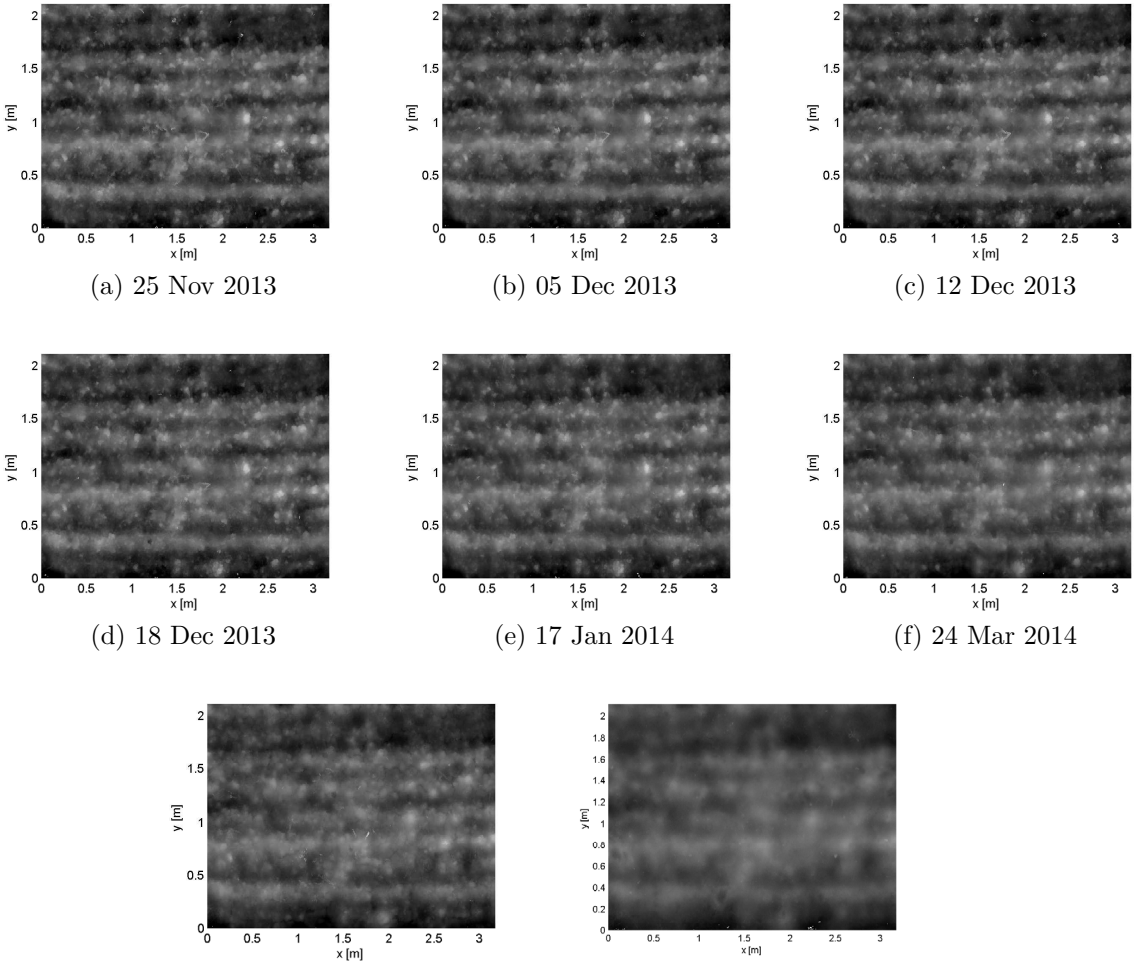

(a) 25 Nov 2013 (b) 05 Dec 2013 (c) 12 Dec 2013

(d) 18 Dec 2013 (e) 17 Jan 2014 (f) 24 Mar 2014

(g) 02 May 2014 (h) 18 Jul 2014

Figure 5.26: Field 2 period 2

Period	Rainfall	Soil T [°C]	Soil moisture [m^3/m^3]	RMS height change
(*A*) 17 Jun - 1 Jul	light rain	15-20	0.20-0.35	slow decrease
(*B*) 1 Jul - 21 Jul	no rain	20-25	0.15	steep increase
(*C*) 21 Jul - 30 Jul	heavy rain	20-25	0.20-0.30	steep decrease

Table 5.10: Three periods characterized by different weather conditions

crease the correlation length, and surface cracking tends to shorten the correlation length.

Period 2 Fig. 5.28 and Fig. 5.29 shows the changes in RMS height and correlation length along with measurements from the data logger for field 1 and field 2. Between the 3 September 2013 and the 18 December 2013, there is a fine time sampling of SfM acquisitions for field 1 because this period also corresponds to the Radarsat-2 acquisitions. Measurements over field 2 started later because of vegetation cover. Then from the 17 January 2014, SfM acquisitions were made only every 1-2 months, to capture mainly seasonal roughness changes.

Measurements from the rain gauge show that period 2 is very wet. Multiple short dry episodes can be identified from the decreases in soil moisture. All in all, the soil remains wet with soil moisture always between $0.20\,m^3/m^3$ and $0.40\,m^3/m^3$. As for the soil temperature, it shows variations in agreement with the seasons. There is a decrease from 20°C to 5°C in Summer/Autumn. The temperature remains around 5°C during Winter, then increases back to 20°C during Spring.

Unlike the various roughness changes observed on Fig. 5.27, changes in RMS height are here monotonic. There is an overall decrease in RMS height throughout the observed period. This is because the weather conditions were constantly wet, unlike during Summer of period 1.

Note that on Fig. 5.28 the roughness parameters are computed after detrending by plane-fit removal, while on Fig. 5.29 the DEMs are detrended with the high-pass filter introduced in section 5.2.2. This different detrending method was required to remove the oriented roughness and compute the autocorrelation function. After verification with the RMS height, the detrending method does not significantly affect how roughness parameters change over time.

Looking at Fig. 5.28, the frequent rainfall produce an exponential decrease in RMS height from the 3 September 2013 to the 18 December 2013. Then the RMS height remains stable around 9.3 mm before decreasing to 8.7 mm for the last acquisition.

On Fig. 5.29, usable SfM acquisitions are only available from the 1 November 2013, as vegetation was covering the soil surface for the previous acquisition dates. For the first four acquisitions, the RMS height is stable as there are only light rainfalls. Then for the last four acquisitions, there is a clear decrease in RMS height which tends to accelerate. Unlike for field 1, the decrease is not exponential.

As before, for both fields, changes in correlation length are inversely correlated to changes in RMS height.

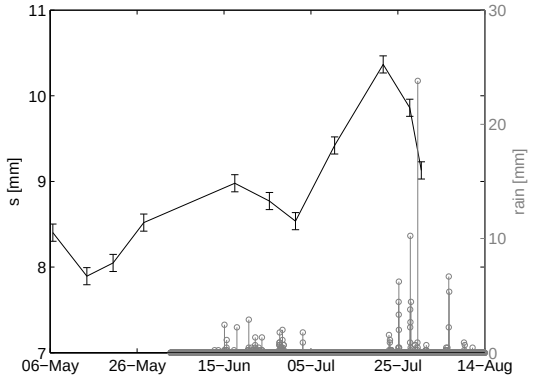

(a) Change of RMS height against rainfall measurements. Rainfall tends to smooth the soil surface.

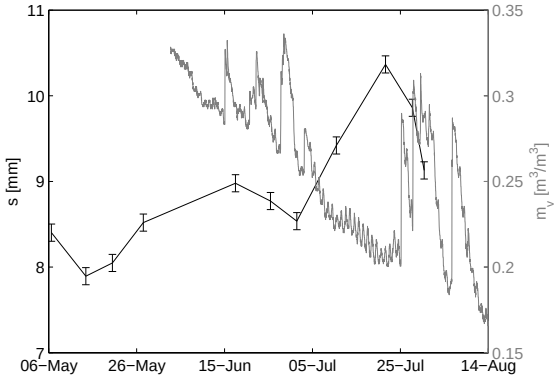

(b) Time series of RMS height and moisture measurements Steep rise in RMS height when soil moisture falls below $0.20\,\mathrm{m}^3/\mathrm{m}^3$ due to cracking.

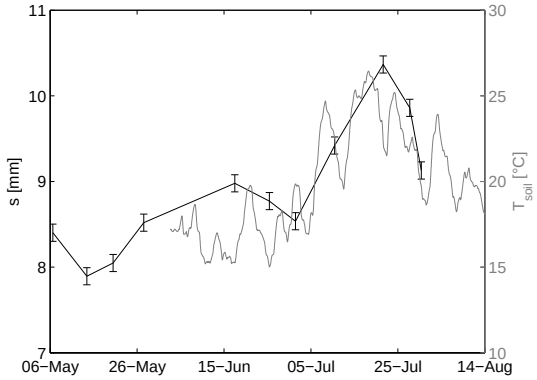

(c) Time series of RMS height and soil temperature.

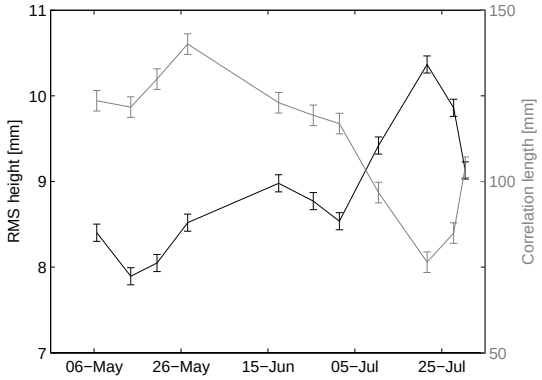

(d) Changes in correlation length and RMS height. RMS height trends follow soil temperature trends. The two parameters are inversely correlated.

Figure 5.27: Time series of RMS height against (a) local rainfall, (b) soil moisture, (c) soil temperature, (d) correlation length for field 2 period 1.

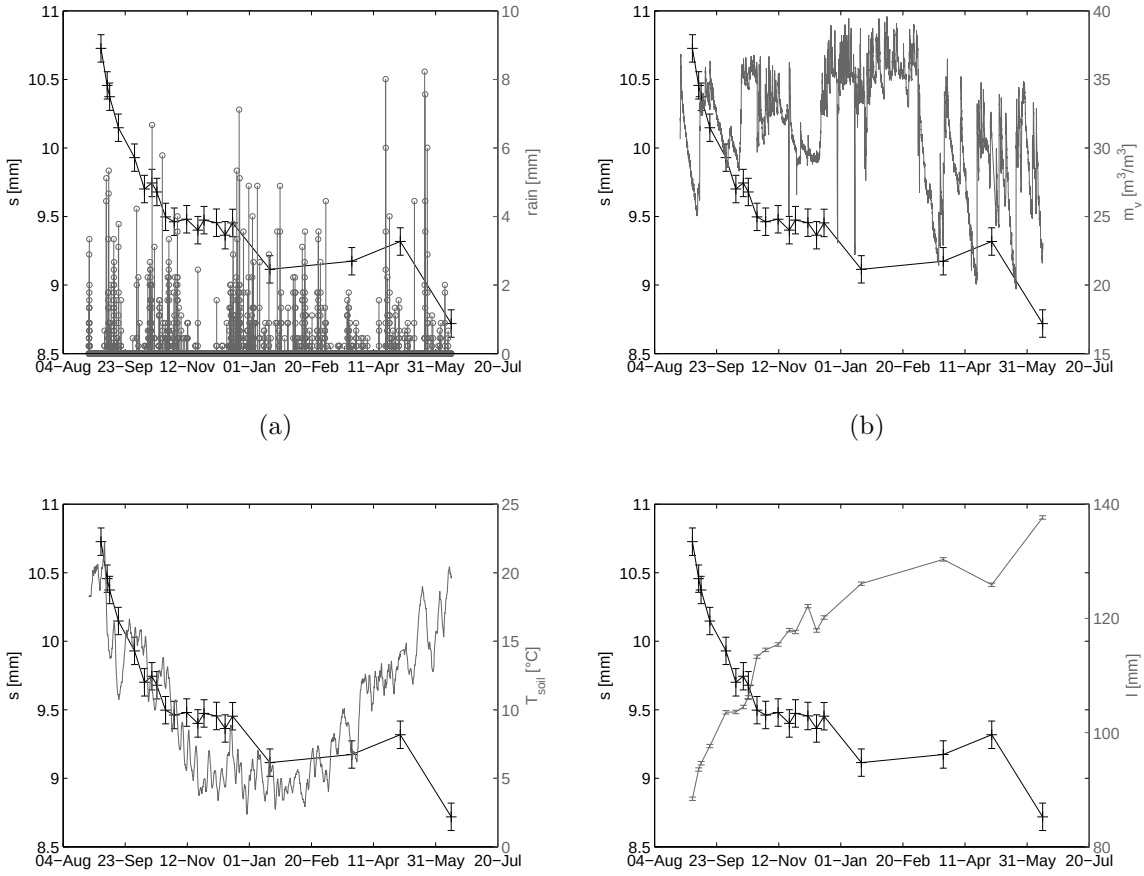

Figure 5.28: Time series of RMS height against (a) local rainfall, (b) soil moisture, (c) soil temperature, (d) correlation length for field 1 period 2.

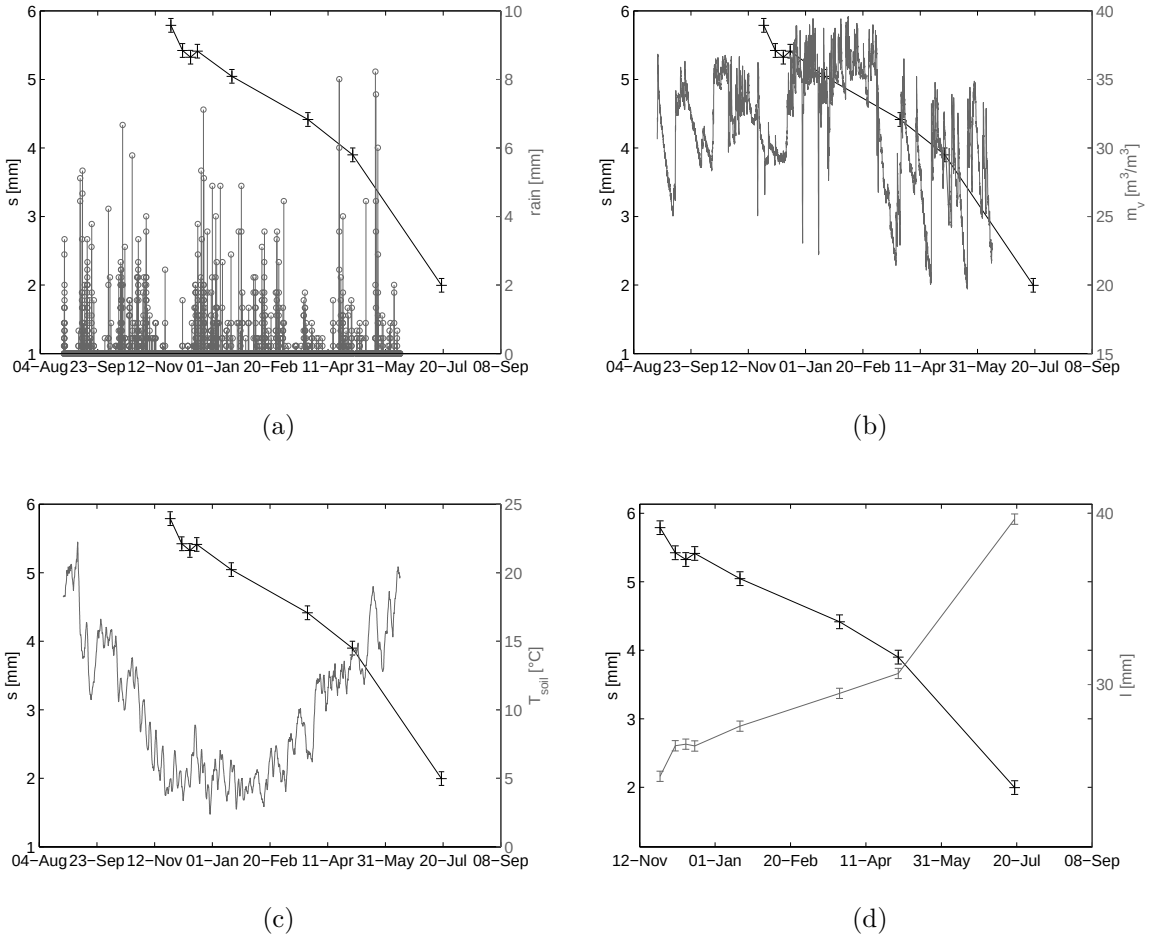

Figure 5.29: Time series of RMS height against (a) local rainfall, (b) soil moisture, (c) soil temperature, (d) correlation length for field 2 period 2.

In summary, from these observations, rainfalls tend to decrease the RMS height. However it is not straightforward to establish a model to predict the decrease following a given amount of rain. Presumably, the decrease depends also (and not exclusively) on the initial state and composition of the soil surface and the type of rain (e.g. size and density of the droplets). In comparison, an increase in RMS height seems possible only in dry conditions. Here such conditions only occurred during July 2013.

While general laws cannot be drawn from this isolated experiment, this section highlights the fact that under some weather conditions, roughness can actually exhibits significant natural changes within a short amount of time. This point is of particular interest as such roughness changes could affect soil moisture retrieval based on change detection methods which assume constant surface roughness over 1-2 months [17, 18, 19, 20]. The consequences of ignoring surface roughness changes is further investigated in section 5.3.4.

5.3.3 Changes in power spectral density

To analyze changes in roughness at different scales, the average PSD from the 1D PSDs of all rows parallel to the x-direction is computed for each DEMs B. The DEMs are not detrended in order to preserve the longest roughness scales. For the sake of clarity only four intermediate acquisitions of each time series are displayed.

Period 1 As before, only field 2 is analyzed. Fig. 5.30a shows that the changes in surface roughness which impact the roughness parameters happen only at small/medium scales. There are no changes for scales larger than 50 cm. A closer view on Fig. 5.30b shows that changes in PSD around the 10 cm scales match changes in RMS height. And these scales correspond to the typical distance between two cracks (10-20 cm) on Fig. 5.24. The arrangement of curves for scales smaller than 1.4 cm is more debatable. It does not follow the changes in RMS height. This is not incoherent, as these smalls scales do not contribute significantly to the total variance (integral of the PSD).

Fig. 5.31 shows 4 pictures of the same patch of soil for the 4 acquisition dates. The soil on the 21 July has the most grainy aspect, which match the large PSD on Fig. 5.30c. The smoothest surface corresponds to the 27 May, but it has one of the largest PSD. At this time, the surface had residuals of dry weeds which might explain why the 27 May acquisition does not have the lowest PSD at small scale. Finally the surface on the 30 July is less grainy than on the 21 July, but it has a punctured aspect from heavy rainfall, this does not seem to be captured on the PSD.

The point density for DEMs B ($57\,\text{points/cm}^2$) suggested that details of a few millimeters can be captured. However height variations at these scales are so small (a few millimeters) that they might be masked by noise, especially considering that the vertical accuracy is not better than a few millimeters. The arrangement of Fig. 5.30c could come from differences in acquisition height since the camera was hand-held. Image sets with overall a smaller acquisition heights might capture more details of the surface. While these details might be smoothed out on image sets which have

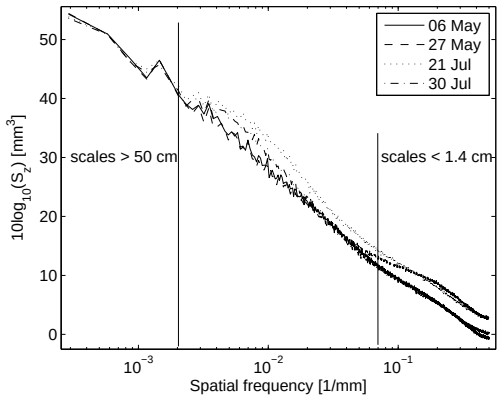

(a) No noticeable changes for scales larger than 50 cm

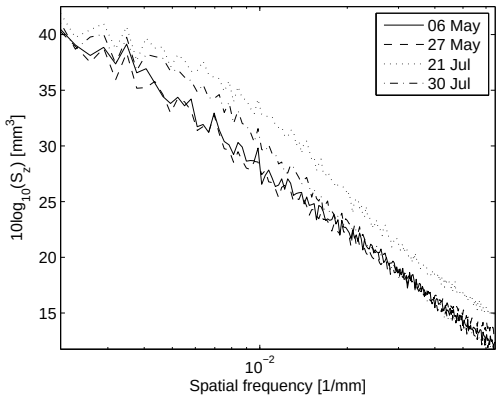

(b) Zoom on medium scales (10 cm). The arrangement of curves matches changes in RMS height.

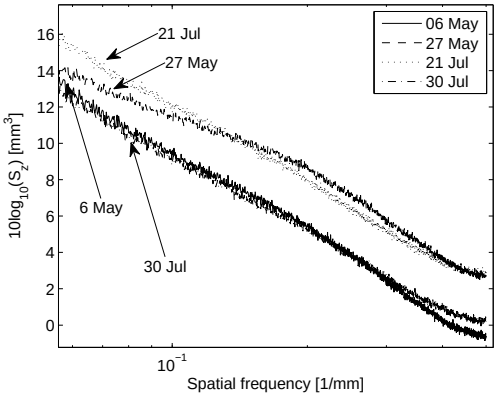

(c) Zoom on small scales (<1.3 cm). The DEMs may be too noisy to capture millimeter changes.

Figure 5.30: Field 2 Period 1. Change in power spectral density for four intermediate dates

slightly higher acquisition heights. All in all, this suggests that roughness features with horizontal scales lower than 1 cm have a characteristic height of only a few millimeters which is not properly reconstructed by the current setup. It follows that the true resolution might be closer to 1 cm than to 1 mm.

Period 2 A similar analysis can be done for field 1 and 2 over period 2.

Fig. 5.32 shows four PSDs for field 1. Again, there are no significant changes at large scales. At medium scales, the PSD decreases with time and reflects the changes in RMS height. The pictures on Fig. 5.33 show that details of the soil surface do not seem to be captured by SfM. The soil surface on 2 May looks smoother than on the other acquisition dates, but on Fig. 5.32b the PSD for 2 May is above the PSDs for 25 October and 17 January.

Fig. 5.34 shows four PSDs for field 2. Looking at the large scales, it appears that between 25 November and 18 July, surface smoothing has occurred at scales as large as 1 m. This is probably because the observation period is longer than for

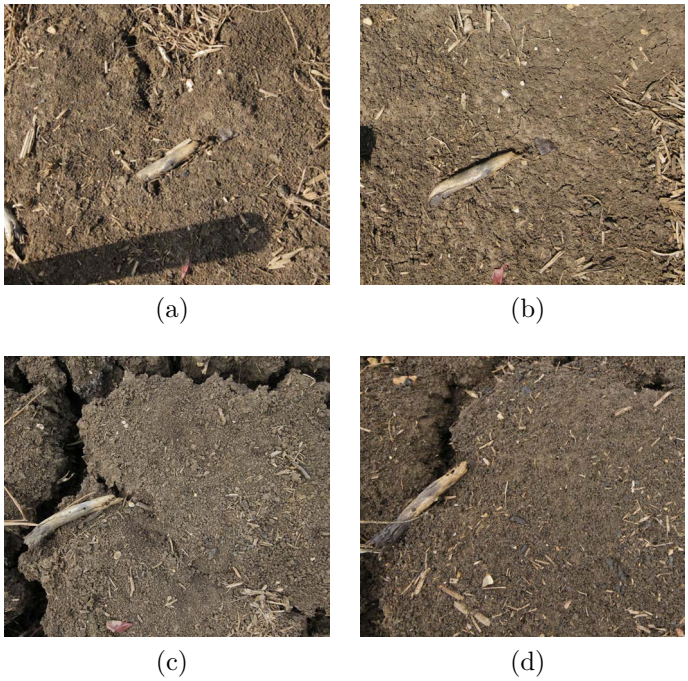

Figure 5.31: Field 2 Period 1. Soil surface texture for (a) 6 May, (b) 27 May, (c) 21 July, and (d) 30 July

the two previous time series, and initially the soil surface was artificially very rough (deep ploughing) which gives room for significant smoothing. Note that at medium scales the decrease in PSD still agrees with the decrease in RMS height on Fig. 5.29 which was computed after high-pass filtering. This is because the cutoff frequency of the filter was selected to attenuate mainly scales larger than 40 cm, while RMS height changes are mainly dictated by surface changes happening around the 10 cm scale.

This time, changes at small scales seems to agree with the overall smoothing of the surface (see Fig. 5.35). Again this could be because initially the height variations at small scales were relatively large after deep ploughing. Therefore SfM may have been able to capture small roughness scales at least for the first observations. This is just a supposition and more work with other acquisitions over prepared soil surfaces would be required to draw conclusions.

In summary, the common assumption regarding the absence of changes in surface roughness remains true for large-scale features, but does not hold for small/medium-scale features. This is of interest for microwave scattering as these scales are in the range of a few wavelengths. Over a period of three months SfM shows that noticeable changes happen for scales smaller than 50 cm. Measurements over a longer period of time (7 months) catch changes at scales as large as 1 m for a surface initially deep-ploughed. Therefore future measurements carried out to study roughness dynamics under natural conditions should cover a surface area relevant to the time extent of the experiment.

As for the measurement resolution, the requirement for radar application was set to 1 mm. This section suggests that in some cases the limited height variability of

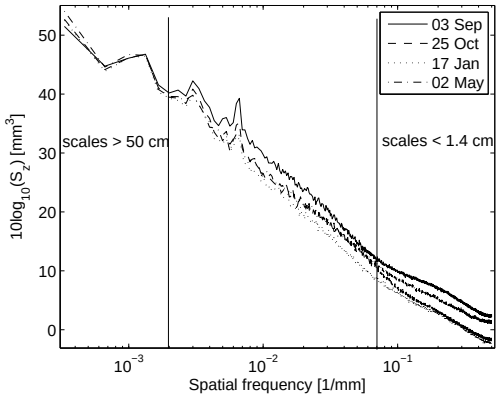

(a) No noticeable changes for scales larger than 50 cm

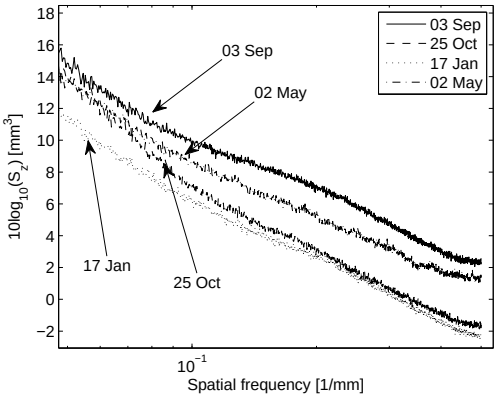

(b) Zoom on small scales

Figure 5.32: Field 1 Period 2. Change in power spectral density for four intermediate dates.

(a) (b)

(c) (d)

Figure 5.33: Field 1 Period 2. Soil surface texture for (a) 3 September 2013, (b) 25 October 2013, (c) 17 January 2014, and (d) 2 May 2014

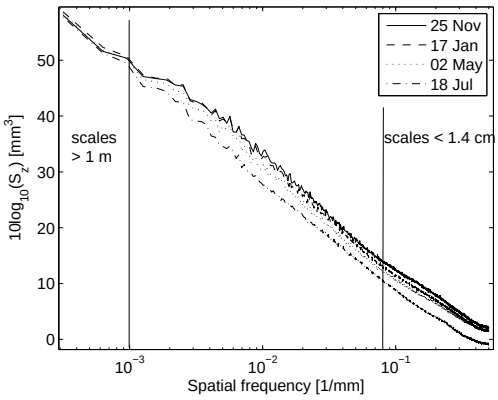

Figure 5.34: Field 2 Period 2. Change in power spectral density for four intermediate dates. No noticeable changes for scales larger than 1 m.

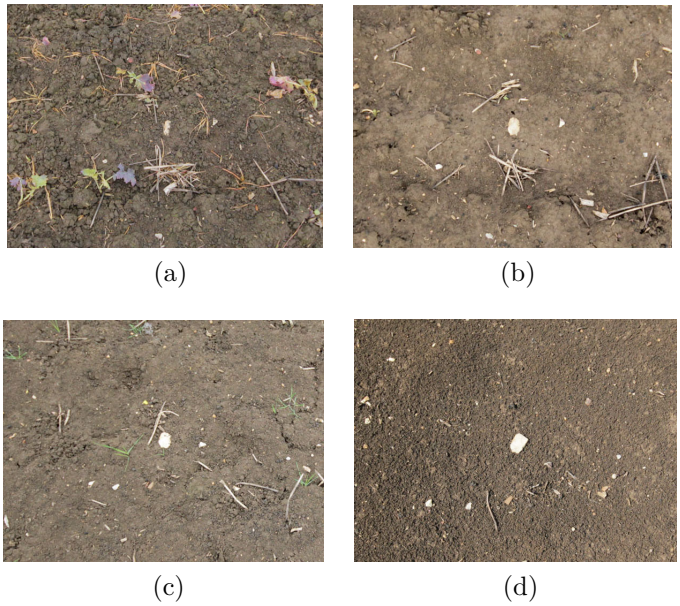

(a) (b)

(c) (d)

Figure 5.35: Field 2 Period 2. Soil surface texture for (a) 25 November 2013, (b) 17 January 2014, (c) 2 May 2014, and (d) 18 July 2014

mm-scale features makes the true measurement resolution close to 1 cm. However, small height variability also means that the power carried by theses small features is very low. Therefore they contribute only marginally to the final value of the roughness parameters, *i.e.* capturing them might not be critical.

5.3.4 Effects of roughness temporal changes on surface backscattering

This section investigates whether the temporal changes in roughness parameters reported in section 5.3.2 are significant for microwave scattering and soil moisture estimation. All the simulations are made with the Oh backscattering model given by equations 2.25 and 2.26.

Effect on microwave scattering Fig. 5.36, 5.37, and 5.38 show the effect of roughness changes on σ^0_{hh} and σ^0_{vv}, respectively for field 2 period 1, field 1 period 2, and field 2 period 2. All simulations assume a constant soil moisture which is set to its mean value over the considered period (for period 1 $m_v = 0.25\,\mathrm{m}^3/\mathrm{m}^3$, and for period 2 $m_v = 0.31\,\mathrm{m}^3/\mathrm{m}^3$). On each plot, the plain curve is obtained by accounting only for changes in s with l set to its mean measured value, the dash-dotted curve is obtained by accounting only for changes in l with s set to its mean measured value, and the dotted curve is obtained by accounting for both changes in s and l.

All in all the behavior of the $hh-$ and $vv-$polarizations is similar. The $hh-$polarization is only slightly more sensitive to changes in the roughness parameters. On Fig. 5.36 and 5.37, as expected the backscattering coefficients are more affected by changes in RMS height than changes in correlation length. Accounting for changes in both parameters leads to smaller variations in backscattering coefficient than when accounting only for changes in s, because changes in s and l are inversely correlated. With changes in both s and l, for field 2 period 1 the maximum variation is $\Delta\sigma^0_{hh} = 0.80\,\mathrm{dB}$, and for field 1 period 2 the maximum variation is $\Delta\sigma^0_{hh} = 0.58\,\mathrm{dB}$.

For field 2 period 2, Fig. 5.38 shows that changes in correlation length have almost no effects on σ^0_{hh} and σ^0_{vv}. This is because after high-pass filtering, the correlation length values are one order of magnitude smaller than those obtained after plane-fit detrending for the two previous time series. On the other hand, the decrease in RMS height produces a decrease of 3.98 dB in σ^0_{hh}. Assuming that detrending with a high-pass filtering is a suitable method, this decrease of several dBs is unlikely to be negligible for soil moisture retrieval.

Effect on soil moisture retrieval This paragraph looks at the error made on soil moisture estimation, when the retrieval is computed assuming that the roughness parameters are constant. Simulations are done only for σ^0_{hh} which is the most sensitive to an error on roughness parameters. First a time series of σ^0_{hh} is generated for each SfM acquisition with the measured values for m_v, s, and l. Then this simulated time series is used to retrieve soil moisture assuming that the roughness parameters are constant and equal to their value on the first SfM acquisition.

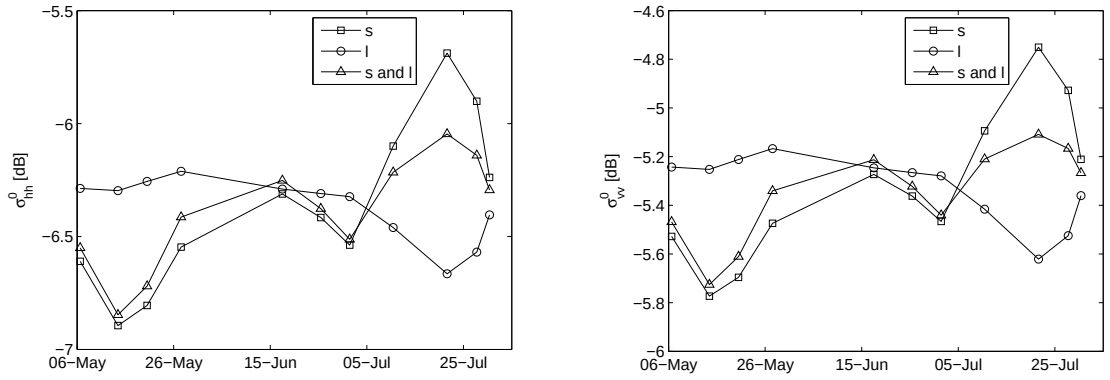

(a) (b)

Figure 5.36: Field 2 Period 1. The coefficients σ^0_{hh} and σ^0_{vv} are computed for $m_v = 0.25\,\mathrm{m}^3/\mathrm{m}^3$ with changes in s (plain curve), with changes in l (dash-dotted curve), and with changes in both s and l (dotted curve).

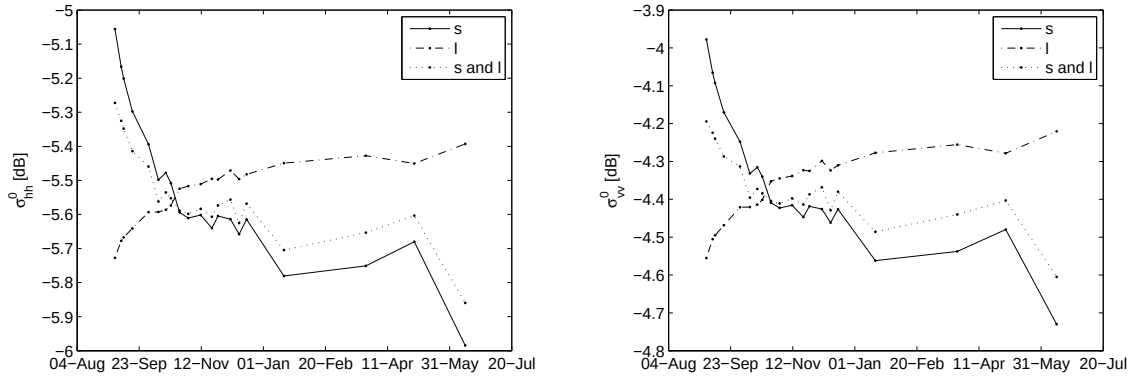

(a) (b)

Figure 5.37: Field 1 Period 2. The coefficients σ^0_{hh} and σ^0_{vv} are computed for $m_v = 0.31\,\mathrm{m}^3/\mathrm{m}^3$ with changes in s (plain curve), with changes in l (dash-dotted curve), and with changes in both s and l (dotted curve).

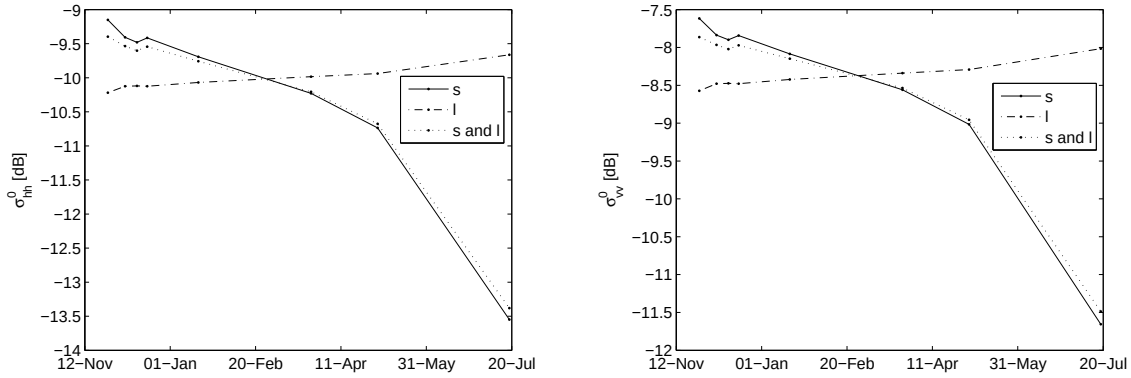

(a) (b)

Figure 5.38: Field 2 Period 2. The coefficients σ^0_{hh} and σ^0_{vv} are computed for $m_v = 0.31\,\mathrm{m}^3/\mathrm{m}^3$ with changes in s (plain curve), with changes in l (dash-dotted curve), and with changes in both s and l (dotted curve).

	RMS error [$\mathrm{m}^3/\mathrm{m}^3$]	Max error [$\mathrm{m}^3/\mathrm{m}^3$]
Field 2 Period 1	0.0445	0.0753
Field 1 Period 2	0.0386	0.0597
Field 2 Period 2	0.0912	0.1821

Table 5.11: Error between the retrieved soil moisture and its in situ measurement

Fig. 5.39 shows the error on soil moisture for the three available time series. As expected, because the soil is rather wet and the surface is smooth, a small error on the roughness parameters affect significantly the retrieved soil moisture. Fig. 5.39a is the most interesting because the acquisition on 21 July 2013 for which the roughness error is maximum, correspond to a soil moisture error not much larger than on other dates. This is because it also corresponds to the driest soil condition of the time series ($m_v = 0.21\,\mathrm{m}^3/\mathrm{m}^3$), thus σ^0 is not very sensitive to roughness error.

Table 5.11 shows that the RMS error is about $0.04\,\mathrm{m}^3/\mathrm{m}^3$, except for field 2 period 1 with high-pass detrending which leads to an error of $0.09\,\mathrm{m}^3/\mathrm{m}^3$. While an error of $0.04\,\mathrm{m}^3/\mathrm{m}^3$ may be acceptable, in practice the backscattering model is not perfect and σ^0_{hh} is not error free. Therefore the error on soil moisture would certainly exceed the uncertainty requirements defined by the OSCAR tool (section 3.5).

In summary this section shows that even though RMS height and correlation length change in opposite fashion, the backscattering coefficient is still primarily affected by changes in RMS height. If ignored, these changes can lead to non-negligible errors when soil moisture is inverted using out-of-date in situ roughness measurements or using change detection methods.

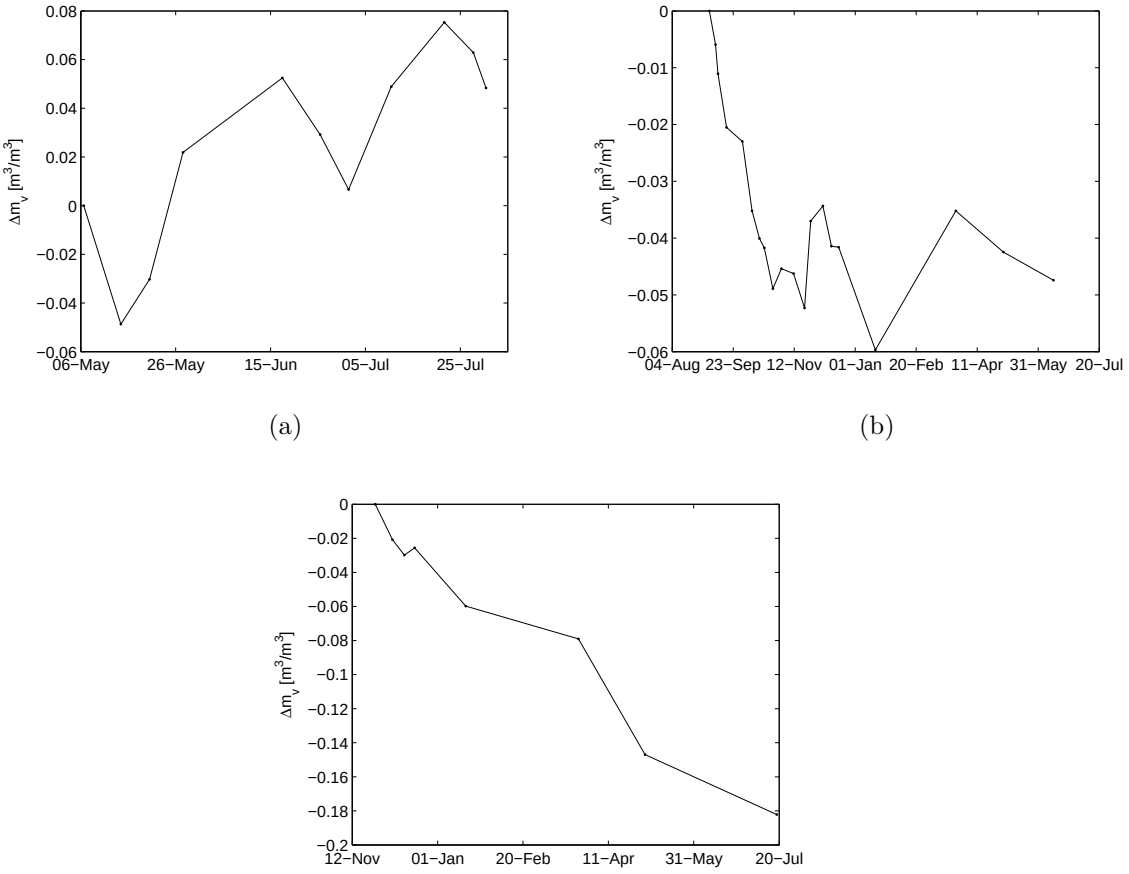

Figure 5.39: Retrieval of soil moisture assuming constant roughness parameters for (a) field 2 period 1, (b) field 1 period 2, and (c) field 2 period 2.

5.4 Summary

The three previous sections focused on roughness characterization with SfM.

Section 5.1 showed that the measurement setup based on SfM is able to produce DEMs over extended soil surfaces with measurement uncertainty good enough for the measurements to be used for microwave scattering. In practice, the height RMS error is close to 3.1 mm and the horizontal RMS error is about 1.5 mm. A broad comparison with the stereo-photogrammetric setup from Marzahn *et al.* [12] suggests that the SfM setup leads to less accurate DEMs, but a dedicated study using identical camera/lens, image compression, soil surface, and RMSE estimation, would be require to draw a definite conclusion. Regardless of measurement uncertainty, an unquestionable advantage of SfM is its practicality. The fact that images can be taken with a hand-held camera makes SfM a very attractive tool for field measurements.

Section 5.2 looked at the spatial variability of the roughness parameters. Measurements over an extended surface area is desirable to produce reliable estimations of the roughness parameters. In practice, for large DEMs, the roughness parameters are very dependent on the detrending technique. In particular, for DEMs with strong oriented roughness, a simple plane-fit detrending does not lead to a surface which can be described by the classical Gaussian/Exponential autocorrelation function. More generally, the inclusion of large-scale features as the DEM length increases leads to non-convergent roughness parameters.

High-pass or band-pass filters are a sensible alternative to linear and polynomial detrending as they can attenuate all the features which the radar is not sensitive to. Also, directional estimation based on the 2D PSD is an interesting method as it handles the soil surface in a similar fashion to theoretical scattering models. For example, it appears to provide some insights regarding the flashing-field phenomenon.

Before deriving other results, these two methods (band-pass filtering and 2D PSD) need to be tested against real SAR measurements over tilled fields with good knowledge of the along-track direction. The roughness measurements could be processed with different methods. Then the obtained roughness parameters could be used as input for a theoretical backscattering model such as the IEM to see which method leads to the best agreement between measured backscattering and simulated backscattering. Or the roughness parameters could be used to define a new semi-empirical backscattering model for which roughness parameters would need to be computed from the 2D PSD, after filtering.

Finally section 5.3 investigated the temporal variability of the roughness parameters from three time series of SfM acquisitions. The measurements show that natural changes in surface roughness are weather dependent. There exist time periods during which there are only minor changes in roughness parameters which are insignificant for microwave scattering. Typically this happens when the soil is cold and wet and in absence of rainfalls. Other than these conditions, the surface tends to smoothen with rain, and to crack during hot/dry weather. It is not clear how rain leads to sometimes small, other times large roughness changes, but it appears that the smoothing effect is particularly strong on soil surface which are artificially rough (rolled/ploughed soil surface). As in the UK, rainfalls can occur all year round, so

does surface smoothing. On the other hand, surface cracking only happened during Summer with low levels of soil moisture ($m_v < 0.20\,\mathrm{m}^3/\mathrm{m}^3$) and high soil temperature ($T_{soil} > 20°\mathrm{C}$). While surface smoothing leads to a decrease in RMS height, surface cracking comes with an increase in RMS height. It is also important to highlight that for the three time series natural changes of RMS height and correlation length were inversely correlated.

In short, there exist weather conditions for which changes in roughness parameters can be as fast as changes in soil moisture. Regarding microwave scattering, these changes can be large enough to compromise any methods which treats the roughness parameters as constants.

Analyzing the PSD of each DEM shows that these changes occur mainly at roughness scales smaller than 0.5-1 m. The analysis also suggests that the current SfM setup is unable to capture the small height changes occurring at scales smaller than 1 cm.

In summary, these results indicate that the roughness parameters, particularly the RMS height, can hardly be assumed constant and that they should be treated as unknown variables just like soil moisture. That is why the next chapter focuses on the simultaneous estimations of soil moisture and surface roughness from radar measurements acquired in different configurations, with emphasis on multi-polarized measurements.

Chapter 6

Results: Model inversion from combination of different radar configurations

This second results chapter investigates model inversion with both soil moisture and RMS height as unknowns, based on the combination of radar measurements acquired with different configurations. In particular, inversion based on multi-polarized images has been tested with the set of Radarsat-2 images. Note that the correlation length does not appear in the simplified Oh model.

Section 6.1 focuses on the model inversion with multi-polarized images. First the variations in σ^0 measured by Radarsat-2 are analyzed against the in situ measurements of soil moisture and surface roughness. Then the χ^2 method is applied to multiple fields and acquisition dates. Finally backscattering simulations are used to investigate what uncertainty on the retrieved parameters can actually be expected considering that the radar measurements are affected by speckle.

Section 6.2 extends the uncertainty analysis based on backscattering simulations to a configuration with multi-incidence measurements and a configuration with multi-frequency measurements.

From this uncertainty analysis, section 6.3 discusses the tradeoff on the type of radar measurements to combine in order to meet the soil moisture requirements defined in section 3.5.

6.1 Soil moisture and RMS height estimation with χ^2 fitting of multi-polarized radar measurements

This section looks at the estimation of soil moisture and RMS height from multi-polarized radar measurements. It focuses on determining which combinations of polarizations lead to the best parameter estimation, and how many looks are necessary to reach the uncertainty requirements on soil moisture and RMS height.

6.1.1 Correlation between Radarsat-2 σ^0 and in situ measurements

Before any attempts at retrieving soil moisture from Radarsat-2 measurements, it is worth looking at whether or not the measured σ^0 follows the variations observed with the in situ measurements of soil moisture.

Fig. 6.1 shows σ^0_{vh}, σ^0_{hh}, σ^0_{vv} measured for fields 6, 8, 9, 12 and 13, against available in situ measurements of soil moisture. The backscattering coefficients are taken as the mean σ^0 for a window of pixels which belongs to a given field. The associated error bar is the standard error on that mean. The error bar for soil moisture is simply the standard deviation over the sampled points.

Finally table 6.1 reports RMS height measurements with SfM. Detailed values for most of the acquisition dates are given in table 6.1a. The RMS height remains the same for fields 6 and 8 which are smooth. For the rough fields 9, 12, and 13, there are variations in RMS height, but their causes are not always clear. For fields 9 and 13, the changes of a few mm in RMS height may not be meaningful considering the standard deviations on the measurements, and the fact that within a field, the measurements were not taken at the same locations on each date. Field 12 went from rolled surface to ploughed surface between acquisitions 6 and 7 which explains the clear increase in RMS height, and it is possible that the newly ploughed surface was smoothed by rainfalls between acquisitions 7 and 8. In what follows, only a rough characterization of the soil surface is required. This is why in table 6.1b, the RMS height is aggregate in a single value for each field except for field 12.

General comments on σ^0_{vh}, σ^0_{hh}, and σ^0_{vv} As expected, the values of σ^0_{vh} are much lower than those of σ^0_{hh} and σ^0_{vv}. All polarizations tend to change in similar fashion which is unfortunate regarding the problem of estimating individually soil moisture and RMS height from the combination of these polarizations. It also worth noticing that in theory for bare soils σ^0_{vv} is supposed to be larger than σ^0_{hh}. Only for rough soil surfaces, or at 0° incidence, $\sigma^0_{hh} = \sigma^0_{vv}$. In practice, bias on the measurements or statistical error on the mean σ^0 can lead to $\sigma^0_{hh} > \sigma^0_{vv}$. This is the case for field 13 which has a rough soil surface.

Correlation with soil parameters For fields 6 and 8, soil moisture remained around $0.30\,\mathrm{m}^3/\mathrm{m}^3$ without significant variations. As shown by the contours of Fig. 2.3, σ^0 is not very sensitive to m_v for wet soil. Therefore it is not surprising that changes in m_v are not directly reflected in changes in σ^0. Overall the changes in σ^0_{hh} and σ^0_{vv} results more from changes in incidence angle, with a decrease in backscattering when the incidence angle increases. Changes in soil moisture have minor effects, but they can still be detected. For example acquisitions 3 and 5 have same incidence angle and same surface roughness, the main difference is a decrease in soil moisture by 0.06 $\mathrm{m}^3/\mathrm{m}^3$. This can be linked to a decrease of 0.80 dB on σ^0_{hh} and 0.25 dB on σ^0_{vv}. Variations in soil moisture seem to have a greater influence on σ^0_{vh} with a decrease of 1.85 dB between acquisitions 3 and 5. It is also reassuring to note that fields 6 and 8 which have similar soil moisture and surface roughness (see table 6.1), have also similar measurements of σ^0.

		Acquisition						
		2	**3**	**4**	**5**	**6**	**7**	**8**
Field	**6**	8.9 ± 1.1	-	-	-	8.9 ± 0.2	9.2 ± 1.1	9.1 ± 0.6
	8		11.5 ± 1.3	10.3 ± 2.4	9.7 ± 1.8	10.6 ± 1.3	10.6 ± 2.8	10.1 ± 1.4
	9				19.5 ± 3.9	15.5 ± 0.1	-	14.6 ± 0.6
	12					9.0 ± 1.0	32.4 ± 2.3	26.3 ± 0.6
	13					17.1 ± 0.8	15.5 ± 2.1	18.0 ± 1.3

(a) RMS height measurements in mm for all acquisition dates. Empty cells mean that no SfM acquisition is available. Cells with a dash mean that SfM acquisitions are available but not processed.

		Acq 1-6	**Acq 7-8**
Field	**6**	9.1 ± 0.7	
	8	10.4 ± 1.7	
	9	17.3 ± 3.5	
	12	9.0 ± 1.0	29.4 ± 3.7
	13	16.8 ± 1.2	

(b) Aggregate RMS height in mm

Table 6.1: Characteristic RMS height in mm for different fields. The standard deviation is computed from multiple SfM acquisitions.

In comparison, field 9 has a rougher soil surface, therefore σ^0 is overall stronger for all polarizations. The same interpretation applies for the variations in σ^0. In particular, from acquisition 7 to 8, there is an increase in σ^0 while the incidence angle goes from 25.8° to 32.4°. This certainly comes from the significant increase in soil moisture from 0.128 m^3/m^3 to 0.230 m^3/m^3.

Field 12 is of particular interest because of the change in surface roughness from rolled to ploughed between acquisitions 6 and 7. On acquisition 6, field 12 had similar roughness conditions to fields 6 and 8, thus similar values of σ^0 at all polarizations. Then on acquisition 7, field 12 had roughness conditions more similar to those of field 9 which is again confirmed by almost identical σ^0 values. It is also clear that the increase in surface roughness leads to $\sigma^0_{hh} \approx \sigma^0_{vv}$.

Similarly, the measurements for field 13 can be explained by considering changes in incidence angle and changes in soil moisture.

Overall, the above analysis confirms that σ^0 is sensitive to soil moisture and that this sensitivity is reduced for very wet soils. It also verifies that σ^0 increases with surface roughness. It also shows that the influence of incidence angle should be accurately accounted for in order to focus on the soil parameters only. All in all, the fact that changes in σ^0 can be explained by considering only soil moisture, surface roughness and incidence angle is rather comforting.

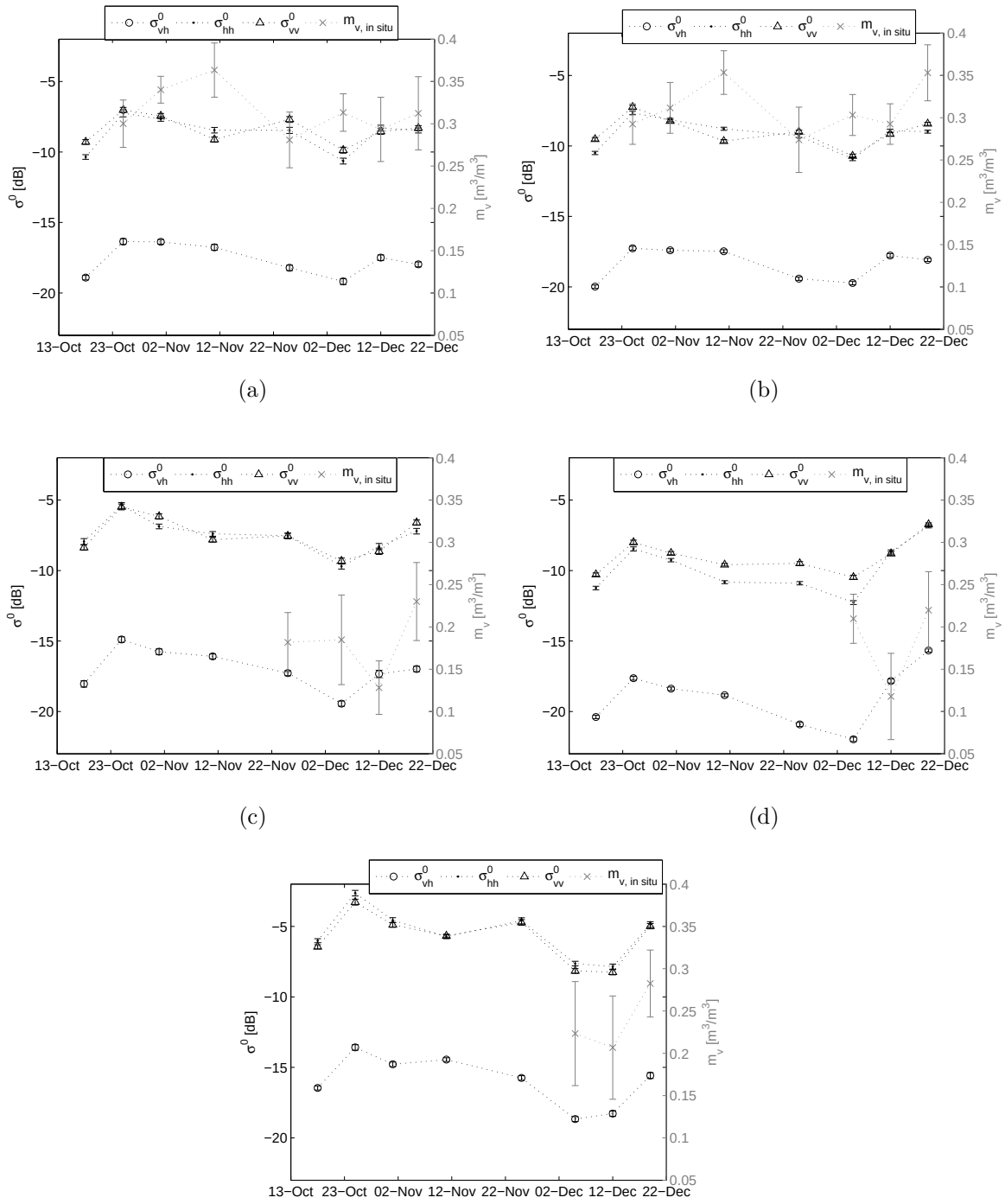

Figure 6.1: Measured σ^0 over fields 6, 8, 9, 12 and 13 against available in situ measurements of soil moisture

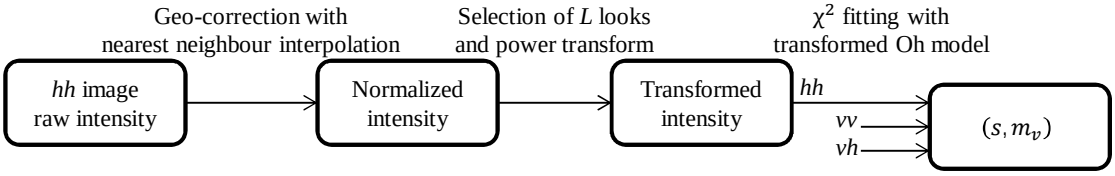

Figure 6.2: Processing steps to retrieve soil moisture and RMS height with χ^2 fitting. Processing of the $vv-$ and $vh-$images does not appear but is identical to the one of hh.

6.1.2 χ^2 fitting of Radarsat-2 images

To apply the χ^2 method described in section 2.3.2, all Radarsat-2 images are first geo-corrected with the Next ESA SAR Toolbox as presented in section 3.4. The next step is to isolate a group of pixels which belong to a given field. Then the power transform is applied to these measurements so that they can be input in the χ^2 method. The flow chart on Fig. 6.2 summarizes the different steps which lead to the retrieval of m_v and s.

In section 6.1.2.1, the χ^2 method is applied to two Radarsat-2 acquisitions over field 12. For different combinations of polarizations, the analysis covers the goodness-of-fit, the presence of systematic errors, the agreement between retrieved parameters and in situ measurements, and the uncertainty on the retrieved parameters. Then in section 6.1.2.2, the χ^2 method is applied more broadly to fields 6, 8, 9, 12 and 13.

6.1.2.1 Detailed analysis for two acquisitions

Figure 6.5 and 6.6 show the output of the χ^2 fitting respectively for Radarsat-2 acquisitions on 25 November 2013 (acquisition 5) and 5 December 2013 (acquisition 6), for four combinations of polarizations ((vh, hh), (vh, vv), (hh, vv), (vh, hh, vv)), over field 12. A set of L pixels is selected over the field. For acquisition 5, $L = 21 \times 49 = 1029$ pixels and for acquisition 6, $L = (L = 29 \times 35 = 1015$ pixels).

For example, Fig. 6.5a shows the retrieval with inversion of $vh-$ and $hh-$measurements. The circle shows the retrieved moisture and RMS height obtained with the set of L pixels of σ^0_{vh} and σ^0_{hh}. The cloud of gray crosses corresponds to retrievals with the Monte Carlo simulation of 500 synthetic data sets $(y_i)_k$ with $i = 1, \ldots, L$ and $k = 1, \ldots, 500$. The 500 synthetic data sets are enough to accurately delimit the confidence region. Each data set contains L bootstrapped samples of σ^0_{vh} and L bootstrapped samples of σ^0_{hh}. Each gray cross represents the inversion with a synthetic data set.

From this Monte Carlo simulation, a 68.3% elliptical confidence region is computed. The AA' and BB' regions delimit confidence intervals respectively on m_v and s, derived from the confidence ellipse. These intervals are larger than the one defined by a one standard deviation on m_v and s taken individually. More precisely, AA' quantifies the uncertainty on m_v knowing that s is also uncertain, and vice versa for BB'. The gray contours correspond to the mean σ^0_{vh} and σ^0_{hh} of the original data set.

Acquisition	5	6
m_v [m^3/m^3]	0.180 ± 0.029	0.210 ± 0.029
s [mm]	9.0 ± 1.0	9.0 ± 1.0

Table 6.2: In situ measurements for the same bare field for acquisition 5 and 6. The standard deviations are derived from the multiple in situ measurements made over the studied field.

Finally the triangle corresponds to in situ measurements of m_v and s with the error bars being their respective standard deviation. Finally the triangle shows the in situ measurements of soil moisture and surface roughness. For this field, in situ measurements are only available for acquisition 6. As there was no significant rainfalls during the 10 days which separate both acquisitions, it is reasonable to assume that the smooth surface roughness remained the same. As for soil moisture, in situ measurements for a neighboring field (field 9) which has similar levels of soil moisture suggest that soil moisture was about $0.03\,m^3/m^3$ wetter on acquisition 6. Therefore, the same in situ roughness measurement is assumed for acquisition 5 and 6, and soil moisture is assumed to be $0.03\,m^3/m^3$ smaller for acquisition 5 compared to its value for acquisition 6 (table 6.2).

Table 6.5 summarizes the results for acquisitions 5 and 6, for the four combinations of polarizations.

Goodness-of-fit The first parameter to check is the goodness-of-fit Q. The value of Q informs on how well the model fits the data considering the specified standard deviations σ_i of the measurements. Here the σ_i are estimated for each polarization by computing the standard deviation of the data sets after power transform. Therefore, the goodness-of-fit cannot be used to detect measurement outliers or non-Gaussianity, but it is still useful to detect poor agreement between the different polarizations due to biases on the measurements or/and on the model.

For acquisition 6, Q is close to 0.5 for all combinations of polarizations which means that the model fits the selected data properly. Acquisition 5 also has a goodness-of-fit close to 0.5 when using two polarizations, but the fit is poorer when using all polarizations ($Q = 0.3$). This can be related to the poor agreement between the three polarizations. Fig. 6.5 and 6.6 show that the retrieved parameters from the χ^2 fitting match the graphical solution given by the intersection between contours of mean σ^0. Ideally, all polarizations would intersect in a single point. For acquisition 5, the retrieved soil moisture is significantly different depending on which polarizations are used. Such mismatch is not only attributable to inaccuracy of the backscattering model, it can also come from systematic error on the radar measurements. These sources of error are investigated in more detail in the next paragraph. In summary the results with acquisition 5 show that meaningful information can be extracted from the goodness-of-fit, even though the σ_i are estimated from the data. This was made possible by first transforming the data so that the measurement error approximately follows a Gaussian distribution.

Error [dB]	$\delta\sigma^0_{vh}$	$\delta\sigma^0_{hh}$	$\delta\sigma^0_{vv}$
Acq 1	0.7688	-0.3392	-0.1235
Acq 2	0.2460	0.0512	0.1832

Table 6.3: Difference between radar measurements and backscattering simulations from the in situ measurements

Systematic errors While the χ^2 method requires zero-mean Gaussian errors, uncorrected systematic errors will propagate into systematic errors on the retrieved parameters. Systematic errors can affect both the model and the radar measurements.

Regarding the model, as mentioned in the literature review, there is no consensus on the use of correction factors as both under- and over-estimations are reported in different studies [69]. In these studies, the accuracy of the model was tested by comparing the radar measurements with backscattering simulation from in situ measurements of soil moisture and surface roughness. Table 6.3 reports the difference between measured and simulated backscatter coefficients for both acquisitions. These differences are relatively small and fall within the ± 1 dB radiometric accuracy of Radarsat-2 [60]. This error analysis takes the in situ measurements as reference values. This is disputable particularly regarding roughness characterization.

As for systematic errors coming from the radar, they are quantified by the specified radiometric accuracy of Radarsat-2 (< 1 dB). More precisely, it is the relative radiometric accuracy obtained by comparing the mean backscatter coefficients of two areas of a uniform distributed target which extends beyond the nominal image coverage, such as the Amazon rainforest [126, 60].

Alternatively, the overall systematic error affecting the retrieval of soil moisture and surface roughness could be estimated from the different combinations of polarizations, without the use of in situ measurements.

The drawings on Fig. 6.3 show the potential effects of systematic errors on the soil parameter retrieval. In the first case (Fig. 6.3a), systematic errors on each polarization compensate each other and lead to a single biased pair of soil parameters. In the second case (Fig. 6.3b), systematic errors lead to different pairs of soil parameters depending on which polarizations are combined. The black dots correspond to retrieval with only two polarizations and the gray dot corresponds to the retrieval with all polarizations. Since the true parameters (black triangle) are unknown, it is a priori not possible to state which combination of polarizations is the most accurate. Because each polarization is likely to produce different biases on the retrieved parameters, it is reasonable to assume that the most accurate retrieval corresponds to the case with combination of all polarizations. As shown by Fig. 6.4, the overall systematic error on each polarization can then be estimated from the difference between the σ^0 measurements and the simulated σ^0 from the soil parameters retrieved with all polarizations. Table 6.4 suggests that there is a positive systematic error on σ^0_{vh} and a negative systematic error on σ^0_{hh} and σ^0_{vv}.

Error [dB]	$\delta\sigma^0_{vh}$	$\delta\sigma^0_{hh}$	$\delta\sigma^0_{vv}$
Acq 1	0.7003	-0.3916	-0.2228
Acq 2	0.0740	-0.0476	-0.0392

Table 6.4: Difference between radar measurements and backscattering simulations from retrieved parameters with all polarizations

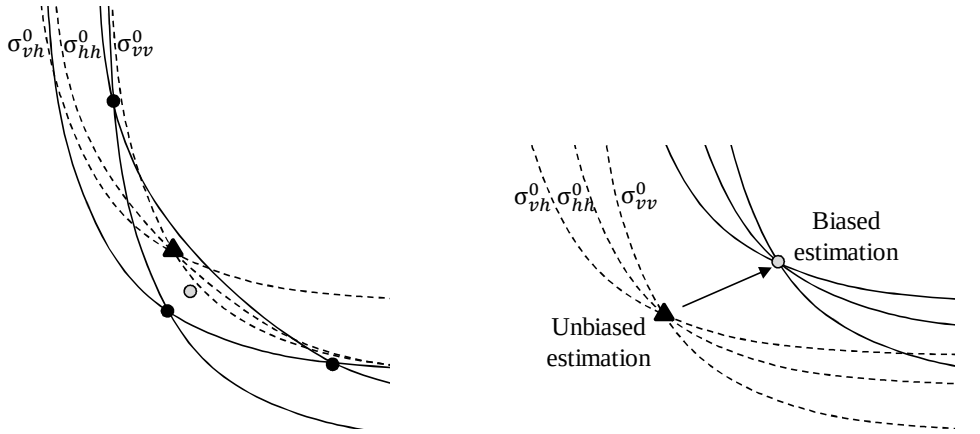

(a) Errors on each polarization will likely result in different parameter estimations depending on the selected polarizations

(b) Though unlikely, different biases on each polarization can still result in a single biased pair of soil parameters

Figure 6.3: Effect of systematic errors on the retrieved parameters. The black and gray dots correspond to the retrieval with respectively two polarizations. and all polarizations. The black triangle is the unknown true soil parameters

Note that because the analysis is limited to two acquisitions, the systematism of these errors is questionable. Such offsets could come from the poor characterization of the mean σ^0 for each polarization due to the limited number of looks. This can be quantified with the standard error on the mean σ^0. As explained in section 2.2.2, the L looks of a distributed target can be assumed to follow an exponential distribution $\mathcal{E}(\sigma^0)$ with σ^0 the underlying backscattering coefficient. The standard error on the estimated mean backscattering coefficient is then $\sigma^0/\sqrt{L}$. Because the exponential distribution has σ^0 for both mean and standard deviation, the relative standard error only depends on L. For $L = 1000$ pixels, $\delta\sigma^0 = \pm 0.1352$ dB which is of the same order of magnitude as the errors reported in table 6.4. Hence, in absence of other errors, statistical uncertainty alone could explain the discrepancies between retrieved parameters and in situ measurements.

All in all, this analysis shows that for an inversion scheme based on multi-polarized measurements, even systematic errors of about 0.5 dB can significantly bias the retrieved soil parameters.

Agreement with in situ measurements For both acquisitions, with the (hh, vv) and (vh, hh, vv) inversions, the retrieved parameters indicates that the RMS height

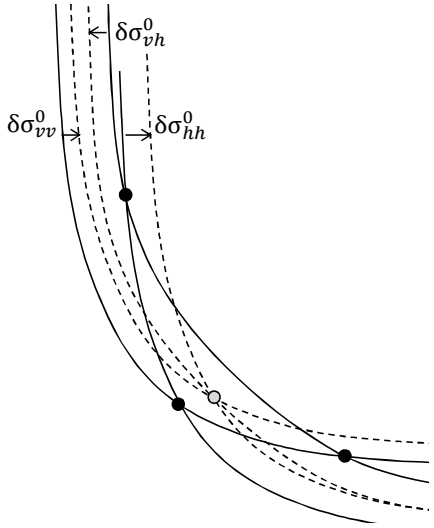

Figure 6.4: Estimation of systematic errors on each polarization

remains constant around 9 mm, and the soil moisture increases from $0.21\,\mathrm{m}^3/\mathrm{m}^3$ to $0.25\,\mathrm{m}^3/\mathrm{m}^3$. This is in close agreement with the in situ measurements. The (vh, hh) and (vh, vv) inversions lead to larger mismatch, especially for acquisition 5 with unphysical results in the (vh, hh) case. Unphysical answers can be returned by the χ^2 because this method supposes a non-informative prior, *i.e.* m_v and s can a priori take any values. Assuming that the in situ measurements are close to the true soil parameters, such a comparison suggests that the retrievals with (hh, vv) and (vh, hh, vv) measurements are accurate, with an overall RMS error of $0.04\,\mathrm{m}^3/\mathrm{m}^3$ on soil moisture and 18% on RMS height.

Uncertainty from Monte Carlo simulation Uncertainty is investigated from the extent of the point clouds on Fig. 6.5 and 6.6 and the size of the confidence intervals AA' and BB'.

First it is worth mentioning that the 68.3% confidence ellipses are adapted for point clouds which follow a bi-variate Gaussian distribution. This is clearly not the case with the (vh, hh) and (vh, vv) inversions for which the point cloud has a banana shape due to the nonlinear backscattering model. For the (hh, vv) and (vh, hh, vv) inversions, the elliptical shape is more applicable because the uncertainty in moisture and roughness remains in a region where the nonlinear model could reasonably be linearized [101]. It is apparent that the retrieval from either (vh, hh) or (vh, vv) leads to the most uncertain estimations. In both cases the point cloud covers nearly the entire range of physically-possible values for soil moisture or roughness, shrinking the extent of the point cloud would require using more looks.

Note that while symmetrical confidence intervals are reported in table 6.5, the RMS height uncertainty on figure 6.5b is clearly asymmetrical. Overestimations of RMS height are much larger than underestimations. Ultimately this does not affect the end result which is that the estimation is very uncertain. In comparison, using (hh, vv) or (vh, hh, vv) leads to point clouds noticeably smaller with uncertainty of about $\pm 0.04\,\mathrm{m}^3/\mathrm{m}^3$ on soil moisture and less than 10% on RMS height which

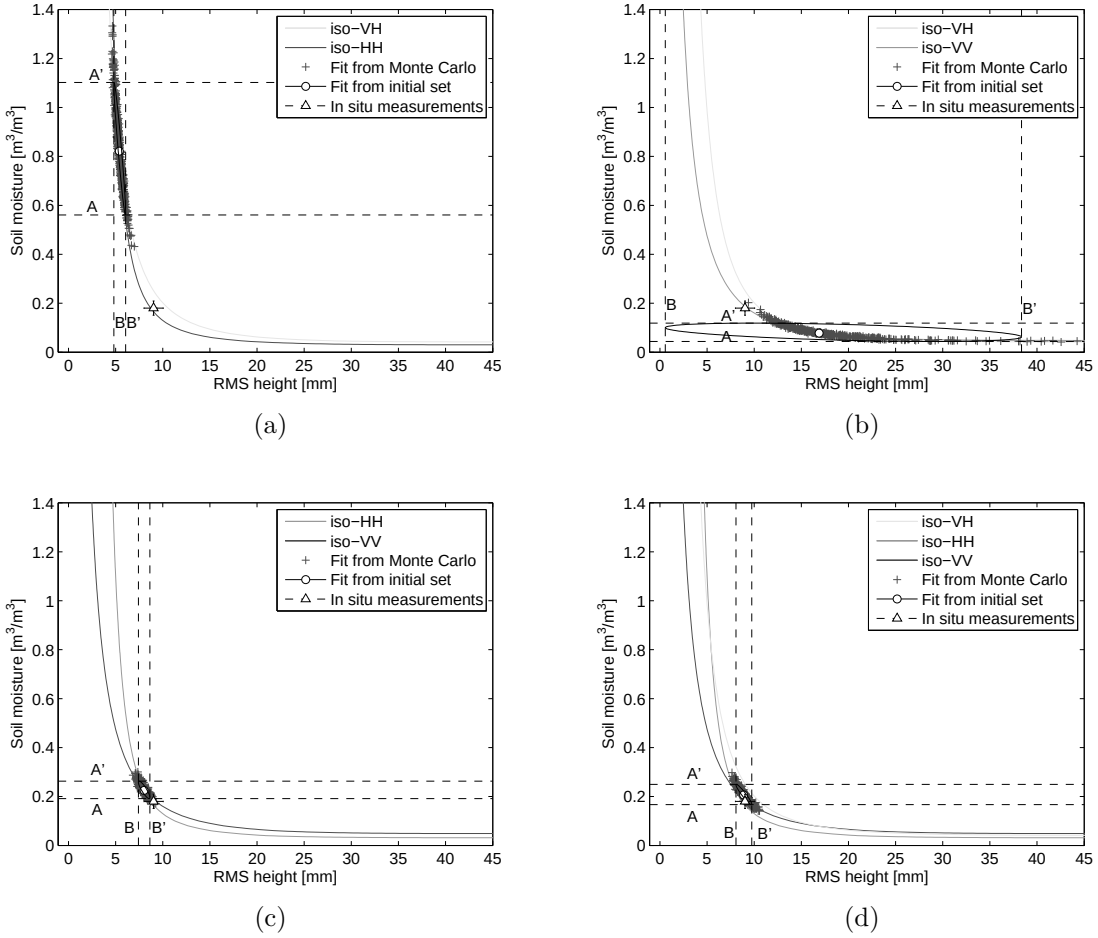

Figure 6.5: Soil moisture and RMS height retrieval with (a) *vh*- and *hh*-measurements, (b) *vh*- and *vv*-measurements, (c) *hh*- and *vv*-measurements, and (d) *hh*-, *vv*- and *hh*-measurements, on the 25 November 2013 (acquisition 5).

match the uncertainty requirements defined in section 6.28. The improvement in uncertainty between the (*vh*, *hh*), (*vh*, *vv*) and (*hh*, *vv*) cases is in agreement with the study from Kweon *et al.* who assessed the parameters error against in situ measurements, with direct inversion of the Oh model [90].

In theory, any added information, even poor information, should improve the final result as long as measurement error is properly accounted for. This is verified with acquisition 6 for which there is a slight improvement in uncertainty between the (*hh*, *vv*) and the (*vh*, *hh*, *vv*) cases. However for acquisition 5, Fig. 6.5 shows that uncorrected systematic errors bias the retrieval toward regions of parameter space where either soil moisture is very uncertain (Fig. 6.5a) or RMS height is very uncertain (Fig. 6.5b). This explains why the (*vh*, *hh*, *vv*) case can be more uncertain than the (*hh*, *vv*) case.

In the next section, the χ^2 method is more broadly applied to other fields and other acquisitions

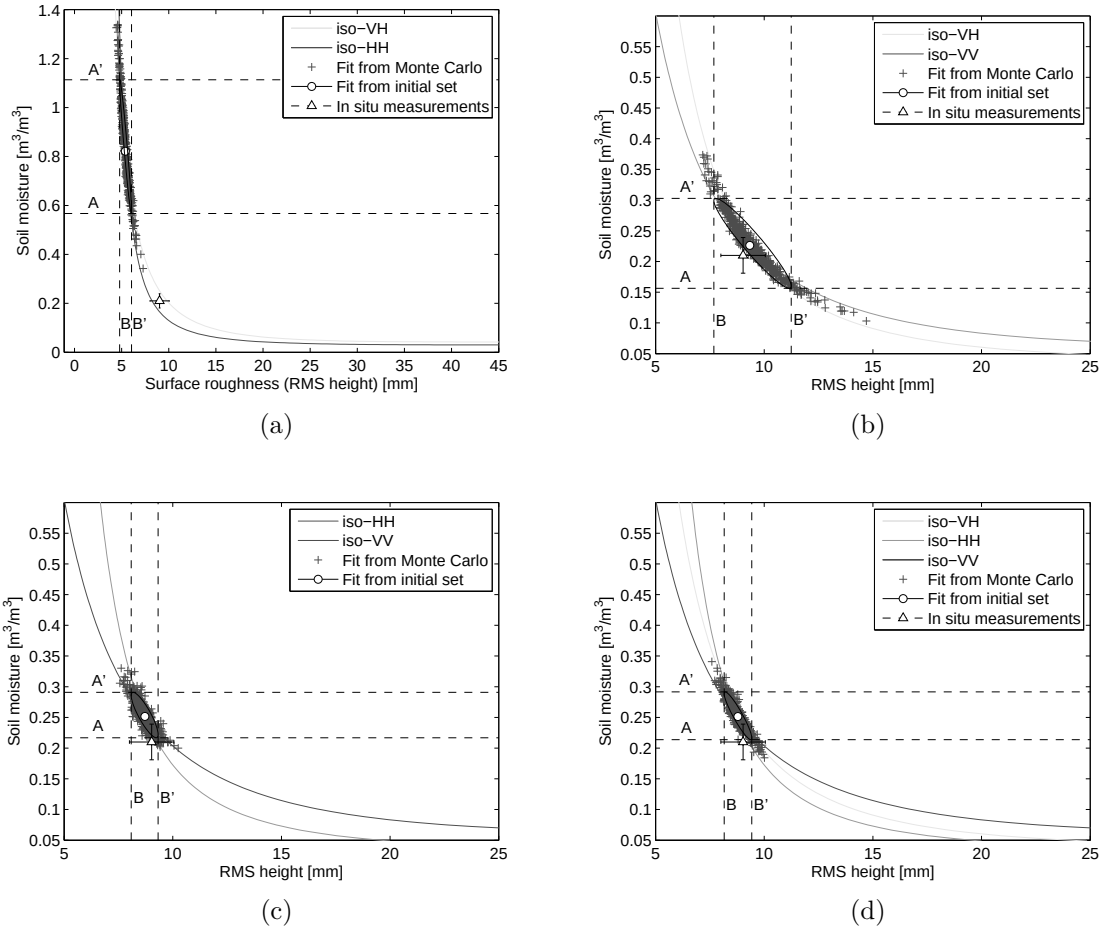

Figure 6.6: Soil moisture and roughness retrieval with (a) *vh*- and *hh*-measurements, (b) *vh*- and *vv*-measurements, (c) *hh*- and *vv*-measurements, and (d) *hh*-, *vv*- and *hh*-measurements, on the 5 December 2013 (acquisition 6).

	vh hh	*vh vv*	*hh vv*	*vh hh vv*
m_v [m^3/m^3]	0.821	0.078	0.225	0.207
s [mm]	5.4	16.9	8.0	8.9
Q	0.49	0.48	0.47	0.34
$AA'/2$[m^3/m^3]	0.271	0.038	0.036	0.041
$BB'/2$[%]	11.6	111.8	7.6	9.4
$m_v - m_{v,in\,situ}$	0.646	-0.102	0.045	0.027
$s - s_{in\,situ}$%	40.0	87.8	11.1	1.1

(a)

	vh hh	*vh vv*	*hh vv*	*vh hh vv*
Retrieved m_v [m^3/m^3]	0.296	0.226	0.252	0.252
Retrieved s [mm]	8.3	9.3	8.7	8.8
Q	0.51	0.52	0.52	0.53
$AA'/2$[m^3/m^3]	0.123	0.078	0.038	0.037
$BB'/2$[%]	19.3	17.4	7.4	6.8
$m_v - m_{v,in\,situ}$	0.610	0.016	0.042	0.042
$s - s_{in\,situ}$ %	7.8	3.3	3.3	2.2

(b)

Table 6.5: Performance of the retrieval for different combinations of polarizations, for (a) acquisition 5, (b) acquisition 6

6.1.2.2 Retrieval for fields 6, 8, 9, 12 and 13

Tables 6.6-6.15 show the retrieved parameters for fields 6, 8, 9, 12 and 13 when using (vh, hh, vv) measurements and (hh, vv) measurements. All in all the goodness-of-fit is better for the (hh, vv) case than for the (vh, hh, vv) case. Low Q values are obtained when the vh-measurements contradict the output obtained with only the $hh-$ and $vv-$measurements. This is visible from the intersection of contours of σ^0_{vh}, σ^0_{hh}, and σ^0_{vv}. The lowest Q values are obtained when the σ^0_{vh} contour has no intersections with the σ^0_{hh} and σ^0_{vv} contours.

In comparison, the σ^0_{hh} and σ^0_{vv} contours intersect for all acquisitions which is why the goodness-of-fit is often better in the dual-polarization case. Note that even with dual-polarization, slightly lower Q values are obtained when the intersection corresponds to σ^0_{hh} and σ^0_{vv} contours nearly parallel (e.g. for large RMS height).

Field 6 Throughout the campaign, field 6 had a very light vegetation cover, and the soil surface was only rolled. From the SfM measurements, the RMS height is close to 8.9 mm which is a typical value for rolled surface [127]. And Fig. 6.7a shows that soil moisture remained around 0.30-0.35 m^3/m^3. Even with the (hh, vv) inversion which leads to the most realistic parameters, there is still a poor agreement with the in situ measurements. Soil moisture is systematically underestimated (Fig. 6.7a) and RMS height is systematically overestimated .

Field 8 Field 8 has the same levels of soil moisture and the same surface preparation (rolled surface) than field 6. Again, for every acquisition, soil moisture is underestimated and surface roughness is overestimated (Fig. 6.7b).

Field 9 Field 9 has a deep ploughed soil surface. The in situ roughness measurements indicate that s is close to 18 mm. Even though most of the retrieved values for the RMS height are unrealistically large (except for the 5 December, $s = 21.6$ mm), they are larger than the values obtained for fields 6 and 8. Therefore the retrieved values do reflect the larger RMS height. As for the retrieved soil moisture, there is still an overall underestimation but the variations are in agreement with the in situ measurements (Fig. 6.7c).

The fact that changes in the retrieved parameters seem to be detected, supports the assumption that soil surface was deep ploughed even on the dates for which no SfM measurements are not available, i.e. before the 25 November (table 6.1).

Field 12 Field 12 is of particular interest because the soil surface changed from rolled to ploughed on the 12 December. The SfM measurements shows that the RMS height changed from $s = 9.0 \pm 1.0$ mm to $s = 26.8 \pm 0.8$ mm (table 6.1). The retrieved RMS height for the(hh, vv) inversion reflects the increase in roughness and is also very close to the in situ measurements for every acquisition. Retrieved soil moisture is also is good agreement with the in situ measurements (Fig. 6.7d). In particular the decrease in m_v on the 12 December is detected.

Field 13 The retrieved RMS height for field 13 is unrealistically large except on the 11 November. Retrieved soil moisture values are high compared to the values obtained for the other fields. Even though in situ measurements are only available for the last 3 dates, these high retrieved values of soil moisture are coherent with the weather conditions. And correct variations in soil moisture are detected for the last 3 dates (Fig. 6.7e).

For most of the inversions, the retrieved parameters do not compare well with their in situ measurements. The fact that soil moisture is systematically underestimated indicates that the mismatch does not originate from statistical uncertainty due to the limited number of pixels. More likely, it comes from inaccuracies in the backscattering model.

Fig. 6.9 shows the difference between measurements of σ^0_{vh}, σ^0_{hh}, σ^0_{vv}, p, and q, and their simulated values from in situ measurements of soil moisture and RMS height. Overall, the model underestimates σ^0_{vh}, p, and q, and it overestimates σ^0_{hh} and σ^0_{vv}. Looking only at σ^0_{vh}, p, and q, it seems that the worst mismatches occur for wet soils. An obvious reason for this is that soil moisture goes beyond the range of validity of the Oh model ($m_{v,max} = 0.291\,\mathrm{m}^3/\mathrm{m}^3$). Fields 6 and 8 which are very wet, exhibits the largest mismatches. And the model for q seems to be the most erroneous (see table 6.16). Unfortunately the expression for q is used to express the model for σ^0_{hh} and σ^0_{vv}. This may explain why the contours of σ^0_{vh} tend to disagree with those of σ^0_{hh} and σ^0_{vv} when retrieving soil moisture with all polarizations.

While so far the analysis relies on in situ measurements, it is further supported by table 6.17 which reports by how much each of the quantities σ^0_{vh}, p, and q exceed their maximum value allowed by the Oh model. Note that none of the measurements falls below their minimum allowed value. The upper limits $\sigma^0_{vh,max}$ ($m_v = 0.291$, $s = 61.7\,\mathrm{mm}$), p_{max} ($m_v = 0.04$, $s = 61.7\,\mathrm{mm}$), and q_{max} ($s = 61.7\,\mathrm{mm}$) are different for each acquisition according to the incidence angle. It is apparent that σ^0_{vh} (blue) seldom falls outside its range of validity. In comparison, q is almost systematically larger than q_{max}, and p is occasionally larger than p_{max}. Large values for q are usually attributed to vegetated soil [80], as depolarization from vegetation leads to large values of σ^0_{vh}. However here, fields 9, 12 and 13 which are perfectly bare also have large q values.

Part of the mismatch may also be due to bias in Radarsat-2 measurements. As mentioned in section 6.1.1, over some fields σ^0_{hh} is larger than σ^0_{vv} which is in theory not possible. Measurement bias may not be negligible particularly when computing the co-polarized and cross-polarized ratios.

The data set under study does not allow identifying an exact cause for the rather poor estimation of the soil parameters. All in all, it seems that poor inversions originate more from the Oh backscattering model than from bias on Radarsat-2 measurements. Indeed inversions of measurements for which $\sigma^0_{hh} > \sigma^0_{vv}$ are guaranteed to fail, but even when the measurements verify $\sigma^0_{hh} < \sigma^0_{vv}$, the agreement between retrieved parameters and in situ measurements can still be poor. Failure from the model can sometimes be explained by the fact that the soil is wetter than the maxi-

	18/10	**25/10**	**01/11**	**11/11**	**25/11**	**05/12**	**12/12**	**19/12**
Retrieved m_v [m^3/m^3]	0.205	0.096	0.107	0.126	0.085	0.074	0.067	0.084
Retrieved s [mm]	14.0	140.7	150.2	135.7	32.7	40.9	135.7	141.4
Q	0.35	0.10	0.08	0.07	0.40	0.13	0.04	0.22
$AA'/2[m^3/m^3]$	0.054	0.007	0.008	0.008	0.078	0.060	0.005	0.005
$BB'/2[\%]$	2.76	17391	60.2	495.8	384.1	148.8	30.0	498.6
L	705	450	646	429	494	456	483	598

Table 6.6: Field 6, retrieval with (vh, hh, vv) measurements

	18/10	**25/10**	**01/11**	**11/11**	**25/11**	**05/12**	**12/12**	**19/12**
Retrieved m_v [m^3/m^3]	0.196	0.108	0.110	0.102	0.182	0.142	0.054	0.087
Retrieved s [mm]	13.2	20.0	22.7	113.5	13.4	14.6	37.3	21.9
Q	0.55	0.48	0.49	0.41	0.50	0.48	0.48	0.50
$AA'/2[m^3/m^3]$	0.046	0.049	0.038	0.009	0.059	0.051	0.011	0.039
$BB'/2[\%]$	2.0	42.4	38.9	14.3	3.5	6.9	44.4	48.6
L	705	450	646	429	494	456	483	598

Table 6.7: Field 6, retrieval with (hh, vv) measurements

mum soil moisture allowed by the Oh model. In other cases, even with soil moisture below the maximum limit the retrieved parameters can be far from their in situ measurements. Within the model, the cross-polarized ratio q seems to be the least accurate, this is very damaging for the retrieval as the model for q is used to express σ^0_{hh} and σ^0_{vv}. This is in agreement with the relatively large RMS error of 2.06 dB reported by Oh *et al.* for the data-fitting of q (see table 2.3). Finally, it should be noted that besides a few exceptions, good retrievals usually corresponded to the driest soil condition with smooth soil surface. In this configuration, the intersection between the contours of σ^0_{vh}, σ^0_{hh} andσ^0_{vv} is more robust to inaccuracies in the model and in the measurements.

From the above analysis, it seems that in order to improve soil moisture estimation, the focus should be on improving the backscattering model.

While this section mainly discussed the validity of the Oh model, the next section focuses on uncertainty in the retrieved parameters due to speckle on the radar measurements.

	18/10	**25/10**	**01/11**	**11/11**	**25/11**	**05/12**	**12/12**	**19/12**
Retrieved m_v [m^3/m^3]	0.174	0.083	0.084	0.108	0.056	0.059	0.053	0.069
Retrieved s [mm]	14.0	116.0	142.4	145.3	134.4	137.6	143.5	142.6
Q	0.45	0.18	0.07	0.02	0.37	0.27	0.01	0.09
$AA'/2[m^3/m^3]$	0.031	0.004	0.004	0.004	0.003	0.006	0.003	0.003
$BB'/2[\%]$	1.5	17.9	1355.2	10.7	47.9	31.5	11.5	15.6
L	1344	1008	1320	1504	1395	1102	1122	1584

Table 6.8: Field 8, retrieval with (vh, hh, vv) measurements

	18/10	**25/10**	**01/11**	**11/11**	**25/11**	**05/12**	**12/12**	**19/12**
Retrieved m_v [m^3/m^3]	0.174	0.131	0.070	0.088	0.087	0.068	0.042	0.130
Retrieved s [mm]	13.5	16.0	113.2	111.7	17.0	21.6	65.9	14.2
Q	0.48	0.51	0.43	0.34	0.47	0.52	0.46	0.46
$AA'/2$[m^3/m^3]	0.029	0.040	0.010	0.005	0.027	0.023	0.006	0.030
$BB'/2$[%]	1.33	9.6	46.7	5.7	6.6	35.0	51.6	2.2
L	1344	1008	1320	1504	1395	1102	1122	1584

Table 6.9: Field 8, retrieval with (hh, vv) measurements

	18/10	**25/10**	**01/11**	**11/11**	**25/11**	**05/12**	**12/12**	**19/12**
Retrieved m_v [m^3/m^3]	0.137	0.1534	0.152	0.188	0.109	0.114	0.061	0.198
Retrieved s [mm]	96.6	7777.2	198.2	295.3	140.3	23.0	135.0	19.2
Q	0.46	0.09	0.38	0.20	0.35	0.46	0.05	0.37
$AA'/2$[m^3/m^3]	0.012	0.012	0.030	0.012	0.008	0.041	0.005	0.0759
$BB'/2$[%]	71.0	15711	12855.0	224.5	30423.0	53.3	22.0	65281.0
L	450	481	512	696	560	527	476	522

Table 6.10: Field 9, retrieval with (vh, hh, vv) measurements

	18/10	**25/10**	**01/11**	**11/11**	**25/11**	**05/12**	**12/12**	**19/12**
Retrieved m_v [m^3/m^3]	0.132	0.115	0.234	0.160	0.094	0.116	0.047	0.198
Retrieved s [mm]	91.9	101.7	17.0	96.1	48.1	21.6	33.7	17.7
Q	0.46	0.46	0.47	0.46	0.49	0.45	0.49	0.43
$AA'/2$[m^3/m^3]	0.013	0.021	0.115	0.014	0.025	0.040	0.011	0.060
$BB'/2$[%]	48.9	919.6	32.2	59.0	56.0	29.4	357.5	22.0
L	450	481	512	696	560	527	476	522

Table 6.11: Field 9, retrieval with (hh, vv) measurements

	18/10	**25/10**	**01/11**	**11/11**	**25/11**	**05/12**	**12/12**	**19/12**
Retrieved m_v [m^3/m^3]	0.142	0.063	0.066	0.208	0.207	0.252	0.054	0.143
Retrieved s [mm]	14.2	140.4	141.4	13.5	8.9	8.8	142.9	155.2
Q	0.42	0.05	0.12	0.07	0.34	0.53	0.01	0.04
$AA'/2$[m^3/m^3]	0.034	0.004	0.003	0.039	0.041	0.037	0.003	0.007
$BB'/2$[%]	14.3	30.5	9.6	1.5	9.4	6.8	17.2	49944.0
L	1395	936	1360	1768	1029	1015	928	1416

Table 6.12: Field 12, retrieval with (vh, hh, vv) measurements

	18/10	**25/10**	**01/11**	**11/11**	**25/11**	**05/12**	**12/12**	**19/12**
Retrieved m_v [m^3/m^3]	0.201	0.171	0.119	0.208	0.225	0.252	0.046	0.126
Retrieved s [mm]	10.6	10.6	14.6	12.1	8.0	8.7	28.4	29.4
Q	0.48	0.50	0.49	0.51	0.47	0.52	0.48	0.53
$AA'/2$[m^3/m^3]	0.055	0.063	0.030	0.031	0.036	0.038	0.013	0.023
$BB'/2$[%]	1.5	2.5	2.9	1.1	7.6	7.4	34.8	46.8
L	1395	936	1360	1768	1029	1015	928	1416

Table 6.13: Field 12, retrieval with (hh, vv) measurements

	18/10	**25/10**	**01/11**	**11/11**	**25/11**	**05/12**	**12/12**	**19/12**
Retrieved m_v [m^3/m^3]	0.251	0.324	0.257	0.367	0.231	0.1326	0.061	0.221
Retrieved s [mm]	121.9	149.1	129.3	31.8	363.1	87.9	131.1	307.5
Q	0.47	0.37	0.42	0.22	0.50	0.42	0.30	0.47
$AA'/2$[m^3/m^3]	0.014	0.024	0.0161	0.038	0.020	0.008	0.005	0.019
$BB'/2$[%]	17115	17832	34155	174100	62635	427.9	41.5	55808
L	851	459	700	1023	616	667	560	486

Table 6.14: Field 13, retrieval with (vh, hh, vv) measurements

	18/10	**25/10**	**01/11**	**11/11**	**25/11**	**05/12**	**12/12**	**19/12**
Retrieved m_v [m^3/m^3]	0.252	0.292	0.232	0.301	0.235	0.140	0.054	0.214
Retrieved s [mm]	129.6	111.3	236.3	44.5	45491.9	98.2	82.1	127.5
Q	0.46	0.45	0.50	0.48	0.50	0.44	0.47	0.46
$AA'/2$[m^3/m^3]	0.018	0.030	0.020	0.027	0.025	0.011	0.06	0.023
$BB'/2$[%]	9664.8	8268.7	7521.7	23276	16524	15.5	116.5	3853.9
L	851	459	700	1023	616	667	560	486

Table 6.15: Field 13, retrieval with (hh, vv) measurements

$\overline{\Delta\sigma^0_{vh}}$	$\overline{\Delta\sigma^0_{hh}}$	$\overline{\Delta\sigma^0_{vv}}$	$\overline{\Delta p}$	$\overline{\Delta q}$
1.59 dB	1.12 dB	0.99 dB	1.11 dB	2.35 dB

Table 6.16: Mean difference between radar measurements and simulations from the in situ measurements, over all fields and all acquisition dates

	Field				
Acquisition	**6**	**8**	**9**	**12**	**13**
1	0.63	-	0.53, 0.43	0.11	0.18, 0.43
2	2.18	1.45	3.99, 0.99	1.98	1.27, 0.64, 0.86
3	2.12	1.89, 0.08	1.37	1.36	1.07, 0.33, 0.13
4	2.60, 0.66	2.46, 0.88	1.92, 0.42	0.95	1.43, 1.44
5	0.51	0.63	1.18, 0.01	-	0.12
6	0.92	1.26	0.07	-	0.52
7	2.59, 0.25	2.85, 0.22	2.94, 0.33	2.59, 0.12	1.57, 0.40
8	1.36	1.40	0.53	2.03	0.39, 0.11

Table 6.17: Measurements outside their range of validity. Black is $\delta q = q - q_{max}$, red is $\delta p = p - p_{max}$, and blue is $\delta\sigma^0_{vh} = \sigma^0_{vh} - \sigma^0_{vh,max}$. All values are in decibels.

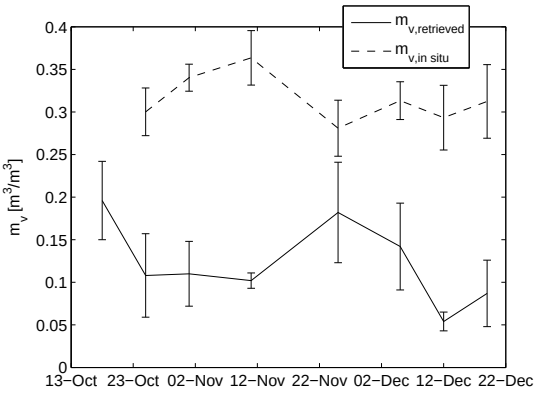

(a) Field 6

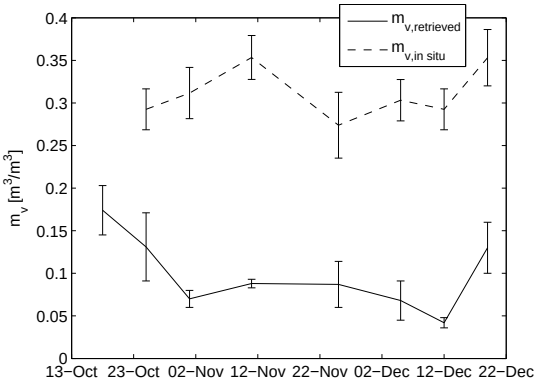

(b) Field 8

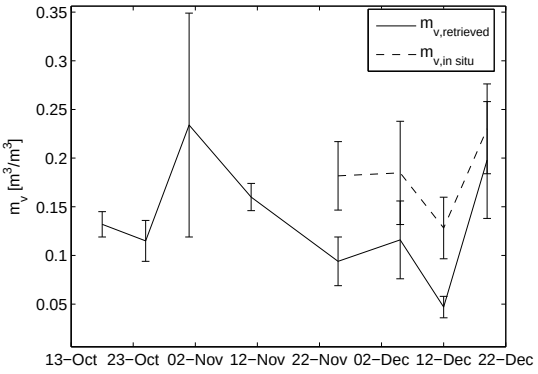

(c) Field 9

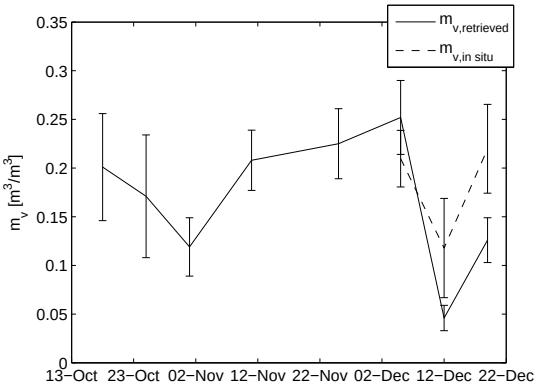

(d) Field 12

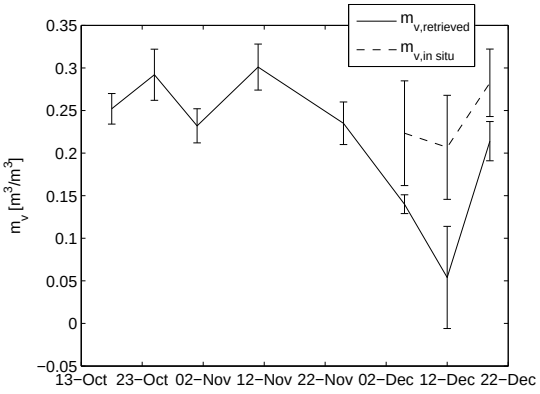

(e) Field 13

Figure 6.7: Comparison between retrieved soil moisture and in situ measurements. The error bar for the retrieved m_v is extracted from the confidence ellipse, for the in situ measurements it is the standard deviation computed from the multiple sampling points.

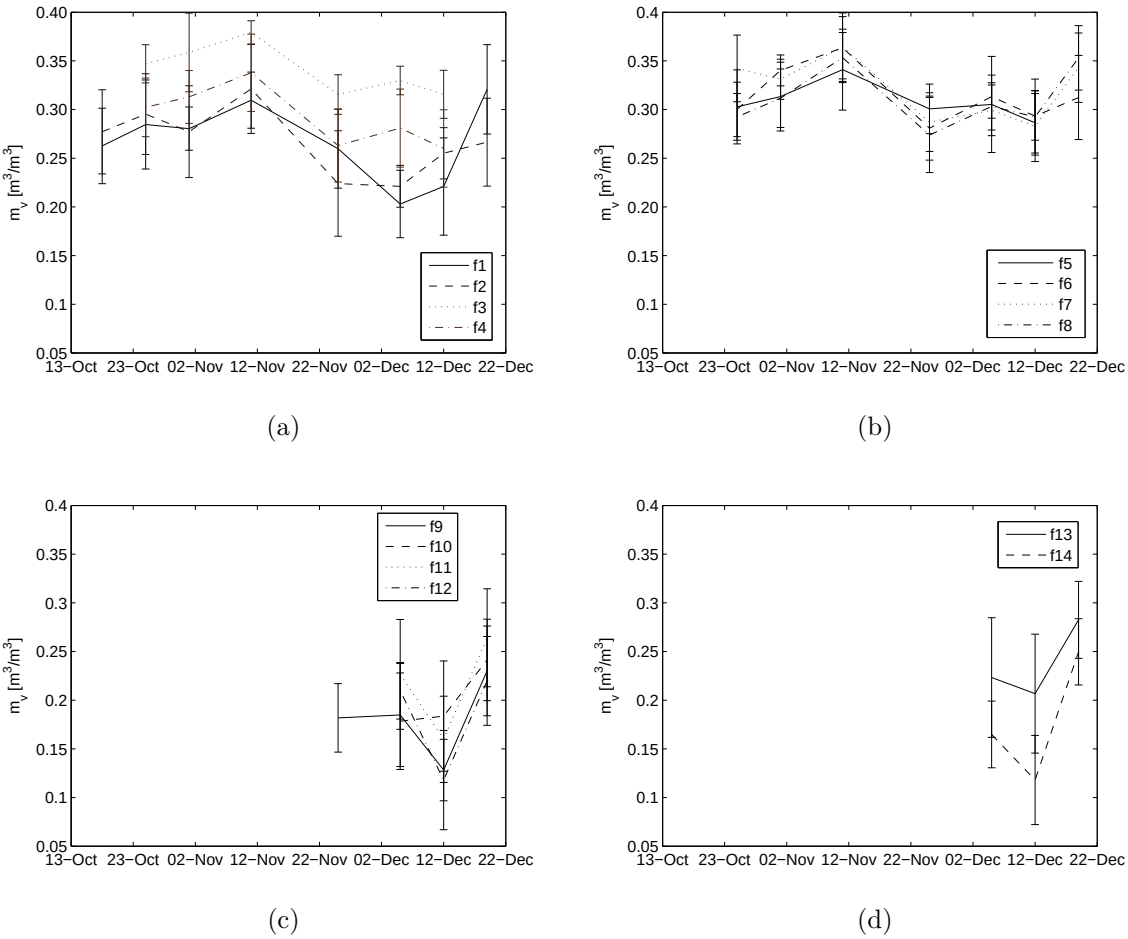

Figure 6.8: In situ measurements of soil moisture for all sampled fields

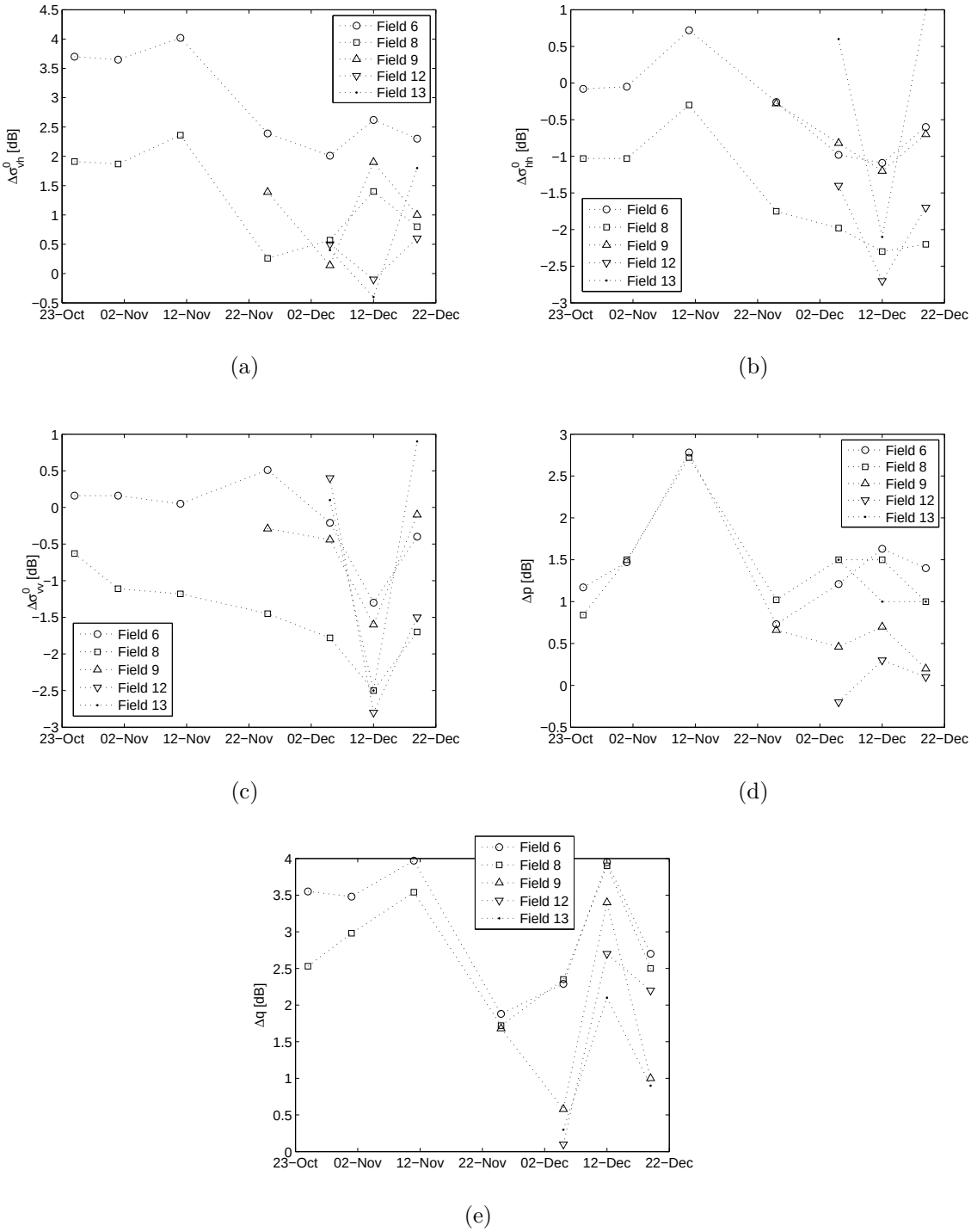

Figure 6.9: Difference between radar measurements and simulations from in situ measurements of soil moisture and RMS height

6.1.3 Speckle and parameters uncertainty

This section relies on simulations of backscattering coefficients affected by speckle to investigate how many looks are required to reach a given uncertainty on the estimated soil moisture and surface roughness. All the simulations are done with the Oh backscattering model at C-band, with a moderate incidence angle of 24°. The only source of noise accounted for is speckle. First, a map of contours of $vh-$, $hh-$, and $vv-$polarizations is analyzed to highlight the different aspects which dictate how uncertainty in the measurements propagates into final uncertainty on the estimated parameters. Then from extensive simulations for a range of soil moisture and RMS height, uncertainty requirements are transformed into a required number of looks.

6.1.3.1 Parameters affecting the propagation of uncertainty

Fig. 6.10 shows bands of $vh-$, $hh-$, $vv-$contours for five scenarios of surface roughness and soil moisture. For each scenario and each polarization, 50 samples of σ^0 are simulated with additive zero-mean Gaussian noise with arbitrary standard deviation of 0.05 dB. These 50 simulations leads to bands of contours.

From Fig. 6.10, two aspects affecting inversion uncertainty can be highlighted: (1) the sensitivity of each polarization to soil moisture and surface roughness, (2) the intersections between contours. The former is related to polarizations taken individually, while the latter is related to how the different polarizations complement each other.

The sensitivity of each polarization to the soil parameters can be analyzed from the differential of σ^0 as a function of surface roughness and soil moisture,

$$\mathrm{d}\sigma^0\,(s,\,m_v) = \frac{\partial\sigma^0}{\partial s}\mathrm{d}s + \frac{\partial\sigma^0}{\partial m_v}\mathrm{d}m_v \tag{6.1}$$

For example in the case of low RMS height and high soil moisture the contours on Fig. 6.10 are nearly vertical. This corresponds to a low sensitivity in soil moisture compared to the sensitivity in RMS height, *i.e.* $\frac{\partial\sigma^0}{\partial s} \gg \frac{\partial\sigma^0}{\partial m_v}$, so that in that region the differential of σ^0 can be simplified into

$$\mathrm{d}\sigma^0\,(s) \approx \frac{\partial\sigma^0}{\partial s}\mathrm{d}s \tag{6.2}$$

All contours verify $\mathrm{d}\sigma^0_{pq} = 0$, which leads to $\mathrm{d}s = 0$, *i.e.* contours with constant RMS height. Note that neglecting $\frac{\partial\sigma^0}{\partial m_v}$ does not necessarily mean that σ^0 is highly sensitive to s. The direction of the contours only gives information on the amplitude of $\frac{\partial\sigma^0}{\partial s}$ compared to the amplitude of $\frac{\partial\sigma^0}{\partial m_v}$ and vice versa.

The actual sensitivity of σ^0 to s can be inferred from the effect of added Gaussian noise, *i.e.* the thickness of a given band of contours. In the region of low RMS height ($s \approx 5\,\mathrm{mm}$) and high soil moisture ($m_v \approx 0.3\,\mathrm{m^3/m^3}$), the reduced thickness of each band means that a given error $\delta\sigma^0$ leads to a small error δs. While for rougher soils ($s \approx 10\,\mathrm{mm}$), the same measurement error leads to a larger δs (thicker bands). From

the approximation $\delta\sigma^0 \approx \frac{\partial\sigma^0}{\partial s}\delta s$, it can be derived that σ^0 is highly sensitive to s for smooth soils, and poorly sensitive to s for rough soils. Following the same reasoning, table 6.18 gives qualitative information regarding the sensitivity of σ^0 for different soil configurations. In particular for wet and rough soils, the retrieval of soil moisture and surface roughness will not be robust to measurement noise because of the poor sensitivity of σ^0 to both parameters. This region was also identified by Lievens *et al.* who simulated soil moisture estimation with the IEM and noisy synthetic roughness measurements [13]. It is also worth noting that Tansey *et al.* reported that in the region of low RMS height, σ^0 is highly sensitive to s, and that therefore it may not be possible to retrieve soil moisture with imperfect in situ measurements of s [128]. Here because s is a parameter to retrieve, having radar measurements highly sensitive to s is actually a positive point.

The second point, *intersection between contours*, indicates how the different polarizations complete each other to solve the inverse problem. For example in the region with low RMS height and high soil moisture, all the polarizations tend to vertical contours as they are mainly sensitive to RMS height. It follows that even a small amount of noise on the measurements will lead to very different intersections between the nearly parallel contours along the soil moisture direction. Ideally robust estimations would be obtained when the intersection between contours is nearly perpendicular.

The diagram on Fig. 6.11 shows two typical configurations with two polarizations which would lead to perpendicular intersection of contours. In practice, such configurations never happen because the three polarizations have similar dependencies to soil moisture and surface roughness which is also why no distinction on the polarization was made in table 6.18.

In the end, the configurations which may require the greatest number of looks to reach acceptable uncertainty correspond to regions where the three polarizations have both poor sensitivity to the soil parameters and similar dependency on these parameters. Therefore achieving reliable soil moisture estimation will be demanding in the region of high soil moisture. Likewise, reliable RMS height estimation will be demanding for rough soil surfaces.

A third aspect is not highlighted on Fig. 6.10. The same amount of Gaussian noise was applied to the five scenarios in order to highlight the effect of a fixed amount of measurement noise on the retrieved parameters. In practice, the speckle of the radar measurements can be considered as a multiplicative noise (Eq. 2.27). Therefore high soil moisture and RMS height, which lead to the strongest soil response, also lead to the strongest speckle. This point will make the already challenging rough/wet soils even more challenging.

In summary, for a retrieval scheme based on the combination of different polarizations, parameter uncertainty is dictated by three aspects:

1. speckle strength: the variance of speckle is larger for soils with a strong radar

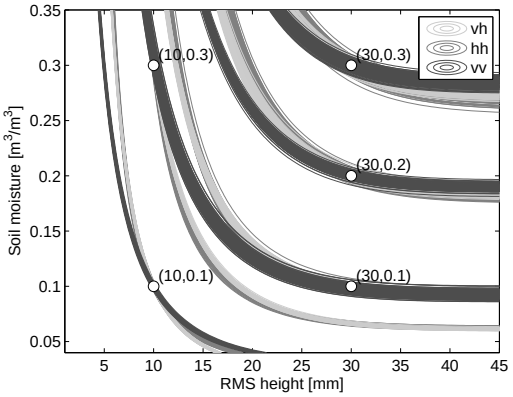

Figure 6.10: Bands of contours for different pairs of RMS height and soil moisture. The thickness of a band corresponds to Gaussian measurement error with a 0.05 dB standard deviation.

response, *i.e.* wet and rough soil,

2. sensitivity of the measurements to the parameters: high sensitivity to the parameters lead to better robustness to measurement noise,

3. complementarity of the different polarizations: to isolate soil moisture from RMS height, the measurements must ideally include either quantities mainly sensitive to soil moisture and quantities mainly sensitive to RMS height, or quantities with similar sensitivity in both parameters but of opposed signs.

More formally, these points can be related to two quantities characteristic of any inverse problem.

Measurement noise (speckle) and sensitivity of the measurements to the parameters are embedded in the Fisher information matrix. In the Gaussian linear case, the Fisher information matrix is the inverse of the covariance matrix of the estimated parameters $\mathbf{\Sigma}$ [25],

$$\mathbf{\Sigma}^{-1} = \mathbf{J}^T \mathbf{\Sigma}_m^{-1} \mathbf{J} \tag{6.3}$$

with $\mathbf{J}$ the jacobian of the backscattering model, and $\mathbf{\Sigma}_m$ the covariance matrix of the measurement errors. $\mathbf{J}$ gives the sensitivity of the measurements to the parameters and $\mathbf{\Sigma}_m$ contains the variances due to speckle. Large sensitivities and small measurement errors lead to a large information matrix, *i.e.* a small covariance matrix of the estimated parameters $\mathbf{\Sigma}$.

Finally, complementarity of the polarizations is related to the phenomenon called *ill-conditioning* [25]. When two contours intersect but their tangents at the intersection point are nearly parallel, then the jacobian at the intersection is nearly rank deficient. In this case, noise on the measurements, or numerical rounding errors can significantly compromise the inversion. The scenarios on Fig. 6.11 correspond to a jacobian far from being rank deficient.

Soil configuration		$\frac{\partial \sigma^0_{pq}}{\partial s}$	$\frac{\partial \sigma^0_{pq}}{\partial m_v}$
s	m_v		
Low	Low	Large	Large
High	Low	Negligible	Medium
Low	High	Large	Negligible
High	High	Small	Small

Table 6.18: Sensitivity of backscatter coefficient to s and m_v for different soil conditions

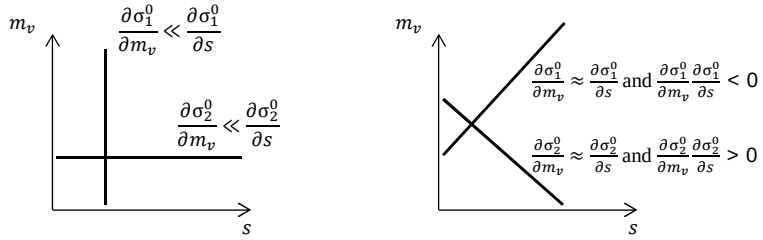

Figure 6.11: Typical configurations with perpendicular intersection of contours for a dual-polarization case

6.1.3.2 Uncertainty against number of looks

In this section, uncertainty in soil moisture and surface roughness is computed for an increasing number of looks. The backscatter coefficients σ^0_{vh}, σ^0_{hh}, and σ^0_{vv} are simulated for four scenarios of moisture and roughness (table 6.19). For each scenario, k Monte Carlo simulations are computed. Fig. 6.12 summarizes the processing steps of a simulation. First, L samples are drawn from the exponential distributions $\mathcal{E}(\sigma^0_{vh})$, $\mathcal{E}(\sigma^0_{hh})$ and $\mathcal{E}(\sigma^0_{vv})$. Each data set is made approximately Gaussian by applying the power transform. The transformed data sets are then used to retrieve m_v and s through χ^2 fitting. The parameter L is successively set to the following values $\{10^2, 10^3, 10^4, 10^5\}$. Compared to the case $L = 10^5$ looks, for $L = 10^2$ looks, numerous Monte Carlo simulations are required to estimate accurately the large confidence intervals. Table 6.20 summarizes the values taken by L and k. With $L = 10^5$ looks and $k = 500$, doubling k only modifies the uncertainty in m_v by 1% and the uncertainty in s by 4% which is negligible. For the case $L = 10^2$ looks and $k = 5 \times 10^5$, the confidence intervals are much larger and their values can change significantly when repeating the same simulation. In the end, this is still acceptable as it does not affect the final conclusion which is that such estimations are not reliable.

Fig. 6.13 shows the retrieval for scenarios A, B, C, and D. Each point represents a model inversion based on L random samples. Points which are obtained with a large number of looks are less scattered. For the sake of clarity, only 500 simulations are plotted for each case. As expected, scenarios C and D correspond to regions where noisy radar measurements produce large uncertainty on soil moisture, and scenarios B and D lead to the most uncertain RMS height estimations.

True parameters	A	B	C	D
$(s_0,\, m_{v0})$ $([\mathrm{mm}]\,,\, [\mathrm{m}^3/\mathrm{m}^3])$	(10, 0.05)	(30, 0.05)	(10, 0.3)	(30, 0.3)

Table 6.19: Uncertainty is computed for four pairs of soil moisture and RMS height

L [pixels]	10^2	10^3	10^4	10^5
k	5×10^5	5×10^4	5×10^3	5×10^2

Table 6.20: Number of Monte Carlo simulations k against number of looks L

Table 6.21 shows the 68.3% interval confidence on m_v and s as given by the AA' and BB' intervals on Fig. 6.5. Regarding soil moisture, the $\pm 0.05\,\mathrm{m}^3/\mathrm{m}^3$ uncertainty requirement is nearly met for every scenario with $L = 1000$.

Regarding the RMS height, the 20% uncertainty is achieved for A and C (smooth surface) with only $L = 10^3$ looks, but 10^5 looks are required to meet this requirement for all scenarios. Because the problem is ill-conditioned (nearly parallel contours observed on Fig. 6.10), small errors on the measurements lead to large error on the RMS height. This suggests that over rough soil surface the RMS height can hardly be retrieved from multi-polarized images. Qualitative information can still be extracted with $L \geq 10^3$ pixels, as unrealistic values of s would indicate that the soil surface is rough.

6.1.3.3 Required number of looks

This section generalized the simulation described above to a grid of soil moisture and RMS height which covers all physically-possible values. For each node of the grid, multiple Monte Carlo simulations are computed for different numbers of available looks ranging from $L = 10^2$ to $L = 10^5$.

Fig. 6.14 shows contours of uncertainty for m_v which correspond to a 68.3% confidence interval, for $L = 10^3$ looks, $L = 2.5 \times 10^3$ looks. As noticed in the previous section, the uncertainty increases with soil moisture. In addition the convexity

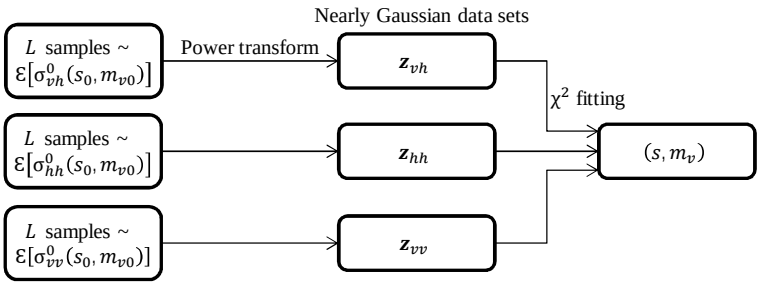

Figure 6.12: Monte Carlo simulation used to determine uncertainty in m_v and s for different available number of looks and different pairs of true soil parameters $(s_0,\, m_{v0})$. This simulation is repeated k times to achieve reliable statistics.

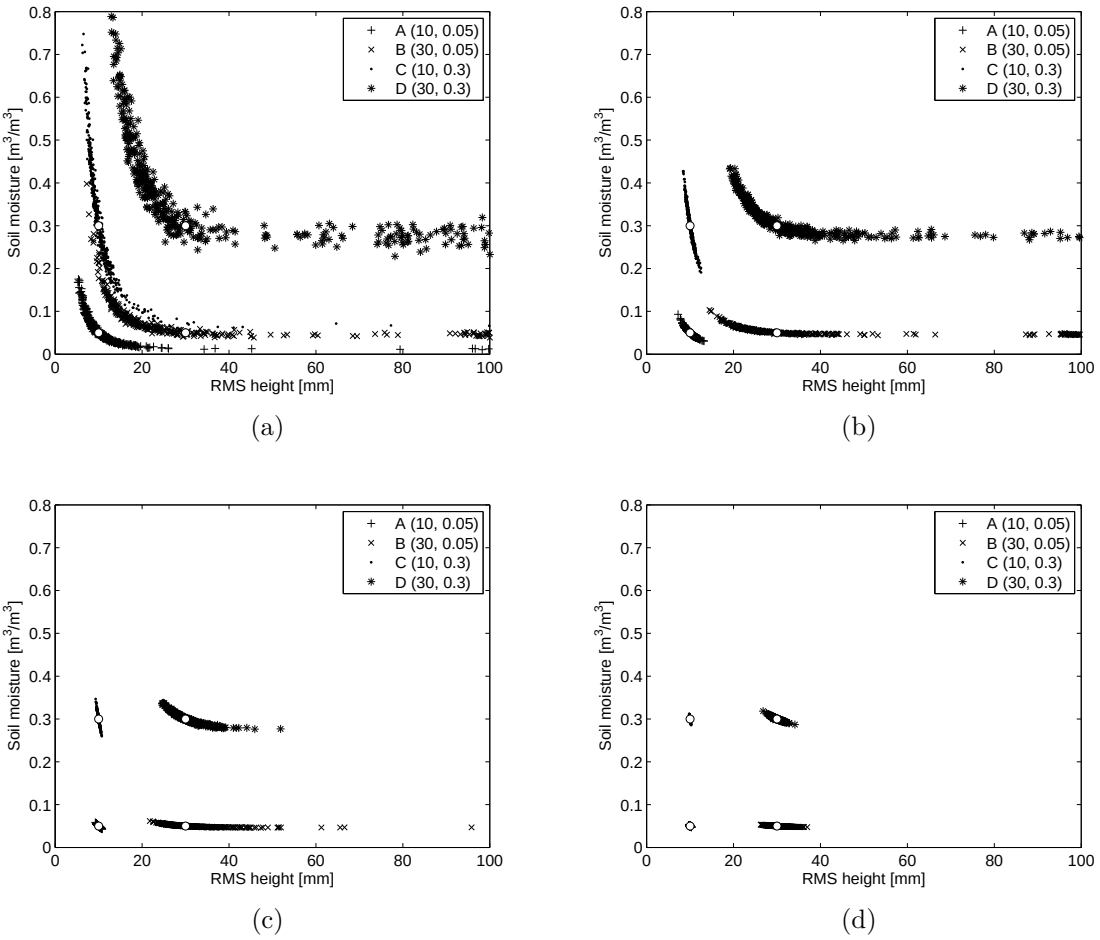

Figure 6.13: Uncertainty regions obtained with (a) 10^2 looks, (b) 10^3 looks, (c) 10^4 looks, (d) 10^5 looks

	$\pm\delta m_v[\mathrm{m}^3/\mathrm{m}^3]$	$\pm\delta s$ [%]
A	0.058	1630
B	0.078	6353
C	0.228	5949
D	0.206	10186

(a)

	$\pm\delta m_v[\mathrm{m}^3/\mathrm{m}^3]$	$\pm\delta s$ [%]
A	0.015	17
B	0.017	7607
C	0.069	12
D	0.058	10486

(b)

	$\pm\delta m_v[\mathrm{m}^3/\mathrm{m}^3]$	$\pm\delta s$ [%]
A	0.005	5.2
B	0.005	8239
C	0.022	3.7
D	0.020	25

(c)

	$\pm\delta m_v[\mathrm{m}^3/\mathrm{m}^3]$	$\pm\delta s$ [%]
A	0.001	1.6
B	0.002	9.3
C	0.007	1.2
D	0.006	4.8

(d)

Table 6.21: 68.3% confidence interval on soil moisture and RMS height for (a) $L = 10^2$, (b) $L = 10^3$, (c) $L = 10^4$, and (d) $L = 10^5$

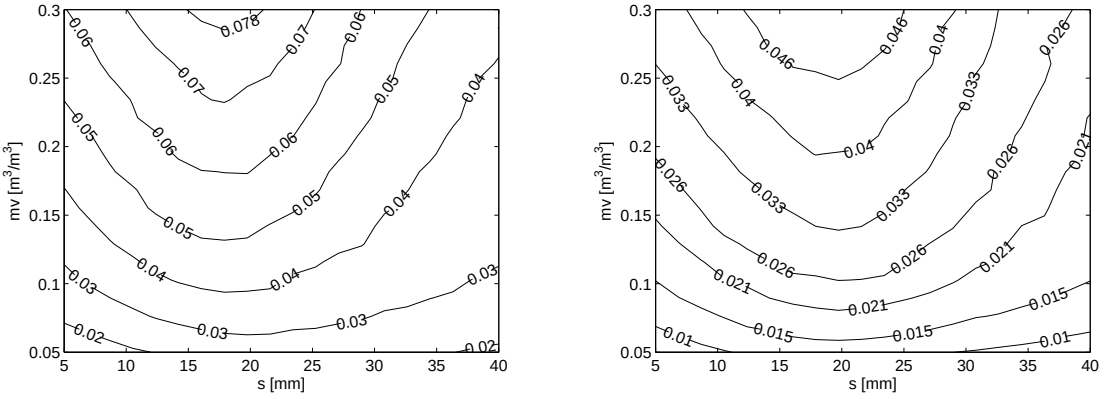

(a) (b)

Figure 6.14: Contours of soil moisture uncertainty in m^3/m^3 corresponding to a 68.3% confidence interval for (a) $L = 10^3$, (b) $L = 2.5 \times 10^3$

of each contour indicates that soil moisture estimations are more uncertain for s between 15 and 20 mm which unfortunately are common values for agricultural soils [113]. This region is characterized by both large speckle noise and poor sensitivity of all polarizations to m_v. Note that for $0.20 < m_v < 0.25\,m^3/m^3$ and $s = 9\,mm$, The uncertainty is about $\pm 0.05\,m^3/m^3$ with $L = 10^3$ looks. This matches the results obtained with Radarsat-2 data in section 6.1.2.1 for which ~1000 looks led to a $\pm 0.04\,m^3/m^3$ uncertainty (table 6.5). This close agreement suggests that the simulation is realistic. Perfect agreement should not be expected since parameters uncertainty depends to some extent on the incidence angle which is different for the simulation and the Radarsat-2 data.

In comparison, Barber *et al.* found more optimistic results [87]. For $m_v = 0.20\,m^3/m^3$ and $s = 12\,mm$, they found uncertainty below $\pm 0.03\,m^3/m^3$ with only $L = 3 \times 10^2$. This improvement certainly comes from the *a priori* information on m_v and s added in the Bayesian method (parameters uniformly distributed over a reasonable range, or normally distributed around their true value), while the χ^2 supposes a non-informative prior (m_v and s can *a priori* take any values).

With $L = 2.5 \times 10^3$ pixels, soil moisture uncertainty remains below $\pm 0.05\,m^3/m^3$ for the entire range of soil moisture.

Similarly, Fig. 6.15 shows contours of uncertainty for s with $L = 10^4$ looks. Again, the rougher the soil surface, the more uncertain is the RMS height estimation. And the shape of the contours shows that the worst case occurs for soil moisture levels around $0.08\,m^3/m^3$. Above $20-25\,mm$, the χ^2 fitting returns unrealistic and uncertain values. As mentioned before failure of the roughness estimation still provides useful information. With $L = 10^4$ pixels, if the retrieved s value is unrealistic, one can infer that the RMS height is at least larger than $20 - 25\,mm$.

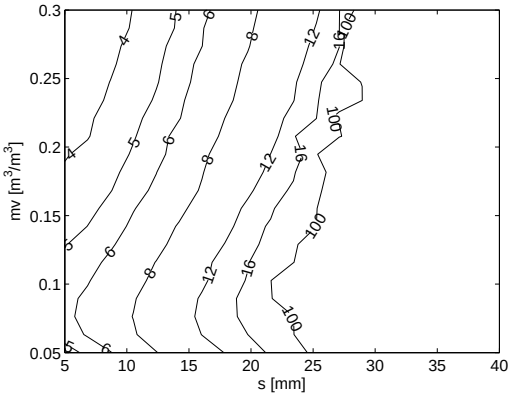

Figure 6.15: Contours of RMS height uncertainty in % corresponding to a 68.3% confidence interval, for $L = 10^4$

From these simulations, the $\pm 0.05\,\mathrm{m}^3/\mathrm{m}^3$ uncertainty requirement can be translated into a required number of looks for all combinations of soil moisture and RMS height. Fig. 6.16a shows contours of L required to meet a $\pm 0.05\,\mathrm{m}^3/\mathrm{m}^3$ uncertainty. The number of required looks ranges from a few hundreds in the most favorable cases (low m_v) to about 2500 looks for the most demanding cases (high m_v).

Fig. 6.16b shows contours of L to reach the ideal $\pm 0.01\,\mathrm{m}^3/\mathrm{m}^3$. At best a few thousand looks would be required over dry soils. Over wet soils, about 6×10^4 looks might be necessary. Assuming a 10 m radar resolution, soil moisture could be estimated at a 2.5 km resolution. Reaching the ideal 0.1 km resolution for agricultural application and the 0.01 km resolution for hydrology would require unrealistic radar resolutions of respectively 0.4 mm and 0.04 mm. As speckle is intrinsic to scattering mechanisms, this simulation suggests that the ideal requirements are not achievable by combining only multi-polarized images.

Since at the moment Radarsat-2 and TerraSAR-X are the only satellites with quad-polarization modes, the same simulations have been done with only $hh-$ and $vv-$ polarizations which are more commonly available. With the Radarsat-2 measurements, Fig. 6.6 suggested that the vh-polarization was not improving significantly the inversion. This is confirmed by Fig. 6.17 which shows that only for low soil moisture levels dual-polarization would require more looks to reach the $\pm 0.05\,\mathrm{m}^3/\mathrm{m}^3$ uncertainty, though it remains feasible.

6.1.4 Discussion

6.1.4.1 Limitations of the simulations

Model dependence Following the sensitivity analysis of section 6.1.3.1, the uncertainty on the estimated parameters is driven by features which depend on the backscattering model: (1) sensitivity of the model to the soil parameters, and (2) complementarity of each polarization. Using a different backscattering model is be expected to lead to similar contours of L as the Oh model agrees with the IEM and the GO models over their respective range of validity [10].

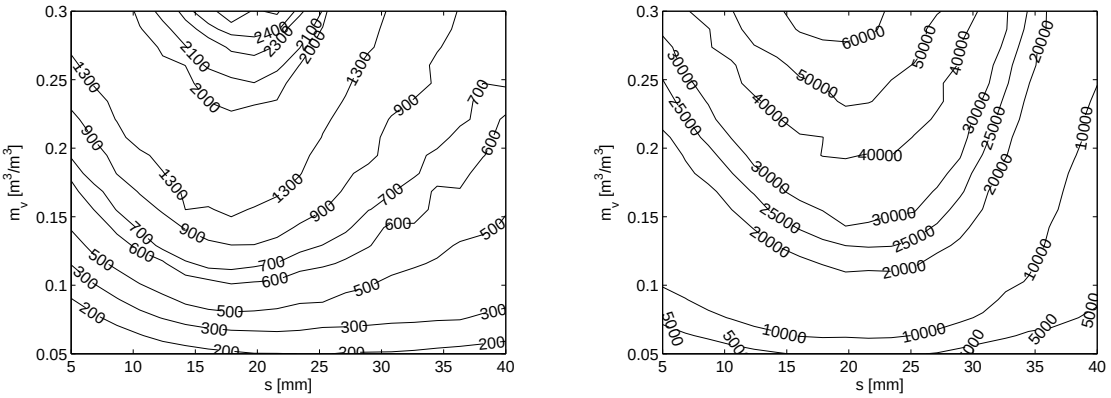

(a) (b)

Figure 6.16: Contours of L to reach (a) a $\pm 0.05\,\mathrm{m}^3/\mathrm{m}^3$ uncertainty, (b) a $\pm 0.01\,\mathrm{m}^3/\mathrm{m}^3$ uncertainty a on soil moisture, with full-polarimetric measurements

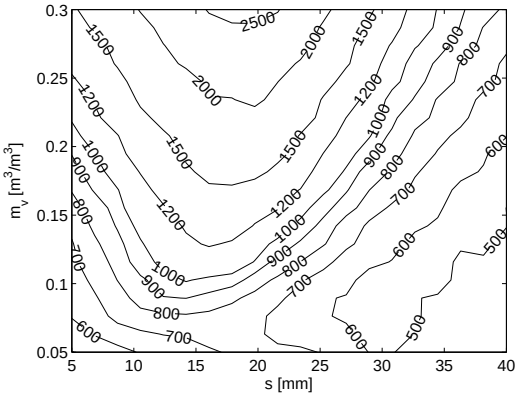

Figure 6.17: Contours of L to reach a $\pm 0.05\,\mathrm{m}^3/\mathrm{m}^3$ uncertainty on soil moisture, by combining $hh-$and $vv-$polarizations

NESZ [dB]	σ^0_{vh} [dB]	σ^0_{hh} [dB]	σ^0_v [dB]
-31	-24.4	-11.0	-11.0

Table 6.22: NESZ and backscatter coefficients for 24° incidence angle, $m_v = 0.05\,\mathrm{m}^3/\mathrm{m}^3$, and $s = 10\,\mathrm{mm}$

As mentioned before, the contours on Fig. 6.14a agree to some extent with the results obtained with Radarsat-2 in section 6.1.2.1. However following the poor results obtained in section 6.1.2.2, the suitability of the Oh model for agricultural soils is still questionable. Therefore the absolute values obtained for the contours of L should be considered carefully. On the bright side, the overall arrangement of the contours is certainly trustworthy as the Oh model is based on function forms which respect well-known scattering behaviors [83].

Thermal noise It was assumed that the main source of uncertainty on the radar measurements is speckle, and thermal noise was ignored. Below, this assumption is discussed and it is shown that ultimately thermal noise can be neglected.

Thermal noise is quantified by the Noise Equivalent Sigma Zero (NESZ) of Radarsat-2 which is estimated at -31 ± 4 dB [60]. Table 6.22 shows the backscatter coefficients simulated with the Oh model for each polarization at a 24° incidence angle, with low soil moisture level ($m_v = 0.05\,\mathrm{m}^3/\mathrm{m}^3$) and smooth soil surface ($s = 10\,\mathrm{mm}$), *i.e.* a configuration with weak backscattering. While the NESZ is well below σ^0_{hh} and σ^0_{vv}, it is only 5 dB below σ^0_{vh} . Thus for such soil conditions, thermal noise contributes to about one third of the true power at vh-polarization.

It is possible to bound on the effects of thermal noise with the simulation using only $hh-$ and $vv-$polarizations. Since using all polarizations will in theory lead to lower uncertainty than using only $hh-$ and $vv-$polarizations, the contours of L with thermal noise on all polarizations can be expected to lie between the optimistic contours of Fig. 6.16, and the conservative contours of Fig. 6.17 for which thermal noise can safely be ignored.

Thermal noise is also not negligible when considering very high radar resolutions. Since multilooking is used to mitigate speckle, very high resolution radar images are desirable. Because of physical limitations in terms of transmitted power and size of antenna, higher radar resolution will come with higher NESZ. Ultimately this increase in NESZ will be compensated by the increase in available looks. Therefore the resulting image would still be useful for soil moisture estimation, but it could hardly be used for target detection as strong point scatterers would be masked by thermal noise.

Exponential speckle model The exponential model to describe the speckle may not be valid in some extreme scenarios mentioned in the results.

First, the exponential model requires the distributed target to be homogeneous. For a distributed target of 1 km, heterogeneity in soil moisture and/or in surface roughness might compromise this assumption. These heterogeneity could be taken into account through the product model described by Oliver *et al.* [88]. The product

model expresses the probability distribution of intensity as a function of the product between speckle distribution (due to random scatterers) and distribution of σ^0 due to scene heterogeneity. This product model was implemented by Barber *et al.* in their Bayesian approach [87].

Second, the exponential speckle model assumes that the radar resolution cell contains a large number of scatterers [88]. For very high resolution, the number of scatterers decreases and the exponential model might not be applicable.

6.1.4.2 Uncertainty and accuracy of retrieval

It must be stressed that a small parameter uncertainty does not guarantee that the retrieval is accurate. For example, with the Radarsat-2 acquisition used in Fig. 6.5b, the uncertainty on soil moisture is acceptable ($\pm 0.035\,\mathrm{m}^3/\mathrm{m}^3$), but the retrieved value ($0.078\,\mathrm{m}^3/\mathrm{m}^3$) seems highly inaccurate compared to its in situ measurement ($0.199\,\mathrm{m}^3/\mathrm{m}^3$). With the bootstrap resampling method, the synthetic data sets lead to values of mean σ^0 distributed around the σ^0 given by the original data set. If the original data set gives an inaccurate characterization of σ^0, then the point cloud from the Monte Carlo simulations can be tightly distributed around the very inaccurate estimation from the original data set.

Ultimately, using in situ measurements or using Monte Carlo simulation to quantify parameters uncertainty come with disadvantages. Uncertainty from comparison with in situ measurements is trustworthy only if the in situ measurements are reliable. And uncertainty from statistical method is trustworthy only if the statistics derived from the original data is reliable. When possible, both methods should be implemented.

In section 6.1.3, the simulations only accounted for speckle and it was assumed that both the measurements and the model were unbiased. In practice, there will always be radiometric errors on the measurements and the backscattering model will never be perfect. Therefore, the contours of number of looks should be interpreted as the minimum number of looks required to reach a given uncertainty, assuming that no other sources of uncertainty affect the retrieval. They are a good tool to identify combinations of measurements which are promising, and sets of requirements which seem unfeasible.

It is not straightforward to assess how the retrieval would be affected if the simulation included radiometric errors / biases. Indeed the effect of having the same bias on all the measurements may be different from that of having random errors on the measurements. However, it is interesting to note that a ± 1 dB radiometric error corresponds to an error of 21-26% on the intensity σ^0. In comparison, L-look data affected only by speckle have a standard deviation of $\sigma^0/\sqrt{L}$ on the intensity . Therefore multilooking with 15-23 looks will also lead to an uncertainty on σ^0 of 21-26%. This suggests that after averaging real radar data with a few hundreds of looks the final error on soil moisture estimation will certainly be driven by radiometric error / bias on the model and not by speckle.

6.1.4.3 Use of additional measurements

Section 6.2.3 showed that meeting the ideal requirements for soil moisture in terms of uncertainty ($\pm 0.01\,\mathrm{m}^3/\mathrm{m}^3$) and resolution (0.1 km) was leading to unrealistic measurement resolution ($< 1\,\mathrm{mm}$). However these ideal requirements might be achievable by combining additional information such as images acquired at different incidence angles or different frequency bands either by the same satellite or from a constellation of satellites such as TanDEM-X or the future Sentinel-1 mission. When the images to be combined are not acquired simultaneously, the time between acquisitions will lead to some temporal averaging. Ultimately this temporal averaging must be linked back to temporal resolution requirements on soil moisture.

All in all, the uncertainty on the estimated parameters can be reduced by combining (1) measurements distributed in space with decrease in spatial resolution, (2) measurements distributed in time with decrease in temporal resolution, or (3) simultaneous measurements without any resolution degradation.

6.1.5 Summary

The previous three sections focused on the retrieval of soil moisture and RMS height using multi-polarized radar measurements.

First, section 6.1.1 looked at the overall correlation between radar measurements and soil parameters. As expected σ^0_{vh} is much weaker than σ^0_{hh} and σ^0_{vv}, and σ^0_{vv} is often larger than σ^0_{hh}. With rough soil surfaces for which $\sigma^0_{hh} \approx \sigma^0_{vv}$ is expected, σ^0_{hh} is sometimes larger than σ^0_{vv} probably because of biases on the measurements (stated to be smaller than 1 dB) or because of statistical uncertainty when estimating the mean backscattering coefficients. Eventually, it was possible to relate changes in σ^0 with changes in incidence angle, soil moisture, and surface roughness.

Second, section 6.1.2 focused on applying the χ^2 method to the Radarsat-2 data set.

A detailed analysis was first carried out for acquisition 5 and 6 over field 12. This analysis highlights all the information that can be extracted from the χ^2. The goodness-of-fit Q can be used to detect inconsistent configuration when the model is overdetermined, though finding the reason for inconsistency still requires careful examination. Here it seems that low Q-values are attributable to biases on the measurements and/or on the model. From the graphical inversion, these biases lead to ambiguous intersections of the contours of σ^0_{vh}, σ^0_{hh}, and σ^0_{vv}.

Biases were analyzed (1) by using simulated σ^0 from the in situ measurements, and (2) by comparing the retrievals obtained with different polarizations. Because the analysis is limited to two acquisitions, it is difficult to conclude on whether a poor retrieval is imputable to the measurements or the model. However it is clear that even a 0.5 dB systematic error can compromise the retrieval.

This detailed analysis also confirmed that any added information improves the uncertainty on the retrieved parameters. This is true on the condition that systematic measurement errors have been removed and the model is correct.

The χ^2 method was then applied more broadly to fields 6, 8, 9, 12 and 13 which have various soil moisture and surface roughness conditions. All in all, Q-values were often low when using all polarizations, and the agreement with in situ measurements was poor. Soil moisture tends to be underestimated and RMS height tends to be overestimated. This systematic mismatch has to come from systematic errors on the measurements or on the model. Because of the numerous quality checks undergone by Radarsat-2 products and the rather positive observations about the data set made in section 6.1.1, the Oh backscattering is more likely to be the main reason for these poor results. After comparing (1) the radar measurements with their simulations from in situ measurements of soil parameters, and (2) the radar measurements and the expected scattering range of the Oh model, the doubts concern mainly the cross-polarized ratio q which are used to model σ^0_{hh} and σ^0_{vv}.

Considering that Oh *et al.* reported an RMS error of 2.06 dB for the data-fitting of q [83], the poor agreement between retrieved parameters and in situ measurements is not too surprising. On the bright side, correct changes in soil moisture and RMS height could be detected on multiple occasions as long as these were large enough.

Third, simulations with the Oh model were carried out to study the effect of speckle on parameters uncertainty. In particular, this section focused on determining how many looks are required to reach a given uncertainty on soil moisture or on RMS height. The results suggest that a $\pm 0.05\,\mathrm{m}^3/\mathrm{m}^3$ uncertainty on soil moisture is achievable when at least 2500 looks for all polarizations, and about 3000 looks when only σ^0_{hh} and σ^0_{vv} are used. The worst case corresponds to high soil moisture and medium RMS height ($15 < s < 20$ mm) which are common values for wet soils with tilled surface. As for the uncertainty on RMS height, an uncertainty of $\pm 20\%$ seems hardly achievable for RMS height larger than 20 mm.

Further improving parameters uncertainty requires averaging more looks/pixels. Spatial averaging is limited by the largest resolution acceptable for the estimated parameters (1 km for agricultural applications of soil moisture). The number of available pixels can also be increased by increasing radar resolution. More elaborated simulations might be required to investigate these scenarios as (1) over scales of 1 km some parameters of the soil might not be homogeneous and (2) at very high resolution the speckle model might not be valid.

So far model inversion was only based on multi-polarized data. The next section investigates whether using multi-frequency or multi-incidence measurements can lead to better soil parameters estimation.

6.2 Inversion with multi-frequency or multi-incidence radar measurements

The use of multi-frequency measurements has been investigated to estimate various parameters. In [129] and [130], multi-frequency data were used over vegetated soils to estimate both soil moisture and the Leaf Area Index (LAI). From simulated data, Mo *et al.* showed that RMS height and correlation length could be estimated by combining L-band and C-band measurements [131]. There seem to be only two studies focusing on soil moisture / surface roughness estimation. Rao *et al.* [132] and Bindlish and Barros [133] used images acquired at multiple bands (L, C, X) and polarizations (hh, vv, vh) to estimate soil moisture, RMS height, and correlation length.

As for multi-incidence data, there has been no attempts made to estimate both parameters from measurements at two incidence angles. Measurements at different incidence angles were used in [134] and [135] to relate empirically $\Delta\sigma^0 = \sigma^0(\theta_1) - \sigma^0(\theta_2)$ to the modified roughness parameter $Z_s = s^2/l$. And Baghdadi *et al.* used multi-incidence ASAR data to estimate soil moisture from a linear empirical backscattering model [11]. This way, they obtained more robust estimation. However multi-incidence data were not used to estimate simultaneously soil moisture and RMS height, as the latter was embedded in the empirical model.

In summary, there do not seem to be studies looking at the robustness of model inversion for different combinations of frequencies / incidence angles.

6.2.1 Model inversion and ill-conditioning

In section 6.1.3.1, a good intersection of contours of different polarizations was shown to be necessary to obtain reliable estimation of soil parameters. This aspect was related to ill-conditioning. In this section, the intersection of contours of σ^0 is analyzed to investigate soil parameters estimation from either multi-frequency or multi-incidence radar measurements. The Oh model is again used for all the simulations.

Fig. 6.18 shows the contour intersection in the case of multi-frequency measurements at L-, C-, and X-band, with a 24° incidence, for four soil conditions. First, there are no noticeable differences between the $vv-$ and $hh-$polarizations. For rough soil surfaces, the intersection is neat. In comparison for smooth soil surfaces, the intersection is ambiguous and could lead to inaccurate estimation because of noisy measurements / rounding errors. This could be expected since the frequency band is accounted for in the backscattering model by the wavenumber k which appears as a multiplicative factor of the RMS height. Therefore the larger the RMS height, the more distinct a frequency band becomes. Assuming that images are available in two frequency bands, it appears that the L-X configuration might lead to the most robust inversion, followed by the C-X configuration, while the L-C configuration looks ill-conditioned for smooth soil surface.

Similarly, Fig. 6.19 shows the contour intersection for multi-incidence C-band measurements at 20°, 30°, and 40°. For the $vv-$polarization, the contours are over-

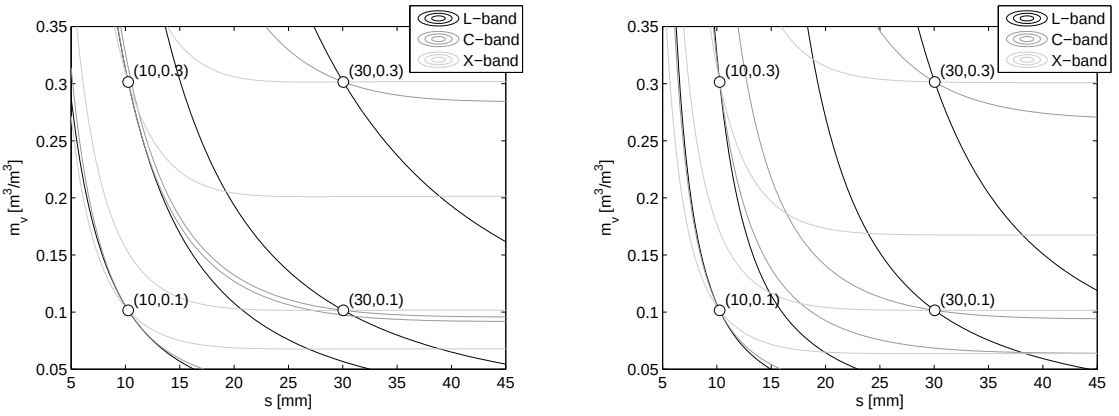

Figure 6.18: Intersections of multi-frequency contours for four soil conditions at (a) $vv-$ and (b) $hh-$polarization

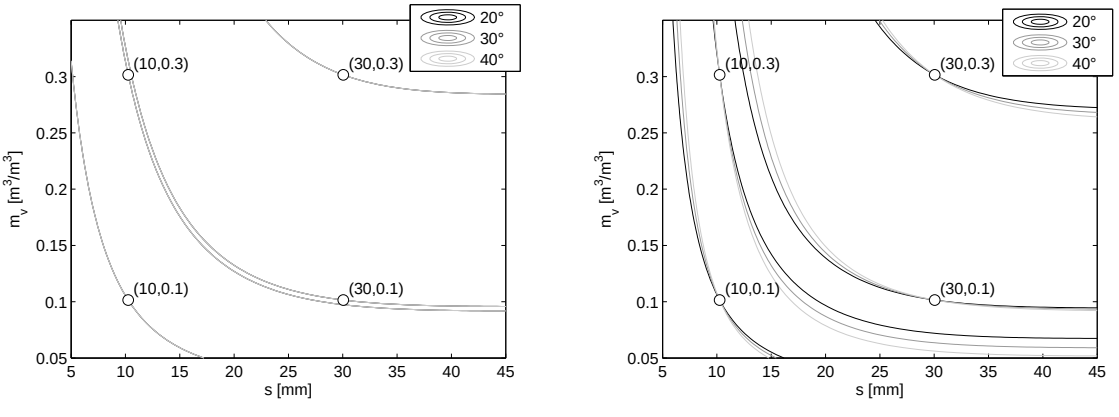

Figure 6.19: Intersections of multi-incidence contours for four soil conditions at (a) $vv-$ and (b) $hh-$polarization

lapping each other because the incidence angle θ appears as a multiplicative factor in the Oh model for σ^0_{vv} (equation 2.25). Thus different θ values simply lead to different offsets in σ^0_{vv}. The contour intersection is slightly better with the $hh-$polarization, but it is not very promising regardless of the soil conditions.

From these simple contour plots, it appears that model inversion based on multiple incidences will be very sensitive to measurement noise. For any values of soil parameters, the problem is ill-conditioned. In comparison, inversion based on multiple frequencies appears very promising, particularly for rough soil surfaces. That is why the next section assesses how many looks are required to reach a $\pm 0.05\,\mathrm{m}^3/\mathrm{m}^3$ uncertainty on soil moisture with multi-frequency data, and compares the results with those obtained with multi-polarized data (section 6.1.3.2).

6.2.2 Required number of looks with multi-frequency data

All the simulations below are done for the $hh-$polarization, with a 24° incidence angle. According to Fig. 6.18, similar results would be obtained at $vv-$polarization. Fig. 6.20 shows contours of required number of looks to reach a $\pm 0.05\,\mathrm{m}^3/\mathrm{m}^3$ uncertainty on soil moisture for different combinations of frequency bands. As expected, the poorest results are obtained for the L-C configuration. The number of looks remains reasonable for RMS height larger than 15 mm, but it becomes surrealistically high for smaller values. This is because on Fig. 6.18, the contours at L-band and C-band are almost overlapping. In comparison, the L-X and C-X configurations lead to reasonable number of looks for RMS height as small as 10 mm. Close to $s = 5$ mm, the problem becomes ill-conditioned and both configuration lead to unrealistic number of looks. Fortunately this region of the parameter space is not fundamental as agricultural soil surface are usually not that smooth.

In summary, for common values of RMS height ($s > 10$ mm), both the L-X and C-X configurations give very acceptable results while the L-C configuration is not an attractive choice for smooth soil surfaces.

Other considerations come into play when comparing the L-X, C-X, and L-C configurations. One of the main attraction of the L-band is that its longer wavelength penetrates deeper into volume scatterers such as vegetation cover and soil. The penetration depth depends also on the incidence angle, and the soil moisture. Images acquired over the Sahara in 1981 during the NASA Shuttle Image Radar mission proved that L-band wavelength can penetrate 1 or 2 m of loose sand [136]. And over non-arid areas, the penetration depth at L-band is of the order of a few centimeters [137]. It is an attractive characteristic for agricultural applications which ideally require soil moisture estimation down to the root region. The main drawback of L-band compared to shorter wavelengths, is that high-resolution images are more challenging in terms of hardware. Following the faulty ALOS mission launched in 2006, at the moment there are no operational satellites with L-band capability. However there are a few L-band SAR missions in concept and in preparation (see table 6.23). In particular, ALOS-2 is expected to provide multi-polarized images at resolutions which match the high-resolution modes of current SARs using shorter wavelengths. Thus multilooking with 1000 looks should be feasible.

Even though the L-C configuration under-performs for smooth soil surfaces, it has the advantage that both the L- and C-bands can penetrate the soil surface. In comparison the X-band will at best sense soil moisture at the surface which might not be of prime interest for agriculture. The weakness of the L-C configuration for smooth soil surfaces could be bypassed by using multiple-polarizations at least for one frequency band. This point is investigated in the next section.

The C-X configuration is also attractive because Radarsat-2 and TerraSAR-X can already provide full-polarimetric data at C-band and X-band respectively. Therefore the model inversion could be tested with both multi-polarization and multi-frequency measurements at high resolution.

This discussion highlights an important trade-off between (1) the theoretical con-

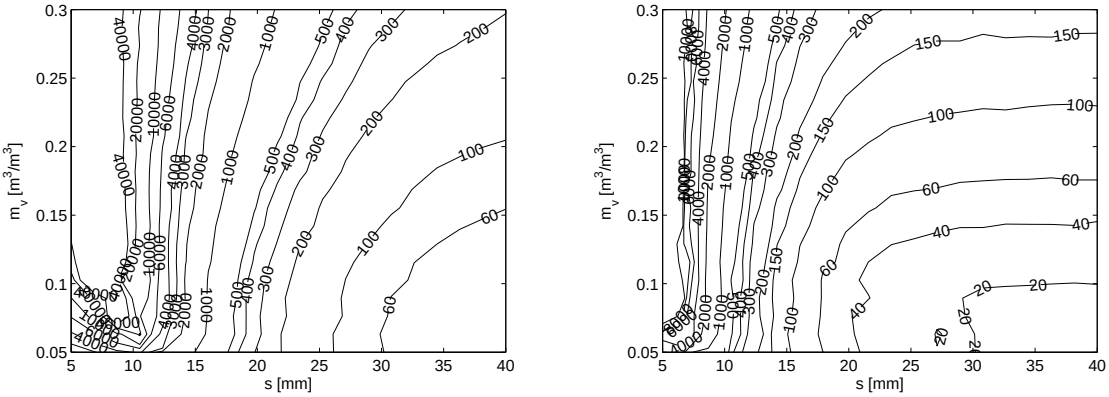

(a) L-C configuration

(b) L-X configuration

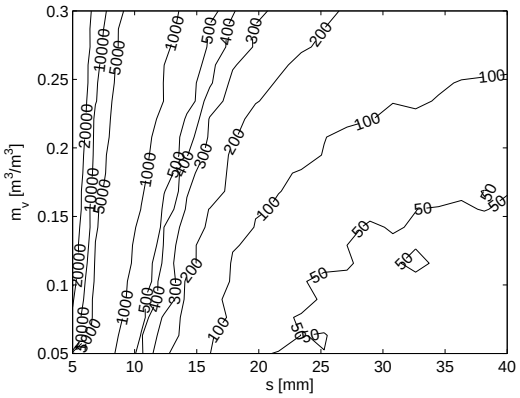

(c) C-X configuration

Figure 6.20: Contours of L to reach a $\pm 0.05\,\mathrm{m}^3/\mathrm{m}^3$ uncertainty for (a) an L-C configuration, (b) a C-X configuration, and (c) a L-X configuration

tours of L for a given configuration, (2) the available measurement resolutions, and (3) the penetration depth of the measurements. Another parameter which did not appear is the temporal resolution of the measurements. At the moment, each satellite carries an instrument which operates only in a given frequency band. Therefore measurements at different frequencies will be acquired by different satellites at different times. Combining these measurements will lead to some temporal averaging. In summary, the improvement in soil moisture resolution which comes from combining multiple frequencies comes at the price of a coarser temporal resolution. This point will be further discussed in section 6.3.

The next section highlights the benefits of combining both multi-frequency and multi-polarization data.

Instrument	Satellite	Date	Nominal resolution [m]
SAR	SeaSat	1978	25
SAR	JERS	1992-1998	18
PALSAR	ALOS	2006-2011	10
PALSAR-2	ALOS-2	2014	3
InSAR	DESDynI	-	10
SAR-L	SAOCOM	$\geq$ 2015	10

Table 6.23: Past and future L-band SAR missions

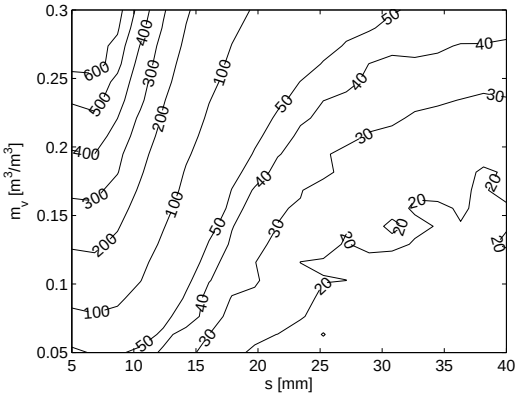

Figure 6.21: Contours of L to reach a $\pm 0.05\,\mathrm{m}^3/\mathrm{m}^3$ uncertainty with full-polarimetric measurements at C- and X-bands

6.2.3 Required number of looks with both multi-frequency and multi-polarization data

Full-polarimetric measurements at C- and X-bands In this configuration, model inversion is robust all over the parameters space. The worst case occurs for smooth and wet soils for which about 600 pixels are required to reach an uncertainty of $\pm 0.05\,\mathrm{m}^3/\mathrm{m}^3$ on soil moisture. Therefore there is margin to improve soil moisture uncertainty by increasing the number of looks while maintaining a soil moisture resolution below 1 km.

Full-polarimetric measurements at L- and C-bands For this configuration, two cases are considered. The first one (*case 1*) assumes that full-polarimetric measurements are available at both L- and C-bands. While the second one (*case 2*) assumes that only dual-polarization is available with $hh + hv$ images at L-band and $vv + vh$ images at C-band.

As expected, case 1 leads to more robust estimation than case 2. Nonetheless, case 2 leads to acceptable numbers of looks with the additional advantage that dual-polarization is available for modes with a larger footprint than those of full-polarimetric modes. This point will be further discussed in section 6.3.3.

Fig. also shows that with full-polarimetric measurements at both L- and C-bands, the ideal $\pm 0.01\,\mathrm{m}^3/\mathrm{m}^3$ uncertainty on soil moisture may require about 10 000 looks in the worst case scenario. With a 5 m radar resolution, this would lead to a 500 m

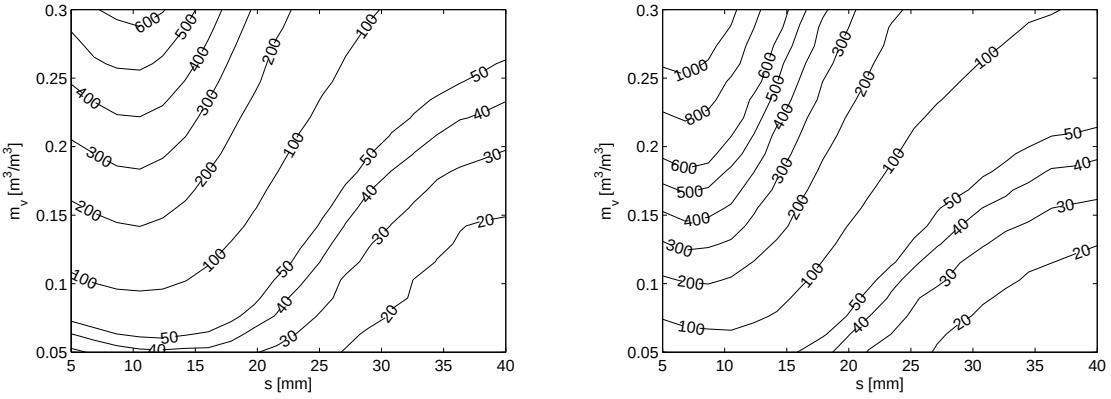

Figure 6.22: Contours of L to reach a $\pm 0.05\,\mathrm{m}^3/\mathrm{m}^3$ uncertainty with measurements at L- and C-bands for (a) case 1 and (b) case 2.

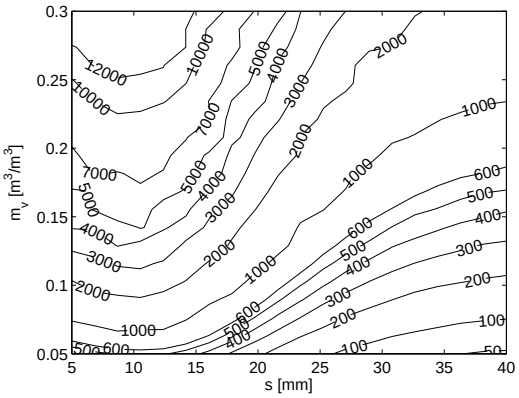

Figure 6.23: Contours of L to reach a $\pm 0.01\,\mathrm{m}^3/\mathrm{m}^3$ uncertainty with full-polarimetric measurements at L- and C-bands

soil moisture resolution which is close to the ideal requirement of 100 m stated for agriculture application. Such a scenario is feasible compared to the unrealistic 60 000 looks required for model inversion with full-polarimetric images only at C-band (Fig. 6.16b).

From these simulations, a combination of for example Radarsat-2 and ALOS-2 data would be a very promising method to reach at the same time (1) low uncertainty on soil moisture, (2) high soil moisture resolution, and (3) soil moisture estimation at a depth of a few centimeters.

The next section analyzes in more details the trade-off which has to be considered when combining measurements from different satellites.

Uncertainty	$\pm 0.05\,\mathrm{m}^3/\mathrm{m}^3$
Spatial resolution	1 km
Coverage	100-1000 km
Time sampling	7 days
Timeliness	5 days
Averaging time	<3.5 days
Penetration depth	few centimeters

Table 6.24: Minimum requirements for agricultural meteorology

6.3 Trade-off on the measurements

This section considers the trade-off involved when selecting the different radar measurements to reach a set of observation requirements on soil moisture. The trade-off solely concerns the measurements , and it is assumed that model inversion is done through a χ^2fit or an equivalent method.

6.3.1 Requirements to be considered in the trade-off

Before discussing the trade-off on the measurements involved in model inversion, the first step is to clearly state the requirements of the soil moisture product for a given application. In the following, a case example is carried out for agricultural meteorology.

Table 6.24 reports the minimum requirements which must be met for soil moisture estimation to be useful for agricultural meteorology. There are certainly other requirements, but here the focus is on those which affect the design of the model inversion. *Uncertainty*, *Spatial resolution, Time sampling,* and *timeliness* were already reported in table 6.28 from the OSCAR tool [7]. Some of these requirements are worth further comments.

Spatial coverage A spatial coverage of 100 km gives regional coverage while a coverage of 1000 km corresponds to a national coverage. The OSCAR tool states that a *global land* coverage is required. Such coverage seems exaggerated particularly as a minimum requirement. An agricultural meteorology service available at regional to national scale appears more sensible.

Time sampling Assuming that two images acquired by two satellites at different frequencies are used for model inversion. The time sampling of soil moisture will be dictated by the longest revisit time of the two satellites. Table 6.25 shows the repeat cycle of different Earth Observation (EO) satellites along with their overall revisit time. All in all, these satellites are in low Earth orbits (500-900 km altitude) with similar ranges of incidence angles (20°-50°) which lead to an average revisit time of ~3 days for a single satellite and less than 3 days for constellations. Therefore soil moisture estimation every 3 days is feasible with any combinations of satellites listed in table 6.25.

Satellite	Repeat cycle [day]	Revisit time	Band
Radarsat-2 [60]	24	3 days	C
COSMO-SkyMed [138]	16	2 h	X
TerraSAR-X [139]	11	3 days	X
ALOS-2 [140]	14	3 days	L
Sentinel-1 (A & B) [141]	6	2 days	C

Table 6.25: Repeat cycle of some of the current and future EO satellites

Penetration depth Penetration depth is sometimes qualitatively set to *root depth* which is not clear as root depth depends on the crops and changes from germination to maturity of the crop. For canola, root depth varies from 3 to 5 cm at emergence, and from 90 cm to 140 cm at maturity depending on the type of canola [142]. This project focuses on bare soil or soil with crops at their early stage for which vegetation cover can be neglected. Therefore sensing soil moisture only at depth of a few centimeters is acceptable.

Averaging time Temporal averaging will occur because of the non-simultaneous measurements used to solve the inverse problem. When combining two images at different frequencies which have not been acquired simultaneously, the retrieved soil moisture can reasonably be considered as an estimation of the average soil moisture between the two acquisition dates. There are two main limitations to how much averaging can be accepted.

The first limitation comes from the eventual error between the sample mean using only two samples and the exact analytical mean. The exact analytical mean soil moisture between two dates t_1 and t_2 is given by

$$\overline{m_v} = \frac{1}{t_2 - t_1} \int_{t_1}^{t_2} m_v(t) dt \tag{6.4}$$

which is to be compared with the two-sample mean,

$$m_{v,12} = \frac{m_v(t_1) + m_v(t_2)}{2} \tag{6.5}$$

Solving the equation $\overline{m_v} = m_{v,12}$ leads to the differential equation $\mathrm{d}^2 m_v / \mathrm{d}t^2 = 0$. Therefore for the two means to be equal, m_v has to change linearly between t_1 and t_2.

Over long time intervals $t_2 - t_1$, m_v is likely to have non-linear variations which may lead to values of $m_{v,12}$ different from $\overline{m_v}$. Below, this difference is quantified using the time series of in situ measurements of soil moisture recorded by the data logger during period 2.

The two-sample mean is computed using only two soil moisture measurements separated by Δt, and the exact mean is computed using all available measurements (30 min time sampling) over Δt. Table 6.26 shows the error between two-sample mean and exact mean for different averaging times Δt. As expected the RMS error increases with the averaging time. With an averaging time of 1.5 days, the RMS

Averaging time [day]	**RMSE** [m^3/m^3]	**Max error** [m^3/m^3]
0.5	0.005	0.060
1.5	0.009	0.060
3.5	0.011	0.064
7	0.014	0.069
14	0.020	0.086
21	0.022	0.079

Table 6.26: Error between two-sample mean and exact mean for various averaging time. The results are based on the time series of in situ measurements of soil moisture recorded by the data logger during period 2.

error is about $0.01\,m^3/m^3$. Even with an averaging time of 21 days, the RMS error remains acceptable ($0.022\,m^3/m^3$). These results suggest that such consideration might be relevant only if one is interested in a $\pm 0.01\,m^3/m^3$ uncertainty on soil moisture. Note that this analysis is based on local soil moisture measurements, but the dynamics of soil moisture may be different in regions with different soil types and weather conditions. Therefore the analysis should be extended to other data sets to confirm the negligibility of the error made with the two-sample mean.

The second limitation comes from timeliness. It can be assumed that the soil moisture estimated from image 1 acquired at t_1 and image 2 acquired at t_2, is an estimation of the mean soil moisture at $t_1 + (t_2 - t_1)/2$. Therefore if timeliness is limited to 5 days, the delay between the first and the second image cannot exceed 10 days.

It is worth mentioning that uncertainty, averaging time, and time sampling are implicitly related.

- Time sampling and uncertainty
  With a time sampling of 7 days, having an uncertainty of $\pm 0.01\,m^3/m^3$ is not necessary, $\pm 0.05\,m^3/m^3$ might be acceptable. This is illustrated by Fig. 6.24. With a 3 day time sampling (Fig. 6.24a), most of the dynamics of soil moisture is captured, only the daily changes (usually small) are missing. In comparison with a 21 day time sampling (Fig. 6.24c), only the overall trend is captured, and large variations over a week are ignored. Therefore an uncertainty of $\pm 0.05\,m^3/m^3$ would be perfectly acceptable. All in all, for monthly estimation one may only need to know that a soil is very wet ($m_v > 0.30\,m^3/m^3$), moderately wet ($0.20 < m_v < 0.30\,m^3/m^3$), dry ($0.10 < m_v < 0.20\,m^3/m^3$), or very dry ($m_v < 0.10\,m^3/m^3$).

- Time sampling and averaging time
  Time sampling and averaging time are related through the Nyquist sampling requirement. If no information on the soil moisture process is to be lost then estimations should be separated by half the length of the longest signal period (the averaging window length), and the averaging windows should overlap by at least half their length. On the other hand, the overlap should not exceed much more than half of the averaging window length (oversampling), otherwise the estimations will be very correlated (redundant).

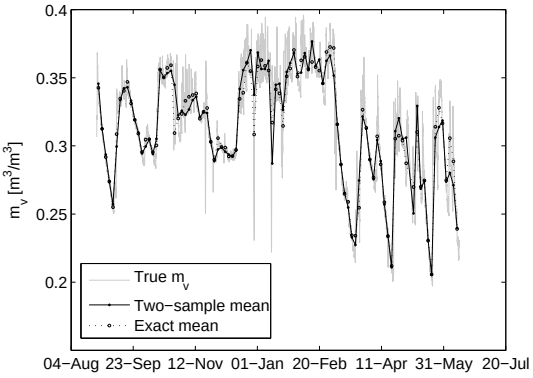

(a) 1.5 day averaging, 3 day resolution

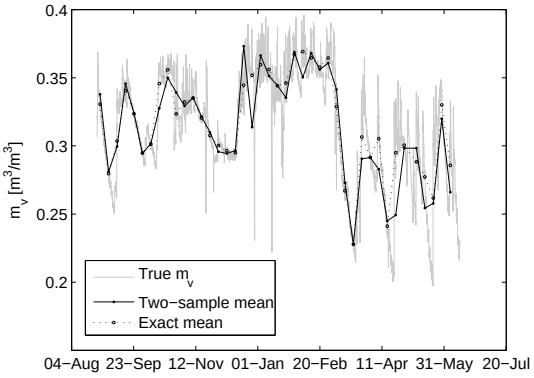

(b) 3.5 day averaging, 7 day resolution

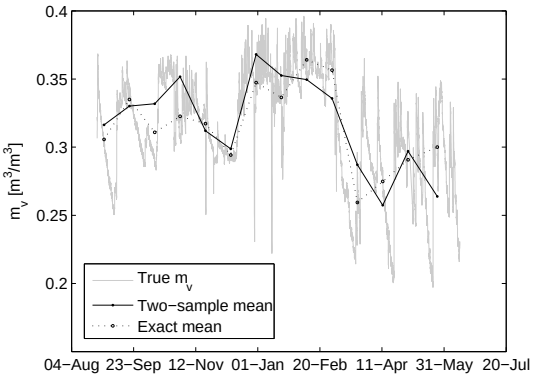

(c) 10 day averaging, 21 day resolution

Figure 6.24: In situ measurements of soil moisture for various averaging times and time resolutions

6.3.2 Design parameters

The design parameters are the characteristics of the radar measurements. They must be adjusted so that the inversion method outputs soil moisture estimates which meet the observation requirements. There are six main design parameters. Fig. 6.25 shows the main connections between design parameters and soil moisture measurement requirements.

Frequency bands The frequency bands are first constrained by the requirement of sensing soil moisture in the top 3-5 cm of soil. As mentioned before, this reduces the options to L-band and C-band, as X-band has a very limited penetration depth.

Using multiple frequency bands is also key for a robust model inversion, *i.e.* a low soil moisture uncertainty.

Robust model inversion also means that fewer looks are required to meet a given uncertainty. Therefore the choice of multiple frequencies is also related to spatial resolution of soil moisture.

Image polarizations The use of different image polarization is essentially related to robustness of model inversion. Thus it affects spatial resolution and uncertainty.

Radar spatial resolution Fine spatial resolution of the radar images makes more pixels available for multilooking to mitigate measurement noise. Therefore radar spatial resolution affects soil moisture spatial resolution and uncertainty.

Radar time sampling The time sampling of a radar image at a given frequency / polarization has to be finer or equal to the desired time sampling of soil moisture estimation. A finer Radar time sampling means that more than one image at a given frequency/polarization will be available. This will only double the number of pixels available for multilooking. As it is not an efficient strategy to improve soil moisture uncertainty / spatial resolution, the diagram does not link Radar time sampling with uncertainty / spatial resolution.

Radar swath Radar swath is directly related to coverage. The smaller the swath, the larger the number of images which need to be acquired and processed. Usually only one image can be acquired with each satellite pass, therefore several passes will be required to cover a large area. This will impact the revisit time, hence the link between radar swath and radar time sampling. Finally, large swath usually comes with coarse resolution, hence the connection with radar spatial resolution.

Time window for multiple images When non-simultaneous images with different polarizations/frequencies are combined, the time window between the first and last image defines the averaging time and limits the time sampling. Timeliness is also affected as model inversion can be done only once all the necessary images have been collected. The time window is indirectly related to Spatial resolution and Uncertainty of soil moisture, because a large time window allows for more images with different polarizations/frequencies to be combined.
In the previous section, the time window was also related to Uncertainty when crude averaging is done over long duration. This link does not appear on Fig. 6.25 because of the implicit connection between time sampling and uncertainty. Concretely, a long time gap between 2 images will lead to a coarse time sampling which supposes that large uncertainty is acceptable, thus uncertainty related to crude averaging may not be of concern.
In summary the time window is related to uncertainty through the availability of radar images, but not because of crude averaging.

It is interesting to note that time sampling is the time counterpart of spatial resolution, and time window is the time counterpart of radar swath.

Requirements which are connected to the same design parameter, can be conflicting. The five main conflicts are:

1. spatial resolution / uncertainty
   High spatial resolution means that fewer looks are available to mitigate measurement noise, *i.e.* fewer looks available to minimize uncertainty.

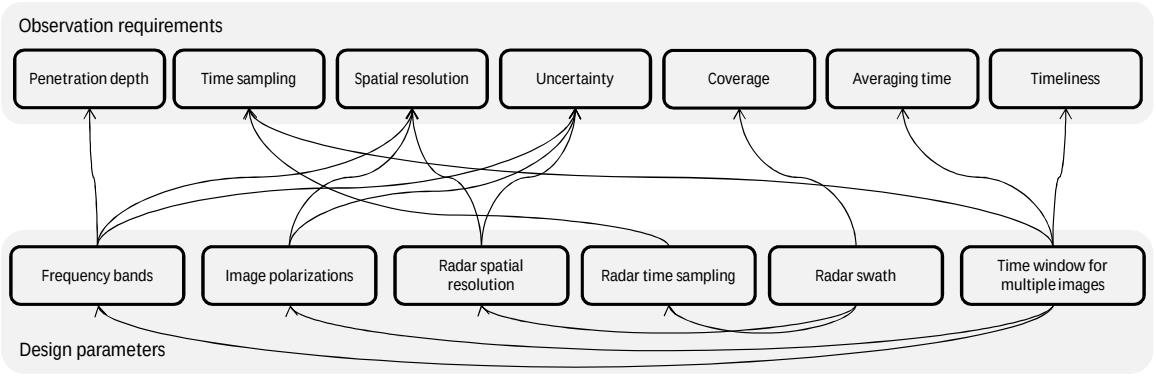

Figure 6.25: Diagram of the design parameters which can be tuned to meet the soil moisture observation requirements

2. coverage / spatial resolution
   Wide coverage usually comes with coarse spatial resolution to keep data handling manageable.

3. coverage / uncertainty
   For the same reason, coverage is usually better for dual-polarization mode than for full-polarimetric mode. Therefore wide coverage can interfere with the uncertainty requirement.

4. time sampling / uncertainty
   Fine time sampling means that the time window available to collect multiple non-simultaneous radar images is short. This may affect soil moisture uncertainty, as the time window may be too short to collect all the radar images required to reach a given uncertainty.

5. timeliness / averaging time / uncertainty
   Timely estimation means limited averaging time which in turn can affect uncertainty because of the limited radar images available.

6.3.3 Example design

Table 6.27 gives two examples of model inversion which could meet the requirements listed in table 6.24. Both examples rely on a combination of Radarsat-2 and ALOS-2 data. The information about the imaging modes of Radarsat-2 and ALOS-2 are respectively extracted from [60] and [143]. Both C- and L-bands have a penetration depth of a few centimeters, with L-band going deeper than C-band. On top of combining different frequencies, the use of at least $hh-$ and $vv-$polarizations guarantees a robust model inversion. According to Fig. 6.22b, about 1000 looks would be required to mitigate measurement noise and reach a $\pm 0.05\,\mathrm{m}^3/\mathrm{m}^3$ soil moisture uncertainty. All scenes would be acquired with a time sampling of at least 7 days. And the time window is maximum 7 days which means that for a given soil moisture estimation, one accepts radar acquisitions taken within a window of maximum 3.5 days prior and 3.5 days post the soil moisture estimation. These settings

allow reaching the required 7 day time sampling of soil moisture with a timeliness of 3.5 days which is less than the required 5 days.

The main difference between the two examples is their spatial resolution / coverage. Table 6.27a is more suitable for a regional coverage (~100 km) because of the 70-100 km swath of both satellites. Assuming that 1000 pixels are required, the 10 m radar resolution would lead to a ~320 m soil moisture resolution which is below the requirement of 1 km. The second example is more adapted for national coverage with a swath of 490-500 km, but the soil moisture resolution would only be about 3.2 km.

Note that the first example can hardly be used to reach a coverage of 1000 km. Even though the time window of 7 days allows combining multiple passes - ~4 passes with asc/dsc paths - the total range coverage would be about 280 km. With the second example, only 2 images from a given satellite would be necessary to reach a total range coverage of about 1000 km. This indicates that with current imaging performance the minimum requirements defined by the OSCAR tool are barely achievable with a national coverage.

From these two examples, it appears that one of the challenges of soil moisture monitoring is to reach national coverage while maintaining a 1 km resolution and a 7 day time sampling. ScanSAR modes are intended for monitoring applications, but their coarse resolution limits multilooking. Fine resolution modes come with a smaller footprint so that all revisit passes have to be exploited to reach the required coverage. This also means that over the area of interest the selected satellites will not be available to acquire different images for other applications.

Data availability for a given band could be improved by combining images from additional satellites or from a constellation of identical satellites such as COSMO-SkyMed, Sentinel-1A/B, or TanDEM-X. For example, with two satellites the revisit time of Sentinel-1 will be about 2 days which is more than enough to provide national coverage using the Extra Wide Swath mode (Swath $>$ 400 km, Resolution $<$ 40 m) [144]. The soil moisture resolution would be about 1.3 km after 1000-look averaging, and Sentinel-1 would remain available for other applications. In comparison, at the moment ALOS-2 is the only L-band SAR and the future ALOS-3 will not complement the ALOS mission with an identical SAR but with an optical sensor [143].

6.3.4 Discussion

Penetration depth requirement While a penetration depth of a few centimeters is acceptable for soils with emerging crops, the problem becomes more complicated for soil with mature crops for multiple reasons. The most obvious reason is that the contribution of vegetation cover to backscattering cannot be neglected. At short wavelengths the incident wave may not even sense soil moisture at all. The second reason is that root depth can take large values which are out of reach even at L-band.

For extended root system, it is actually not suitable to talk about root depth. Some root systems can have small ramifications deep into the soil, while the core of

Satellite	Radarsat-2 (Standard)	ALOS-2 (Fine Stripmap)
Frequency	C-band	L-band
Polarization	$hh + hv$	$vv + vh$
Radar spatial Resolution	10 m	10 m
Radar time sampling	<7 days	<7 days
Radar swath	100 km	70 km
Time window	7 days	

(a)

Satellite	Radarsat-2 (ScanSAR wide)	ALOS-2 (ScanSAR wide)
Frequency	C-band	L-band
Polarization	$hh + hv$	$vv + vh$
Radar spatial Resolution	100 m	60 m
Radar time sampling	<7 days	<7 days
Radar swath	500 km	490 km
Time window	7 days	

(b)

Table 6.27: Two examples of design parameters to meet the requirements of table

the root remains at shallow depths. As used by Metselaar *et al.* [145], a more appropriate parameter could be the depth D_{50} at which the cumulative root weight density (integral of root weight density over a given depth) is equal to 50% . For example for wheat $D_{50} \approx 13$ cm , and for canola $D_{50} \approx 14$ cm. Over a wet soil, such depths are not directly accessible for most of the wavelength useful for soil moisture measurement. Only the P-band ($\lambda = 30 - 100$ cm) has been reported to offer penetration depth of the order of a meter [146]. At the moment, P-band radar measurements are only available from airborne instruments. The future BIOMASS mission with launch planned in 2020, will be designed to provide P-band SAR imagery to measure forest biomass and forest height [147]. Because of the long wavelength, the spatial resolution will be limited to ~50 m with a swath of ~100 km. The revisit time will also be limited to 25 days. With these characteristics, biomass information will be available on a global scale twice a year [148]. While this is acceptable to monitor forest disturbance/recovery, the achieved spatial resolution, time sampling, and revisit time seem to coarse to benefit soil moisture estimation.

As an alternative, surface soil moisture can be used as input of a hydrological model to retrieve soil moisture profiles down to a depth of ~1 m [149]. Additional errors will have to be accounted for because of approximate modeling of the different soil layers.

Independent estimations Fig. 6.26 shows a possible arrangement for Radarsat-2 and ALOS-2 images based on the design parameters of table 6.27. Because a given Radarsat-2 image can be combined with the previous or the next ALOS-2 image, it is actually possible to estimate soil moisture every 3.5 days. However these estimations will not be independent. The time sampling of independent soil moisture estimation is only 7 days. This is similar to the difference between computing independent

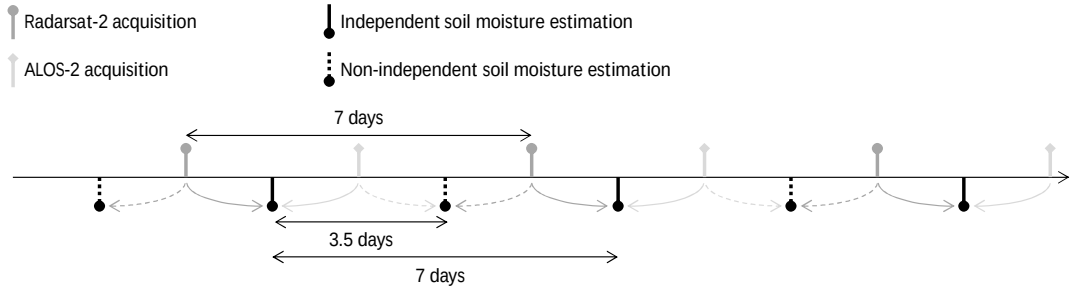

Figure 6.26: Independent and non-independent soil moisture estimations. The diagram shows independent estimations every 7 days, and intermediate estimations obtained with radar acquisitions used twice.

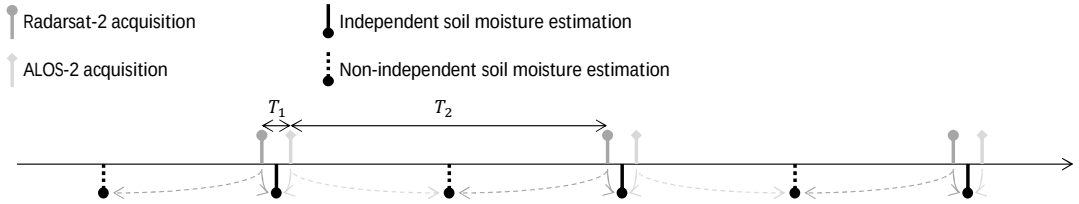

Figure 6.27: Importance of synchronization of Radarsat-2 and ALOS-2 on the averaging time. Both T_1 and T_2 have to match the timeliness requirements ($T_1/2 <$ timeliness and $T_2/2 <$ timeliness).

averages or computing non-independent averages using a moving averaging window.

Synchronization between satellites Depending on the synchronization of the satellites selected for the model inversion, the averaging time of each soil moisture estimation can be different (Fig. 6.27). As a result, the error due to crude averaging alternates and the timeliness also alternates from very timely to a more delayed estimation. While it has been shown that crude averaging may not be an issue, the synchronization of the satellites should be selected so that all estimations are timely delivered. For example on Fig. 6.27, the time sampling of both satellites may be $T_1 + T_2 = 7$ days, but a timeliness of 2 days would also require T_1, $T_2 \leq 4$ days.

Model inversion methods The previous trade-off only discussed which radar measurements were used in the model inversion. Because it relies on the contours of number of looks presented in section 6.2.3, it was implicitly assumed that soil moisture is estimated through a least-square minimization as expressed in the χ^2. Assuming that there exist a dynamic model able to provide useful a priori information on soil moisture / RMS height, Data Assimilation methods which can handle prior knowledge about the parameters could outperform the χ^2.

Following the overview of the different Data Assimilation methods in section 2.3.3, the choice of a given method will depend in particular on (1) the size of the problem, (2) the frequency of assimilation of new measurements, (3) non-linearity of the models, and (4) whether measurements posterior to the estimation date are assimilated.

1. the size of the problem is related to spatial resolution, coverage, number of assimilated images, and number of estimated parameters. Variational methods are the preferred choice for very large problems. For example, for its medium-range weather forecast, the European Centre for Medium-Range Weather Forecasts (ECMWF) assimilates every 12 hours 13 million observations in order to estimate 80 million parameters [150].
   Soil moisture estimation is a smaller problem as it is a soil surface parameter compared to the multiple layers used to model the atmosphere for weather forecasting. With two images at C-band ($hh + hv$) and two images at L-band ($vv + vh$) with a resolution of ~1 km after multilooking for a total coverage of 1000 km, there will be about 16 million measurements. And if soil moisture is estimated along with RMS height there will be about 2 million parameters. Therefore even though speckle averaging is done prior to data assimilation, the size of the problem remains a challenge for monitoring at national coverage.

2. when the parameters have to be updated as new measurements become available, a Kalman filter is more suitable than a variational method. Here, model inversion is possible only once the different images have been collected. Therefore a variational method is acceptable.

3. Backscattering models are not strongly non-linear, hence there is no need for a Particle filter.

4. In case the model inversion at a given time relies on future measurements, a (Kalman/Particle) smoother or a 4D-variational method must be used. Filters and 3D-variational method only handle information prior to the estimation.

In this thesis, the χ^2 method was suitable because soil moisture was estimated for one field at a time. From the points mentioned above, it appears that for operational monitoring, the choice of the DA method is mainly driven by the size of the problem. With millions of measurements and parameters, a Variational method may be the most suitable option. And because measurements are collected over several days, a 4D variational method might be required to include measurements posterior to the estimation date.

More is not always merrier The tradeoff on the the radar measurements to be combined, showed on multiple aspects that more does not necessarily brings merrier. On deciding whether or not adding an extra measurement, one has to verify that the improvement of one characteristic of the output does not come at the sacrifice of other aspects. For example, the minor improvement obtained when adding a $vh-$image to a combination of $hh-$ and $vv-$images might not be worth the added complexity of the inversion (longer computational time). Also adding a satellite to the inversion scheme may improve the uncertainty of the output but may also degrade to an unacceptable level its time sampling or timeliness.

Ideal soil moisture requirements This tradeoff aimed at achieving the minimum observation requirements for soil moisture. Regarding the ideal observation

requirements, Fig. 6.23 suggested that 10 000 looks would be required to reach a $\pm 0.01\,m^3/m^3$ soil moisture uncertainty. The ideal 100 m soil moisture resolution would then require a 1 m radar resolution. Spatial resolutions of this order of magnitude are only achievable by concentrating the transmitted power into a narrow beam which results in a footprint smaller than 100 km. The ideal 24 h time sampling may be achievable with a constellation of 3-4 satellites, but this will only provide a strip of images per day. Therefore, the imaged scene will be less than 100 km in the range direction.

In other words, even when neglecting all sources of uncertainty but speckle, the ideal observation requirements seem only achievable for a narrow coverage. However, considering that backscattering models and SAR measurements will never be perfect, the ideal requirements may actually be out of reach of SAR instruments.

Consequences of other applications The focus of this research was soil moisture estimation for hydrology and agriculture. Nonetheless, the reasoning involved in the trade off can be applied to other applications listed by the OSCAR tool which would also benefit from soil moisture estimation.

For hydrology and agriculture, the contours of number of looks showed that speckle may be an intrinsic physical limitation to achieve both low soil moisture uncertainty, fine spatial resolution, and wide coverage. Low uncertainty requires significant multilooking, the latter is limited by the required high fine spatial resolution of soil moisture. Sufficient multilooking can be achieved only if the radar resolution is very fine which is not compatible with wide coverage.

For the other applications listed in table 6.28, the spatial resolution requirement is not as demanding as that of hydrology/agriculture. Therefore there do not seem to be any physical limitations to achieve the uncertainty requirement.

Uncertainty requirements below $0.02\,m^3/m^3$ are marked in blue, because speckle may not be an issue but such levels of uncertainty will require accurate compensation of any biases on the measurements and on the models which may be possible in the future. Note that if one consider only speckle, even a $0.005\,m^3/m^3$ would require about 50 000 looks (with full-polarimetric L-, C-bands data) which is feasible as the 50 km soil moisture resolution would only require a ~200 m radar resolution. At this coarse resolution, the estimation could also be improved with passive radiometers.

Time sampling of less than one day are also marked in blue, because daily global land coverage would require a dense constellation of LEO SARs or GeoSARs. This is not impossible to achieve but will certainly involve large costs and intensive ground operations.

Finally, three sets of requirements are marked in red because they require both low uncertainty, medium resolution, and very fine time sampling. For example Global Numerical Weather Prediction would necessitate a ~90 m radar resolution to achieve the ideal uncertainty / spatial resolution. Even a GeoSAR which remains continuously above a given region, would hardly achieve such performance with a time sampling of just a few hours. Though not impossible, this would involve complex engineering.

Application (confidence)	**Uncertainty** [m^3/m^3]	**Resolution** [km]	**Time sampling**	**Timeliness**	**Coverage**
GEWEX[1] (tentative)	0.01 0.02 0.05	15 50 250	1 d 3 d 10 d	10 d 15 d 30 d	Global land
Global NWP[2] (reasonable)	0.02 0.04 0.08	5 15 100	3 h 1 d 5 d	3 h 1 d 5 d	Global land
High Res NWP (reasonable)	0.02 0.04 0.08	1 5 40	1 h 3 h 6 h	30 min 1 h 6 h	Global land
Nowcasting / VSRF[3] (reasonable)	0.01 0.02 0.05	5 10 50	1 h 6 h 1 d	1 h 6 h 1 d	Global land
SIA forecasts[4] (reasonable)	0.01 0.02 0.05	50 100 500	1 d 2 d 5 d	1 d 2 d 5 d	Global land
TOPC[5] (speculative)	0.005 0.007 0.01	50 60 100	7 d 11 d 30 d	1 y 1 y 2 y	Global land

[1]Global Energy and Water Cycle Experiment, [2]Global Numerical Weather Prediction, [3]Very Short Range Forecasting, [4]Seasonal and Inter-Annual forecasts, [5]Terrestrial Observing Panel for Climate

Table 6.28: Observation requirements for other soil moisture applications [7]. Black values are achievable requirements. Blue values may become achievable in the future. Red values are at the limit of being achievable even in the future. For each application the first row corresponds to the ideal requirements, while the third row corresponds to the minimum requirements. The confidence indicates how likely such a soil moisture product would benefit a given application.

Chapter 7

Discussion

This chapter is an overall discussion on the soil moisture estimation problem.

Section 7.1 highlights the need for a standard roughness measurement method.

Section 7.2 discusses change detection methods from an operational point of view.

Section 7.3 examines how backscattering models could be improved.

Section 7.4 considers the challenge of fields with crops.

Finally, section 7.5 questions the benefits for soil moisture of future SAR missions.

7.1 A standard measurement method of the roughness parameters

As seen in the literature review (section 2.1.1), there are now numerous methods available to measure surface roughness for radar scattering (pin profilers, laser profilers, meshboards, laser scanner, photogrammetry). This large range of methods is related to the fact that the potential of SAR for measuring soil moisture has been identified almost 40 years ago [151]. News methods have been developed because the existing ones did not meet all the measurement requirements identified at a given time. This variety of methods produces individual datasets of roughness measurements which are difficult to unify as they may not contain the same physical quantities. In order to build up on existing and future experiments, there is a need for a standard roughness measurement method.

To become standard, the measurement method has to be affordable financially and technically. Stereo-photogrammetry and laser scanner do not yet meet these conditions. This may be why some experiments done after 2012 still rely on roughness measurement with a simple 1-2 m pin profiler [152, 153, 90]. In section 5.1, SfM was introduced as an affordable and flexible method which can meet all the measurement requirements imposed by microwave scattering. More work is still required to fully characterize the performance of SfM against the number and type of pictures, but SfM could be suitable tool as the basis of a standard 3D measurement method.

Beyond the surface roughness measurement method, the processing chain to obtain the roughness parameters needs also to be standardized. Luckily the different computational method to access the RMS height and the correlation length are usually mathematically equivalent. The only ambiguous processing step is the detrending of the raw height measurements. Again throughout years of research, the simplest method seems to prevail, *i.e.* linear detrending of profiles. Even though it has not been tested with radar measurements, filtering the height measurements with a band-pass filter seems to be a more sensible technique. Cutoff frequencies of the filter could be recommended after a dedicated study which would examine the correlation between radar measurements and roughness measurements for various cutoff frequencies. In terms of complexity, built-in functions that implements band-pass filters are available in most numerical computing software.

Such a standard measurement method will not directly solve the soil moisture estimation problem, but it will certainly make global research more efficient.

7.2 Change detection methods

The roughness measurements analyzed in this report suggested that the soil surface can undergo over a short period of time natural changes which are not negligible for microwave scattering. Most of these changes occurred for rainy weather conditions which are not uncommon throughout the year in the UK, but could be more occasional in other countries at lower latitudes. Surface roughness changes also depends on the type of soil. Some soil compositions may be more resistant than the one available for this study.

For these two reasons change detection techniques are certainly suitable for some regions of the world and at some periods of the year. When applicable they are very attractive methods as the contribution of surface roughness to scattering does not need to be explicitly modeled. This bypasses the main challenge of soil moisture estimation at field scale.

As can be expected change detection method are not flawless. For example Moran *et al.* used the difference $\sigma^0 - \sigma^0_{dry}$ with σ^0_{dry} the backscattering response for dry soil conditions. They noticed that good results were obtained only when σ^0 corresponded to wet soil conditions ($m_v \geq 0.20\,\mathrm{m}^3/\mathrm{m}^3$). All in all, techniques relying on a difference of radar measurements will be more sensitive to measurement noise.

Even though some studies report encouraging results over a given region and a given period of time, change detection techniques seem poorly suited for continuous monitoring with large coverage. Throughout the year, changes (natural or man made) in surface roughness would need to be detected, not necessarily quantified, in order to reset the reference of the change detection algorithm.

For continuous monitoring and for estimation over regions where weather conditions make surface roughness variable, techniques which explicitly solve the ambiguity soil moisture / surface roughness are required.

7.3 Backscattering model

From the experiment with Radarsat-2, it appears that estimation of soil moisture was not successful mainly because of inaccuracy of the Oh backscattering model. The comparison between measured σ^0 and simulated σ^0 led to values which are within the RMS error obtained for the original data fitting of the model. Therefore the validity of the model may not be to blame. It is simply not accurate enough. To go further, it would be interesting to know how the different data sets used for the original data fitting may contribute differently to the final RMS error. With the Radarsat-2 data at hand, the error was systematic with underestimation of σ^0_{vh}, p, and q. The original data fitting was done with 7 data sets forming a total of 651 measurements acquired with POLARSCAT, AirSAR, and a scatterometer, at multiple locations in the US and in South Korea. If each data set led to different systematic errors, this would indicate that the model may be neglecting a property of the soil which differs for each location, or that a correction factor needs to be applied depending on the instrument.

Eventually, deriving a simple model for backscattering over agricultural surfaces is still work in progress. The flashing field phenomenon may not be describable with a simple model [16], but flashing occurs only for particular viewing directions perpendicular to the row structure of a field. Therefore, when it occurs this phenomenon could probably be avoided by preparing the soil surface in a direction which is unlikely to be perpendicular to the flying direction of SARs. Since all current SARs are placed in a sun-synchronous orbit, this restriction on the tillage direction still leaves many alternative directions.

With the exception of flashing fields, the development of a global backscattering model for bare agricultural fields, simple enough to be used operationally, seems still achievable. In order to derive an accurate model with a wide range of validity, a collection of datasets acquired with different sensors at different locations would certainly be beneficial. Such a database could already be available from the numerous published studies carried out around the world with both radar measurements and in situ measurements. To be combine together, the datasets must contain in situ measurements acquired with similar methods. This motivates again the need for standard measurement methods particularly for the roughness parameters.

7.4 Vegetation

Vegetation might be the second main challenge of soil moisture estimation after surface roughness. Similarly to the scattering of soils, the scattering of vegetation depends on the dielectric properties of vegetation (water content) and its structure [61]. For large biomass such as thick forest, soil backscattering is negligible as the signal does not penetrate the thick vegetation cover. Over agricultural fields with crops, the backscattered signal is usually modeled as the sum of a contribution from the crops and a contribution from the soil. The most commonly used vegetation model must be the Water Cloud Model which represents vegetation as a cloud of dielectric spheres parametrized by its density and its height [154]. The Water Cloud Model can then be coupled with any bare soil backscattering model. Vegetation

has been deliberately ignored in this project as it represents an additional difficulty which can be fully solved only if backscattering from the soil surface alone is clearly understood.

Since the effect of sparse vegetation on backscattering can safely be neglected, soil moisture estimation over bare soils is directly usable for a large fraction of the crop cycle. Even when vegetation is not accounted for, vegetation must still be detected to classify fields for which a bare-field method is applicable. This can be done by using visible / near infrared band imagery (SPOT or Landsat satellites) [155, 49] or a combination of radar polarizations [156, 80, 49] like the cross-polarized ratio q. Manninen *et al.* even found the co-polarized ratio $\sigma^0_{vv}/\sigma^0_{hh}$ from Envisat more effective than Spot imagery [157]. Using ratio of polarizations is also attractive from an operational point of view because the same images used for soil moisture retrieval can be used for field classification.

7.5 Future Earth Observation missions

7.5.1 Satellite constellation

For the past 20 years most of the SAR missions have been based on a single satellite at a time, with successors launched one after the other to ensure data continuity. For example it is the case of TOPEX/Poseidon, followed by Jason-1, followed by Jason-2; all from a collaboration NASA/CNES. The same goes for ERS-1 followed by ERS-2 followed by Envisat, all from ESA. And of course it applies for Radarsat-1 followed by Radarsat-2, by the Canadian Space Agency. There are also been many one-off missions, more science based, such as the Gravity Recovery And Climate Experiment (GRACE) or the Tropical Rainfall Measuring Mission (TRMM). One of the main limitations of having one satellite at a time for monitoring applications like soil moisture estimation is data availability [69, 5]. In response to this shortcoming, future missions seem to opt for satellite constellations. COSMO-Skymed (4 satellites) and TanDEM-X (2 satellites) are already operational at X-band. ESA is leading the Sentinel-1 mission with a 2 satellite constellation at C-band in the continuity of Envisat and Radarsat-2 [144]. Sentinel-1A is already providing images. The CSA is also planning the Radarsat constellation at C-band with three satellites (launch in 2018) [158].

This improvement in data availability will benefit change detection methods which rely on a series of images. It is also necessary for inversion methods based on different radar configurations. Indeed section 6.3.3 suggested that weekly estimation of soil moisture with a 1 km resolution and a coverage of 1000 km was hardly achievable with only a single satellite at L-band and a single satellite at C-band.

For operational monitoring having satellite constellations may not be the only requirement. The latest SAR instruments are targeting multiple applications thanks to a complete range of imaging modes and polarizations. These platforms are useful at the moment as they allow investigating the challenges of different applications. However for continuous monitoring of soil moisture, it is likely that a constellation of satellites with different frequency bands and operating in a single mode with long

duty cycle, will be required. In other words, there may have to be a specific soil moisture mission [151].

7.5.2 Geosynchronous SAR

All the current and announced SAR missions are with satellites in Low Earth Orbit (LEO) at altitudes ranging from 600 km to 900 km. The Geostationary ring has been used for visible and infrared bands, but has not been used yet for radar. In 1978, Tomiyasu introduced the idea of placing a SAR on a geosynchronous orbit close to the geostationary ring [159]. Because a Geosynchronous SAR (GeoSAR) would remain continuously above a selected region, it is an attractive concepts for monitoring applications. It could provide frequent measurements over a given area, and spatial resolution would remain fine enough thanks to a long integration time to build a large synthetic antenna [160].

Since Tomiyasu's early work, different concepts have been suggested with either a high inclination orbit or a low inclination orbit. The former would require a large antenna with significant transmitted power [161]. The latter has more reasonable antenna size and transmitted power as it relies on a long integration time to build a very large synthetic antenna [160]. While LEO SARs have an integration time shorter than a second (TerraSAR-X 0.25s, Radarsat-2 0.24s, ALOS-1 1.47s) [162], a GeoSAR could have an integration time from a few minutes to a few hours. One of the advantages of such a long integration time is that changes of parameters affecting backscattering will be averaged throughout the integration. On the one hand, for weekly soil moisture estimation, an integration time of a second (LEO SAR) or of several hours (GeoSAR) may not make any significant differences as both can be considered as snapshots. On the other hand, for daily soil moisture estimation, the average soil moisture sensed by GeoSAR over a window of a few hours may be more valuable than LEO SAR snapshots. Eventually a constellation of GeoSAR placed above a given region could provide daily images with a resolution of 10-100 m and continental coverage. With such characteristics, GeoSAR could be the solution to provide the measurements needed for continuous soil moisture monitoring with a performance better than the minimum observation requirements listed in table 6.28. Ultimately both LEO SAR and GeoSAR images could be combined to improve soil moisture estimation.

7.5.3 System of systems and Data Assimilation

The combination of data at different frequency bands from different satellites suggested in section 6.3.3, illustrates the benefits of a System of Systems. When it is difficult to design an EO mission which meets all the requirements of its potential applications, a System of Systems approach can compensate the gaps of the systems taken individually.

All the SAR constellations COSMO-Skymed, TanDEM-X, Sentinel-1, Radarsat constellation, are constellations of identical satellites. Using identical satellites simplifies the development of the mission because the design, manufacturing, and tests of each unit are identical. It also makes the constellation more robust in case one

satellite is lost since the satellites are interchangeable. Eventually this strategy is leading to constellations at C-band and constellations at X-band, while section 6.2.3 suggested that a combination of different frequency bands could be very beneficial for soil moisture estimation. Ideally a constellation dedicated to soil moisture would include 2 twin satellites at L-band, and 2 twin satellites at C-band. As an alternative, a System of Systems approach could be used to combine images from different single-band SAR constellations.

System of Systems is already operational for weather forecasting. Every 12 hours, the medium-range weather forecast of the ECMWF combines measurements from satellites, aircraft, automatic weather stations on land and ships, radiosondes, and other sources [150].

Similarly a System of Systems for soil moisture estimation could combine measurements from other instruments than SARs within a 24 hours window. Such instruments include for example passive radiometers, Lidar measurements, visible / near infrared sensors, and in situ measurements from permanent networks.

The L-band passive radiometer of the SMOS mission already provides global soil moisture measurements at a resolution close to 50 km. The future SMAP mission (launch in January 2015) is also going to provide L-band measurements from both a passive radiometer (~40 km resolution) and a SAR (~1-3 km resolution).

Lidars could also provide direct estimation of surface roughness. At the moment, ground-based Lidar can provide mm accuracy DEMs over plots of a few meters [163]. Airborne Lidar can provide DEMs of 100×100 m with a cm accuracy [164]. Measurement accuracy is mainly limited by system thermal noise and uncertainty on the position of the platform [165]. At the time of writing, Lidar is only available with airborne platforms as an expensive alternative to ground-based surveys. Systematic assimilation of Lidar roughness measurements seem reasonable only if spaceborne Lidar measurements become available.

As mentioned in section 7.4, visible / near infrared sensors can be used to classify bare/vegetated soils and to quantify parameters related to vegetation (Leaf Area Index, Vegetation Water Content). These vegetation parameters are useful measurements as they required to retrieve soil moisture over vegetated soils.

Finally, networks of in situ probes already provide local measurements of soil moisture [3] which could be assimilated as accurate point references.

In summary, multiple sources of measurements are already available but in practice, an operational System of Systems would require an infrastructure similar to the ECMWF dedicated to gathering and assimilating the outputs of the individual systems .

Data Assimilation methods provide an optimal implementation of System of Systems. The two main steps of Data Assimilation techniques are the *analysis step* and the *forecast step*. At the analysis step, measurements are combined with the output of the previous forecast step to generate an optimal estimation of the parameters. Then the output of the analysis step is propagated forward with the forecast step.

In this project, no Data Assimilation method was used - the χ^2 method does not handle prior information from a forecast step. Nonetheless the results obtained with

the χ^2 method can be related to Data Assimilation. Indeed, the χ^2 can be thought of an analysis step without prior information from a forecast. Thus it allows studying the benefits of the measurements alone on the estimation. In turn, the results of this study could be used for selecting the most useful measurements to be input in a Data Assimilation method.

Chapter 8

Conclusion

In this chapter, section 8.1 summarizes the main results. Section 8.2 gives a conclusion of the thesis with regard to the initial objectives. Finally section 8.3 gives recommendations for future work.

8.1 Summary

8.1.1 Surface roughness characterization

Change detection technique relies on the assumption that surface roughness remains stable over a given time window during which soil moisture is the only changing parameter to be estimated. As there is little data available to verify the constancy assumption of surface roughness for agricultural soils, an experimental setup based on Structure from Motion was designed to provide data to test this assumption. The three main outcomes of this experiment are (1) a valuable characterization of the SfM measurement method, (2) the introduction of a different approach to compute the roughness parameters (band-pass filtering / 2D PSD), and (3) information about the temporal variability of surface roughness.

Characterization of the SfM-based method Characterizing the performance of the measurement method was valuable for the experiment as it insures that the measurements can be trusted, but also for future experiments as it gives pointers in terms of how the setup should be designed to reach a set of requirements. All in all, the SfM method was able to provide high resolution DEMs ($57\,\text{points/cm}^2$) of a $\sim 6\,\text{m}^2$ soil surface with a vertical accuracy of about 3 mm. And the flexibility of SfM makes the measurement method easily adaptable to larger surface area or higher resolution/accuracy by changing mainly the number of images, the acquisition height and the focal length.

Roughness spatial statistics Surface roughness is commonly estimated over multiple transects of 1 m after linear detrending. The improved accessibility of methods based on laser scanner or photogrammetry (SfM) makes roughness measurements at higher resolution and over larger surface area possible and brings addi-

tional questions regarding how surface roughness must be accounted for in microwave scattering.

In particular, computing the roughness parameters for different sizes of DEM and different detrending methods (detrending by plane-fitting or high-pass filtering) highlighted the need to investigate which spatial scales are actually relevant for microwave scattering as this point is not clear at the moment. While not proven, applying a high-pass/band-pass filter to the DEM seem to be a sensible method to isolate the spatial scales which the radar is sensitive to.

Beyond the detrending method, the values of the roughness parameters also depend on the method used to compute these parameters. This is particularly true for anisotropic soil surface which is a common configuration when dealing with agricultural soil surfaces. After detrending the DEM, the roughness parameters are usually computed along directional 1D transects or all over the DEM. This thesis suggested computing the roughness parameters from the 2D PSD. On top of making full use of the 3D roughness measurement, two main clues suggest that this method is worth further investigation. First, in theoretical models (Small Perturbation Method, Physic Optics Model, and Integral Equation Method) σ^0 is proportional to the PSD. Second, section 5.2.5 showed that the flashing field phenomenon which was observed in [62] and [122], could be explained to some extent when computing the roughness parameters along different directions of the 2D PSD, while this was not possible with the classically used computational methods.

Finally, band-pass filtering and 2D PSD could easily be implemented together since the filtering is done efficiently in the frequency domain.

Roughness temporal variability While the two previous outcomes can be considered as byproducts of the SfM experiment, the results related to the temporal variability of surface roughness are directly related to soil moisture estimation with the change detection method.

The straightforward acquisition procedure with SfM along with permanent reference targets allowed generating multiple time series of DEMs. Visually, the DEMs captured some surface processes which are connected with weather conditions. Two notable processes are smoothing of the soil surface with rainfall and cracking of the soil surface during dry periods. As expected for the roughness parameters, smoothing comes with a decrease in RMS height and an increase in correlation length, and vice versa for the cracking process. Even though it is clear that these changes are related to soil moisture, soil temperature, and rainfall, deducting a model between these parameters and the roughness parameters is not straightforward. To date, it is nonetheless the first dataset which shows clear opposite changes between the two roughness parameters under natural conditions.

These changes are detected whatever the detrending technique which is a first indication that roughness changes mainly concern small roughness scales. This was confirmed by analyzing changes in PSD. The changes occur at roughness scales smaller than 0.5-1 m. It was not possible to explain changes in PSD happening for scales below 1 cm. This suggests that the current setup is unable to capture the small height variations happening at these scales.

Even though there exist periods with stable weather conditions during which

surface roughness can reasonably be assumed constant, backscattering simulations with the Oh model and the SfM measurements show that it is not rare to have non-negligible changes in RMS height over periods of a couple of months. Over these periods, change detection methods will be unable to provide reliable soil moisture estimation. The RMS height has to be treated as an unknown variable just like soil moisture.

To solve the inverse problem for both soil moisture and RMS height, model inversion was investigated for different combinations of radar measurements (multi-polarization, multi-incidence, multi-frequency).

8.1.2 Soil moisture estimation with multi-polarization, multi-incidence, and/or multi-incidence radar measurements

This second part of the study made use of power transform, χ^2 fitting and Monte Carlo simulation to investigate which combination of radar measurements lead to the most reliable soil moisture estimation. First, inversion with multi-polarized measurements was investigated with a set of Radarsat-2 images. Then simulated measurements were used to determine which combination of measurements was the most robust against radar speckle. Finally the last section discussed the trade-off involved when selecting the different measurements to reach the observation requirements for soil moisture.

Inversion with multi-polarized Radarsat-2 images An overall inspection of the radar measurements showed encouraging correlations with the in situ measurements of soil moisture and RMS height. Then the χ^2 method applied to two acquisition dates highlighted three points.

1. The goodness-of-fit can be used to assess the agreement between each polarization, particularly in the full-polarimetric case.

2. Correcting systematic errors on the measurements and/or on the model is critical as a 0.5 dB error can compromise soil moisture estimation.

3. The $hh-$ and $vv-$polarizations are driving the inversion, while the $vh-$polarization is not a crucial measurement.

The agreement between retrieved parameters and in situ measurements was good for these two acquisition dates in the (hh, vv) and (hh, vv, vh) cases. However it was quite poor when the method was applied to other fields and other acquisition dates. This was attributed more to the Oh model than to errors on the radar measurements. Following a comparison between measured values and simulated values from in situ measurements, the expression for q seems to be the most erroneous with systematic underestimation by the Oh model. This mismatch is not related to bad in situ measurements. Indeed another analysis which does not rely on in situ measurements showed that the measured values for q often exceed the theoretical maximum values allowed by the Oh model. In the end, the observed errors are not too surprising as they fall within the range of the RMS error of the original fit of the Oh model.

Robustness to radar speckle An overall analysis of contours at multiple polarizations showed that parameter uncertainty is driven by three factors, (1) speckle strength, (2) sensitivity of the measurements to the parameters, and (3) conditioning of the problem. Speckle is stronger for rough and wet soil surfaces and can be mitigated by multilooking at the price of spatial resolution. Sensitivity of the measurements depends on the radar configuration and the actual values of the retrieved parameters. Conditioning of the problem is related to how the different radar measurements have an independent contribution to solving the inverse problem, it also varies with the actual values of the retrieved parameters.

Simulations show that with full-polarimetric measurements, at least 2500 looks are required to reach a $\pm 0.05\,\mathrm{m}^3/\mathrm{m}^3$ uncertainty on soil moisture, which leads to a 500 m soil moisture resolution if the radar resolution is 10 m. The worst case corresponds to wet soils with RMS height close to 15-20 mm. In comparison, reliable estimation of RMS height does not seem feasible for RMS height below 20-25 mm. Above that threshold, the χ^2 returns unrealistic values from which one can only infer that the soil surface is rough with an RMS height larger than 25 mm.

The cases of multi-incidence measurements and multi-frequency measurements were then investigated. The former is not suitable to solve the inverse problem as according the Oh model a change in incidence angle only produces an offset on the measurements. The multi-frequency case turned out to be particularly robust for RMS height above 10 mm. When combined together, multi-polarization data and multi-frequency data compensate most of their respective weaknesses. With full-polarimetric measurements at both L- and C-band, at worst 600 looks are required to reach a $\pm 0.05\,\mathrm{m}^3/\mathrm{m}^3$ uncertainty on soil moisture (for wet soils and RMS height close to 10 mm).

Even though the Oh model did not seem very accurate when applied to Radarsat-2 measurements, the overall arrangement of contours agree with well known scattering behaviors and with other backscattering models. Therefore these results are fairly reliable and provide a good basis to highlight configurations which are worth further investigation.

Model inversion trade off Besides a low uncertainty, there are other conflicting requirements on soil moisture which must be considered when selecting the different sources of measurements. In short, a low uncertainty on soil moisture can be attained by (1) combining measurements in space (multilooking) and/or (2) combining measurements in time (images from multiple satellites). The first point has to be balanced with spatial resolution of soil moisture, and can be improved by using high resolution images at the price of spatial coverage. The second point must be balanced with time sampling and timeliness. In the end, merging $hh-$ and $hv-$images at C-band from Radarsat-2 with $vv-$ and $vh-$images at L-band from the ALOS-2 mission seems to be a promising combination to reach the minimum requirements defined by the OSCAR tool. The retrieval could be improved to some extent by combining more images and by taking advantage of predictive models through a Data Assimilation method. In particular, a dense constellation of LEO SARs, and/or a constellation of GeoSARs would directly improve time sampling and coverage. Such a measurement system would need to be specially designed for

soil moisture monitoring. In comparison, even when neglecting all sources of uncertainty but speckle, the results showed that the ideal requirements might only be achievable for a narrow coverage. In practice, backscattering models will never be perfect, therefore the ideal requirements might be out of reach of SAR instruments.

8.2 Conclusion

The aim of this study was to investigate the feasibility of estimating soil moisture at field scale from radar measurements. At the moment the ambiguity soil moisture / surface roughness is the main challenge of soil moisture estimation. The project was defined around two main objectives. The first one was to investigate the validity of change detection methods by generating a data set of roughness measurements which would inform on roughness temporal dynamics. The second objective was to investigate to which extend the ambiguity moisture/roughness can be solved from a combination of radar measurements.

The first objective has been met with the numerous roughness measurements acquired with SfM over more than a year. Valuable knowledge has emerged from the analysis of both the measurements method and the measurements.

First, SfM was proved to be a good alternative to roughness measurements with laser scanner or stereo-photogrammetry. It is affordable (commercial grade camera, open-source software), accessible (no expert knowledge required), flexible (unconstrained image acquisition), and measurement quality is good enough for microwave scattering (mm accuracy).

Beyond the acquisition method, an innovative processing method was also presented. Band-pass filtering is a sensible method to detrend the DEM as it isolates only the roughness scales the radar is presumably sensitive to. And computing the roughness parameters from the 2D PSD appears to match closely the way the incident wave interacts with the soil surface.

Eventually the generated time series of roughness measurements provided clear evidence that the common practice of neglecting changes in surface roughness over periods of a couple of months is not always valid. Surface roughness tends to smoothen with rainfall which leads to a decrease in RMS height and an increase in correlation length. This is particularly true for ploughed soils which have an unnatural rough aspect. Over summer, cumulative days of dry weather can lead to surface cracking which results in an increase in RMS height and a decrease in correlation length. Backscattering simulations indicates that σ^0 is mainly affected by changes in RMS height. Retrieving soil moisture without taking into account changes in roughness, can lead to error of more than $0.05\,\mathrm{m}^3/\mathrm{m}^3$ within a month. Considering that there are additional errors from the radar measurements and the backscattering model, changes in RMS height should be taken into account to obtain useful soil moisture estimation. This suggests that for some soil/weather conditions, change detection methods are not always applicable, and that operational estimation

of soil moisture all year around requires a method which solves the inverse problem for both soil moisture and RMS height.

As for the second objective, solving the ambiguity moisture/roughness with a combination of radar measurements has been investigated with both real radar measurements and simulated measurements.

Solving the inverse problem with Radarsat-2 full-polarimetric images was not entirely successful. Qualitatively, the radar measurements related well with the in situ measurements of moisture/roughness. However significant and systematic discrepancies between retrieved parameters and in situ measurements were observed - under estimation of soil moisture and over estimation of RMS height. This disagreement has been mainly attributed to inaccuracy of the backscattering model. The error between radar measurements and simulations from in situ measurements matched the error of the original data fitting of the Oh model. The systematism of this error suggests that in order to improve the retrieval, additional work is required to characterize any biases of the Oh model with regard to different radar instruments.

On the bright side, the χ^2 method coupled with power transformation of the data and Monte Carlo simulation has been a useful tool to investigate the robustness of model inversion for different combinations of radar measurements affected by speckle. The different contour maps obtained from the simulations provide good guidelines regarding the performance which can be expected from a given combination of measurements. Such information is essential for the trade off involved when selecting a combination of radar measurements to reach a set of soil moisture requirements. While the ideal observation requirements defined by the OSCAR tool seem out of reach of SAR imaging capabilities, the results suggest that using both L-band (vv and vh) measurements and C-band (hh and hv) measurements would be an attractive combination to reach the minimum requirements. It appears that time sampling and coverage are the main limitations with the current operational radar missions. But these two points will improve with future radar constellations. Ultimately, assimilating multi-polarized and multi-frequency measurements seems to be a good basis for an eventual Data Assimilation system for global soil moisture monitoring.

In conclusion, this thesis suggests the SfM measurement method along with new processing techniques (band-pass filtering / 2D PSD) are good tools to improve understanding on the interaction between the incident electromagnetic wave and the soil surface.

While the SfM measurements indicates that change detection techniques may not always be applicable, this thesis suggests that the ambiguity moisture/roughness can be reliably resolved by combining both multi-polarized and multi-frequency radar measurements. Even though, current EO radars may allow reaching only the minimum requirements of soil moisture observation, this point will certainly improve with future radar constellations and/or with different EO platforms such

as GeoSAR.

The ambiguity soil moisture / surface roughness remains a challenge for field-scale soil moisture estimation, but research on this matter is still progressing with the availability of new instruments and analysis tools. As no fundamental limitation has yet been identified, operational soil moisture monitoring still appear feasible.

8.3 Future work

The SfM measurement method The SfM method has been characterized to a degree which is acceptable for its use in this project but further work is required to convince the scientific community to use SfM as a standard measurement method.

First it would be interesting to test with different setups, the linear regression which predicts the point cloud density on Fig. 5.2c. In this project only two types of acquisitions (DEM A and DEM B) were available and all the images were acquired with a nadir-pointed camera. Therefore further work is also needed to assess how the combination of different acquisition heights and different viewing angles impacts the SfM reconstruction.

Once the effects of the different acquisition parameters have been characterized, a direct comparison of SfM with other measurement methods (laser scanner, photogrammetry) would be necessary. SfM and photogrammetry are more comparable, as both techniques generate DEM from pictures. Following the attempt to compare SfM and photogrammetry in section 5.1.2, a setup with identical camera/lens, image compression, soil surface, and method for estimating the RMS error would be needed to compare the two methods rigorously.

Estimation of roughness parameters In section 5.2, a high-pass filter was used to remove unwanted roughness features before computing the roughness parameters, and the 2D PSD was used to generate directional estimation of roughness parameters. The former seems an efficient detrending method especially with large DEMs for which linear detrending is clearly not suitable. And the 2D PSD is a sensible method with regard to how surface roughness is accounted for in theoretical backscattering models. It also explains to some extent the flashing field phenomenon.

The next step would be to test these methods against radar measurements. The filtering technique could be tested by looking at the correlation between radar measurements and the roughness parameters estimated from the 2D PSD after filtering with different cutoff frequencies. And the directional roughness estimation with the 2D PSD could be tested against radar acquisitions taken along different directions over a field with a strong row structure. Some preliminary tests could be done with the Radarsat-2 images and the SfM measurements available for this study. Ideally, the radar measurements would be acquired with a truck-mounted scatterometer for better controllability, and the axes of the DEMs generated with SfM should be referenced with regard to the radar azimuth to control the direction of the roughness estimation.

Model inversion In section 6.1, the Radarsat-2 images have been used to test model inversion based on multi-polarized radar measurements. All in all the absolute value of soil moisture was poorly retrieved, but the change in σ^0 for the different polarization seemed to match the largest variations in soil moisture. Therefore, it would be interesting to test some change detection techniques for a given polarization. Even though there were many rainfalls throughout the experimental campaign, the time gap between successive acquisitions may be small enough (7-14 days) to neglect changes in surface roughness particularly over smooth soil surfaces. In parallel, changes in roughness parameters could be evaluated more thoroughly after processing all the SfM measurements available for each acquisition dates. This was not done for this project, as only a rough estimation of the RMS height was needed for comparison with its retrieved value.

Regarding the systematic underestimation of σ^0_{vh}, p, and q in section 6.1, one should investigate how the different data sets used to determine the Oh model [83] might have a systematic contribution to the final RMS error, according to the different radar instruments used for each data set. Such information appears to be missing in [83] and it could certainly be obtained by contacting the main author.

Using the same Radarsat-2 data set, it would also be interesting to test the model inversion with different backscattering model. Using only the $hh-$ and $vv-$polarizations, a comparison could be done between inversions of the Oh model, the Dubois model, or the IEM. The fact that no expression is available for the $vh-$polarization in the Dubois model is not an issue, as inversion of the Oh model showed that the $vh-$measurements were not critical. Using the IEM may not be straightforward, mainly because one must choose a shape of autocorrelation function and because the correlation length is another unknown parameter.

Operational monitoring In this project, the focus was on the ambiguity soil moisture / surface roughness over bare agricultural soils. Future work will be required to assess the feasibility of the whole processing chain in particular (1) the automatic detection of agricultural fields for which the bare soil assumption is valid, (2) speckle averaging before or after the detection of bare field, and (3) soil moisture estimation with a Data Assimilation method which can handle all the detected fields.

The first two points could be investigated with the Radarsat-2 dataset. Detection of the bare field could be investigated with the cross-polarized ratio $\sigma^0_{vh}/\sigma^0_{vv}$ [80] or the co-polarized ratio $\sigma^0_{vv}/\sigma^0_{hh}$ [157]. Detection may also rely on the fact that pixels which belong to a uniform field are expected to take values which are exponentially distributed. Then the speckle averaging required to reliably estimate soil moisture should be done only after the detection step, as it may smooth out all the features of the image if it is done before.

Regarding the Data Assimilation method, one should investigate to what extent the retrieval can be improved by incorporating a priori information on soil moisture and RMS height, and by accounting for spatial correlation between neighboring fields.

Dissemination of the results So far only the description of the SfM setup has been published in a scientific journal. Future work should also include dissemination of the results regarding (1) the temporal variability of surface roughness, (2) the benefits of using directional roughness estimation with the 2D PSD and (3) the robustness of model inversion for different combinations of radar measurements.

Priority should be given to the dissemination of the current results and then to the tasks which reuse the data sets already available for this project. Among those, the tasks with the lowest priority might be those related to operational monitoring. In comparison, testing the filtering / 2D PSD method with truck-mounted radar measurements will be more demanding in terms of time and funding, therefore preliminary tests should be done with the current data set.

References

[1] M. J. Escorihuela. *Estimation de l'humidité du sol à partir de données radiométriques en bande-L: préparation de la mission SMOS*. PhD thesis, Institut National Polytechnique de Toulouse, 2006.

[2] J. Komma, G. Blöschl, and C. Reszler. Soil moisture updating by ensemble Kalman filtering in real-time flood forecasting. *Journal of Hydrology*, 357(3-4):228–242, Aug 2008.

[3] International soil moisture network. `https://ismn.geo.tuwien.ac.at/`.

[4] P. Dobriyal, A. Qureshi, R. Badola, and S. A. Hussain. A review of the methods available for estimating soil moisture and its implications for water resource management. *Journal of Hydrology*, 458-459:110–117, Aug 2012.

[5] S. Nichols. Review and evaluation of remote sensing methods for soil-moisture estimation. *J. Photon. Energy*, page 028001, Jan 2011.

[6] Y.H. Kerr, P. Waldteufel, J.-P. Wigneron, S. Delwart, F. Cabot, J. Boutin, M.-J. Escorihuela, J. Font, N. Reul, C. Gruhier, S.E. Juglea, M.R. Drinkwater, A. Hahne, M. Martin-Neira, and S. Mecklenburg. The smos mission: New tool for monitoring key elements ofthe global water cycle. *Proceedings of the IEEE*, 98(5):666–687, May 2010.

[7] World Meteorological Organization. Oscar, observing systems capability analysis and review tool. `http://www.wmo-sat.info/oscar/variables/view/14`.

[8] Y. Oh. Radar measurement of soil moisture: From professor fawwaz ulaby's pioneering works in the early 1970s to its current status. In *Geoscience and Remote Sensing Symposium (IGARSS), 2012 IEEE International*, pages 1258–1261, July 2012.

[9] I. Gherboudj, R. Magagi, A. A. Berg, and B. Toth. Soil moisture retrieval over agricultural fields from multi-polarized and multi-angular Radarsat-2 SAR data. *Remote Sensing of Environment*, 115(1):33–43, Jan 2011.

[10] Y. Oh. Quantitative retrieval of soil moisture content and surface roughness from multipolarized radar observations of bare soil surfaces. *IEEE Transactions on Geoscience and Remote Sensing*, 42(3):596–601, Mar 2004.

[11] N. Baghdadi, N. Holah, and M. Zribi. Soil moisture estimation using multi-incidence and multi-polarization asar data. *International Journal of Remote Sensing*, 27(10):1907–1920, May 2006.

[12] P. Marzahn, D. Rieke-Zapp, and R. Ludwig. Assessment of soil surface roughness statistics for microwave remote sensing applications using a simple photogrammetric acquisition system. *ISPRS Journal of Photogrammetry and Remote Sensing*, 72:80–89, Aug 2012.

[13] H. Lievens, H. Vernieuwe, J. Ãlvarez Mozos, B. De Baets, and N. E. C. Verhoest. Error in radar-derived soil moisture due to roughness parameterization: An analysis based on synthetical surface profiles. *Sensors*, 9(2):1067–1093, Feb 2009.

[14] N. E.C Verhoest, H. Lievens, W. Wagner, J. Ãlvarez Mozos, M. S. Moran, and F. Mattia. On the soil roughness parameterization problem in soil moisture retrieval of bare surfaces from synthetic aperture radar. *Sensors*, 8(7):4213–4248, Jul 2008.

[15] X. Blaes and P. Defourny. Characterizing bidimensional roughness of agricultural soil surfaces for SAR modeling. *IEEE Transactions on Geoscience and Remote Sensing*, 46(12):4050–4061, 2008.

[16] F. Mattia. Coherent and incoherent scattering from tilled soil surfaces. *Waves in Random and Complex Media*, 21(2):278–300, May 2011.

[17] A. Balenzano, F. Mattia, G. Satalino, and M. W. J. Davidson. Dense Temporal Series of C- and L-band SAR Data for Soil Moisture Retrieval Over Agricultural Crops. *IEEE Journal of Selected Topics in Applied Earth Observations and Remote Sensing*, 4(2):439–450, Jun 2011.

[18] H. Yang, J. Shi, Z. Li, and H. Guo. Temporal and spatial soil moisture change pattern detection in an agricultural area using multi-temporal Radarsat ScanSAR data. *International Journal of Remote Sensing*, 27(19):4199–4212, Oct 2006.

[19] A. J. Wickel, T. J. Jackson, and E. F. Wood. Multitemporal monitoring of soil moisture with Radarsat SAR during the 1997 Southern Great Plains hydrology experiment. *International Journal of Remote Sensing*, 22(8):1571–1583, Jan 2001.

[20] K. Seung-Bum, T. Leung, J.T. Johnson, H. Shaowu, J.J. van Zyl, and E.G. Njoku. Soil moisture retrieval using time-series radar observations over bare surfaces. *Geoscience and Remote Sensing, IEEE Transactions on*, 50(5):1853–1863, May 2012.

[21] L. Brocca, F. Melone, T. Moramarco, and R. Morbidelli. Spatial-temporal variability of soil moisture and its estimation across scales. *Water Resources Research*, 46(2), Feb 2010.

[22] L. Brocca, T. Tullo, F. Melone, T. Moramarco, and R. Morbidelli. Catchment scale soil moisture spatial-temporal variability. *Journal of Hydrology*, 422-423:63–75, Feb 2012.

[23] B.P Mohanty and T.H Skaggs. Spatio-temporal evolution and time-stable characteristics of soil moisture within remote sensing footprints with varying soil, slope, and vegetation. *Advances in Water Resources*, 24(9-10):1051–1067, Nov 2001.

[24] A. W. Western, S.L. Zhou, R. B. Grayson, T. A. McMahon, G. Blöschl, and D. J. Wilson. Spatial correlation of soil moisture in small catchments and its relationship to dominant spatial hydrological processes. *Journal of Hydrology*, 286(1-4):113–134, Jan 2004.

[25] C.D. Rodgers. *Inverse Methods for Atmospheric Sounding: Theory and Practice*. Series on atmospheric, oceanic and planetary physics. World Scientific, 2000.

[26] B. Snapir, S. Hobbs, and T.W. Waine. Roughness measurements over an agricultural soil surface with structure from motion. *ISPRS Journal of Photogrammetry and Remote Sensing*, 96:210–223, Oct 2014.

[27] Canadian Space Agency. Specific Request for SOAR Proposal, SOAR Education International (SOAR-EI) Initiative . `http://www.asc-csa.gc.ca/pdf/eng/ao/soar-ei-rfp-2012.pdf`, December 2012.

[28] B. Snapir and S. Hobbs. Effect of temporal sampling and timing for soil moisture measurements at field scale. *EGU General Assembly, Geophysical Research Abstracts*, 14, 2012.

[29] M.A. Aguilar, F.J. Aguilar, and J. Negreiros. Off-the-shelf laser scanning and close-range digital photogrammetry for measuring agricultural soils microrelief. *Biosystems Engineering*, 103(4):504–517, Aug 2009.

[30] M. Mirzaei, M. S. Ruy, T. Ziarati, and A. Salehi. Monitoring of soil roughness caused by rainfall using stereo-photogrammetry. *International Research Journal of Applied and Basic Sciences*, 3:322–338, 2012.

[31] R. Szeliski. *Computer vision: algorithms and applications*. Springer, 2010.

[32] M. R. James and S. Robson. Straightforward reconstruction of 3D surfaces and topography with a camera: Accuracy and geoscience application. *Journal of Geophysical Research*, 117(F3), 2012.

[33] D. G. Lowe. Distinctive image features from scale-invariant keypoints. *International Journal of Computer Vision*, 60(2):91–110, Nov 2004.

[34] E. K. Stathopoulou, A. Valanis, J. L. Lerma, and A. Georgopoulos. High and low resolution textured models of complex architectural surfaces. *Int. Arch. Photogramm. Remote Sens. Spatial Inf. Sci.*, XXXVIII-5/W16:77–81, Sep 2012.

[35] A. Irschara, V. Kaufmann B, M. Klopschitz A, H. Bischof A, and F. Leberl A. Towards fully automatic photogrammetric reconstruction using digital images taken from uavs. In *In Proc. International Society for Photogrammetry and Remote Sensing Symposium*, 2010.

[36] M.J. Westoby, J. Brasington, N.F. Glasser, M.J. Hambrey, and J.M. Reynolds. Structure-from-Motion photogrammetry: A low-cost, effective tool for geoscience applications. *Geomorphology*, 179:300–314, Dec 2012.

[37] F. Bretar, M. Arab-Sedze, J. Champion, M. Pierrot-Deseilligny, E. Heggy, and S. Jacquemoud. An advanced photogrammetric method to measure surface roughness: Application to volcanic terrains in the piton de la fournaise, Reunion island. *Remote Sensing of Environment*, 135:1–11, Aug 2013.

[38] A. Wayman. Space applications for structure from motion using automatic feature detection. *Cranfield University - Msc report*, 2012.

[39] X. Blaes, P. Defourny, M. Callens, and N.E.C. Verhoest. *Bi-dimensional soil roughness measurement by photogrammetry for SAR modeling of agricultural surfaces*, pages 4038–4041. Institute of Electrical and Electronics Engineers, 2004.

[40] O. Taconet and V. Ciarletti. Estimating soil roughness indices on a ridge-and-furrow surface using stereo photogrammetry. *Soil and Tillage Research*, 93(1):64 – 76, 2007.

[41] M. Davidson, F. Mattia, G. Satalino, N.E.C. Verhoest, T. Le Toan, M. Borgeaud, J.M.B. Louis, and E. Attema. Joint statistical properties of rms height and correlation length derived from multisite 1-m roughness measurements. *Geoscience and Remote Sensing, IEEE Transactions on*, 41(7):1651–1658, July 2003.

[42] L. Zhixiong, C. Nan, U.D. Perdok, and W.B. Hoogmoed. Characterisation of soil profile roughness. *Biosystems Engineering*, 91(3):369–377, Jul 2005.

[43] W. H. Press, S. A. Teukolsky, W. T. Vetterling, and B. P. Flannery. *Numerical Recipes, The Art of Scientific Computing, Third Edition*, chapter Chapter 13 Fourier and Spectral Application, page 722. Cambridge University Press, 2007.

[44] P. Marzahn, M. Seidel, and R. Ludwig. Decomposing dual scale soil surface roughness for microwave remote sensing applications. *Remote Sensing*, 4(12):2016–2032, Dec 2012.

[45] Y. Oh and Y. C. Kay. Condition for precise measurement of soil surface roughness. *IEEE Transactions on Geoscience and Remote Sensing*, 36(2):691–695, Mar 1998.

[46] W. Dierking. Quantitative roughness characterization of geological surfaces and implications for radar signature analysis. *Geoscience and Remote Sensing, IEEE Transactions on*, 37(5):2397–2412, 1999.

[47] D.P. Thoma, M.S. Moran, R. Bryant, M.M. Rahman, C.D. Holifield Collins, T.O. Keefer, R. Noriega, I. Osman, S.M. Skrivin, M.A. Tischler, and et al. Appropriate scale of soil moisture retrieval from high resolution radar imagery for bare and minimally vegetated soils. *Remote Sensing of Environment*, 112(2):403–414, Feb 2008.

[48] M. Shoshany, T. Svoray, P. J. Curran, G. M. Foody, and A. Perevolotsky. The relationship between ers-2 Sar backscatter and soil moisture: Generalization from a humid to semi-arid transect. *International Journal of Remote Sensing*, 21(11):2337–2343, Jan 2000.

[49] M. Susan Moran. Soil moisture evaluation using multi-temporal synthetic aperture radar (SAR) in semiarid rangeland. *Agricultural and Forest Meteorology*, 105(1-3):69–80, Nov 2000.

[50] T. M. Zobeck and C. A. Onstad. Tillage and rainfall effects on random roughness: A review. *Soil and Tillage Research*, 9(1):1–20, Jan 1987.

[51] J. Álvarez-Mozos, N. E.C. Verhoest, A. Larrañaga, J. Casalí, and M. González-Audícana. Influence of surface roughness spatial variability and temporal dynamics on the retrieval of soil moisture from SAR observations. *Sensors*, 9(1):463–489, Jan 2009.

[52] S. Moritani, T. Yamamoto, H. Andry, M. Inoue, T. Nishimura, H. Fujimaki, R. Kimura, and H. Saito. Monitoring of soil surface under wind and water erosion by photogrammetry. *Wind Tunnels and Experimental Fluid Dynamics Research*, Jul 2011.

[53] C. Berger, M. Schulze, D. Rieke-Zapp, and F. Schlunegger. Rill development and soil erosion: a laboratory study of slope and rainfall intensity. *Earth Surface Processes and Landforms*, 35(12):1456–1467, Sep 2010.

[54] B. C. Peter Heng, Jim H. Chandler, and Alona Armstrong. Applying close range digital photogrammetry in soil erosion studies. *The Photogrammetric Record*, 25(131):240–265, Sep 2010.

[55] D. H. Rieke-Zapp and M. A. Nearing. Digital close range photogrammetry for measurement of soil erosion. *Photogrammetric Record*, 20(109):69–87, Mar 2005.

[56] C. Huang and J. M. Bradford. Applications of a laser scanner to quantify soil microtopography. *Soil Science Society of America Journal*, 56(1):14, 1992.

[57] A. C. Guzha. Effects of tillage on soil microrelief, surface depression storage and soil water storage. *Soil and Tillage Research*, 76(2):105–114, April 2004.

[58] M. Callens, N. E C Verhoest, and M. Davidson. Parameterization of tillage-induced single-scale soil roughness from 4-m profiles. *Geoscience and Remote Sensing, IEEE Transactions on*, 44(4):878–888, April 2006.

[59] A. T. Manninen. Multiscale surface roughness description for scattering modelling of bare soil. *Physica A: Statistical Mechanics and its Applications*, 319:535–551, Mar 2003.

[60] C.E. Livingstone, I. Sikaneta, C. Gierull, S. Chiu, and P. Beaulne. Radarsat-2 system and mode description. Technical report, DTIC Document, 2006.

[61] F. T. Ulaby, R. K. Moore, and A. K Fung. *Microwave remote sensing: active and passive*, volume 2. Artech House, Boston, MA, 1982.

[62] U. Wegmüller, M. Santoro, F. Mattia, A. Balenzano, G. Satalino, P. Marzahn, G. Fischer, R. Ludwig, and N. Floury. Progress in the understanding of narrow directional microwave scattering of agricultural fields. *Remote Sensing of Environment*, 115(10):2423–2433, Oct 2011.

[63] U. Wegmüller, R.A. Cordey, C. Werner, and P.J. Meadows. "flashing fields" in nearly simultaneous envisat and ers-2 C-band SAR images. *IEEE Transactions on Geoscience and Remote Sensing*, 44(4):801–805.

[64] M. Zribi, O. Taconet, V. Ciarletti, and D. Vidal-Madjar. Effect of row structures on radar microwave measurements over soil surface. *International Journal of Remote Sensing*, 23(24):5211–5224, Jan 2002.

[65] N. Baghdadi, N. Holah, and M. Zribi. Soil moisture estimation using multi-incidence and multi-polarization asar data. *International Journal of Remote Sensing*, 27(10):1907–1920, May 2006.

[66] H.S. Srivastava, P. Patel, M.L. Manchanda, and S. Adiga. Use of multiincidence angle RADarsat-1 Sar data to incorporate the effect of surface roughness in soil moisture estimation. *IEEE Transactions on Geoscience and Remote Sensing*, 41(7):1638–1640, Jul 2003.

[67] A. Weimann, M. Von Schonermark, A. Schumann, P. Jorn, and R. Gunther. Soil moisture estimation with ers-1 Sar data in the east-german loess soil area. *International Journal of Remote Sensing*, 19(2):237–243, Jan 1998.

[68] N. Baghdadi, M. Aubert, O. Cerdan, L. Franchistéguy, C. Viel, M. Eric, M. Zribi, and J. F. Desprats. Operational mapping of soil moisture using synthetic aperture radar data: Application to the touch basin (France). *Sensors*, 7(10):2458–2483, Oct 2007.

[69] K. C. Kornelsen and P. Coulibaly. Advances in soil moisture retrieval from synthetic aperture radar and hydrological applications. *Journal of Hydrology*, 476:460–489, Jan 2013.

[70] D. P. Thoma, M. S. Moran, R. Bryant, M. Rahman, C. D. Holifield-Collins, S. Skirvin, E. E. Sano, and K. Slocum. Comparison of four models to determine surface soil moisture from c-band radar imagery in a sparsely vegetated semiarid landscape. *Water Resources Research*, 42(1), Jan 2006.

[71] I. Hajnsek and K. Papathanassiou. Rough surface scattering models. http://earth.eo.esa.int/polsarpro/Manuals/2_Rough_Surface_Scattering_Models.pdf, January 2005.

[72] A.K. Fung, Z. Li, and K.S. Chen. Backscattering from a randomly rough dielectric surface. *IEEE Transactions on Geoscience and Remote Sensing*, 30(2):356–369, Mar 1992.

[73] K.S. Chen, Tzong-Dar Wu, Leung Tsang, Qin Li, Jiancheng Shi, and A.K. Fung. Emission of rough surfaces calculated by the integral equation method with comparison to three-dimensional moment method simulations. *IEEE Transactions on Geoscience and Remote Sensing*, 41(1):90–101, Jan 2003.

[74] L. Rakotoarivony, O. Taconet, D. Vidal-Madjar, P. Bellemain, and M. Benallegue. Radar backscattering over agricultural bare soils. *Journal of Electromagnetic Waves and Applications*, 10(2):187–209, Jan 1996.

[75] N. Baghdadi, I. Gherboudj, M. Zribi, M. Sahebi, C. King, and F. Bonn. Semi-empirical calibration of the iem backscattering model using radar images and moisture and roughness field measurements. *International Journal of Remote Sensing*, 25(18):3593–3623, Sep 2004.

[76] R. Bryant, M. S. Moran, D. P. Thoma, C. D. Holifield Collins, S. Skirvin, M. Rahman, K. Slocum, P. Starks, D. Bosch, and M. P. Gonzalez Dugo. Measuring surface roughness height to parameterize radar backscatter models for retrieval of surface soil moisture. *IEEE Geoscience and Remote Sensing Letters*, 4(1):137–141, 2007.

[77] M. M. Rahman, M. S. Moran, D. P. Thoma, R. Bryant, E. E. Sano, C. D. Holifield Collins, S. Skirvin, C. Kershner, and B. J. Orr. A derivation of roughness correlation length for parameterizing radar backscatter models. *International Journal of Remote Sensing*, 28(18):3995–4012, Sep 2007.

[78] S. Jiancheng, J. Wang, A.Y. Hsu, P.E. O'Neill, and E.T. Engman. Estimation of bare surface soil moisture and surface roughness parameter using l-band SAR image data. *IEEE Transactions on Geoscience and Remote Sensing*, 35(5):1254–1266, 1997.

[79] Y. Oh, K. Sarabandi, and F.T. Ulaby. An empirical model and an inversion technique for radar scattering from bare soil surfaces. *IEEE Transactions on Geoscience and Remote Sensing*, 30(2):370–381, Mar 1992.

[80] P.C. Dubois, J. van Zyl, and T. Engman. Measuring soil moisture with imaging radars. *IEEE Transactions on Geoscience and Remote Sensing*, 33(4):915–926, Jul 1995.

[81] M. Hallikainen, F. Ulaby, M. Dobson, M. El-rayes, and L.K. Wu. Microwave dielectric behavior of wet soil-part 1: Empirical models and experimental observations. *IEEE Transactions on Geoscience and Remote Sensing*, GE-23(1):25–34.

[82] Y. Oh, K. Sarabandi, and F.T. Ulaby. An inversion algorithm for retrieving soil moisture and surface roughness from polarimetric radar observation. In *Geoscience and Remote Sensing Symposium, 1994. IGARSS '94. Surface and Atmospheric Remote Sensing: Technologies, Data Analysis and Interpretation., International*, volume 3, pages 1582–1584 vol.3, Aug 1994.

[83] Y. Oh, K. Sarabandi, and F.T. Ulaby. Semi-empirical model of the ensemble-averaged differential mueller matrix for microwave backscattering from bare soil surfaces. *IEEE Transactions on Geoscience and Remote Sensing*, 40(6):1348–1355, Jun 2002.

[84] K. Sarabandi, L.E. Pierce, Y. Oh, M.C. Dobson, F.T. Ulaby, A. Freeman, and P. Dubois. Cross-calibration experiment of jpl AIRSar and truck-mounted polarimetric scatterometer. *IEEE Transactions on Geoscience and Remote Sensing*, 32(5):975–985, 1994.

[85] N. Baghdadi and M. Zribi. Evaluation of radar backscatter models iem, oh and dubois using experimental observations. *International Journal of Remote Sensing*, 27(18):3831–3852, Sep 2006.

[86] N. Baghdadi, E. Saba, M. Aubert, M. Zribi, and F. Baup. Evaluation of radar backscattering models iem, oh, and dubois for sar data in x-band over bare soils. *Geoscience and Remote Sensing Letters, IEEE*, 8(6):1160–1164, 2011.

[87] M. Barber, F. Grings, P. Perna, M. Piscitelli, M. Maas, C. Bruscantini, J. Jacobo-Berlles, and H. Karszenbaum. Speckle noise and soil heterogeneities as error sources in a bayesian soil moisture retrieval scheme for sar data. *Selected Topics in Applied Earth Observations and Remote Sensing, IEEE Journal of*, 5(3):942–951, June 2012.

[88] S. Quegan C. Oliver. *Understanding Synthetic Aperture Radar Images*, chapter 4, pages 85–99. SciTech Publishing - Technology & Engineering, 2004.

[89] L. Jong-Sen, K.W. Hoppel, S.A. Mango, and A.R. Miller. Intensity and phase statistics of multilook polarimetric and interferometric SAR imagery. *IEEE Transactions on Geoscience and Remote Sensing*, 32(5):1017–1028, 1994.

[90] S.K. Kweon and Y. Oh. Estimation of soil moisture and surface roughness from single-polarized radar data for bare soil surface and comparison with dual- and quad-polarization cases. *Geoscience and Remote Sensing, IEEE Transactions on*, 52(7):4056–4064, July 2014.

[91] N. E. C. Verhoest, B. De Baets, and H. Vernieuwe. A takagi-sugeno fuzzy rule-based model for soil moisture retrieval from SAR under soil roughness uncertainty. *IEEE Transactions on Geoscience and Remote Sensing*, 45(5):1351–1360.

[92] A. K. Jain, J. Mao, and K.M. Mohiuddin. Artificial neural networks: A tutorial. *Computer*, 29(3):31–44, 1996.

[93] S.Y. Hsu, T. Masters, M. Olson, M. F. Tenorio, and T. Grogan. Comparative analysis of five neural network models. *Remote Sensing Reviews*, 6(1):319–329, Jan 1992.

[94] C. Notarnicola, M. Angiulli, and F. Posa. Soil moisture retrieval from remotely sensed data: Neural network approach versus Bayesian method. *IEEE Transactions on Geoscience and Remote Sensing*, 46(2):547–557.

[95] N. Baghdadi, S. Gaultier, and C. King. Retrieving surface roughness and soil moisture from synthetic aperture radar (sar) data using neural networks. *Canadian Journal of Remote Sensing*, 28(5):701–711, 2002.

[96] N. Pierdicca, P. Castracane, and L. Pulvirenti. Inversion of electromagnetic models for bare soil parameter estimation from multifrequency polarimetric SAR data. *Sensors*, 8(12):8181–8200, Dec 2008.

[97] S. Said, U. C. Kothyari, and M. K. Arora. ANN-Based Soil Moisture Retrieval over Bare and Vegetated Areas Using ers-2 Sar data. *J. Hydrol. Eng.*, 13(6):461–475, Jun 2008.

[98] C. K. Wikle and L. M. Berliner. A Bayesian tutorial for data assimilation. *Physica D: Nonlinear Phenomena*, 230(1-2):1–16, Jun 2007.

[99] Z.S. Haddad, P. Dubois, and J.J. van Zyl. Bayesian estimation of soil parameters from radar backscatter data. *Geoscience and Remote Sensing, IEEE Transactions on*, 34(1):76–82, Jan 1996.

[100] C. Notarnicola and F. Posa. Bayesian algorithm for the estimation of the dielectric constant from active and passive remotely sensed data. *IEEE Geoscience and Remote Sensing Letters*, 1(3):179–183, Jul 2004.

[101] W. H. Press, S. A. Teukolsky, W. T. Vetterling, and B. P. Flannery. *Numerical Recipes, The Art of Scientific Computing, Third Edition*, chapter Chapter 15 Modelling Data, pages 773–839. Cambridge University Press, 2007.

[102] J. Edward Jackson. *A User's Guide to Principal Components*. Wiley-Interscience, 1991.

[103] P. J. Ossenbruggen, H. Spanjers, and A. Klapwik. Assessment of a two-step nitrification model for activated sludge. *Water Research*, 30(4):939–953, Apr 1996.

[104] R. Du Plessis. *Poor Man's Explanation of Kalman Filtering: Or How I Stopped Worrying & Learned to Love Matrix Inversion*. Taygeta Scientific Incorporated, 1997.

[105] J. H. Neal. The effect of the degree of slope and rainfall characteristics on runoff and soil erosion1. *Soil Science Society of America Journal*, 2(C):525, 1938.

[106] Delta-T Devices. Thetaprobe soil moisture sensor. *User Manual ML2x-UM-1.21*, 1999.

[107] D. Small and A. Schubert. Guide to ASAR Geocoding. Technical report, Remote Sensing Laboratories, University of Zurich, 2008.

[108] Earthnet Online. Radar course III - 15. Slant range / ground range. `http://earth.esa.int/applications/data_util/SARDOCS/spaceborne/Radar_Courses/Radar_Course_III/slant_range_ground_range.htm`.

[109] P. Mach, J. Thuring, and D. Samal. Transformation of data for statistical processing. In *Electronics Technology, 2006. ISSE '06. 29th International Spring Seminar on*, pages 278–282, May 2006.

[110] G. E.P. Box and D. R. Cox. An analysis of transformations. *Journal of the Royal Statistical Society, Series B*, 26(2):211–252, 1964.

[111] W. H. Press, S. A. Teukolsky, W. T. Vetterling, and B. P. Flannery. *Numerical Recipes, The Art of Scientific Computing, Third Edition*, chapter Chapter 14 Statistical Description of Data, page 722. Cambridge University Press, 2007.

[112] A. Remond, A. Beaudoin, and C. King. SAR imagery to estimate roughness parameters when modelling runoff risk. *International Journal of Remote Sensing*, 20(13):2613–2625, Jan 1999.

[113] T.J. Jackson, H. McNairn, M.A. Weltz, B. Brisco, and R. Brown. First order surface roughness correction of active microwave observations for estimating soil moisture. *Geoscience and Remote Sensing, IEEE Transactions on*, 35(4):1065–1069, Jul 1997.

[114] M. Trudel, F. Charbonneau, and R. Leconte. Surface roughness classification with multipolarized c-band sar data. In *IGARSS (2)*, pages 727–730, 2008.

[115] Weather Underground. Cranfield Airport Weather Station. `http://www.wunderground.com/global/stations/03557.html?`

[116] ISO VIM. International vocabulary of basic and general terms in metrology (vim). *International Organization*, 2004:09–14, 2004.

[117] Corporate Communications. Company profile, an introduction to the lego group. Technical report, 2010.

[118] F. Vincent. Traitement numérique du signal. *Lecture Notes, ISAE ENSICA*, 2008-2009.

[119] Q. Li, J. Shi, and K.S. Chen. A generalized power law spectrum and its applications to the backscattering of soil surfaces based on the integral equation model. *IEEE Transactions on Geoscience and Remote Sensing*, 40(2):271–280, 2002.

[120] N. Baghdadi, M. Aubert, and M. Zribi. Use of TerraSAR-X data to retrieve soil moisture over bare soil agricultural fields. *IEEE Geoscience and Remote Sensing Letters*, 9(3):512–516.

[121] A. Merzouki, H. McNairn, and A. Pacheco. Mapping soil moisture using RADARSAT-2 data and local autocorrelation statistics. *IEEE Journal of Selected Topics in Applied Earth Observations and Remote Sensing*, 4(1):128–137.

[122] P.C. Dubois, E. Rignot, and J.J. van Zyl. Direction angle sensitivity of agricultural field backscatter with airsar data. *[Proceedings] IGARSS '92 International Geoscience and Remote Sensing Symposium*.

[123] Y. Oh and J.Y. Hong. Effect of surface profile length on the backscattering coefficients of bare surfaces. *IEEE Transactions on Geoscience and Remote Sensing*, 45(3):632–638.

[124] M. Levoy. *Volume rendering using the fourier projection-slice theorem*. Computer Systems Laboratory, Stanford University, 1992.

[125] M. N. Asl. Analytical image reconstruction methods in emission tomography. *Journal of Biomedical Science and Engineering*, 06(01):100–107, 2013.

[126] S. Srivastava, S. Cote, S. Muir, and R. Hawkins. The radarsat-1 imaging performance, 14 years after launch, and independent report on radarsat-2 image quality. In *Geoscience and Remote Sensing Symposium (IGARSS), 2010 IEEE International*, pages 3458–3461, July 2010.

[127] M. W. J. Davidson, T. Le Toan, F. Mattia, G. Satalino, T. Manninen, and M. Borgeaud. On the characterization of agricultural soil roughness for radar remote sensing studies. *IEEE Transactions on Geoscience and Remote Sensing*, 38(2):630–640, Mar 2000.

[128] K. J. Tansey and A. C. Millington. Investigating the potential for soil moisture and surface roughness monitoring in drylands using ers SAR data. *International Journal of Remote Sensing*, 22(11):2129–2149, Jan 2001.

[129] L. Prévot, I. Champion, and G. Guyot. Estimating surface soil moisture and leaf area index of a wheat canopy using a dual-frequency (c and x bands) scatterometer. *Remote Sensing of Environment*, 46(3):331–339, Dec 1993.

[130] M.S. Moran, A. Vidal, D. Troufleau, Y. Inoue, and T.A. Mitchell. Ku- and c-band SAR for discriminating agricultural crop and soil conditions. *IEEE Transactions on Geoscience and Remote Sensing*, 36(1):265–272, 1998.

[131] T. Mo, J.R. Wang, and T.J. Schmugge. Estimation of surface roughness parameters from dual-frequency measurements of radar backscattering coefficients. *IEEE Transactions on Geoscience and Remote Sensing*, 26(5):574–579, 1988.

[132] K.S. Rao, S. Raju, and J.R. Wang. Estimation of soil moisture and surface roughness parameters from backscattering coefficient. *IEEE Transactions on Geoscience and Remote Sensing*, 31(5):1094–1099, 1993.

[133] R. Bindlish and A. P. Barros. Multifrequency soil moisture inversion from SAR measurements with the use of iem. *Remote Sensing of Environment*, 71(1):67–88, Jan 2000.

[134] M. Zribi and M. Dechambre. A new empirical model to retrieve soil moisture and roughness from c-band radar data. *Remote Sensing of Environment*, 84(1):42–52, Jan 2003.

[135] M.M. Rahman, M.S. Moran, D.P. Thoma, R. Bryant, C.D. Holifield Collins, T. Jackson, B.J. Orr, and M. Tischler. Mapping surface roughness and soil moisture using multi-angle radar imagery without ancillary data. *Remote Sensing of Environment*, 112(2):391–402, Feb 2008.

[136] J. Mccauley, C. Breed, G. Schaber, W. Mchugh, B. Issawi, C. Haynes, M. Grolier, and A. Kilani. Paleodrainages of the eastern sahara-the radar rivers revisited (sir-a/b implications for a mid-tertiary trans-afnrcan drainage system). *IEEE Transactions on Geoscience and Remote Sensing*, GE-24(4):624–648, Jul 1986.

[137] A. Le Morvan, M. Zribi, N. Baghdadi, and A. Chanzy. Soil moisture profile effect on radar signal measurement. *Sensors*, 8(1):256–270, Jan 2008.

[138] F. Covello, F. Battazza, A. Coletta, G. Manoni, and G. Valentini. Cosmoskymed mission status: Three out of four satellites in orbit. *2009 IEEE International Geoscience and Remote Sensing Symposium*, 2009.

[139] Airbus Defense and Space. Technical information, terrasar-x. `http://www.geo-airbusds.com/en/903-technical-information`.

[140] Gisat. Satellite data information, ALOS. `http://www.gisat.cz/content/en/satellite-data/supplied-data/high-resolution/satelite/alos`.

[141] ESA, Sentinel Online. Sentinel-1 SAR, Revisit and Coverage. `https://sentinel.esa.int/web/sentinel/user-guides/sentinel-1-sar/revisit-and-coverage`.

[142] The Canola Council of Canada. Growth Stages of the Canola Plant. `http://www.canolacouncil.org/crop-production/canola-grower's-manual-contents/chapter-3-growth-stages/growth-stages`.

[143] S. Suzuki, Y. Kankaku, H. Imai, and Y. Osawa. Overview of alos-2 and alos-3. *Earth Observing Missions and Sensors: Development, Implementation, and Characterization II*, Nov 2012.

[144] R. Torres, P. Snoeij, D. Geudtner, D. Bibby, M. Davidson, E. Attema, P. Potin, B. Rommen, N. Floury, M. Brown, and et al. GMES Sentinel-1 mission. *Remote Sensing of Environment*, 120:9–24, May 2012.

[145] K. Metselaar, V Versace, and R Feddes. Root-depth profiles of important agricultural crops. In *International symposium 'Root Research and Application'*, pages 2–4, 2009.

[146] A. Tabatabaeenejad, M. Burgin, X. Duan, and M. Moghaddam. P-band radar retrieval of subsurface soil moisture profile as a second-order polynomial: First airmoss results. *IEEE Transactions on Geoscience and Remote Sensing*, 53(2):645–658, Feb 2015.

[147] P. Dubois-Fernandez, H. Oriot, C. Coulombeix, H. Cantalloube, O. Ruault du Plessis, T. Le Toan, S. Daniel, J. Chave, L; Blanc, M. Davidson, and et al. Tropisar: Exploring the temporal behavior of p-band SAR data. *2010 IEEE International Geoscience and Remote Sensing Symposium*, Jul 2010.

[148] K. Scipal, M. Arcioni, J. Chave, J. Dall, F. Fois, T. LeToan, C-C. Lin, K. Papathanassiou, S. Quegan, F. Rocca, and et al. The biomass mission - an esa earth explorer candidate to measure the biomass of the earth's forests. *2010 IEEE International Geoscience and Remote Sensing Symposium*, Jul 2010.

[149] R. Hoeben and P. A. Troch. Assimilation of active microwave observation data for soil moisture profile estimation. *Water Resources Research*, 36(10):2805–2819, Oct 2000.

[150] M. Bonavita. Numerical Weather prediction at the European Centre for Medium-Range Weather Forecasts. `http://www.inverseproblems.info/reading:summer_school_2013`, 2013.

[151] W. Wolfgang and P. Carsten. Has SAR failed in soil moisture retrieval? `http://earth.esa.int/workshops/salzburg04/papers_posters/4B4_wagner_76.pdf`, 2004.

[152] M. Trudel, F. Charbonneau, and R. Leconte. Using radarsat-2 polarimetric and envisat-asar dual-polarization data for estimating soil moisture over agricultural fields. *Canadian Journal of Remote Sensing*, 38(4):514–527, 2012.

[153] H. McNairn, A. Merzouki, A. Pacheco, and J. Fitzmaurice. Monitoring soil moisture to support risk reduction for the agriculture sector using radarsat-2. *Selected Topics in Applied Earth Observations and Remote Sensing, IEEE Journal of*, 5(3):824–834, June 2012.

[154] E. P. W. Attema and Fawwaz T. Ulaby. Vegetation modeled as a water cloud. *Radio Science*, 13(2):357–364, Mar 1978.

[155] T. Jackson. Vegetation water content mapping using landsat data derived normalized difference water index for corn and soybeans. *Remote Sensing of Environment*, 92(4):475–482, Sep 2004.

[156] F. T. Ulaby, P. C. Dubois, and J. van Zyl. Radar mapping of surface soil moisture. *Journal of Hydrology*, 184(1-2):57–84, Oct 1996.

[157] T. Manninen, P. Stenberg, M. Rautiainen, P. Voipio, and H. Smolander. Leaf area index estimation of boreal forest using envisat asar. *IEEE Transactions on Geoscience and Remote Sensing*, 43(11):2627–2635, Nov 2005.

[158] G. Seguin and S. Ahmed. RADARSAT constellation, project objectives and status. *2009 IEEE International Geoscience and Remote Sensing Symposium*, 2009.

[159] K. Tomiyasu. Synthetic aperture radar in geosynchronous orbit. *1978 Antennas and Propagation Society International Symposium*, 1978.

[160] S. Hobbs, C. Mitchell, B. Forte, R. Holley, B. Snapir, and P. Whittaker. System design for geosynchronous synthetic aperture radar missions. *IEEE Transactions on Geoscience and Remote Sensing*, 52(12):7750–7763, Dec 2014.

[161] NASA SESWG. Global Earthquake Satellite System (GESS): A 20-Year Plan to Enable Earthquake Prediction. `http://solidearth.jpl.nasa.gov/gess2.html`, March 2003.

[162] D. Bruno and S. Hobbs. interferometry, vegetation , and sar integration time. *ESA, Fringe workshop*, 2009.

[163] R. J. Barneveld, M. Seeger, and I. Maalen-Johansen. Assessment of terrestrial laser scanning technology for obtaining high-resolution DEMs of soils. *Earth Surface Processes and Landforms*, 38(1):90–94, Nov 2012.

[164] I.J. Davenport, N. Holden, and R.J. Gurney. Characterizing errors in airborne laser altimetry data to extract soil roughness. *IEEE Transactions on Geoscience and Remote Sensing*, 42(10):2130–2141, Oct 2004.

[165] R. Turner, R. Panciera, M. A. Tanase, K. Lowell, J. M. Hacker, and J. P. Walker. Estimation of soil surface roughness of agricultural soils using airborne LiDAR. *Remote Sensing of Environment*, 140:107–117, Jan 2014.

Appendix A

All DEMs for field 1 period 1

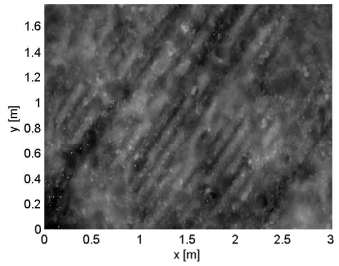

Figure A.1: 03 Sep 2013

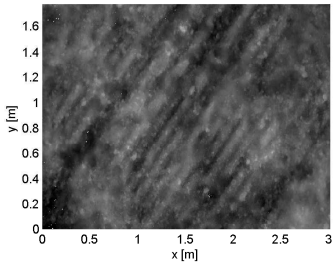

Figure A.2: 08 Sep 2013

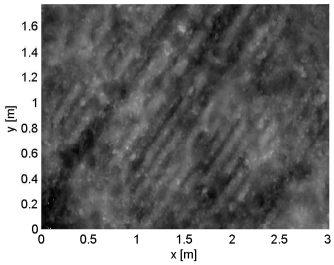

Figure A.3: 10 Sep 2013

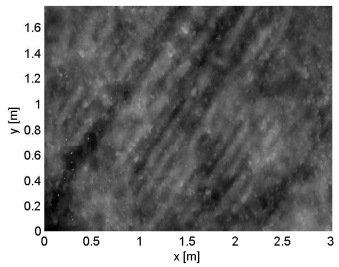

Figure A.4: 17 Sep 2013

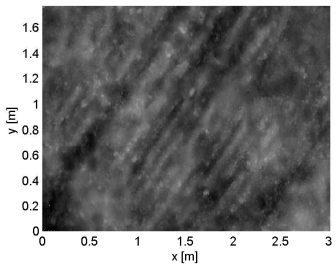

Figure A.5: 30 Sep 2013

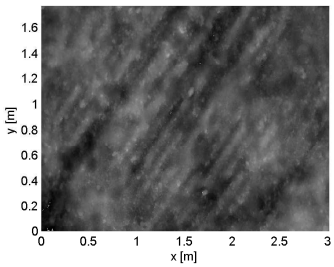

Figure A.6: 08 Oct 2013

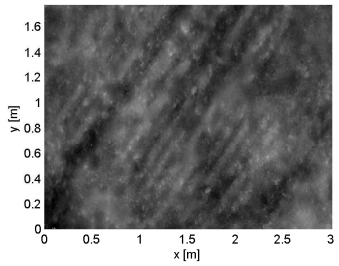

Figure A.7: 14 Oct 2013

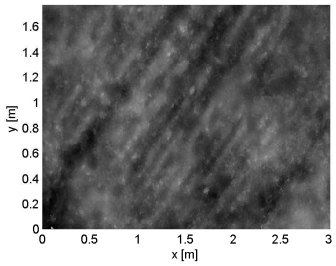

Figure A.8: 18 Oct 2013

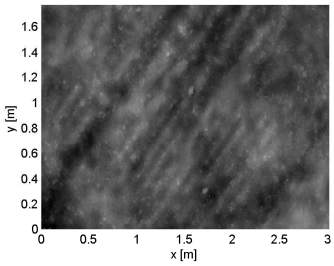

Figure A.9: 25 Oct 2013

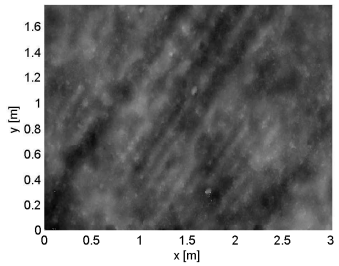

Figure A.10: 25 Nov 2013

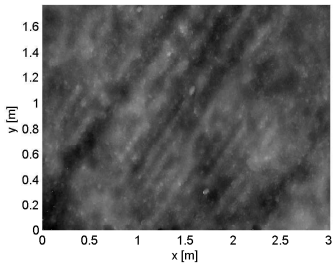

Figure A.11: 11 Nov 2013

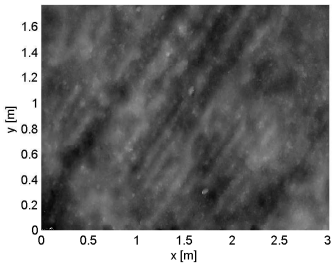

Figure A.12: 20 Nov 2013

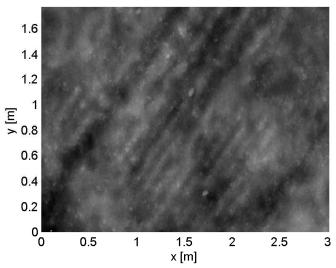

Figure A.13: 01 Nov 2013

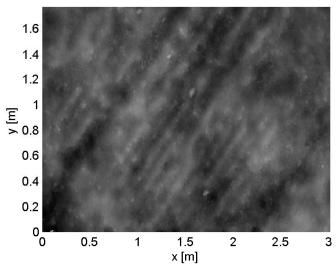

Figure A.14: 05 Dec 2013

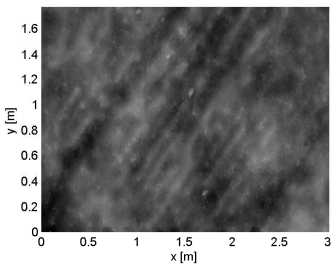

Figure A.15: 12 Dec 2013

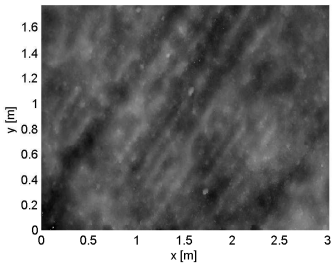

Figure A.16: 18 Dec 2013

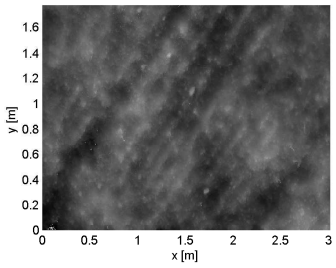

Figure A.17: 17 Jan 2014

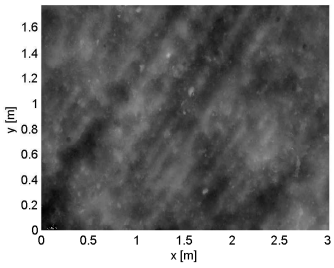

Figure A.18: 24 Mar 2014

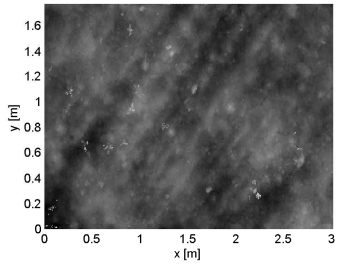

Figure A.19: 02 May 2014

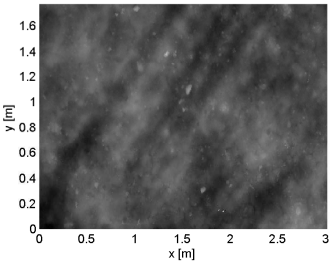

Figure A.20: 12 Jun 2014

Appendix B

List of Matlab codes

OhModel_contours Displays contours of the different quantity of the Oh model - σ^0_{vh}, p, q, σ^0_{hh}, σ^0_{vv}. This code is used for Fig. 2.3.

points_vs_nberOfImages Multiple linear regression between (1) number of point of the point cloud and number of images, (2) point density and pixel density, (3) point density and pixels density divided by pixel size. This code is used for Fig. 5.2.

comparisonDEMAvsDEMB Plots DEM A, DEM B, and (DEM B - DEM A) for the field 2 05/12/2013. This code is used for Fig 5.3 and 5.4.

RMSheight_spatialStatistics Plots RMS height against DEM length, for detrending with plane fit removal or detrending with high-pass filtering. This code is used for section 5.2.

correlationLength_spatialStatistics Plots correlation length against DEM length, for detrending with plane fit removal or detrending with high-pass filtering. This code is used for section 5.2.

anisotropy Computes RMS height and correlation length for multiple rainbows of transects from 0° to 180°. This code is used for section 5.2.4.

flashingFields_2Dpsd Simulates a rough surface with sinusoidal pattern, and compare results obtained roughness parameters computed along transects and directional roughness parameters computed from the 2D PSD. This code is used for section 5.2.5.

readDataLogger_period1 Reads and displays the data recorded by the data logger along with available SfM measurements of RMS height and correlation length. for period 1, field 1 and field 2. This code is used for section 5.3.2.

readDataLogger_period2 Reads and displays the data recorded by the data logger along with available SfM measurements of RMS height and correlation length. for period 2, field 1 and field 2. This code is used for section 5.3.2.

changeInPowerSpectrum_f2_per1 Displays change in PSD for DEMs A field 2 period 1. This code is used for section 5.3.3.

changeInPowerSpectrum_f1_per2 Displays change in PSD for DEMs A field 2 period 1. This code is used for section 5.3.3.

changeInPowerSpectrum_f2_per2 Displays change in PSD for DEMs A field 2 period 1. This code is used for section 5.3.3.

effectOfRoughnessTemporalChanges Analyzes the effect of changes in surface roughness on σ^0_{hh} and σ^0_{vv} with the Oh model. In particular, the simulation shows error on estimation of soil moisture when changes in surface roughness are neglected. This code is used for section 5.3.4.

sigma0vsSoilMoisture Display time series of Radarsat-2 measurements (σ^0_{hh}, σ^0_{vv}, σ^0_{vh}) and time series of in situ soil moisture measurements for fields 6, 8, 9, 12, 13. This code is used for section 6.1.1.

modelInversion_vh_hh_vv Model inversion with radarsat-2 measurements of σ^0_{hh}, σ^0_{vv}, σ^0_{vh}. First, measurement error is made Gaussian with power transform. Then soil moisture and RMS height are retrieved from χ^2 minimization. Finally the χ^2 is applied to resampled data set to determine confidence region. This code is used for section 6.1.2.

modelInversion_hh_vv Model inversion with radarsat-2 measurements of σ^0_{hh}, σ^0_{vv}. First, measurement error is made Gaussian with power transform. Then soil moisture and RMS height are retrieved from χ^2 minimization. Finally the χ^2 is applied to resampled data set to determine confidence region. This code is used for section 6.1.2.

bandsOfContours Plots bands of contours of σ^0_{hh}, σ^0_{vv}, σ^0_{vh} simulated with the Oh model, to analyze the features which drives soil moisture / RMS height uncertainty. This code is used for section 6.1.3.1.

uncertaintyMap_simulation Computes the joint uncertainy on soil moisture and RMS height for a grid of soil moisture and RMS height, and a range of available looks. Uncertainty is determined from repeated χ^2 minimization with synthetic data. In the simulation, different wave lengths and polarizations can be combined. The final results are saved, and can be displayed with the script uncertaintyMap_plot.m. This code is used for section 6.1.3, 6.2.2 and 6.2.3.

uncertaintyMap_plot Gathers the results obtained from uncertaintyMap_simulation.m for different ranges of number of looks. And displays contours of number of looks to reach a given uncertainty on soil moisture or on RMS height. This code is used for section 6.1.3, 6.2.2 and 6.2.3.